UNIWERSYTET MARII CURIE-SKŁODOWSKIEJ
W LUBLINIE
Wydział Matematyki, Fizyki i Informatyki

Kierunek: **Fizyka**

Błażej Kuźma
Nr albumu: 983772

Symulacje numeryczne magnetycznie zdominowanej atmosfery Słońca

Numerical simulations of magnetically dominated atmosphere of the Sun

Praca doktorska
napisana w Zakładzie Astrofizyki i Teorii Grawitacji
pod kierunkiem prof. dr hab. Krzysztofa Murawskiego

LUBLIN ROK 2020

Prawda blisko jest

Idąc za nią tak łatwo się potknąć

Dlatego tak niewielu chce jej dotknąć

Piotr ”donGURALesko” Górny

Składam serdeczne podziękowania mojemu promotorowi prof. dr hab. Krzysztofowi Murawskiemu za opiekę naukową, wyrozumiałość, cierpliwość oraz za wszelką pomoc okazaną mi w realizacji tej pracy. W szczególności zaś dziękuję za zaszczepienie we mnie ciekawości i pokazanie, jak fascynujący obiekt miałem szczęście badać.

Spis treści

Niniejsza praca została napisana w oparciu o badania własne zaprezentowane w publikacjach [1] - [3] oraz [5] - [9] z poniższej listy. Badania te są obecnie kontynuowane w ramach złożonego do druku artykułu “Numerical simulations of the lower solar atmosphere heating by two-fluid nonlinear Alfvén waves” [10], a kolejne publikacje są w przygotowaniu. Wszystkie wykorzystane publikacje zostały załączone w dalszej części niniejszej pracy (strona 48 i kolejne).

Lista publikacji własnych

1. **Kuźma, B.**, Murawski, K., Solov’ev, A. 2015, A&A, 577, A138.
2. **Kuźma, B.**, Murawski, K., Zaqarashvili, T. V., et al. 2017, A&A 597, A133.
3. **Kuźma, B.**, Murawski, K., Kayshap, P., et al. 2017, ApJ, 849, 78.
4. Murawski, K., Kayshap, P., Srivastava, A. K., Pascoe, D. J., Jelínek, P., **Kuźma, B.**, Fedun, V. 2018, MNRAS, 474, 77.
5. **Kuźma, B.**, Murawski, K. 2018, ApJ, 866, 50.
6. Srivastava, A. K., Murawski, K., **Kuźma, B.**, et al. 2018, Nature Astronomy, 2, 951.
7. **Kuźma, B.**, Wójcik D., Murawski, K. 2019, ApJ, 878, 81.
8. Wójcik D, **Kuźma, B.**, Murawski, K., Srivastava, A., 2019, ApJ, 884, 127.
9. Wójcik D, **Kuźma, B.**, Murawski, K., Musielak, Z. E., 2019, ApJ, przyjęty do druku.
10. **Kuźma, B.**, Wójcik D, Murawski, K., Yuan, D., Poedts, S., 2019, A&A, w recenzji.

1 Wstęp

W pierwszej części niniejszej rozprawy doktorskiej przedstawiam ogólny obraz przedmiotu prowadzonych badań, to jest magnetycznie zdominowanej atmosfery Słońca, jak również obecny stan wiedzy na jej temat na podstawie wybranej literatury. Wyszczególniam tu dwa główne problemy heliofizyki, do rozwiązania których mogą przyczynić się prowadzone przeze mnie badania: problem ogrzewania korony słonecznej oraz początków wiatru słonecznego. Omawiam również cele i motywacje, które stały za wyborem konkretnych metod badawczych, a przede wszystkim nowatorskich dwupłynowych symulacji numerycznych.

1.1 Atmosfera Słońca

Medium znajdujące się bezpośrednio nad widoczną powierzchnią Słońca (fotosferą) nazywane jest atmosferą słoneczną. Składa się ona z rozrzedzonej, częściowo zjonizowanej i przenikniętej polem magnetycznym plazmy, stąd jest unikalnym środowiskiem badawczym, pozwalającym bezpośrednio obserwować szereg interesujących procesów zachodzących w jej ekstremalnych warunkach. Ze względu na duże różnice we właściwościach fizycznych, temperaturze (Erdélyi i Ballai 2007), gęstości masy i poziomie jonizacji (Hansteen i in. 1997), rozróżniamy kilka warstw w atmosferze słonecznej (Rys. 1, Rys. 2). U jej podstawy umiejscowiona jest wspomniana już fotosfera o grubości 500 km i o średniej temperaturze wynoszącej około 5600 K. Jest ona około 10^4 razy bardziej rozrzedzona niż próżnia uzyskiwana w laboratorium. Wyżej znajduje się warstwa o grubości około 1500 km, zwana chromosferą. Intuicyjnie spodziewamy się spadku temperatury plazmy w miarę oddalania się od powierzchni Słońca. Jest jednak dokładnie odwrotnie - obserwacje potwierdzają stopniowy wzrost temperatury w chromosferze i gwałtowny jej skok w tak zwanym obszarze przejściowym, aż do ponad jednego miliona Kelvinów w znajdującej się powyżej koronie słonecznej (Grotrian 1939, Edlén 1943, Aschwanden 2004). Ta, rozciągając się do 2-3 promieni słonecz-

nych, stopniowo przekształca się w międzyplanetarny wiatr słoneczny - strumień cząstek docierających do Ziemi i poza nią (Meyer-Vernet 2007). Okazuje się, że ze względu na stosunkowo niskie temperatury w fotosferze i chromosferze, warstwy te są zdominowane przez cząstki neutralne (neutrały), podczas gdy korona powyżej jest praktycznie całkowicie zjonizowana. Zasadnym jest stwierdzenie, że chromosfera stanowi swoiste przejście pomiędzy dwiema bardzo różniącymi się warstwami - powierzchnią Słońca i jego koroną.

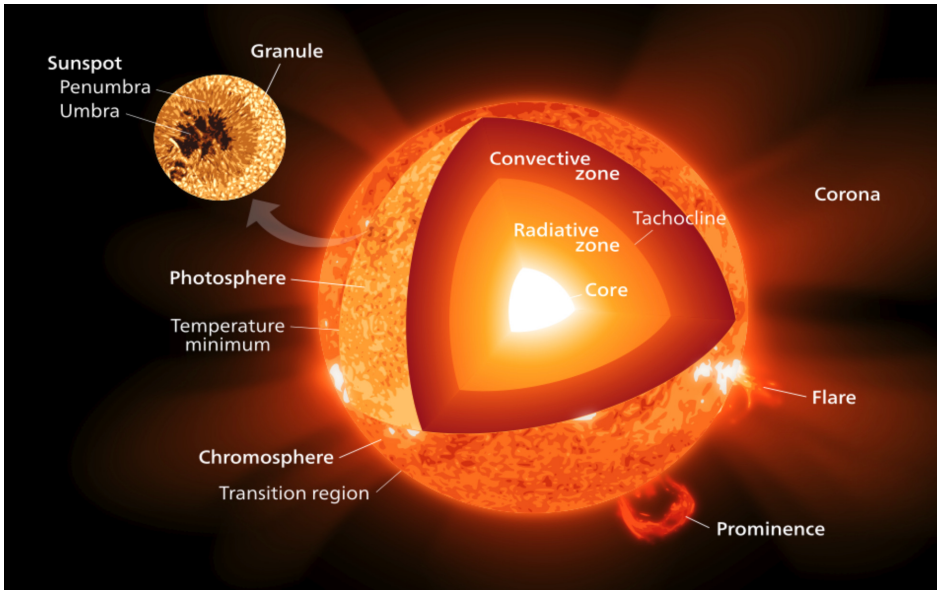

Rysunek 1: Schemat budowy Słońca z zachowaniem skali (dzięki uprzejmości NASA).

Wbrew nasuwającym się po przeczytaniu powyższego akapitu skojarzeniom o statycznych warstwach, atmosfera Słońca to wysoce dynamiczny ośrodek (Rys. 3). Warstwy wyróżnić można dopiero po uśrednieniu cech plazmy w kierunku poziomym. Pod fotosferą znajdują się komórki konwekcyjne, w których plazma pozostaje w nieustającym ruchu - unosi się ku górze gorącymi strumieniami, aby następnie gwałtownie ostygnąć po osiągnięciu fotosfery i rozpocząć swój ruch z powrotem w głąb warstwy konwekcyjnej. Widocznym na powierzchni Słońca efektem działania tych komórek konwekcyjnych jest granulacja. Granule mają

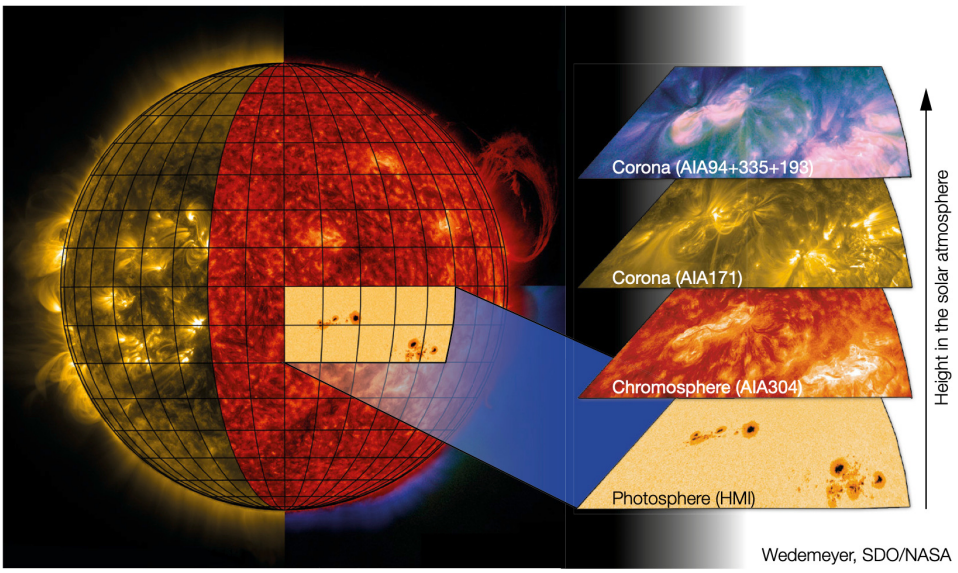

Rysunek 2: Obserwowane warstwy atmosfery Słońca: od fotosfery po koronę (Wedemeyer 2016).

nieregularny kształt ze średnicą około 1.5 Mm, istnieją średnio przez 8 - 20 minut i są one z kolei skupione w tak zwane supergranule (Rys. 1, Rys. 3).

Powyżej fotosfery, czyli w chromosferze, obserwujemy liczne wyrzuty plazmy, nazywane strumieniami (z ang. jets). Szczególnym ich przypadkiem są spikule. Wyłaniając się z tła chromosferycznego ponad brzegami supergranul przypominają swoistą trawę pokrywającą Słońce (Rys. 3). Omówione zostaną one szczegółowo w dalszej części niniejszej pracy.

Nawet zjonizowana, gorąca i skrajnie rozrzedzona korona słoneczna pozostaje w ciągłym ruchu. Wiatr słoneczny, to jest strumień naładowanych cząstek (głównie elektronów i protonów z wodoru, wraz z jądrami atomowymi, takimi jak helu) wymiatający jej materię w kierunku przestrzeni kosmicznej, jest znacznie zróżnicowany pod względem prędkości (Bierman 1951; Parker 1965). Wyróżniamy szybki, równomierny wiatr, emanujący z polarnych dziur koronalnych i w odległości 1 au od Słońca poruszający się z prędkością około 750 km s^{-1}, a także powolny,

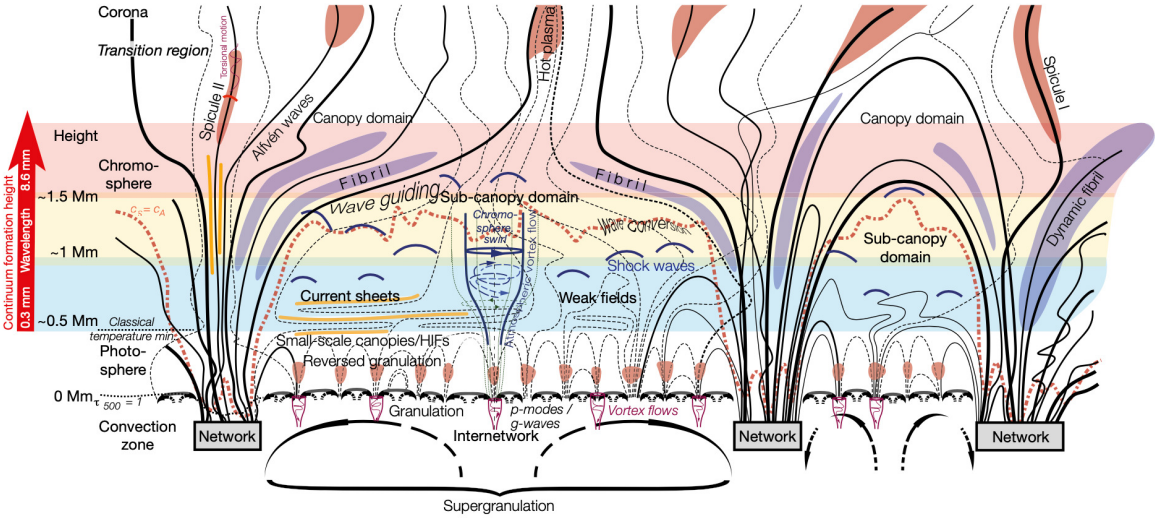

Rysunek 3: Schemat budowy atmosfery w obszarze spokojnego Słońca, od fotosfery, umiejscowionej w $y = 0$, po koronę (Wedemeyer 2016).

sporadyczny, pochodzący z aktywnych obszarów równikowych i osiągający 400 km s^{-1}. Linie pola magnetycznego rozciągają się promieniowo w obszarach dziur koronalnych i nie zapętlają się bezpośrednio z powrotem do Słońca, zapewniając otwartą ścieżkę dla szybkiej plazmy, która wymyka się grawitacji.

Na uwagę zasługuje problem pola magnetycznego w atmosferze Słońca. Wytwarzane w jego głębi w procesie dynama magnetycznego w pobliżu tachokliny (w warstwie pomiędzy radiacyjnie zdominowanym centrum, a konwekcyjnie zdominowanymi warstwami zewnętrznymi), unoszone jest poprzez plazmę ku powierzchni Słońca. Tam, wmrożone w plazmę pole magnetyczne wyłania się ponad fotosferę w formie dwóch najczęściej spotykanych struktur (Rys. 3). Pierwszą są zamknięte magnetyczne pętle koronalne, często zgrupowane w postaci arkad. Drugą natomiast - są tuby magnetyczne o otwartych liniach pola. W obszarach szczególnie silnego pola magnetycznego plazma pozostaje chłodna i rozrzedzona. Stąd też obszary te pozostają ciemne na tle tarczy słonecznej i nazywane są plamami słonecznymi. W momencie zetknięcia się przeciwnych linii pola magne-

tycznego dochodzi do ”rekoneksji” - przełączenia linii, w wyniku którego energia uwięziona w postaci pola magnetycznego zostaje uwolniona do otaczającej plazmy.

Warto podkreślić, że poprzez proces ”wmrożenia” w plazmę pole magnetyczne odgrywa jedną z kluczowych ról w procesach zachodzących w atmosferze Słońca. Ruchy plazmy wpływają na kształt pola magnetycznego - a pole magnetyczne zmienia ruch plazmy. Do szczególnego przypadku dochodzi, kiedy ciśnienie magnetyczne znacząco przewyższa ciśnienie hydrostatyczne plazmy. Wtedy zachodzące procesy są zdominowane przez pole magnetyczne. Jest tak głównie w obszarze plam słonecznych i w koronie.

1.2 Centralne problemy heliofizyki

Wspomniane wcześniej zjawiska, to jest gwałtowny skok temperatury plazmy w obszarze przejściowym oraz generacja i przyspieszanie wiatru słonecznego, stanowią dwa najpoważniejsze i do tej pory nie rozwiązane problemy heliofizyki. W celu ich rozwiązania musimy odpowiedzieć na kilka powiązanych ze sobą pytań:

a) jak transportowana jest energia do wyższych warstw atmosfery słonecznej?

b) w jakich procesach energia ta zamieniana jest na energię cieplną?

c) jak i w których warstwach atmosfery generowany jest wiatr słoneczny?

d) jak do wyższych warstw atmosfery słonecznej transportowana jest materia uzupełniająca straty związane z wiatrem słonecznym?

Aby wywołać gwałtowny skok/spadek właściwości fizycznych w obszarze przejściowym a także, aby uzupełniać straty radiacyjne, do korony słonecznej musi być dostarczana energia. Fale jako potencjalne źródło i mechanizm transportu potrzebnej energii zostały zaproponowane już przez Biermanna (1946), Schwarzschilda (1948) i Schatzmana (1949). Typowe fale rozchodzące się w plazmie w obecności pola magnetycznego stają się falami magnetohydrodynamicznymi (MHD) (Alfvén 1942). Fale te można podzielić na fale Alfvéna oraz powolne i szyb-

kie fale magnetoakustyczne (Nakariakov i Verwichte 2005, Priest 2014). Ostatnie dwa rodzaje stają się odpowiednio wolnymi i szybkimi falami magnetoakustyczno-grawitacyjnymi w obecności pola grawitacyjnego. Jednakże, gdy rozpatrywane są niższe warstwy atmosfery słonecznej, jednopłynowe podejście MHD należy uznać za zbyt uproszczone i musi być ono zastąpione teorią wielopłynową.

Problem wiatru słonecznego wymaga z kolei ustalenia źródeł przepływu materii, który dostarcza unoszoną wraz z wiatrem plazmę. Wcześniej opracowane modele zakładały, że wiatr słoneczny bierze swój początek w wewnętrznych obszarach korony (np. Tu 1987). Niedawno Tu (2005) odkrył odpływy plazmy przechodzące w wiatr słoneczny już na wysokościach 5 do 20 Mm ponad fotosferą. Odpływy te osiągają prędkość do 10 km s^{-1} na wysokości 20 Mm. Nacisk położono również na poszukiwanie podobnych odpływów w regionie chromosfery / obszaru przejściowego. Stwierdzono, iż odpływy plazmy mogą być wywoływane zarówno przez strumienie i wyrzuty plazmy (np. De Pontieu i in. 2007), wynurzające się skręcone pole magnetyczne (np. Yang i in. 2013) a za zapewnienie pędu poruszającej się w górę plazmie odpowiadać mogą fale MHD (np. Arber i in. 2016), w tym fale Alfvéna (Matsumoto i Suzuki 2012).

Pomimo badań teoretycznych, prowadzonych na szeroką skalę obserwacjach kosmicznych i naziemnych oraz licznych symulacjach numerycznych oba problemy uznaje się oficjalnie za nierozwiązane.

1.3 Cele niniejszej pracy

Celem niniejszej pracy jest zbadanie, poprzez wykonanie symulacji numerycznych, zjawisk zachodzących w realistycznej, grawitacyjnie uwarstwionej i przenikniętej polem magnetycznym atmosferze Słońca. Skupiając się na modelach płynowych (jednopłynowy model MHD oraz dwupłynowy model częściowo zjonizowanej plazmy), zbadane zostały mechanizmy powstawania i ewolucji różnego typu wyrzutów plazmy chromosferycznej, oraz rozchodzenia fal w strukturach atmosfery Słońca. Panuje zgoda, że procesy falowe odgrywają istotną rolę w trans-

porcie energii i jej wyzwalaniu w plazmie atmosfery słonecznej. Do tej pory były one badane w ramach modeli MHD. Jednak, ze względu na dominację neutrałów w niższych warstwach atmosfery, rola oddziaływań pomiędzy jonami i neutrałami nie może być pomijana, i w rezultacie modele MHD nie mogą być uznane za wystarczające. Procesy fizyczne zachodzące w fotosferze i chromosferze powinny być ponownie zbadane przy użyciu bardziej realistycznych modeli opisujących dokładniej częściowo zjonizowaną plazmę. Efekty dwupłynowe zdają się być istotne dla przepływu energii, masy i pędu, z tego też względu mogą być związane z ciągle nierozwiązanymi problemami heliofizyki, to jest: ogrzewaniem chromosfery i korony (np. Aschwanden 2004) oraz generacją i przyspieszaniem wiatru słonecznego (np. Meyer-Vernet 2007). Atmosfera słoneczna działa jak filtr, przepuszczając do wyższych warstw tylko fale o częstotliwościach powyżej częstotliwości odcięcia, podczas gdy fale o długich okresach zanikają wraz z wysokością (Lamb 1909, 1910). W związku z tym, że dwupłynowe fale o wysokich częstotliwościach mają potencjał do dostarczenia masy i energii do wyższych warstw atmosfery słonecznej, różne sposoby zamiany tej energii na energię cieplną, jak poprzez zderzenia jonów i neutrałów, powinny być zbadane w następnej kolejności.

Omawiane symulacje numeryczne stymulowane są przez najnowsze dane obserwacyjne dotyczące mechanizmów związanych z ogrzewaniem chromosfery i korony, generowaniem strumieni i wyrzutów plazmy, wiatru słonecznego i falami w chromosferze - jest to szeroki zakres zjawisk słonecznych, w których medium zmienia się z zimnego, zdominowanego przez neutrały, w gorące i prawie całkowicie zjonizowane. Część procesów jest rozważana w ramach modeli MHD, w większości jednak skupiamy się na zjawiskach, dla zrozumienia których prawidłowe modelowanie neutrałów może się okazać niezbędne. Zjawiska te nie były dotychczas analizowane ani symulowane w takim zakresie, dlatego uzyskane dane mają szanse być przełomowe, dając bezprecedensowy wgląd we wszystkie wyżej wymienione kluczowe procesy heliofizyki. Do wykonania symulacji zostały użyte wysoce zaawansowane kody numeryczne FLASH, PLUTO i JOANNA, które

rozwiązują wiele problemów fizycznych w szerokim zakresie modeli plazmy (HD, MHD, dwupłynowym). Przeprowadzone porównania wykazały wyraźną korelację pomiędzy uzyskanymi numerycznie wynikami, a danymi obserwacyjnymi.

1.4 Organizacja pracy

Praca została uporządkowana tematycznie. Równania użyte do opisu plazmy astrofizycznej w przyjętych modelach opisane są w rozdziale 2.0. Pierwsze z omawianych projektów skupiają się wokół symulacji numerycznych spikul i strumieni plazmy (3.1 - 3.3). Następnie omówione zostały symulacje generowanych w fotosferze fal monochromatycznych (3.4 - 3.6). Finalne dwa projekty - to złożone symulacje atmosfery słonecznej, od górnych warstw konwekcyjnych aż po koronę (3.7 - 3.8). Każdy z nich opisany jest pod względem zakładanego celu, w szczególności obserwowanych zjawisk i procesów, które odtwarza i stara się wytłumaczyć . W podrozdziałach "Metodologia" opisane są szczegóły użytego modelu numerycznego i wykorzystanego kodu. Mogą one posłużyć w celu powtórzenia uzyskanych wyników, ich weryfikacji, jak i kontynuowania konkretnych badań. W opisie wyników i podsumowaniu każdego projektu ukazano jak wpłynął on na poszerzenie aktualnego stanu wiedzy. Pracę wieńczy "Podsumowanie" (4.0), skrócona literatura i załączone publikacje własne.

2 Modele plazmy astrofizycznej

Na wstępie omawiam dwa modele plazmy słonecznej użyte w symulacjach numerycznych. Ze względu na zróżnicowaną postać wykorzystanych w poszczególnych projektach modeli/równań (równania idealne, równania nieadiabatyczne), jak również na zmienne użycie członów dodatkowych (np. przewodnictwo cieplne, promieniowanie), szczegółowe omówienie użytego modelu oraz postać równań zawarta jest osobno w każdym artykule. Poniżej przedstawiam jedynie podstawowe omówienie równań użytych w modelu MHD oraz modelu dwupłynowym.

2.1 Równania magnetohydrodynamiczne

Opis plazmy słonecznej poprzez równania MHD łączy w spójną całość hydrodynamikę (równania Naviera-Stokesa) oraz elektrodynamikę (równania Maxwella). Dzięki temu możliwy jest opis przewodzącego prąd płynu w obecności pola magnetycznego. Istotne jest, iż w skutek indukcji magnetycznej w poruszającym się w obecności pola magnetycznego płynie powstaje prąd elektryczny. W wyniku działania siły Lorentza zachodzi oddziaływanie zwrotne powstałych prądów z polem magnetycznym, co z kolei wpływa na wielkość tego pola oraz ruch płynu. W dużym skrócie możemy powiedzieć, że pole magnetyczne wpływa na ruch plazmy, a ruch plazmy wpływa na pole magnetyczne. Dodatkowo w ośrodku opisywanym równaniami MHD może rozchodzić się dodatkowy rodzaj fal – tak zwane fale Alfvéna. Idealne, adiabatyczne równania MHD mają postać (Priest i in. 1982):

$$\frac{\partial \varrho}{\partial t} + \nabla \cdot (\varrho \mathbf{V}) = 0\,, \tag{1}$$

$$\frac{\partial (\varrho \mathbf{V})}{\partial t} + \nabla \cdot (\varrho \mathbf{V}\mathbf{V} + p) = \frac{1}{\mu}(\nabla \times \mathbf{B}) \times \mathbf{B} + \varrho \mathbf{g}\,, \tag{2}$$

$$\frac{\partial p}{\partial t} + \mathbf{V} \cdot \nabla p = -\gamma p \nabla \cdot \mathbf{V}\,, \tag{3}$$

$$\frac{\partial \mathbf{B}}{\partial t} = \nabla \times (\mathbf{V} \times \mathbf{B})\,, \quad \nabla \cdot \mathbf{B} = 0\,, \tag{4}$$

gdzie ϱ oznacza gęstość masy, p - ciśnienie gazu, $\mathbf{V}$ to prędkość plazmy, γ - indeks adiabatyczny, $\mathbf{B}$ - pole magnetyczne, μ - przenikalność magnetyczna, T to temperatura determinowana przez równanie gazu doskonałego:

$$p = \frac{k_\mathrm{B}}{m}\varrho T\,, \tag{5}$$

k_B - stała Boltzmanna, m - masa cząsteczkowa, a $g = 274.78\ \mathrm{m\,s^{-2}}$ - przyspieszenie grawitacyjne przy powierzchni Słońca.

2.2 Równania dwupłynowe

Równania MHD zakładają całkowitą jonizację płynu. W rzeczywistości poniżej obszaru przejściowego i powyżej fotosfery poziom jonizacji spada poniżej 1. Oznacza to, że chłodna plazma chromosferyczna składa się w większości z cząsteczek neutralnych. W związku z tym do opisu częściowo zjonizowanej plazmy używamy tak zwanych równań dwupłynowych (Braginskii 1956). Pierwszym płynem jest w pełni zjonizowana, oddziałująca z polem magnetycznym plazma, natomiast drugim jest nieoddziałujący magnetycznie gaz neutralny. Udział każdego z tych płynów determinowany jest przez stopień jonizacji, zaś sprzężone są one ze sobą poprzez zderzenia. Ze względu na małą masę elektronów, nie rozważamy trzeciego płynu, a zamiast tego wiążemy elektrony z jonami jako jeden płyn jonowo - elektronowy. Równania dwupłynowe zapisujemy w postaci (Oliver i in. 2016):

$$\frac{\partial \varrho_\mathrm{n}}{\partial t} + \nabla\cdot(\varrho_\mathrm{n}\mathbf{V}_\mathrm{n}) = S_\mathrm{r}\,, \tag{6}$$

$$\frac{\partial \varrho_\mathrm{i}}{\partial t} + \nabla\cdot(\varrho_\mathrm{i}\mathbf{V}_\mathrm{i}) = -S_\mathrm{r}\,, \tag{7}$$

$$\frac{\partial(\varrho_\mathrm{n}\mathbf{V}_\mathrm{n})}{\partial t} + \nabla\cdot(\varrho_\mathrm{n}\mathbf{V}_\mathrm{n}\mathbf{V}_\mathrm{n} + p_\mathrm{n}\mathbf{I}) = \varrho_\mathrm{n}\mathbf{g} + \mathbf{S}_\mathrm{m}\,, \tag{8}$$

$$\frac{\partial(\varrho_\mathrm{i}\mathbf{V}_\mathrm{i})}{\partial t} + \nabla\cdot(\varrho_\mathrm{i}\mathbf{V}_\mathrm{i}\mathbf{V}_\mathrm{i} + p_\mathrm{ie}\mathbf{I}) = \frac{1}{\mu}(\nabla\times\mathbf{B})\times\mathbf{B} + \varrho_\mathrm{i}\mathbf{g} - \mathbf{S}_\mathrm{m}\,, \tag{9}$$

$$\frac{\partial \mathbf{B}}{\partial t} = \nabla \times (\mathbf{V}_\mathrm{i} \times \mathbf{B}) \,, \quad \nabla \cdot \mathbf{B} = 0 \,, \tag{10}$$

$$\frac{\partial E_\mathrm{n}}{\partial t} + \nabla \cdot [(E_\mathrm{n} + p_\mathrm{n})\mathbf{V}_\mathrm{n}] = q_\mathrm{n} + \varrho_\mathrm{n} \mathbf{g} \cdot \mathbf{V}_\mathrm{n} + S_\mathrm{E} \,, \tag{11}$$

$$\frac{\partial E_\mathrm{i}}{\partial t} + \nabla \cdot \left[\left(E_\mathrm{i} + p_\mathrm{ie} + \frac{\mathbf{B}^2}{2\mu} \right) \mathbf{V}_\mathrm{i} - \frac{\mathbf{B}}{\mu} (\mathbf{V} \cdot \mathbf{B}) \right] = L_\mathrm{r} + q_\mathrm{i} + \varrho_\mathrm{i} \mathbf{g} \cdot \mathbf{V}_\mathrm{i} - S_\mathrm{E} \,. \tag{12}$$

Człony źródłowe opisujące jonizację/rekombinację, S_r, zmianę pędu ze względu na zderzenia, $\mathbf{S}_\mathrm{m}$, i zmiany energii, S_E, są dane przez:

$$S_\mathrm{r} = \varrho_\mathrm{i} (\alpha_\mathrm{r} \varrho_\mathrm{i} - \alpha_\mathrm{i} \varrho_\mathrm{n}) \,, \tag{13}$$

$$\mathbf{S}_\mathrm{m} = \alpha_\mathrm{c} \varrho_\mathrm{i} \varrho_\mathrm{n} (\mathbf{V}_\mathrm{i} - \mathbf{V}_\mathrm{n}) \,, \tag{14}$$

$$S_\mathrm{E} = \frac{1}{2} \alpha_\mathrm{c} \varrho_\mathrm{i} \varrho_\mathrm{n} (V_\mathrm{i}^2 - V_\mathrm{n}^2) + \frac{1}{\gamma - 1} \alpha_\mathrm{c} \varrho_\mathrm{i} \varrho_\mathrm{n} \frac{k_\mathrm{B}}{m_\mathrm{H} \mu_\mathrm{n}} (T_\mathrm{i} - T_\mathrm{n}) \,. \tag{15}$$

W powyższych równaniach indeksy $_\mathrm{i}$, $_\mathrm{n}$ i $_\mathrm{e}$ oznaczają odpowiednio jony, neutrały i elektrony, symbole $\varrho_\mathrm{i,n}$ gęstości masy, $\mathbf{V}_\mathrm{ie,n}$ prędkości, $p_\mathrm{ie,n}$ ciśnienia, $\mathbf{B}$ natężenie pola magnetycznego. Tak jak poprzednio temperatury, $T_\mathrm{i,n}$, określone są przez równania gazu doskonałego:

$$p_\mathrm{n} = \frac{k_\mathrm{B}}{m_\mathrm{H} \mu_\mathrm{n}} \varrho_\mathrm{n} T_\mathrm{n} \,, \quad p_\mathrm{ie} = \frac{k_\mathrm{B}}{m_\mathrm{H} \mu_\mathrm{i}} \varrho_\mathrm{i} T_\mathrm{i} \,. \tag{16}$$

Oddziaływanie pomiędzy gazem neutralnym i zjonizowaną plazmą, charakteryzuje się przez współczynnik tarcia (Zaqarashvili i in. 2011): $\alpha_\mathrm{in} = \alpha_\mathrm{ni} = \alpha_\mathrm{c}$, który możemy wyznaczyć używając formuły (Braginskii 1965):

$$\alpha_\mathrm{c} = \frac{4}{3} \sigma_\mathrm{in} \frac{\varrho_\mathrm{i} \varrho_\mathrm{n}}{m_\mathrm{H} \mu_\mathrm{i} + m_\mathrm{H} \mu_\mathrm{n}} \sqrt{\frac{8 k_\mathrm{B}}{\pi m_\mathrm{H}} \left(\frac{T_\mathrm{i}}{\mu_\mathrm{i}} + \frac{T_\mathrm{n}}{\mu_\mathrm{n}} \right)} . \tag{17}$$

Przekrój czynny na zderzenia σ_in zależy ściśle od zakładanego modelu zderzeń. W naszych badaniach korzystamy zarówno z modelu klasycznego, jak i kwantowo - mechanicznego (Vranjes i Krstic 2013). Warto zauważyć, że częstotliwość zderzeń między jonami a neutrałami różni się co do wartości od częstotliwości zderzeń neutrały - jony (Ballester i in. 2018), i można je zapisać jako:

$$\nu_\mathrm{in} = \frac{\alpha_\mathrm{c}}{\varrho_\mathrm{i}} \,, \quad \nu_\mathrm{ni} = \frac{\alpha_\mathrm{c}}{\varrho_\mathrm{n}} \,. \tag{18}$$

3 Badania własne - symulacje numeryczne zjawisk w atmosferze Słońca

W trzeciej części niniejszej rozprawy prezentuję opis opublikowanych wyników badań własnych. Publikacje zostały przedstawione w porządku tematycznym.

Pierwsze trzy z omawianych projektów skupiają się na problematyce wyrzutów strumieni plazmy w atmosferze Słońca. Jest to temat istotny, gdyż strumienie te są najłatwiejszymi do zaobserwowania przepływami masy pomiędzy poszczególnymi warstwami atmosfery Słońca. Symulowane spikule mimo lokalnej natury, ze względu na ich liczną obecność w obserwacjach, mogą być odpowiedzialne za procesy w skali globalnej. Z kolei mody entropii zasługują na uwagę jako stosunkowo świeże odkrycie, rzucające nowe światło na transport masy i energii w obszarach aktywnych (Srivastava i in. 2018).

W dalszej części prezentowane są symulacje rozchodzenia się fal akustycznych i magnetohydrodynamicznych (w tym fal magnetoakustycznych i fal Alfvéna), w różnych strukturach magnetycznych obserwowanych na Słońcu. Kluczowa jest tu próba odpowiedzenia na pytania: czy fale te mogą transportować energię do wyższych warstw atmosfery Słońca? W jakim stopniu oraz w jakich procesach energia ta może zamieniać się w energię cieplną ogrzewającą plazmę?

Ostatnie dwa z omawianych projektów próbują odpowiedzieć na pytanie, czy rozwiązanie problemów ogrzewania atmosfery słonecznej oraz początków wiatru słonecznego może leżeć dosłownie u podstaw tejże atmosfery – czyli w granulacji. Zaproponowanym procesem wydzielania energii cieplnej są zderzenia jonowo-neutrałowe, a więc efekt możliwy do zbadania wyłącznie w symulacjach dwupłynowych.

3.1 Spikule - efekty adiabatyczne i nieadiabatyczne

Cel badań

Chcąc w pełni zrozumieć cel pierwszego projektu (Kuźma i in. 2017a) ko-

nieczne jest na wstępie krótkie omówienie problematyki spikul. Spikule, w polskiej nomenklaturze znane również jako bryzgi chromosferyczne, są wyrzutami chłodnej i gęstej plazmy chromosferycznej w obszarze dolnych warstw korony słonecznej. Zaobserwowane zostały po raz pierwszy ponad 130 lat temu (Secchi 1887) w postaci cienkich podłużnych struktur widocznych na tarczy słonecznej. Od tego czasu są przedmiotem intensywnych studiów (Beckers 1968, 1972, Suematsu 1998, Sterling 2000, Zaqarashvili i Erdélyi 2009). W obserwacjach spikule unoszą się z chromosferycznego tła na wysokości około 2000 km nad powierzchnią Słońca, gdzie ujawniają prędkości wynoszące około 25 km s^{-1}. Po osiągnięciu maksymalnej wysokości materia chromosferyczna albo spada w dół, z powrotem w kierunku obszaru przejściowego (spikule typu I), albo rozprasza się w koronie, a sama spikula zanika (spikule typu II). Typowy czas życia spikul wynosi 5 – 15 min, ze średnią wartością około 7 min, zaś ich średnica jest szacowana na 660 ± 200 km (Pasachoff i in. 2009). Spikule wydają się składać z podwójnych wrzecionowatych struktur (Tanaka 1974, Dara i in. 1998, Suematsu i in. 2008) i ujawniają dwukierunkowe przepływy (Tsiropoula i in. 1994, Tziotziou i in. 2003, 2004, Pasachoffet i in. 2009). Typowa temperatura elektronowa i gęstość elektronów w spikulach to $(15 - 17) \times 10^3$ K i $2 \times 10^{11} - 3.5 \times 10^{10}$ cm^{-3} na wysokości 4 – 10 Mm nad powierzchnią Słońca (Beckers 1968). W rezultacie spikule są znacznie chłodniejsze i gęstsze niż typowa plazma w dolnej koronie słonecznej.

Opracowano szereg modeli teoretycznych w celu wyjaśnienia mechanizmu powstawania spikul w niższych warstwach atmosfery słonecznej. Wykonano również wiele modeli numerycznych, mających symulować spikule wywoływane poprzez impulsowe uwolnienie energii u ich podstawy w chromosferze lub nawet w fotosferze. Pod uwagę wzięto takie mechanizmy, jak impuls prędkości plazmy, ciśnienia lub falę Alfvéna, która przechodzi w falę uderzeniową (Sterling 2000). Hansteen i in. (2006) oraz De Pontieu i in. (2007) symulowali tworzenie się i ewolucję dynamicznych włókien plazmy, powstałych z powolnych szoków magnetoakustycznych w dwuwymiarowych symulacjach numerycznych. Zasugerowali oni, że szoki te

powstają, gdy fale akustyczne generowane przez przepływy konwekcyjne i mody p rozchodzące się z niższej fotosfery do przenikniętej polem magnetycznym chromosfery. Heggland i in. (2007) użyli okresowego oscylatora do wywoływania jednowymiarowych szoków przemieszczających się w górę atmosfery słonecznej, a Martinez-Sykora i in. (2009) rozważyli wyłaniający się strumień magnetyczny, w którym spikula miałaby powstać w wyniku energii wyzwolonej w zapadającej się granuli w górnej fotosferze lub dolnej chromosferze. W symulacjach tych nie uzyskano jednak struktur podwójnych i przepływów dwukierunkowych. Z drugiej strony Murawski i Zaqarashvili (2010) przeprowadzili dwuwymiarowe symulacje plazmy opisywanej równaniami MHD i pokazali, że model szoków 2D Hollwega (1982) może wyjaśniać zarówno podwójne struktury, jak i przepływy dwukierunkowe. Użyli oni pojedynczego impulsu początkowego w prędkości plazmy, co doprowadziło do powstawania kolejnych szoków w wyniku nieliniowego rozchodzenia się impulsu w uwarstwionej atmosferze. Martinez-Sykora i in. (2018) wykonali symulacje atmosfery słonecznej z uwzględnieniem dyfuzji ambipolarnej. W rezultacie otrzymali oni struktury w znacznym stopniu przypominające spikule słoneczne.

Zrozumienie dokładnych mechanizmów powstania i ewolucji spikul wymaga dalszych badań. Dodatkowo więcej niż jeden mechanizm może odgrywać tu rolę, w zależności od lokalnych właściwości plazmy i pola magnetycznego.

Metodologia

Do rozwiązania równań MHD użyliśmy kodu numerycznego PLUTO (Mignone i in. 2007, 2012). Nasz obszar symulacji w 2D przestrzeni o symetrii osiowej (r, y) został zadany jako $(0.0 \leq r \leq 5.12)$ Mm $\times$ $(1.0 \leq y \leq 40.0)$ Mm, gdzie $y = 0$ oznacza dolną warstwę fotosfery. Do naszego badania wykorzystaliśmy jednolitą siatkę w obrębie $(0.0 \leq r \leq 5,12)$ Mm $\times$ $(1.0 \leq y \leq 1.24)$ Mm, który to obszar został pokryty przez 1024×2048 punktów siatki. Prowadzi to do 5-kilometrowej rozdzielczości w dolnej części obszaru symulacji, a więc tam, gdzie zachodzi ewolucja spikul. Powyżej, to jest w obszarze $(0.0 < r < 5.12)$

Mm $\times$ ($11.24 \leq y \leq 40.0$) Mm, wprowadziliśmy wzdłuż osi y rozciągniętą siatkę o 648 komórkach rosnących wraz z wysokością. Taka rozciągnięta siatka pełni rolę gąbki pochłaniając sygnał wejściowy pozwalając na uniknięcie znaczących odbić od górnej granicy obszaru symulacji. Narzuciliśmy otwarte warunki brzegowe dla $r = 5$ Mm, równocześnie ustalając wszystkie wielkości charakteryzujące plazmę na ich wartości równowagowe na górnej i dolnej krawędzi obszaru symulacji. Lewa krawędź, ($r = 0$), została ustawiona jako osiowo symetryczna.

Aby wygenerować spikule wykorzystaliśmy zlokalizowany w górnej chromosferze impuls w prędkości plazmy. Metoda ta jest podobna do obliczeń przeprowadzonych przez Shibatę (1982), Sterlinga i in. (1993), Murawskiego i Zaqarashviliego (2010) oraz Guerreiro i in. (2013). Podejście to różni się od modeli, które próbują modelować spikule zakłóceniami w fotosferze (np. Suematsu i in. 1982, Hollweg 1982).

Wyniki badań

Symulacje numeryczne wykazały, że sygnał rozchodzący się w górę szybko wystramia się w falę uderzeniową, który rozprzestrzenia się w koronie wzdłuż linii pola magnetycznego. Chłodny i gęsty strumień plazmy chromosferycznej, który wykazuje właściwości fali uderzeniowej osiąga znaczną wysokość (zwykle 4-5 Mm powyżej fotosfery), a następnie powraca do chromosfery (Rys. 4). Średnia prędkość przepływu plazmy w górę wynosi 20-25 km s^{-1}. Uzyskane wartości odpowiadają wartościom podanym przez Beckera (1968, 1972). Zachodzące później oscylacje obszaru przejściowego wzbudzane są w chromosferze, a ich okres jest zbliżony do chromosferycznego okresu odcięcia. Są one wynikiem nieliniowego wzbudzenia za impulsem, który rozprzestrzenia się w atmosferze uwarstwionej (Kuridze i in. 2009). Te szoki podnoszą chromosferyczną plazmę do korony i generują quasi-okresowe strumienie plazmy. Jest to zgodne z modelem zaproponowanym przez Hollwega (1982). Symulacje numeryczne pokazują, że fala rozrzedzeniowa, która następuje po fali uderzeniowej, powoduje zmniejszenie gęstości masy w obrębie struktury spikuli. Zarówno idealne, jak i nieadiabatyczne

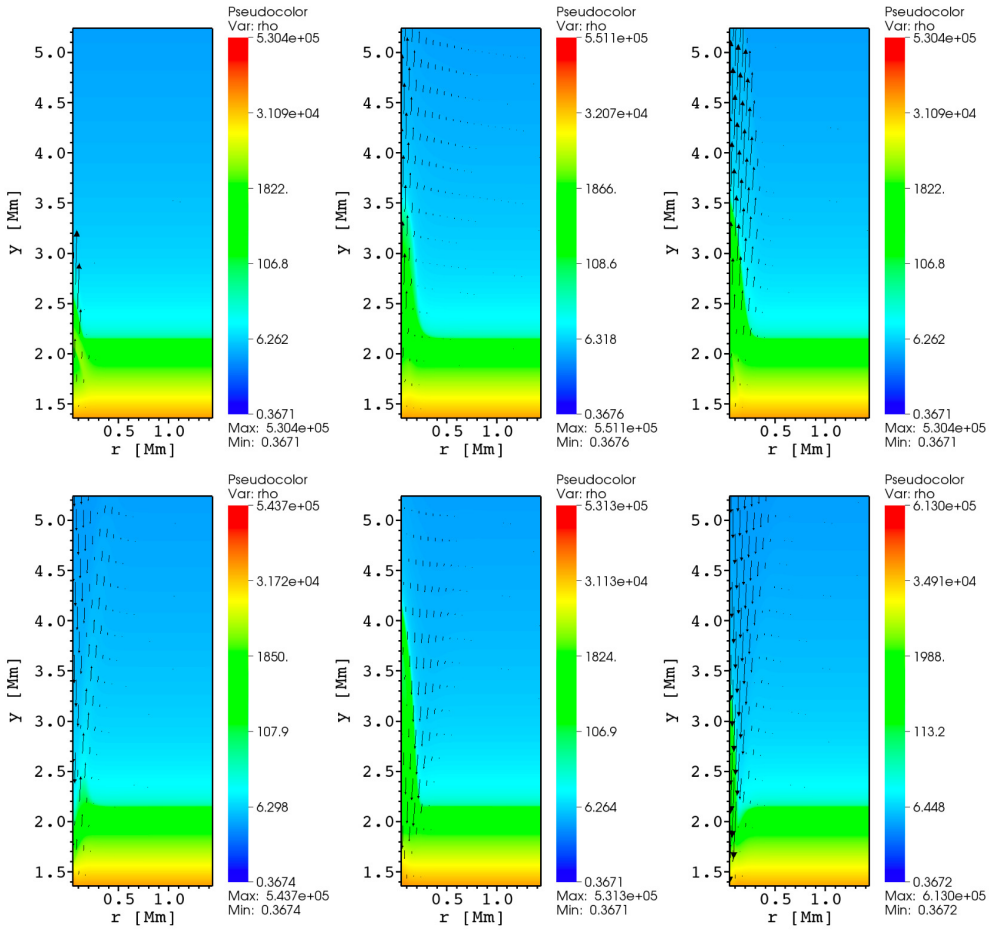

Rysunek 4: Symulacja numeryczna spikuli - przypadek adiabatyczny. Kolory ukazują ewolucję w czasie gęstości masy, wektorami oznaczono prędkość plazmy (Kuźma i in. 2017a).

symulacje dają zbliżone wyniki jeśli chodzi o maksymalną wysokość, prędkości wznoszenia, czas życia spikuli i okresowość oscylacji wtórnych. Efekty nieadiabatyczne powodują wzrost maksymalnej wysokości o około 10-15 %, a czas życia o około 15-20 %. Konkludując, efekty nieadiabatyczne nie wpływają znacząco na dynamikę spikul, jedynie nieznacznie zwiększają maksymalne wysokości i czas życia.

3.2 Spikule - efekty dwupłynowe

Cel badań

Jako że obszar, w którym generowane są spikule, zdominowany jest przez cząstki neutralne, przeprowadziliśmy symulacje spikul w reżimie dwupłynowym (Kuźma i in. 2017b). Osobne potraktowanie całkowicie zjonizowanej plazmy oraz gazu neutralnego jako dwóch płynów powiązanych wyłącznie przez zderzenia pozwoliło na prześledzenie ich ewolucji i ewaluację wpływu efektów dwupłynowych na generację i ewolucję spikul.

Metodologia

Rozwiązując równania dwupłynowe numerycznie, użyliśmy kodu numerycznego JOANNA (Wójcik 2017). W naszym problemie określony został dwuwymiarowy obszar symulacji w (x, y) jako $(-1.28 \leq x \leq 1.28)$ Mm $\times$ $(1.75 \leq y \leq 50.0)$ Mm, gdzie $y = 0$ oznacza dolną warstwę fotosfery. W symulacjach numerycznych przyjęliśmy jednolitą siatkę w obszarze $(-1.28 \leq x \leq 1.28)$ Mm $\times$ $(1.75 \leq y \leq 6.12)$ Mm, który jest pokryty 256×512 punktami siatki. Ta siatka prowadzi do rozdzielczości 10 km w głównym obszarze pola symulacji, to jest poniżej $y = 6.12$ Mm. Ponownie powyżej tego obszaru, a mianowicie w prostokącie $(-1.28 \leq x \leq 1.28)$ Mm $\times$ $(6.12 \leq y \leq 50.0)$ Mm, wykorzystaliśmy rozciągniętą siatkę ze 128 komórkami wydłużającymi się w kierunku y wraz z wysokością. Narzuciliśmy otwarte warunki brzegowe umożliwiające wypływ sygnału na granicach bocznych, podczas gdy na górze i na dole wszystkie parametry plazmy ustawione zostały na ich wartości w stanie równowagi.

Zmianie uległa metoda generacji spikuli. Prosty impulsowy sygnał w prędkości zastąpiony został przez realistyczny, zmienny w czasie sygnał w ciśnieniu plazmy. Podstawowy mechanizm tych symulacji polega na tym, że sygnały, umiejscowione w obszarze o $\beta = \frac{p}{(B^2/2\mu)} < 1$, rozdzielają się na dwie rozprzestrzeniające się wzdłuż linii pola magnetycznego powolne fale magnetoakustyczne; w dół rozchodzą się fale powolne zanikające w czasie (nie pokazane w ramach tych obliczeń), podczas gdy w górę rozchodzą się fale powolne o rosnących amplitudach. Te ostat-

nie przekształcają się w powolną falę uderzeniową ze względu na spadek gęstości masy wraz z wysokością. Plazma chromosferyczna pozostaje w tyle za frontem fali uderzeniowej, tworząc falę entropii (kontaktową) formującą spikulę. Zauważmy, że sygnał w ciśnieniu generuje również szybkie fale magnetoakustyczne, są to jednak fale o małej amplitudzie, które rozprzestrzeniają się w przestrzeni w sposób quasi-izotropowy. Zaznaczmy również, że zaburzenie generuje jonowe fale magnetoakustyczne i neutralne fale akustyczne (Zaqarashvili et al. 2011).

Wyniki badań

Kluczowe wnioski z naszych symulacji można podsumować w następujący sposób: a) dynamika spikul jest nieco inna, kiedy obserwowana jest w zjonizowanej plazmie, niż kiedy obserwowana jest w gazie neutralnym; b) rdzeń spikuli jest zdominowany przez chłodne neutrały; c) średnica spikuli neutralnej jest większa w porównaniu do spikuli jonowej; d) jonizacja pozostaje w zasadzie niezmienna wraz z wysokością i odległością poziomą od środka spikuli, jedynie czubek spikuli jest gęstszy i chłodniejszy (a więc także słabiej zjonizowany). Ogólny scenariusz ewolucji w czasie jest zbliżony dla jonów i neutrałów i równocześnie zbieżny z ustaleniami dla równań MHD (Rys. 5). Szczyt spikuli, podobnie jak jej boki stanowi stosunkowo gęsta plazma, podczas gdy wnętrze rozrzedza się w czasie z powodu fali rozrzedzeniowej przemieszczającej się w górę. Powyżej wierzchołka spikuli możemy dostrzec stały strumień jonów wtłaczanych w wyższe warstwy korony słonecznej. Ponadto, wraz z upływem czasu rozpoczyna się opadanie spikuli, poczynając od jej części zewnętrznej. Duża częstość zderzeń między jonami i neutrałami jest kluczowym czynnikiem przeciwdziałającym różnicom w dynamice jonów i neutrałów w spikulach. Bezpośredni wpływ pola magnetycznego na jony kontroluje szerokość spikuli jonowej. W związku z tym spikule jonowe są bardzo dobrze skupioną kolumną jonów o niewielkiej szerokości. Niewrażliwe na bezpośredni wpływ pola magnetycznego, neutrały mają zdolność rozprzestrzeniania się w kierunku poziomym; wszelkie ograniczenia wynikają z kolizji jonowo-neutrałowych. W rezultacie spikula neutralna jest nieznacznie tylko szersza. Po-

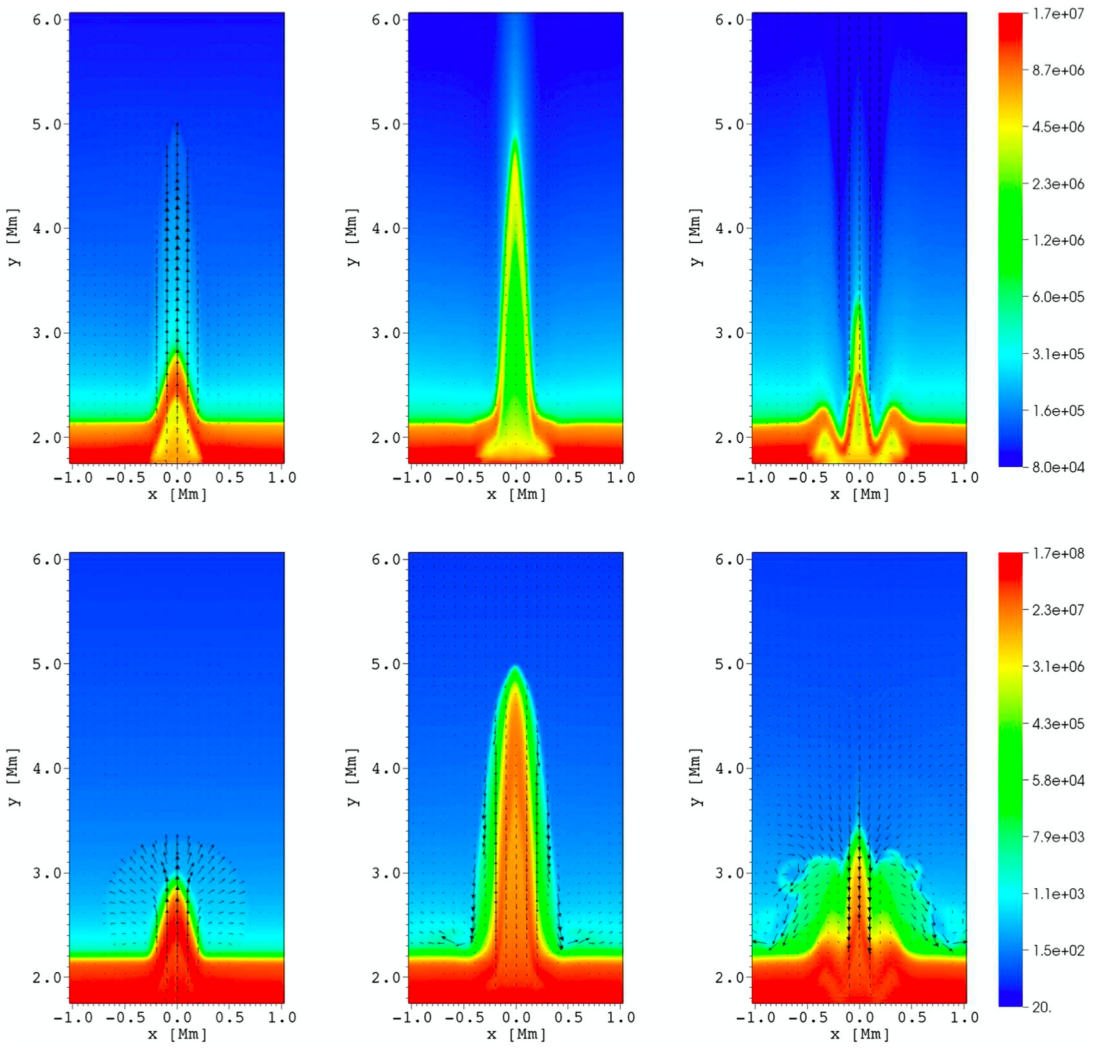

Rysunek 5: Dwupłynowa symulacja numeryczna spikuli. Kolory ukazują ewolucję w czasie gęstości masy jonów (górne panele) i neutrałów (dolne panele), wektorami oznaczono prędkość plazmy (Kuźma i in. 2017b).

nieważ pole magnetyczne wpływa na jony również w fazie ich spadku w dół, powstaje dobrze skupiony słup opadającej plazmy, który zwiększając ciśnienie u podstawy spikuli wytwarza strukturę w kształcie litery V. Opadający gaz neutralny nie jest utrzymywany przez pole magnetyczne i może przenikać do otaczającej korony. W fazie opadania w chmurze neutrałów otaczającej spikule, pojawiają się niesta-

bilności Rayleigha-Taylora (Allen i Hughes 1984) (Rys. 5, prawy dolny panel).

3.3 Mody entropii w obszarze półcienia plamy słonecznej

Cel badań

Mody entropii zostały po raz pierwszy zauważone w przepływach naddźwiękowych spowalnianych do prędkości poddźwiękowych i opisano je jako potencjalną samokorektę rozkładu prędkości (Crocco 1958). Na Słońcu zostały one zaobserwowane w wysokiej rozdzielczości mapach różnicowych uzyskanych przez Interface Region Imaging Spectrograph (IRIS) wykonanych dla linii C II (długość 1330 Å). Obserwowany obszar skupiał się na otoczeniu plamy słonecznej w dniu 8 października 2014 r. z rozdzielczością przestrzenną 0.4" na piksel (gdzie 1"= 725 km), odpowiadającą 290 km na Słońcu na piksel (Rys. 6). Uzyskano sekwencję obejmującą 2 godziny miary łukowej z 19 sekundową rozdzielczością czasową z kilkoma zaobserwowanymi źródłami modów entropii. Mapy różnicowe zostały wykonane poprzez pobranie każdego obrazu i odjęcie poprzedniego w sekwencji czasu. Obserwowana plama słoneczna stanowi zakotwiczenie pętli magnetycznej, rozciągającej się do leżącej powyżej aktywnej korony. Ponieważ zaobserwowane strumienie plazmy powstają lokalnie i pozostają takie przez cały czas życia, mówimy tu o "zlokalizowanych modach entropii" (Srivastava i in. 2018). Wszystkie zaobserwowane wyrzuty plazmy są widoczne w linii C II 1330 Å, nie są natomiast widoczne w mapach różnicowych linii Mg II 2796 Å, co wskazuje, że powstają one w obszarze przejściowym / koronie wewnętrznej po ewolucji perturbacji umiejscowionej w górnych warstwach chromosfery. Gęsta plazma zostaje wyrzucona na wysokość $\sim$ 5 Mm formując kształt zbliżony do kuli, za którą podąża rozrzedzony "ogon". Szacowana prędkość rozchodzenia się modu entropii w widzianej płaszczyźnie wynosi $\sim$ 30 km s^{-1}. Jest to dolna granica, ze względu na inklinację trajektorii strumienia plazmy, rzeczywista prędkość może być wyższa. Jest to wartość wyższa niż prędkość dźwięku oszacowana w temperaturze formowania linii C II (log[T]= 4.5). Charakterystyczna prędkość dźwięku w temperaturze formo-

wania się linii C II jest szacowana na 26 km s^{-1}. Prędkość wyrzucanej plazmy jest więc nieznacznie wyższa niż charakterystyczna prędkość dźwięku.

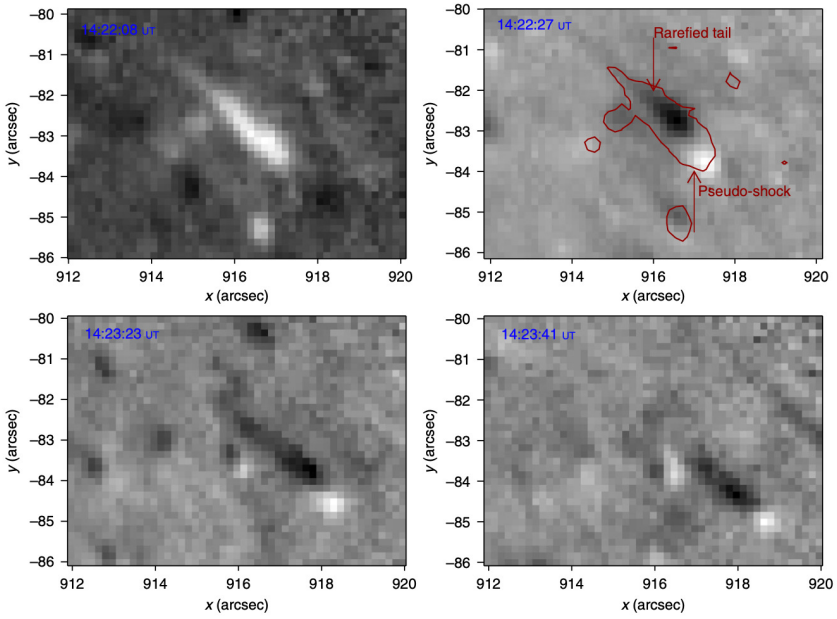

Rysunek 6: Obserwacje modów entropii. Jasny kolor ukazuje silnie zagęszczone czoło strumienia plazmy, ciemny kolor oznacza postępujące za nim rozrzedzenie (Srivastava i in. 2018).

Metodologia

Dwupłynowe równania opisujące częściowo zjonizowaną plazmę rozwiązaliśmy numerycznie używając kodu JOANNA. Dwuwymiarowy obszar symulacji określony został poprzez $(-2.56 \leq x \leq 2.56)$ Mm $\times$ $(1.75 \leq y \leq 15.0)$ Mm, gdzie $y = 0$ oznacza dolną warstwę fotosfery. Poniżej wysokości $y = 6.87$ Mm wykorzystaliśmy jednorodną siatkę numeryczną o pojedynczej komórce 5 km $\times$ 5 km. Powyżej tego obszaru znalazła się rozciągnięta siatka z 64 komórkami wydłużającymi się w kierunku y wraz z wysokością.

Bazując na modelach użytych wcześniej do symulowania spikul, opracowaliśmy model fizyczny zlokalizowanych modów entropii powstających w silnym polu

magnetycznym obszaru półcienia plamy słonecznej. Równowaga hydrostatyczna w plazmie została zakłócana przez zlokalizowane, zmienne w czasie zaburzenie w ciśnieniu jonów i gazu neutralnego. Pozycja zaburzenia odpowiada obszarowi $\beta < 1$, czyli magnetycznie zdominowanej, częściowo zjonizowanej plazmy w górnej warstwie chromosfery słonecznej. W obszarze tym wolne i szybkie fale magnetoakustyczne są słabo sprzężone. W założeniu zastosowane przez nas zaburzenie, odpowiada energii uwalnianej podczas potencjalnych mikrorekoneksji pomiędzy poskręcanymi liniami silnego pola magnetycznego w obszarze półcienia plamy słonecznej. Zasadniczo generowane są powolne fale magnetoakustyczne, które rozprzestrzeniają się wzdłuż linii pola magnetycznego. Po przejściu przez obszar przejściowy fala rozchodzi się dalej, jako słaby powolny szok. Plazma ciągnąca się za jasnym i gęstym czołem tworzy rozrzedzony ogon, co w znacznym stopniu zgadza się z obserwacjami. Mod entropii i postępujące rozrzedzenie odpowiadają fali kontaktowej i fali rozrzedzeniowej.

Wyniki badań

Czasowa ewolucja powolnej fali uderzeniowej i modu entropii wskazuje, że fala uderzeniowa opuszcza domenę magnetoplazmy we wczesnej fazie jej ewolucji, podczas gdy postępujący strumień plazmy pozostaje z nią związany podczas całkowitego okresu życia, to jest $\sim$ 150 s (Rys. 7). Dlatego transport energii i masy jest związany w zasadzie wyłącznie z modem entropii. Strumień energii powiązany z modem entropii jest o rząd wielkości większy niż dla powolnego szoku. W górnej chromosferze i obszarze przejściowym ten strumień energii ($\sim 8 \times 10^3$ W m^{-2}) jest wystarczający do lokalnego pobudzenia niższej atmosfery słonecznej. Porównanie strumieni energii przenoszonych przez mod entropii i powolną falę uderzeniową wykazuje znaczenie modów entropii również w koronie, gdzie przenosi znaczną ilość energii ($\sim 10^3$ W m^{-2}), która lokalnie jest wystarczająca do zrekompensowania strat radiacyjnych przy założeniu odpowiedniego mechanizmu rozpraszania tej energii. Również strumień masy poruszającej się wraz z modem entropii jest większy niż w przypadku powolnej fali uderzeniowej. Wartość

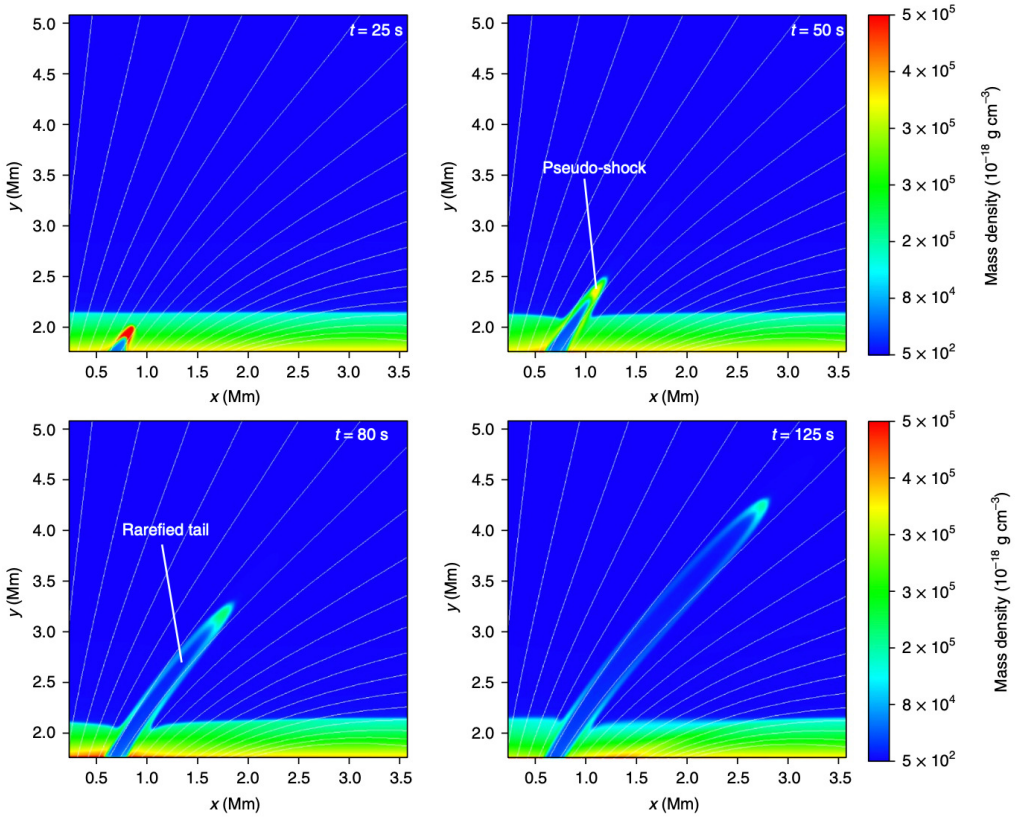

Rysunek 7: Symulacja numeryczna modu entropii. Kolor ukazuje ewolucję w czasie gęstości masy jonów (Srivastava i in. 2018).

strumienia masy ($\sim 10^{-5}$ kg m^{-2} s^{-1}) obliczonego w naszym modelu wskazuje, że mody entropii mogą doprowadzać plazmę do korony powyżej regionów aktywnych i w efekcie przynajmniej częściowo rekompensować także ubytki masy. Ze względu na miejsce powstawania, czyli chłodną, zdominowaną przez neutrały plazmę chromosferyczną, większość strumienia masy i energii jest przenoszona do obszaru przejściowego i korony właśnie przez neutralne cząstki. Neutrały mogą przekazywać swoją energię do otaczającej plazmy koronalnej w procesie zderzeń z jonami. Zderzenia te termalizują energię kinetyczną cząstek, powodując lokalne ogrzewanie plazmy. W ten sposób mody entropii mogą stopniowo zanikać po do-

tarciu do korony, gdzie ich energia zostaje rozproszona. Jest to zgodne z obserwacjami, w których nie zauważamy wyraźnej fazy opadania strumienia plazmy z powrotem w kierunku obszaru przejściowego - zdają się zanikać w otaczającej plazmie. Ze względu na znaczną ilość modów entropii występujących równocześnie na niewielkim obszarze mogą one odgrywać kluczową rolę w kompensowaniu strat radiacyjnych i dostarczaniu materii do obszarów aktywnych korony słonecznej. Konieczne są jednak dalsze badania w celu ustalenia, czy są one bezpośrednio związane z tworzeniem się powolnego wiatru słonecznego?

3.4 Fale Alfvéna w otoczeniu magnetycznego punktu zerowego

Cel badań

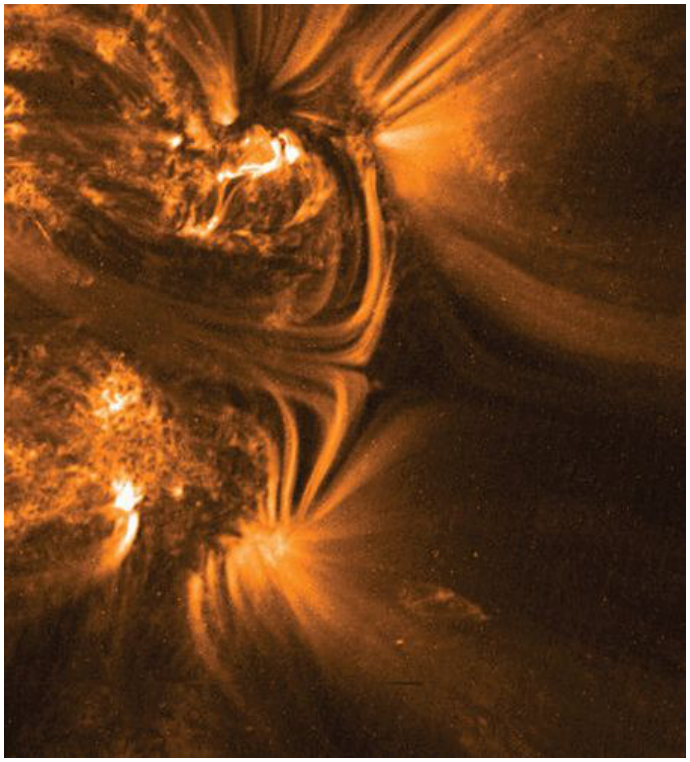

Rysunek 8: Obserwacja magnetycznego punktu zerowego wykonana podczas misji TRACE, 4 września 2000 roku (Parnell i in. 2015).

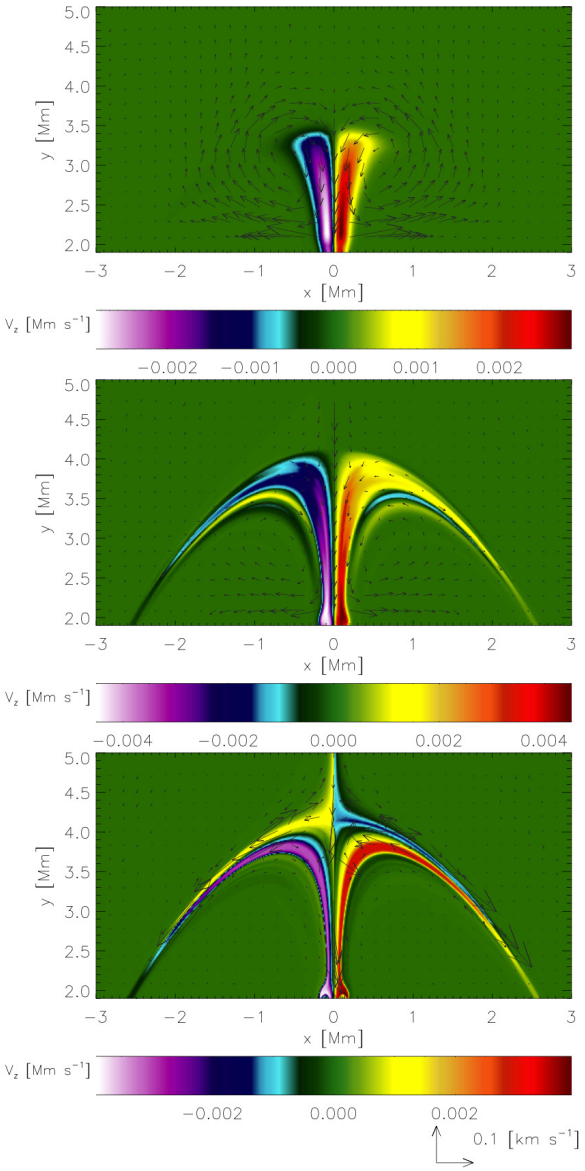

Rysunek 9: Symulacja numeryczna fali Alfvéna w otoczeniu magnetycznego punktu zerowego, umiejscowionego w punkcie $x = 0, y = 4.2$ Mm (Kuźma i in. 2015). Kolor ukazuje ewolucję w czasie z-owej składowej prędkości, wektory natomiast obrazują prędkość plazmy w płaszczyźnie $x - y$.

Celem tego projektu było opracowanie analitycznego i numerycznego modelu skrętnej fali Alfvéna, rozchodzącej się wzdłuż struktury złożonej z dwóch wyłania-

jących się arkad magnetycznych (Kuźma i in. 2015). Arkady, będące złożeniem pętli koronalnych są powszechnie obserwowane w obszarach aktywnych. Istotnym elementem rzeczonej struktury jest magnetyczny punkt zerowy/linia zerowa znajdująca się ponad nimi (Rys. 8). Jako, że fala Alfvéna nie może rozchodzić się w ośrodku, w którym brak jest pola magnetycznego, chcieliśmy tu sprawdzić jakie konsekwencje dla jej rozchodzenia się będzie miała linia zerowa oraz czy fala Alfvéna bedzie w stanie przedostać się do korony słonecznej powyżej linii zerowej?

Metodologia

Przy użyciu kodu FLASH z siatką samoadaptacyjną wykonaliśmy symulacje numeryczne skręcenia linii magnetycznych w konfiguracji magnetycznej linii zerowej dwóch arkad magnetycznych, które są osadzone w grawitacyjnie uwarstwionej i magnetycznie zamkniętej koronie słonecznej. Opracowaliśmy model atmosfery słonecznej w 2.5 wymiarach (2.5D), a więc umożliwiający rozchodzenie się zaburzeń w $z-$towej składowej wektorów prędkości, V_z i pola magnetycznego, B_z. Do rzeczonego modelu zaimplementowaliśmy pole magnetyczne w kształcie dwóch arkad magnetycznych, powyżej których znajduje się zerowa linia magnetyczna. U podstawy tej struktury linie pola magnetycznego skręcane zostały przez oscylator w $z-$towej składowej wektora prędkości, V_z.

Wyniki badań

Skręcenie linii pola magnetycznego, umiejscowione około 200 km poniżej obszaru przejściowego, generuje fale Alfvéna i magnetoakustyczne, które rozchodzą się wzdłuż linii pola magnetycznego (Rys. 9). W wyniku sprzężenia tych fal zachodzi częściowe odbicie od obszaru przejściowego i rozpraszanie w obszarze niejednorodnej prędkości Alfvéna. W skutek tego część fal jest w stanie ominąć magnetyczną linię zerową i penetrować obszary koronalne powyżej. Fale Alfvéna doświadczają szybkiego tłumienia w skalach czasowych porównywalnych z ich okresami falowymi, a system fizyczny doświadcza relaksacji w czasie.

3.5 Fale w strukturach subtelnych tub magnetycznych

Cel badań

Duża część dynamiki plazmy słonecznej determinowana jest przez pole magnetyczne i wydaje się, że to ostatnie jest kluczem do zrozumienia wielu procesów fizycznych na Słońcu. Pole magnetyczne jest rozproszone na całym Słońcu zarówno w postaci bardzo złożonych (tj. obszarów aktywnych), jak i prostych konfiguracji (w obszarach spokojnego Słońca i dziur koronalnych). Tuby magnetyczne koncentrują pole magnetyczne o sile około 10^3 Gs na poziomie fotosfery. W epoce obserwacji o wysokiej rozdzielczości możemy z całą pewnością stwierdzić, że są one powszechne w chromosferze (np. Hansteen i in., 2006, De Pontieuet, 2007, Rouppe van der Voort i in., 2009, Kuridzeet al.2015, Srivastava i in. 2017). Połączona dynamika tub magnetycznych i plazmy słonecznej prowadzi do różnorodności struktur w chromosferze (np. spikule, strumienie plazmy, mody entropii). Fale MHD są integralną częścią tych struktur magnetycznych i mogą być badane za pomocą wysokiej rozdzielczości zaawansowanych symulacji numerycznych (np. DePontieu i in., 2007, Zaqarashvili i Erdélyi2009, Okamoto i De Pontieu 2011, Tavabi i in., 2015, Wójcik i in. 2017). Najnowsze obserwacje CRISP / SST (CRisp Imaging SpectroPolarimeter/Swedish 1 m Solar Telescope) ujawniły, że tuby magnetyczne nie są koniecznie strukturami monolitycznymi, ale zamiast tego dzielą się na bardzo wyraźne nici magnetyczne. Srivastava i in. (2017) ogłosili jako pierwsi obserwację krótkookresowych ($\sim$ 50 s) fal skrętnych rozchodzących się w takiej ustrukturyzowanej tubie magnetycznej. Fale te zostały zinterpretowane jako torsyjne fale Alfvéna. Autorzy opracowali monolityczny model trójwymiarowej tuby magnetycznej i pokazali, że rzeczone fale wykazują potencjał do ogrzewania korony słonecznej. W naszych badaniach skupiliśmy się na stworzeniu odpowiadającej obserwacjom, a więc nie monolitycznej, a ustrukturyzowanej (składającej się z wrzecionowatych pasm plazmy) tuby magnetycznej poddanej działaniu skrętnego zaburzenia (wiru) umiejscowionego u jej podstawy (Kuźma i Murawski 2018).

Metodologia

W celu numerycznego rozwiązania równań MHD ponownie użyliśmy kodu PLUTO. Ponieważ interesuje nas skręcenie struktury w trzech wymiarach, wykorzystaliśmy trójwymiarowy obszar symulacji (x, y, z): $(-0.64, 0.64)$ Mm $\times$(1.75, 20.0) Mm $\times$(−0.64, 0.64) Mm, gdzie $y = 0$ Mm oznacza dolną warstwę fotosfery. W symulacjach numerycznych użyliśmy jednolitej siatki w obrębie regionu $(-0.64 \leq x \leq 0.64)$ Mm $\times(1.75 \leq y \leq 4.31)$ Mm $\times(-0.64 \leq z \leq 0.64)$ Mm. Ten obszar został pokryty przez $256 \times 512 \times 256$ punktów siatki, co sprowadza się do rozdzielczości wynoszącej 5 km, a więc wystarczającej do prześledzenia ewolucji badanych struktur. Powyżej tego obszaru, mianowicie dla $(-0.64 \leq x \leq 0.64)$ Mm $\times(4.31 \leq y \leq 20.0)$ Mm $\times(-0.64 \leq z \leq 0.64)$ Mm, zaimplementowaliśmy siatkę rozciągniętą wzdłuż kierunku y, która jest podzielona na 128 rosnących wraz z wysokością komórek.

W celu wywołania wyrzutu chłodnej chromosferycznej plazmy w obszar korony zastosowaliśmy, podobnie jak w przypadku generowania spikul, zmienne w czasie zaburzenie w ciśnieniu plazmy umieszczone na dole obszaru symulacji, poniżej obszaru przejściowego. Narastające zaburzenie w ciśnieniu gazu generuje pięć strumieni chłodnej plazmy chromosferycznej wypełniając magnetyczną strukturę także powyżej obszaru przejściowego i w koronie. Dodatkowo u podstawy tuby magnetycznej umieściliśmy oscylator skręcający ją z okresem $P_{\mathrm{d}} = 50$ s.

Wyniki badań

Zbadaliśmy fale rozchodzące się wzdłuż ustrukturyzowanej tuby magnetycznej składającej się z pięciu gęstych wrzecion plazmowych (Rys. 10). We wszystkich wzbudzonych strukturach można zobaczyć powłoki opisane wcześniej przez Murawskiego i in. (2015), które mogą być również dowodem absorpcji rezonansowej (Goossens i in. 2013). Struktura powłok może również wynikać z poziomego profilu temperatury w poprzek struktur, wpływając na prędkość dźwięku i rozchodzenie się fal. W rezultacie zaburzenia skrętnego u podstawy tuby magnetycz-

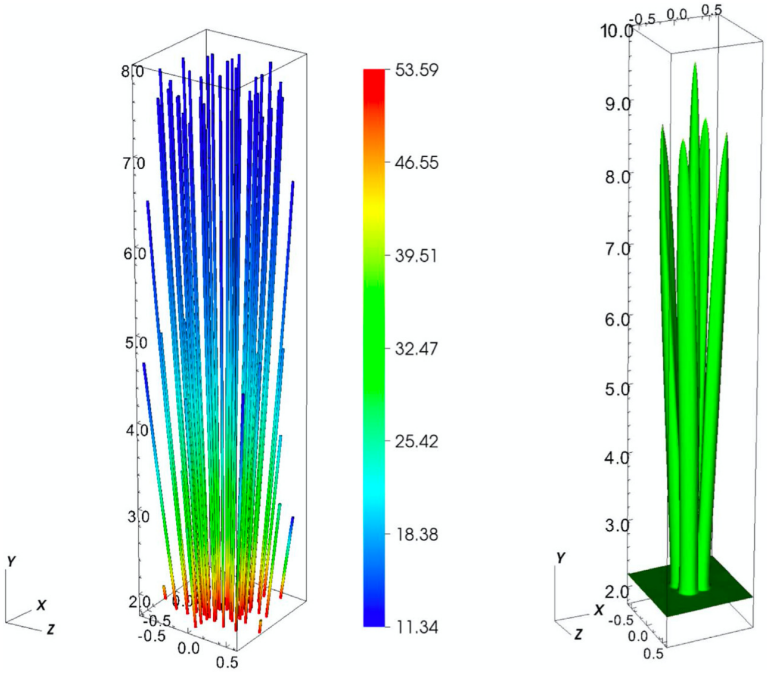

Rysunek 10: Linie pola magnetycznego (lewy panel) i gęstość masy struktur subtelnych (prawy panel) symulowanej tuby magnetycznej (Kuźma i Murawski 2018).

nej obserwujemy skrętne fale Alfvéna w strukturze centralnej i fale typu żmijki w strukturach niecentralnych. Okresy fal wzbudzonych w górnej chromosferze nie zmieniają się znacząco wraz z wysokością. W wyniku niehomogeniczności plazmy wzdłuż kierunku rozchodzenia się fal, wygenerowanych jest kilka okresów krótszych lub dłuższych niż okres dominujący, $P = 50$ s. Dla $P_{\mathrm{d}} = 50$ s, otrzymane długości fal Alfvéna znajdują się w zakresie 20-25 Mm, podczas gdy odpowiednie długości fal typu żmijki waha się pomiędzy 5 a 50 Mm.

Poprzeczne fale MHD (tj. zarówno skrętne Alfvéna jak i fale typu żmijki) przenoszą energię do górnych warstw atmosfery słonecznej, która to energia może odgrywać znaczącą rolę w ogrzewaniu korony (Rys. 11). Struktury tuby magnetycznej przenoszą strumienie energii o wartości około 10^3 Wm^{-2}. U podstawy tuby magnetycznej maksimum tego przepływu znajduje się w centralnej struk-

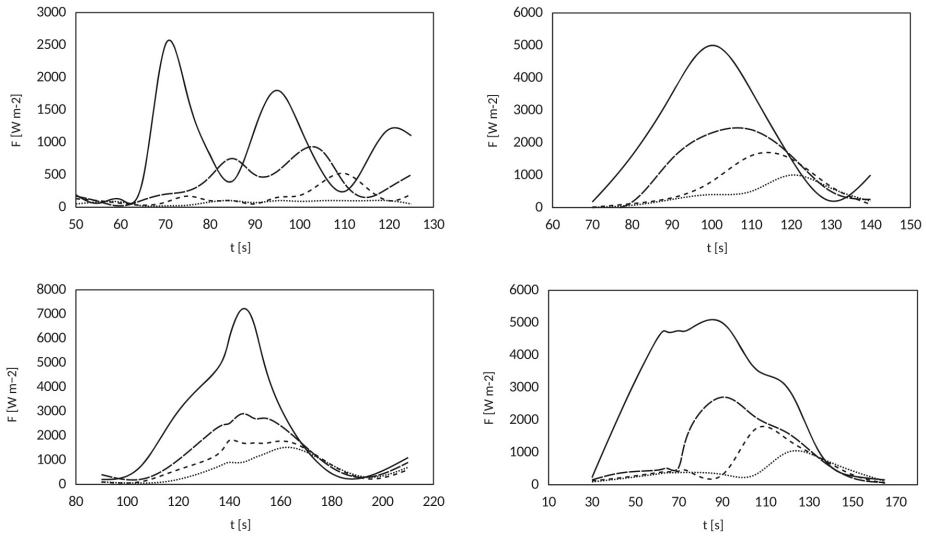

Rysunek 11: Ewolucja w czasie strumienia energii, F, na wysokości $y = 3$ Mm (linia ciągła), $y = 5$ Mm (długie linie przerywane) $y = 7$ Mm (krótkie linie przerywane) i $y = 9$ Mm (lina kropkowana), dla przypadków $P_{\rm d} = 50$ s, $P_{\rm d} = 126$ s, $P_{\rm d} = 180$ i $P_{\rm d} = 300$ s (od górnego lewego po dolny prawy panel). Rys. z pracy Kuźma i Murawski (2018).

turze. Wraz z wysokością ta tendencja się zmienia, strumień energii w środkowej strukturze znacznie maleje, podczas gdy nie obserwujemy takiego procesu w strukturach niecentralnych. Dochodzimy tu do istotnego wniosku, że w strukturze niejednorodnej tuby magnetycznej za przenoszenie energii do wyższych warstw korony odpowiedzialne są głównie fale typu żmijki, a nie skrętne fale Alfvéna. Przy odpowiednich mechanizmach dysypacji przenoszonej energii, których nasz model nie uwzględnia, ta ilość energii może być wystarczająca do ogrzania korony słonecznej (Withbroe i Noyes 1977).

Oprócz nowo obserwowanych krótkotrwałych oscylacji skrętnych ($P_{\rm d} = 50$ s), zbadaliśmy również oscylacje o okresach $P_{\rm d} = 126$ s (Jess i in. 2009), a także oscylacje 3 i 5 minutowe ($P_{\rm d} = 180$ s i 300 s). Krótkookresowe oscylacje poprzeczne przenoszą strumień energii o wartości maksymalnej około 2.5×10^3 Wm^{-2} u podstawy tuby magnetycznej. Ta wartość zmniejsza się w kolejnych okresach z po-

wodu ekspansji i ciągłego rozrzedzania się plazmy wewnątrz struktury. Wartość strumienia energii spada także wraz z wysokością. Na wysokości $y = 9$ Mm osiąga pomijalnie małą wartość, poniżej 10^2 Wm^{-2}. Fale o dłuższych okresach przenoszą energię do wyższych warstw korony słonecznej z większą efektywnością. Warto zauważyć, że najmniejsze straty energii odpowiadają oscylacjom 3-minutowym. Uzyskane wyniki wskazują, że krótkotrwałe oscylacje poprzeczne zanikają gwałtownie wraz z wysokością, podczas gdy oscylacje o dłuższych okresach skutecznie rozchodzą się powyżej wysokości $y = 9$ Mm. Na podstawie przeprowadzonych badań wnioskujemy, że te niejednorodne tuby magnetyczne mogą skutecznie przenosić zarówno skrętne fale Alfvéna, jak i fale typu żmijki i wraz z nimi transportować istotne ilości energii z chromosfery do wyższych warstw korony słonecznej.

3.6 Ogrzewanie plazmy dwupłynowymi falami akustycznymi

Cel badań

Jak już zostało wspomniane we wstępie, idea, że fale akustyczne mogą ogrzewać atmosferę słoneczną, został przedstawiona przez Biermana (1946) i Schwarzschilda (1948). Oni to po raz pierwszy zaproponowali, że fale akustyczne mogą być głównym czynnikiem grzewczym chromosfery, przy czym wskazali na czoło wystramiającej się wraz z wysokością w atmosferze fali szokowej, jako główny mechanizm ogrzewania plazmowego. Później szeroko zbadano problem ogrzewania chromosferycznego przez fale akustyczne. W 1995 r. Carlsson i Stein zakwestionowali średni wzrost temperatury plazmy w akustycznie ogrzewanej chromosferze. Fossum i Carlsson (2005, 2006) przeprowadzili symulacje numeryczne fal akustycznych o wysokiej częstotliwości i doszli do wniosku, że nie są one wystarczające do ogrzania chromosfery. Z drugiej strony Ulmschneider i Musielak (2003) stwierdzili, że fale akustyczne są głównym źródłem ogrzewania w niemagnetycznych regionach chromosfery, a Cuntz i in. (2007) dostarczyli istotnych dowodów, że to ogrzewanie może być lokalnie dominujące. Używając dwuwymiarowych symulacji numerycznych Maneva i in. (2017) pokazali, że fale magnetoaku-

styczne, rozchodząc się w uwarstwionej grawitacyjnie chromosferze, prowadzą do zmian w temperaturze plazmy. Naszym celem jest kontynuacja i zweryfikowanie wspomnianych powyżej badań poprzez wykonanie nowatorskich, w pełni dwupłynowych symulacji fal akustycznych rozchodzących się w atmosferze Słońca, oraz ilościowe określenie ciepła uwalnianego w procesach dwupłynowych w chromosferze (Kuźma i in. 2019).

Metodologia

Dwupłynowe, jednowymiarowe równania opisujące plazmę rozwiązaliśmy numerycznie przy użyciu kodu JOANNA. Nasz jednowymiarowy obszar symulacji pokrywa region pomiędzy fotosferą ($y = 0$ Mm) i niską koroną ($y = 2.5$ Mm) i został podzielony na 25×10^3 jednakowych komórek numerycznych. W ten sposób uzyskaliśmy region charakteryzujący się wysoką rozdzielczością przestrzenną, $\Delta y = 100$ m. Powyżej tego regionu, to jest dla obszaru 2.5 Mm $< y <$ 30 Mm, użyliśmy 128 komórek numerycznych o długości rosnącej wraz z wysokością. Region ten pochłania fale pochodzące z dolnych warstw obszaru symulacji i więzi sygnał zmniejszając odbicia od górnej krawędzi. Dla krótszych okresów zastosowaliśmy odpowiednio wyższą rozdzielczość przestrzenną w celu uniknięcia numerycznego tłumienia fal. U dołu obszaru symulacji zaimplementowany został sinusoidalny oscylator wzbudzający jonowe i neutralne fale akustyczne o zadanych okresach i amplitudzie równej 0.1 km s^{-1}.

Wyniki badań

Odkryliśmy, że fale akustyczne o okresach pomiędzy 30 s a 200 s prowadzą do podgrzewania chromosfery, podczas gdy temperatura górnej fotosfery pozostaje prawie niezmieniona (Rys. 12). Amplituda fali rośnie wraz z wysokością z powodu spadku gęstości masy (np. Murawski i in. 2018), a zatem wzrost amplitudy może dominować nad tłumieniem w wyniku kolizji jonowo-neutrałowych. Takie fale mają zdolność przenikania wyższych warstw atmosfery słonecznej i rozpraszania swojej energii w chromosferze. Jednak w przypadku fal o niskiej amplitudzie przenoszona energia pozostaje niska, a ogrzewanie plazmowe jest tam

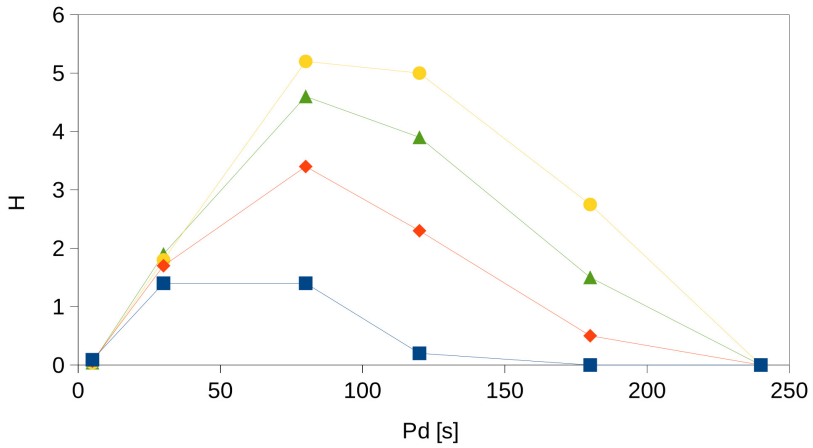

Rysunek 12: Uśredniona po czasie relatywna temperatura jonów, $H = T_i/T_0$ w zależności od okresu zaburzenia, P_d, na wysokości$y$ = 1 Mm (kwadraty), y = 1.25 Mm (romby), y = 1.5 Mm (trójkąty) i y = 1.75 Mm (koła). Rys. z pracy: Kuźma i in. (2019).

niewystarczające do zrekompensowania strat radiacyjnych. Wykonując nasze symulacje, daliśmy kolejny przyczynek do trwającej dyskusji na temat ogrzewania plazmowego za pomocą fal akustycznych. Poprzednie prace, takie jak wykonane przez Carlssona i in. (2007), Andicę i in. (2008) oraz Sobotkę i in. (2014), opierające się na oszacowaniach obserwacyjnych i równaniach jednopłynowych prowadziły do wniosku, że energia przenoszona przez fale akustyczne może skompensować pewną część strat radiacyjnych. Nasze wyniki pokazują, że ogrzewanie plazmy wynikające ze zderzeń jonowo-neutrałowych w falach akustycznych o amplitudzie równej 0.1 km s^{-1}, choć istotne w dłuższych interwałach czasowych, to nie wystarcza do pełnego skompensowania strat radiacyjnych i dodatkowy mechanizm ogrzewania jest w tym wypadku niezbędny.

3.7 Granulacja a ogrzewanie atmosfery słonecznej

Cel badań

Niniejszy projekt (Wójcik i in. 2019a), wraz z następującym po nim, a oma-

wiającym początki wiatru słonecznego (Wójcik i in. 2019b), są w zasadzie ukoronowaniem kilkuletniej pracy badawczej. Celem omawianego projektu było sprawdzenie, czy energia przenoszona przez fale dwupłynowe i wyzwalana jako energia cieplna w procesie zderzeń jonów z neutrałami jest w stanie skutecznie ogrzewać plazmę w fotosferze, chromosferze i obszarze przejściowym. Poprzez skuteczne ogrzewanie mamy tu na myśli osiągnięcie stanu quasi-stacjonarnego, to jest takiego, w którym wszelkie straty energetyczne w skutek radiacji, jak i przekazywanie ciepła w procesie przewodnictwa cieplnego będą całkowicie rekompensowane przez deponowaną energię. W naszym eksperymencie numerycznym chcieliśmy uniknąć sztucznego wywoływania zaburzeń, aby osiągnąć stan jak najbardziej zbliżony do realistycznej atmosfery Słońca. Dlatego też rzeczone fale dwupłynowe generowane są naturalnie w górnych warstwach konwekcyjnych, gdzie zachodzi samoistnie zjawisko granulacji.

Metodologia

Symulowany obszar ma wymiary w kierunku poziomym (x-) i pionowym (y-), tak, że $(-5.12 < x < 5.12)$ Mm $\times$ $(-5.12 < y < 30)$ Mm. Dzięki temu jesteśmy w stanie symulować zarówno niestabilny konwekcyjnie obszar tuż poniżej fotosfery, jak i atmosferę słoneczną. Poniżej wysokości $y = 5.12$ Mm, ustawiliśmy jednorodną siatkę numeryczną 20 km $\times$ 20 km, natomiast powyżej, startując od podstawy korony umiejscowionej na wysokości $y = 2.1$ Mm, znajduje się siatka rozciągnięta. Wszystkie parametry plazmy górnej i dolnej krawędzi symulacji ustawione są na ich hydrostatyczne wartości, pozostałe dwie krawędzie mają ustawione periodyczne warunki brzegowe. Symulacje zostały przygotowane i wykonane w kodzie JOANNA.

W przeprowadzonych symulacjach numerycznych fal dwupłynowych w częściowo zjonizowanej atmosferze słonecznej, uwzględniliśmy: przewodnictwo cieplne, lepkość i dyfuzyjność magnetyczną. Do opisujących atmosferę Słońca równań dwupłynowych włączony został również człon radiacyjny. Składa się on z dwóch części: optycznie grubego chłodzenia, które działa w dolnych warstwach

atmosfery oraz optycznie cienkiego chłodzenia, które działa w górnych obszarach atmosferycznych. W każdym kroku czasowym obliczamy głębokość optyczną, zaczynając od nieskończoności. Dla głębokości optycznych większych niż 0.1 używamy aproksymacji optycznie grubego chłodzenia (Abbett i Fisher 2012). Dla głębokości optycznych poniżej 0.1 używamy cienkiej krzywej chłodzenia (Cox i Tucker 1969), która jest interpolowana przez wielomian 10 rzędu. Aby uwzględnić transport energii do obszaru symulacji z niżej położonych obszarów konwekcyjnych, dolna warstwa jest dodatkowo podgrzewana przez człon o 10% przewyższający radiację. Na dolnej krawędzi obszaru symulacji zaimplementowany został także jednostajny wpływ plazmy, o prędkości $V = 0.25$ km s^{-1} uzupełniający straty masy związane z plazmą wypływającą przez górną krawędź obszaru symulacji oraz straty energii związane z radiacją (Chatterjee 2018). W obszarze symulacji ustawione zostało pionowe pole magnetyczne.

Wyniki badań

Zaobserwowaliśmy, iż poniżej fotosfery, w niestabilnym konwekcyjnie regionie pojawią się i ewoluują samoorganizujące się komórki konwekcyjne z granulacją na ich szczycie. Początkowe pionowe pole magnetyczne tworzy szereg tub magnetycznych zakorzenionych pomiędzy granulami (Rys. 13). W wyniku ewolucji układu już na poziomie fotosfery generowane są neutralne fale akustyczne i jonowe fale magneto-akustyczne. Część energii przenoszonej przez te fale jest rozpraszana w procesie zderzeń neutralno-jonowych w fotosferze i chromosferze. W rezultacie dwupłynowe fale generowane przez granulację skutecznie ogrzewają plazmę, kompensując straty radiacyjne i wynikające z przewodnictwa cieplnego. Co istotne, uzyskana quasi-stacjonarna atmosfera Słońca charakteryzuje się rozkładem temperatur zbliżonym do półempirycznego modelu Avretta i Loesera (2008) (Rys. 14). Ponieważ po raz pierwszy udało się uzyskać zgodność z modelem opartym na obserwacjach, bez uwzględnienia ogrzewania przez bezpośrednio wzbudzone fale szokowe, dochodzimy do wniosku, że nasze wyniki wyjaśniają główne mechanizmy falowego ogrzewania regionów spokojnego Słońca.

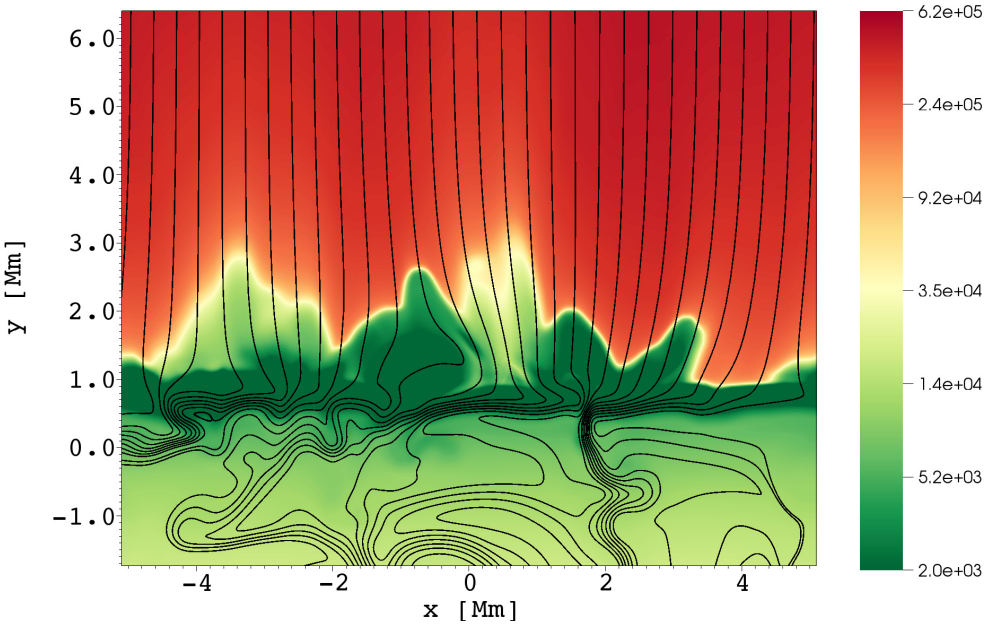

Rysunek 13: Symulacja numeryczna realistycznej granulacji i atmosfery słonecznej. Kolory obrazują logarytm wyrażonej w Kelvinach temperatury jonów, $\log T_{\mathrm{i}}$, z nałożonymi liniami pola magnetycznego (Wójcik i in. 2019a).

Wartym odnotowania jest fakt, że zarówno: lepkość, dyfuzyjność magnetyczna, jonizacja i rekombinacja, które zostały konsekwentnie wdrożone w użytym modelu, mają swój udział w utrzymaniu stanu równowagi, jednak to ogrzewanie wynikające ze zderzeń jonów z neutrałami pozostaje mechanizmem dominującym.

3.8 Granulacja a powstawanie wiatru słonecznego

Cel badań

Projekt ten, będący w istocie rozwinięciem powyżej przedstawionego projektu badającego ogrzewanie atmosfery Słońca generowanymi przez granulację falami dwupłynowymi, miał na celu zbadanie generowanych przez granulację przepływów plazmy (Wójcik i in. 2019b). Chcieliśmy odpowiedzieć na pytanie, czy przepływy te mogą mieć istotny udział w generacji wiatru słonecznego, dostarczaniu materii i energii w celu jego podtrzymania, oraz przede wszystkim - czy uzy-

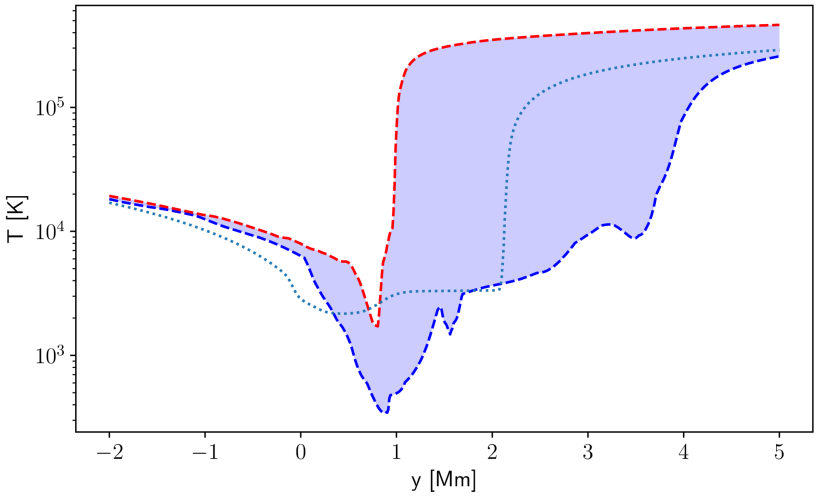

Rysunek 14: Uzyskany numerycznie horyzontalny profil temperatury jonów, wartość minimalna (niebieska linia przerywana), maksymalna (czerwona linia przerywana) i średnia (linia ciągła). Linia kropkowana obrazuje temperaturę w modelu Avretta i Loesera (2008). Rys. z pracy Wójcik i in. (2019a).

skane parametry fizyczne przepływów są zgodne z danymi obserwacyjnymi dla obszarów, w których zgodnie z obecnym stanem wiedzy ma swój początek wiatr słoneczny (Tu i in. 2005)?

Metodologia

W naszych symulacjach zastosowaliśmy metodologię analogiczną do tej użytej podczas badań ogrzewania atmosfery. Inny jest natomiast obszar symulacji. W kierunku poziomym (x-) i pionowym (y-) został on ustawiony tak, że $(-2.56 < x < 2.56)$ Mm $\times$ $(-2.56 < y < 30)$ Mm. Poniżej wysokości $y = 5.12$ Mm, ustawiliśmy siatkę numeryczną o rozmiarze komórki 10 km $\times$ 10 km, powyżej tego obszaru rozciągnęliśmy siatkę w kierunku pionowym dzieląc ją na komórki, których rozmiar rośnie wraz z wysokością.

Wyniki badań

Ponownie zaobserwowaliśmy, jak w niestabilnym konwekcyjnie regionie umiejscowionym poniżej fotosfery pojawią się i ewoluują samoorganizujące się komórki

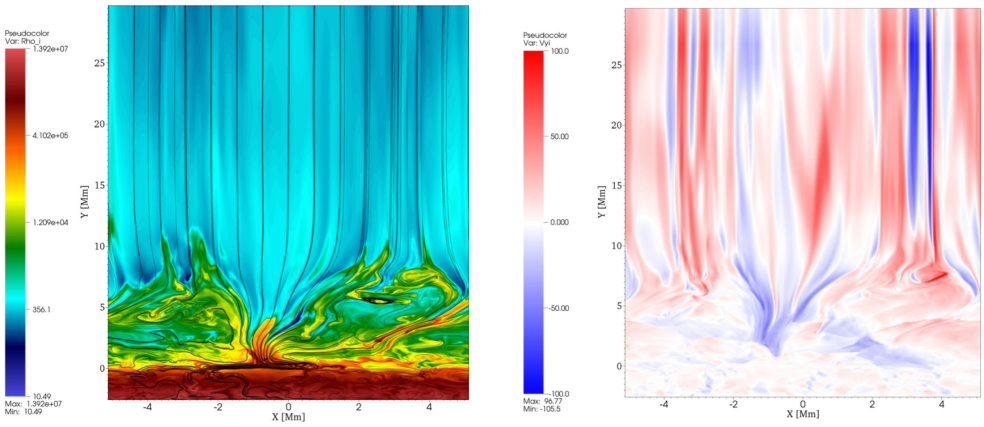

Rysunek 15: Symulacja numeryczna realistycznej granulacji i powiązanych odpływów plazmy słonecznej (Wójcik i in. 2019b). Kolory obrazują logarytm gęstości jonów, $\log(\varrho_{\rm i}(x,y))$, z nałożonymi liniami pola magnetycznego (lewy panel) oraz pionową składową prędkości jonów $V_{{\rm i}\,y}(x,y)$. Gęstość masy jonów wyrażona jest w 10^{-18} g cm^{-3} a prędkość jonów w km s^{-1}.

konwekcyjne z granulacją na ich szczycie. Początkowe pionowe pole magnetyczne tworzy szereg tub magnetycznych zakorzenionych pomiędzy granulami (Rys. 15, lewy panel). Powyżej granul generowane są odpływy plazmy, których amplituda wzrasta wraz z wysokością. Uwięzione w odpływach pole magnetyczne oddziałuje z otaczającym polem magnetycznym. Po osiągnięciu obszaru przejściowego plazma uwalniana jest do korony, w której kontynuuje ucieczkę wzdłuż otwartych linii pola magnetycznego (Rys. 15, prawy panel). Są to pierwsze tak zaawansowane symulacje łączące poprzez chromosferę zjawiska zachodzące w fotosferze z koronalnymi odpływami masy, stanowiącymi początkową fazę wiatru słonecznego. Należy podkreślić, iż uzyskane właściwości fizyczne tychże odpływów pozostają w całkowitej zgodności z danymi obserwacyjnymi.

4 Podsumowanie

Przeprowadzone badania rzuciły nowe światło na mechanizmy powstawania i ewolucję spikul i modów entropii, a także na transport energii w dolnych warstwach atmosfery słonecznej. Jednak co szczególnie istotne, zbliżyliśmy się znacznie do udzielenia odpowiedzi na najważniejsze pytania zaprzątające głowy heliofizyków.

Wiemy już, że efekty dwupłynowe odgrywają ważną, jeśli nie kluczową rolę, w procesach związanych z ogrzewaniem plazmy w fotosferze i chromosferze. Pełnym sukcesem zakończyły się symulacje atmosfery słonecznej z radiacją, przewodnictwem cieplnym i samoistnie powstającą granulacją. Okazało się, że ta ostatnia generuje całe spektrum fal (neutralnych fal akustycznych i jonowych magnetoakustycznych), które przenoszą energię do wyższych warstw atmosfery słonecznej. Ciepło wydzielane w procesie zderzeń między jonami i neutrałami jest wystarczające do uzupełnienia strat radiacyjnych, a więc i do podtrzymania stabilnej atmosfery Słońca. Udało się nam ustalić, iż to właśnie ciepło wydzielane w zderzeniach, a nie to związane z lepkością czy też ciepło Joule'a, jest dominującym mechanizmem ogrzewającym chromosferę. Co więcej, wywołane granulacją przepływy fotosferycznej plazmy generują i podtrzymują odpływy plazmy koronalnej przechodzące w wiatr słoneczny. Wszystkie uzyskane rezultaty pozostają w zgodzie z danymi obserwacyjnymi i wnoszą istotny wkład w zrozumienie procesów zachodzących na Słońcu.

5 Literatura

Poniżej przedstawiona została podstawowa literatura użyta w toku prowadzonych badań. Szczegółowa literatura załączona jest do każdego z omawianych artykułów własnych.

1. Alfvén, H. 1942, Nature, 150, 405

2. Aschwanden, M. J. 2004, ApJ, 608, 554

3. Aschwanden, M. J. 2004, SOHO 15 Coronal Heating, 575, 97

4. Avrett, E. H., & Loeser, R. 2008, ApJS, 175, 228

5. Biermann, L. 1946, Naturwissenschaften, 33, 118

6. Braginskii, S.I. 1965, Reviews of Plasma Physics, 1, 205

7. Edlén, B. 1943, Zeitschrift für Astrophysik, 22, 30

8. Erdélyi, R., & Ballai, I. 2007, Astronomische Nachrichten, 328, 726

9. Grotrian, W. 1939, Naturwissenschaften, 27, 214

10. Hansteen, V. H., Leer, E., & Holzer, T. E. 1997, ApJ, 482, 498

11. Kuźma, B., Murawski, K. 2018, ApJ, 866, 50

12. Kuźma, B., Murawski, K., Kayshap, P., et al. 2017, ApJ, 849, 78

13. Kuźma, B., Murawski, K., Solov'ev, A. 2015, A&A, 577, A138

14. Kuźma, B., Murawski, K., Zaqarashvili, T. V., et al. 2017, A&A 597, A133

15. Kuźma, B., Wójcik D., Murawski, K. 2019, ApJ, 878, 81

16. Lamb H. 1909, Proc. Lond. Math. Soc., 7, 122

17. Lamb H. 1910, Proc. R. Soc. London, A, 34, 551

18. Leake, J. E., Lukin, V. S., Linton, M. G., & Meier, E. T. 2012, ApJ, 760, 109

19. Low, B. C. 1985, ApJ, 293, 31

20. Maneva, Y. G., Alvarez Laguna, A., Lani, A., & Poedts, S. 2017, ApJ, 836, 197

21. Martínez-Gómez, D., Soler, R., & Terradas, J. 2016, ApJ, 832, 101

22. Martínez-Gómez, D., Soler, R., & Terradas, J. 2017, ApJ, 837, 80

23. Meier, E. T. 2011, Ph.D. Thesis, University of Washington, Seattle

24. Meier, E. T., & Shumlak, U. 2012, Physics of Plasmas, 19, 072508

25. Meyer-Vernet, N. 2007, Basics of the Solar Wind, by Nicole Meyer-Vernet. ISBN-10 0-521-81420-0(HB); ISBN-13 978-0-521-81420-1 (HB). Published by Cambridge University Press, Cambridge, UK,2007

26. Murawski, K., Kayshap, P., Srivastava, A. K., Pascoe, D. J., Jelínek, P., Kuźma, B., Fedun, V. 2018, MNRAS, 474, 77.

27. Murawski, K., & Musielak, Z. E. 2016, MNRAS, 463, 4433

28. Musielak, Z. E., & Murawski, K. 2017, American Astronomical Society Meeting Abstracts, 229, 325.01

29. Nakariakov, V. M., & Verwichte, E. 2005, Liv. Rev. Sol. Phys., 2, 3

30. Oliver, R., Soler, R., Terradas, J., & Zaqarashvili, T. V. 2016, ApJ, 818, 128

31. Priest, E. 2014, Magnetohydrodynamics of the Sun, by Eric Priest, Cambridge, UK: Cambridge University Press, 2014

32. Schatzman, E. 1949, Annales d'Astrophysique, 12, 203

33. Schwarzschild, M. 1948, ApJ, 107, 1

34. Soler, R., Terradas, J., Oliver, R., Ballester, J. L. 2017, ApJ, 840, 20

35. Srivastava, A. K., Murawski, K., Kuźma, B., et al. 2018, Nature Astronomy, 2, 951

36. Srivastava, A. K., Shetye, J., Murawski, K., et al. 2017a, Scientific Reports, 7, 43147

37. Stark, B. A., & Musielak, Z. E. 1993, ApJ, 409, 450

38. Wedemeyer, S. 2016, The Messenger, 163, 15

39. Withbroe, G. L., & Noyes, R. W. 1977, ARA&A, 15, 363

40. Wójcik, D., 2017, MSc thesis, UMCS

41. Wójcik D, Kuźma, B., Murawski, K., Musielak, Z. E., 2019, ApJ, przyjęty do druku

42. Wójcik D, Kuźma, B., Murawski, K., Srivastava, A., 2019, ApJ, 884, 127

43. Zaqarashvili, T. V., Murawski, K., Khodachenko, M. L., & Lee, D. 2011, ApJ, 529, A85

44. Zaqarashvili, T. V., Oliver, R., & Ballester, J. L. 2006, A&A, 456, L13

A&A 597, A133 (2017)
DOI: 10.1051/0004-6361/201628747

Astronomy & Astrophysics

Numerical simulations of solar spicules: Adiabatic and non-adiabatic studies

B. Kuźma[1], K. Murawski[1], T. V. Zaqarashvili[2,3,4], P. Konkol[1], and A. Mignone[5]

[1] Group of Astrophysics, University of Maria Curie-Skłodowska, ul. Radziszewskiego 10, 20-031 Lublin, Poland
e-mail: blazejkuzma1@o2.pl
[2] IGAM, Institute of Physics, University of Graz, Universitätsplatz 5, 8010 Graz, Austria
[3] Abastumani Astrophysical Observatory at Ilia State University, 0160 Tbilisi, Georgia
[4] Space Research Institute, Austrian Academy of Sciences, Schmiedlstrasse 6, 8042 Graz, Austria
[5] Dipartimento di Fisica Generale, Univesità di Torino, via Pietro Giuria 1, 10125 Torino, Italy

Received 20 April 2016 / Accepted 30 September 2016

ABSTRACT

Aims. We aim to study the formation and evolution of solar spicules using numerical simulations of a vertical velocity pulse that is launched from the upper chromosphere.
Methods. With the use of the PLUTO code, we numerically solved adiabatic and non-adiabatic magnetohydrodynamic (MHD) equations in 2D cylindrical geometry. We followed the evolution of spicules triggered by pulses that are launched in a vertical velocity component from the upper chromosphere. Then we compared the results obtained with and without non-adiabatic terms in the MHD equations.
Results. Our numerical results reveal that the velocity pulse is steepened into a shock that propagates upward into the corona. The chromospheric cold and dense plasma follows the shock and rises into the corona with the mean speed of 20–25 km s^{-1}. The nonlinear wake behind the pulse in the stratified atmosphere leads to quasi-periodic rebound shocks, which lead to quasi-periodic rising of chromospheric plasma into the corona with a period close to the acoustic cut-off period of the chromosphere. We found that the effect of non-adiabatic terms on spicule evolution is minor; the general properties of spicules such as their heights and rising-time remain slightly affected by these terms.
Conclusions. In the framework of the axisymmetric model we devised, we show that the solar spicules can be triggered by the vertical velocity pulses, and thermal conduction and radiative cooling terms do not exert any significant influence on the dynamics of these spicules.
Key words. Sun: activity – magnetohydrodynamics (MHD) – methods: numerical – Sun: corona – Sun: transition region

1. Introduction

Spicules are thin, cool, and dense structures that are observed in the solar limb (Beckers 1968, 1972; Suematsu 1998; Sterling 2000; Zaqarashvili & Erdélyi 2009). They are seen to emerge from the chromospheric background at an altitude of about 2000 km above the solar surface where they reveal a speed of 25 km s^{-1}, reach a maximum level, and then either disappear or sink down to the chromosphere. A typical lifetime of spicules is within the range of 5–15 min with an average value of ∼7 min (Pasachoff et al. 2009). Spicules seem to consist of double-thread structures (Tanaka 1974; Dara et al. 1998; Suematsu et al. 2008), and they reveal bidirectional flows (Tsiropoula et al. 1994; Tziotziou et al. 2003, 2004; Pasachoff et al. 2009). Typical electron temperature and electron density in spicules are (15–17) × 10^3 K and 2 × 10^{11}–3.5 × 10^{10} cm $^{-3}$ at altitudes of 4–10 Mm above the solar surface (Beckers 1968) with a diameter estimated as 660 ± 200 km (Pasachoff et al. 2009). As a result, spicules are much cooler and denser than ambient coronal plasma. High-resolution observations by the Solar Optical Telescope onboard Hinode have revealed another type of spicules with many features different from those of classical limb spicules, and they are referred to as type II spicules (De Pontieu et al. 2007). The type II spicules are distinguished by (a) smaller diameters (≤200 km) in the Ca II H line and a significantly shorter height of 4 Mm; (b) a lifetime of 10–150 s; (c) the evolution, which shows an upflow and then disappears; and finally by (d) much higher speeds of 50–100 km s^{-1} (e.g., De Pontieu et al. 2007, 2009; Rouppe van der Voort et al. 2009; Kuridze et al. 2015). Macrospicules were recently discussed by Nóbrega-Siverio et al. (2016), who considered whether the relevance of the entropy sources in the surges, such as the optically thin losses, can be applied to similar phenomena as macrospicules.

In spite of various theoretical models that have been brought forward to explain the spicule ejection in the lower solar atmosphere, many recent numerical methods have been developed to simulate the solar spicules or macrospicules with an energy input at their base in the photosphere such as a gas pressure pulse or an Alfvén wave that steepens into a shock wave (Sterling 2000, and references therein). Hansteen et al. (2006) and De Pontieu et al. (2007) simulated the formation of dynamic fibrils that are due to slow magneto-acoustic shocks through two-dimensional (2D) numerical simulations. They suggested that these shocks are formed when acoustic waves generated by convective flows and global p-modes in the lower lying photosphere leak upward into the magnetized chromosphere. Heggland et al. (2007) used the initial periodic piston to drive the upward propagating shocks in 1D simulation, and Martinez-Sykora et al. (2009) considered the emergence of

new magnetic flux, but the drivers of spicules originate from collapsing granules, energy release in the photosphere, or in the lower chromosphere. However, these simulations were unable to mimic the double structures and bidirectional flows in spicules. On the other hand, Murawski & Zaqarashvili (2010) performed 2D numerical simulations of magnetohydrodynamic (MHD) equations and showed that the 2D rebound shock model of Hollweg (1982) may explain both the double structures and bidirectional flows. They used a single initial velocity pulse, which led to the formation of consecutive shocks as a result of the nonlinear wake in the stratified atmosphere. However, they considered a simple model of atmospheric temperature that was approximated by a smoothed step function for the temperature profile.

Understanding exact drivers of spicules requires further investigation, and more than one mechanism may trigger their evolution depending on the local plasma and magnetic field conditions. The goal of this paper is to contribute to the above-mentioned studies by performing simulations of the generation and evolution of the spicules in the solar atmosphere and compare our results for adiabatic and non-adiabatic MHD equations. The method we chose to trigger a spicule is a localized vertical velocity pulse launched from the upper chromosphere. This method is similar to the calculations performed by Shibata (1982), Sterling et al. (1993), Murawski & Zaqarashvili (2010), and Guerreiro et al. (2013). This approach differs from the models that attempt to model spicules with a disturbance in the photosphere (e.g., Suematsu et al. 1982; Hollweg 1982). Guerreiro et al. (2013) studied the mid-chromospheric energy inputs of earlier simulations by adding additional physics to the radiative loss term and including hydrogen ionization and recombination. They concluded that it would be difficult to produce spicules through those previously suggested mechanisms (specifically that of Sterling et al. 1993). Our simulations do not include the detailed energy losses of Guerrero et al. However, the energy input is different from that assumed by Guerrero et al. and Sterling et al., who adopted localized increase in the heating rate. Since the form of input energy is different, it is not clear whether the losses Guerrero et al. took into account would have any effect on the velocity of pulse-driven spicules. This will be tested in the future studies.

This paper is organized as follows. A numerical model is presented in Sect. 2, and the corresponding numerical results are shown in Sect. 3. Our paper is concluded by a summary of the numerical results in Sect. 4.

2. Physical model of the solar atmosphere

2.1. MHD equations

We consider a gravitationally stratified and magnetically confined solar plasma that is governed by the following set of non-adiabatic MHD equations:

$$\frac{\partial \varrho}{\partial t} + \nabla \cdot (\varrho \boldsymbol{V}) = 0, \tag{1}$$

$$\varrho \frac{\partial \boldsymbol{V}}{\partial t} + \varrho \left(\boldsymbol{V} \cdot \nabla\right) \boldsymbol{V} = -\nabla p + \frac{1}{\mu} (\nabla \times \boldsymbol{B}) \times \boldsymbol{B} + \varrho \boldsymbol{g}, \tag{2}$$

$$\frac{\partial p}{\partial t} + \boldsymbol{V} \cdot \nabla p + (\gamma - 1) p \nabla \cdot \boldsymbol{V} = -(\gamma - 1)(L + \nabla \cdot \boldsymbol{q} - H), \tag{3}$$

$$\frac{\partial \boldsymbol{B}}{\partial t} = \nabla \times (\boldsymbol{V} \times \boldsymbol{B}), \quad \nabla \cdot \boldsymbol{B} = 0, \tag{4}$$

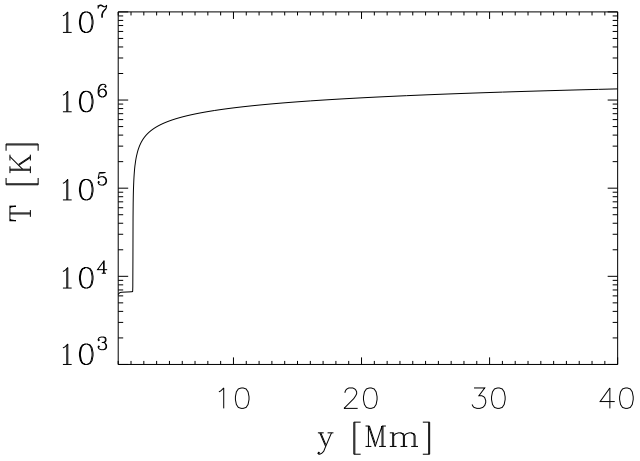

Fig. 1. Hydrostatic solar atmospheric temperature vs. height y.

where ϱ is the mass density, p the gas pressure, $\boldsymbol{V}$ represents the plasma velocity, $\boldsymbol{B}$ is the magnetic field, T the temperature, $\boldsymbol{q}$ the anisotropic thermal conduction flux, $L(\varrho, T)$ radiatively thin cooling terms (Mignone et al. 2007), and $H(\varrho_e, T_e)$ denotes the external heating therm that balances L and $\nabla \cdot \boldsymbol{q}$ at the equilibrium that is specified in Sect. 2.2. This term depends only on the equilibrium plasma quantities and therefore it does not vary in time. The symbol k_B denotes the Boltzmann constant, $\gamma = 5/3$ is the adiabatic index, m is the particle mass that is specified by a mean molecular weight of 0.6, and $\boldsymbol{g} = (0, -g, 0)$ is the gravitational acceleration. The value of g is equal to 274 m s^{-2}.

2.2. Equilibrium solar atmosphere

In a static solar atmosphere all plasma quantities are time-invariant, which means that $\partial f_e / \partial t = 0$, where f_e denotes a plasma quantity and the subscript e corresponds to the equilibrium. Then, from Eqs. (1)–(4) it follows that for a still ($\boldsymbol{V}_e = \boldsymbol{0}$) medium the Lorentz force must be balanced by the gravity force and the gas pressure gradient,

$$\frac{1}{\mu} (\nabla \times \boldsymbol{B}_e) \times \boldsymbol{B}_e - \nabla p_e + \varrho_e \boldsymbol{g} = \boldsymbol{0}, \tag{5}$$

and the heating term must compensate for the radiative losses and thermal conduction,

$$H = L(\varrho_e, T_e) + \nabla \cdot \boldsymbol{q}_e. \tag{6}$$

This model of the solar atmosphere corresponds to a quiet Sun.

2.2.1. Force-free magnetic field of the hydrostatic atmosphere

A hydrostatic atmosphere corresponds to the force-free ($(\nabla \times \boldsymbol{B}_e) \times \boldsymbol{B}_e = \boldsymbol{0}$) magnetic field. We additionally assume a current-free ($\nabla \times \boldsymbol{B}_e = \boldsymbol{0}$) magnetic field whose radial B_{er}, azimuthal $B_{e\theta}$, and vertical B_{ey} components are given as

$$B_{er}(r, y) = \frac{3 S r (a - y)}{(r^2 + (a - y)^2)^{\frac{5}{2}}},$$

$$B_{e\theta}(r, y) = 0,$$

$$B_{ey}(r, y) = \frac{S (r^2 - 2(a - y)^2)}{(r^2 + (a - y)^2)^{\frac{5}{2}}}, \tag{7}$$

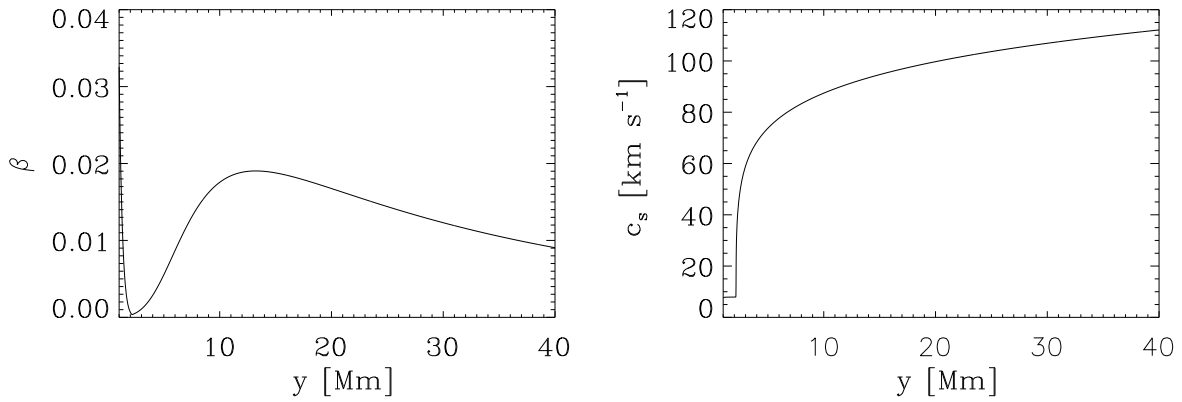

Fig. 2. Vertical profile of plasma β (*left*) and sound speed c_s (*right*) at the plasma equilibrium.

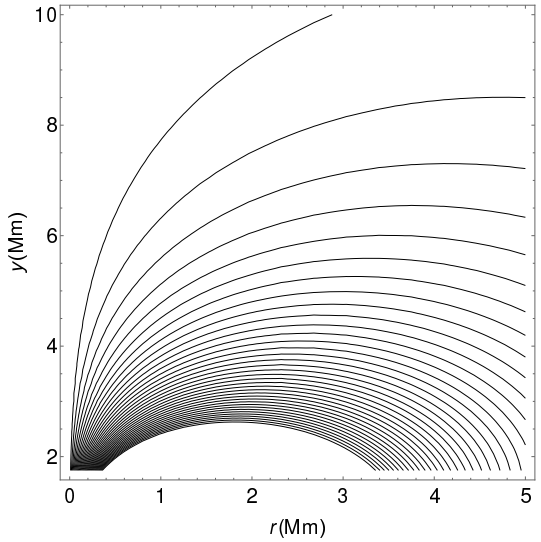

Fig. 3. Magnetic field lines at the plasma equilibrium.

where a and S are free parameters corresponding to the vertical location of the singularity in the magnetic field and the magnetic field strength, respectively. We set $a = -1$ Mm and S in such way that at the reference point $(r = 0, y = y_r = 6)$ Mm the magnitude of magnetic field $B_e = 9.5$ Gauss. The corresponding magnetic field lines are displayed in Fig. 3. We note that the magnetic lines diverge with height and $\boldsymbol{B}_e$ is vertical along the symmetry axis, $r = 0$ Mm.

For a force-free magnetic field it follows from Eq. (5) that the gas pressure gradient has to be balanced by the gravity force,

$$\nabla p_h = \varrho_h \boldsymbol{g}. \tag{8}$$

The subscript h corresponds to a hydrostatic quantity. With the use of the ideal gas law and the vertical y-component of Eq. (8), we express the hydrostatic gas pressure and mass density as

$$p_h(y) = p_0 \exp\left(-\int_{y_r}^{y} \frac{dy'}{\Lambda(y')}\right), \quad \varrho_h(y) = \frac{p_h(y)}{g\Lambda(y)}, \tag{9}$$

where

$$\Lambda(y) = \frac{k_B T_h(y_r)}{mg} \tag{10}$$

is the pressure scale height, and p_0 denotes the gas pressure at the reference level, $y = y_r$.

For simplicity reasons we assume that T_h varies with height y only, and it specifies a hydrostatic atmosphere that is determined by the semi-empirical model of Avrett & Loeser (2008) that is extrapolated into the solar corona (Fig. 1). In this model, the temperature attains a value of about 7×10^3 K at the top of the chromosphere, $y \approx 2.0$ Mm. At the transition region, which is located at $y \simeq 2.1$ Mm, T_h exhibits an abrupt jump (Fig. 1) and grows to about 1.0×10^6 K in the solar corona at $y = 10$ Mm. Higher up in the solar corona, the temperature increases very slowly, tending to its asymptotic value of about 2 MK at $y = 40$ Mm. The temperature profile uniquely determines the equilibrium mass density and gas pressure profiles, which decrease with height (not shown).

We specify the plasma β as the ratio of gas to magnetic pressures,

$$\beta(y) = \frac{p_e(y)}{B^2(y)/2\mu}. \tag{11}$$

The vertical profile of plasma β is illustrated in Fig. 2 (left panel). We note that for the coronal plasma, the value of plasma β is lower than 1 within the displayed region. The vertical profile of the sound speed

$$c_s(y) = \sqrt{\frac{\gamma p_e(y)}{\varrho_e(y)}} \tag{12}$$

is displayed in the right panel of Fig. 2. Below the transition region, $c_s \approx 10$ km s^{-1}. Higher up c_s grows, first fast right above the transition region, and higher up slowly, reaching a value of about 100 km s^{-1} at $y \approx 20$ Mm.

2.2.2. Perturbation

Initially, at $t = 0$ s we perturb the model equilibrium by the initial pulse in the y-component of velocity, which is expressed as follows:

$$V_y(r, y) = A_V \times \exp\left(-\frac{r^2 + (y - y_0)^2}{w^2}\right), \tag{13}$$

where y_0 is the vertical position of the initial pulse, w is its width, and A_V its amplitude. We set and hold fixed $w = 0.25$ Mm, while allowing other parameters to vary. For our studies, the initial position of y_0 varies between 1.5 Mm and 1.75 Mm, and the amplitude A_V varies between 30 km s^{-1} and 50 km s^{-1}. The detailed studies were performed for the case of $A_V = 40$ km s^{-1} and $y_0 = 1.75$ Mm. The value of A_V may be associated with reconnection of magnetic field lines.

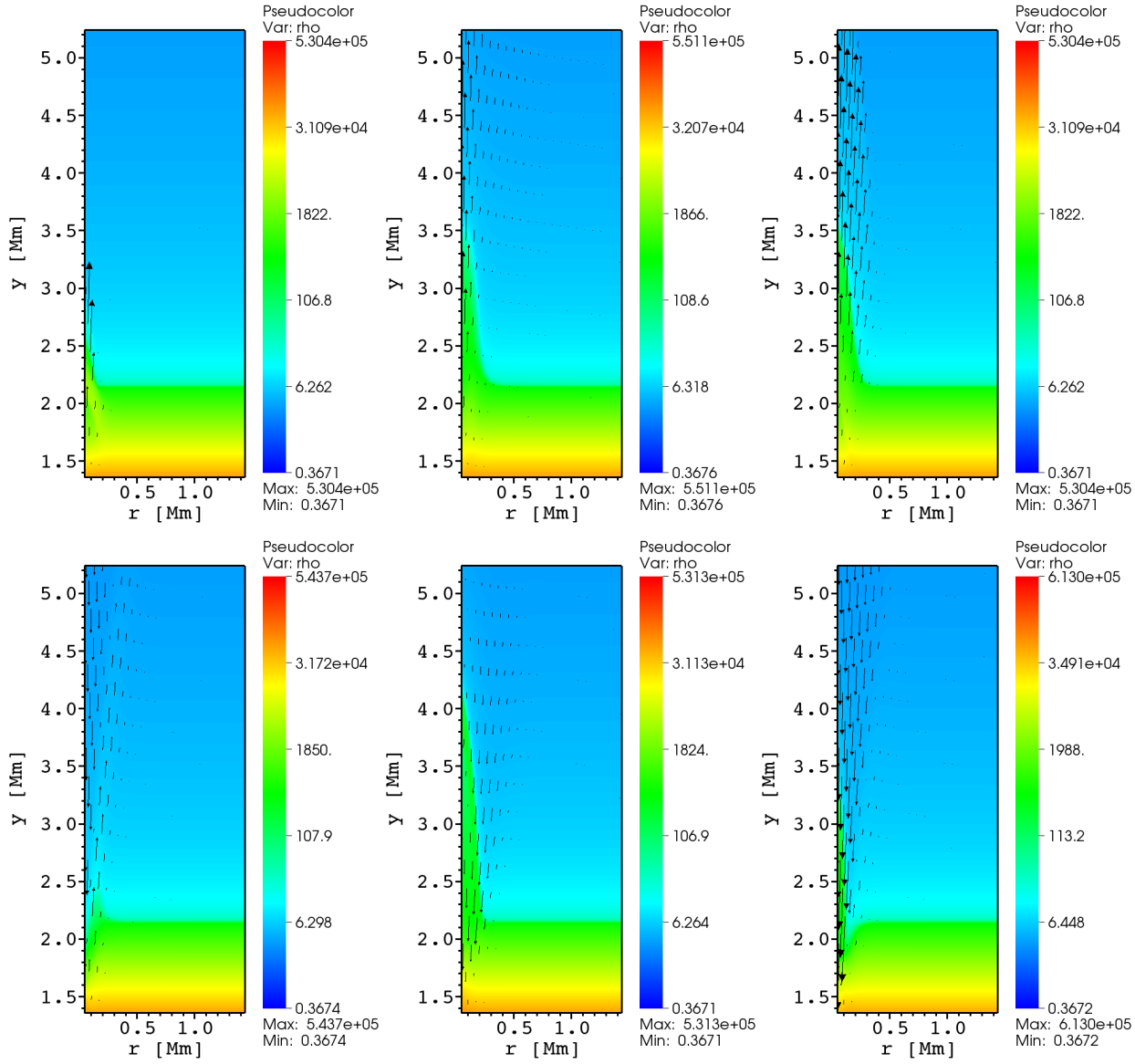

Fig. 4. Temporal evolution of $\log(\varrho(r, y))$ at $t = 20$ s, $t = 50$ s, $t = 110$ s, $t = 175$ s, $t = 220$ s, $t = 300$ s (*from top left to bottom right*), for adiabatic MHD equations and for the case of $A_V = 40$ km s^{-1} and $y_0 = 1.75$ Mm. Arrows represent velocity vectors in the $r - y$ plane, $[V_r, V_y]$.

3. Numerical simulations of MHD equations

To solve Eqs. (1)–(3) numerically, we used the PLUTO code (Mignone et al. 2007, 2012). In our problem, we set the Courant-Friedrichs-Levy number equal to 0.3 and chose piecewise TVD linear interpolation in a second-order Runge-Kutta method, which leads to second-order accuracy in space and time. Additionally, we adopted the Harten-Lax-van Leer discontinuities (HLLD) approximate Riemann solver (Miyoshi & Kusano 2005).

Our simulation box in (r, y) was set as $(0.0, 5.12)$ Mm $\times$ $(1.0, 40.0)$ Mm, where $y = 0$ denotes the bottom of the photosphere. For our study we used the uniform grid within the region $(0.0 \le r \le 5.12)$ Mm $\times$ $(1.0 \le y \le 11.24)$ Mm, which is covered by 1024×2048 grid points. This leads to a resolution of 5 km in the lower regions of the simulation box. Above this region, namely within the box $(0.0 \le r \le 5.12)$ Mm $\times$ $(11.24 \le y \le 40.0)$ Mm, we implemented a stretched grid along the y-direction; this box was divided into 648 cells whose size grows with y. Such a stretched grid plays the role of a sponge as it absorbs incoming signal and allows us to avoid significant reflections from upper boundary. We imposed open boundary conditions at $r = 5$ Mm, but at the bottom and top, we fixed all plasma quantities to their equilibrium values. The left boundary $(r = 0)$ was set as axisymmetric.

The heating source term H in Eq. (3) was implemented as follows. The code computed the residuum $\boldsymbol{R}^0$ using the initial condition and then it subtracted $\boldsymbol{R}^0$ also at later times during the update over time step Δt as

$$\boldsymbol{U}^{n+1} = \boldsymbol{U}^n + \Delta t(\boldsymbol{R}^n - \boldsymbol{R}^0), \tag{14}$$

where $\boldsymbol{U}^n$ is a plasma vector state at time $t = n\Delta t$, $n = 1, 2, \ldots$ This automatically mimics the heating term without any need to explicitly write it.

To fully understand the influence of non-adiabatic effects on simulated spicules, we performed first simulations of the adiabatic case, that is, without the thermal conduction and cooling terms. Figure 4 shows the spatial profiles of logarithm of $\varrho(r, y)$ at six instants of time. We note that the system is axisymmetric along $r = 0$ Mm. The initial pulse in V_y is launched from

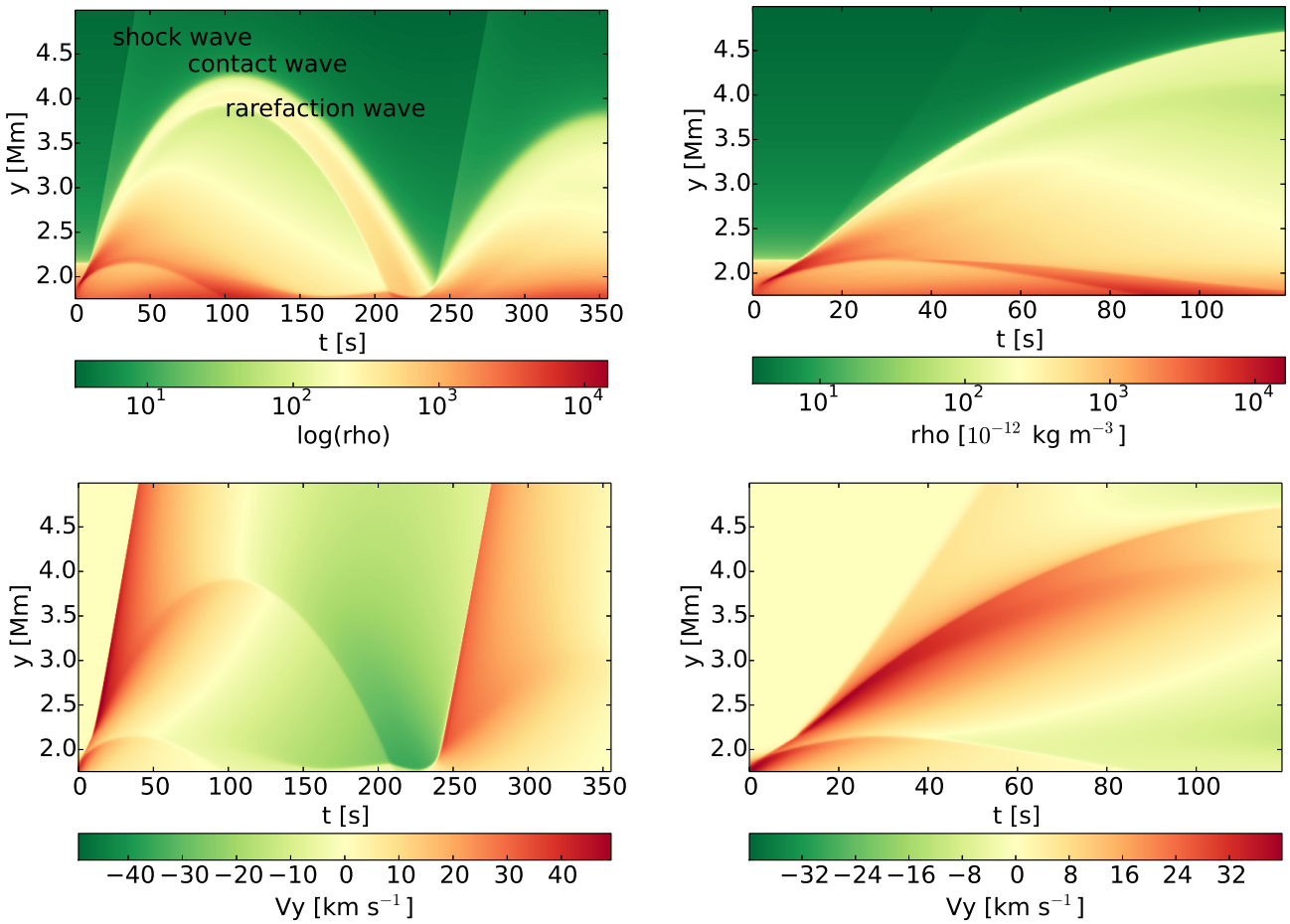

Fig. 5. Temporal evolution of $\varrho(r = 0, y)$ (*top*) and $V_y(r = 0, y)$ (*bottom*) for the case of adiabatic (*left*) and non-adiabatic (*right*) MHD equations and for $A_V = 40$ km s^{-1} and $y_0 = 1.75$ Mm.

$r = 0$ Mm, $y = 1.75$ Mm, which is located about 0.35 Mm below the transition region. The amplitude of the initial pulse is $A_V = 40$ km s^{-1}. The shock front that results from the initially launched pulse arrives at the transition region and triggers the plasma jet (top panels), which reaches its maximum height of ≈4.3 Mm (top right panel). At later moments in time, the chromospheric plasma injected into the corona begins to fall toward the transition region (bottom left panel). The falling plasma then triggers the second pulse (bottom middle panel), which results in the second spicule (bottom right panel).

Figure 5 shows the temporal evolution of $\varrho(r = 0, y)$ (top panels) and $V_y(r = 0, y)$ (bottom panels) for adiabatic (left panels) and non-adiabatic (right panels) cases. The rise time of the spicule to its maximum height in the adiabatic case is ≈110 s, which is shorter by about 15 s than in the non-adiabatic case (≈125 s), and the chromospheric plasma reaches a height of ≈4.3 Mm. This value is lower than in non-adiabatic case (≈4.7 Mm). In the adiabatic case we spot three waves (Fig. 5, top left panel): the leading wave is a shock wave, which travels with velocity ≈170 km s^{-1}; this shock is followed by the contact wave, and the rarefaction wave. We note that all plasma quantities are continuous across a contact wave; the only exception is the mass density, which is discontinuous. As a result, all three waves are seen on the mass density profiles, while $V_y(r = 0, y)$ profiles reveals only two of these waves. As in the non-adiabatic case, in later moments, the system becomes thermally unstable. The right panels show the initial phase of the system evolution. The cross-section of Fig. 5 for the adiabatic case for a fixed value

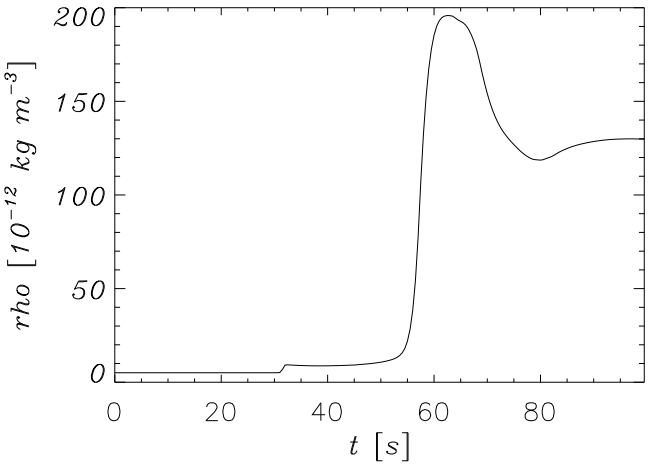

Fig. 6. Temporal evolution of $\varrho(r = 0, y = 5)$ Mm for the case of $A_V = 40$ km s^{-1} and $y_0 = 1.75$ Mm.

of $y = 3.5$ Mm is presented in Fig. 6. The corresponding three waves (shock, contact, and rarefaction) are represented by steep gradients at $t \approx 30$ s, $t \approx 55$ s, and $t \approx 75$ s. As the formation mechanism of the spicule is a shock wave, we assume that it is the crest-shock-type jet (Shibata 1982). The mass density at the top of the spicule is ~10^2 higher than in the ambient coronal plasma (Fig. 6, $t \approx 75$ s), and it matches the predicted value for the crest-shock-type jet.

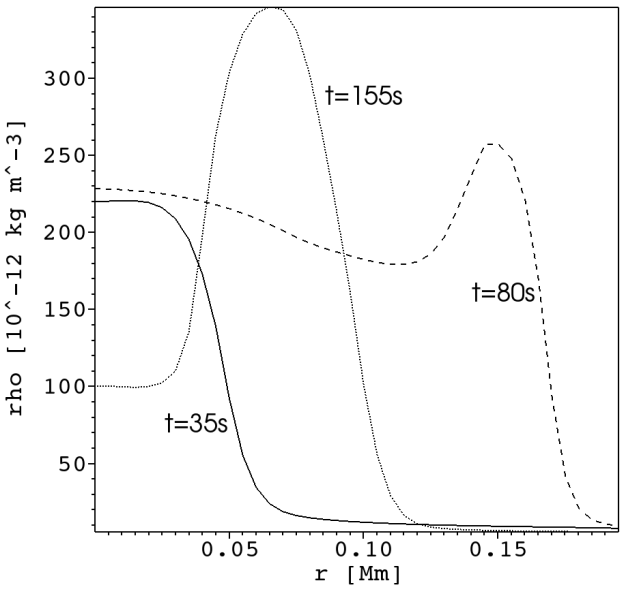

Fig. 7. Radial profile of $\varrho(r, y = 3.1\,\mathrm{Mm})$ at $t = 35$ s (solid line), $t = 80$ s (dashed line), and $t = 155$ s (dotted line) in the case of adiabatic MHD equations. The case of $A_\mathrm{V} = 40\,\mathrm{km\,s^{-1}}$ and $y_0 = 1.75$ Mm.

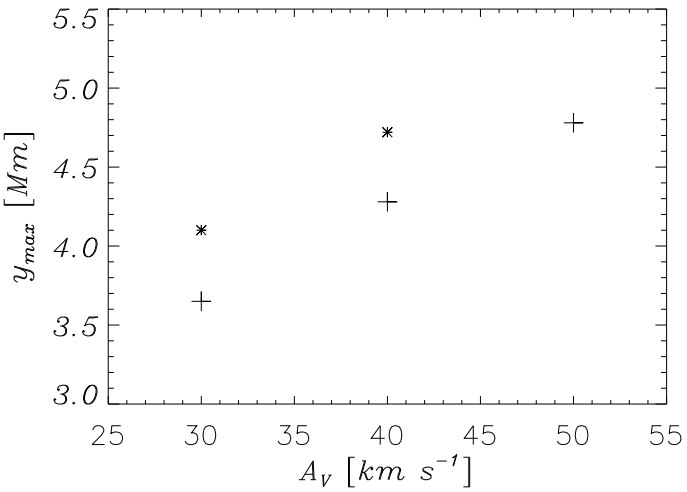

Fig. 8. Maximum height of spicule y_max vs. amplitude of the initial pulse A_V for $y_0 = 1.75$ Mm. The case of adiabatic (+) and non-adiabatic (⁎) MHD equations.

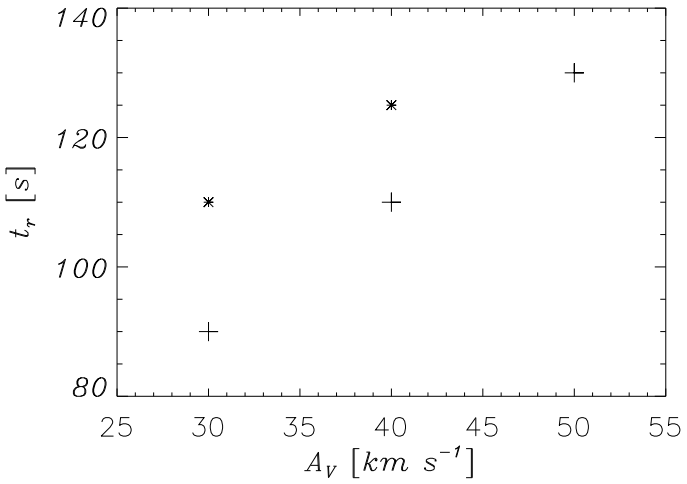

Fig. 9. Rise time of spicule t_r vs. amplitude of the initial pulse A_V for $y_0 = 1.75$ Mm. The case of adiabatic (+) and non-adiabatic (⁎) MHD equations.

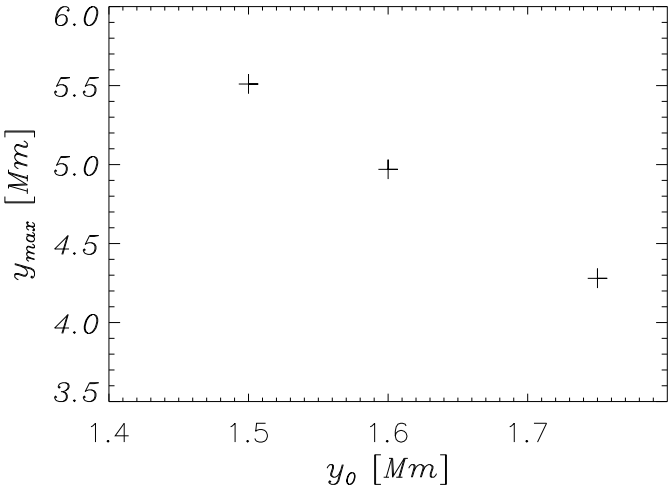

Fig. 10. Maximum height of spicule y_max vs. vertical position of the initial pulse y_0 for $A_V = 40\,\mathrm{km\,s^{-1}}$ and in the case of adiabatic MHD equations.

Figure 7 shows the effect caused by the rarefaction wave. The horizontal plane is located at $y = 3.5$ Mm. The plasma inside the spicule-like structure becomes rarefied. The time at which this rarefaction occurs is clearly shown: the dense plasma at $t = 35$ s (solid line) experiences rarefaction within the central part of the spicule at $t = 80$ s (dashed line), which keeps its trend up to $t = 155$ s (dotted line). At this time, plasma is so rarefied that it may be missed by the detectors. This may mimic the disappearance of II type spicules.

Figure 8 illustrates spicule height y_max vs. amplitude of the initial pulse A_V with a fixed position of the initial pulse $y_0 = 1.75$ Mm. Hence we infer that a larger amplitude pulse results in chromospheric plasma reaching a higher maximum altitude, which is intuitively expected as a larger amplitude corresponds to more energy being launched initially. This more energetic pulse leads to higher jets. Figure 9 shows a similar trend in the arise time of the spicule for a growing amplitude of the pulse. The comparison of results for adiabatic (+) and non-adibatic (*) MHD equations reveals that the non-adiabatic effects have a minor influence on both spicule height and rise time of the spicule. The non-adiabatic terms result in a growth of the maximum height by about ~10–15%, while the rise time of the spicule grows by about ~15–20%.

Figure 10 illustrates the influence of the vertical position of the initial pulse on the maximum height of the spicule. For a pulse launched closer to the transition region, the mass density of the upward-pushed plasma is lower. Thus such a pulse exhibits a lower momentum, and we can expect it to penetrate lower coronal regions. We also expect that the rise time of the spicule becomes shorter with a higher value of y_0. Indeed, Fig. 11 illustrates this declining trend. The obtained values of spicule height lie within the range of the observed height of the spicules.

Figure 12 displays the dependence of spicule velocity on time. The location of the top of the spicule is determined by the vertical position of the contact wave. The upward movement of the transition region plasma starts at $t \approx 10$ s, and at this time the spicule reaches its speed of about 45 km s^{-1}. At later moments in time, this spicule decelerates until at $t \approx 100$ s the spicule

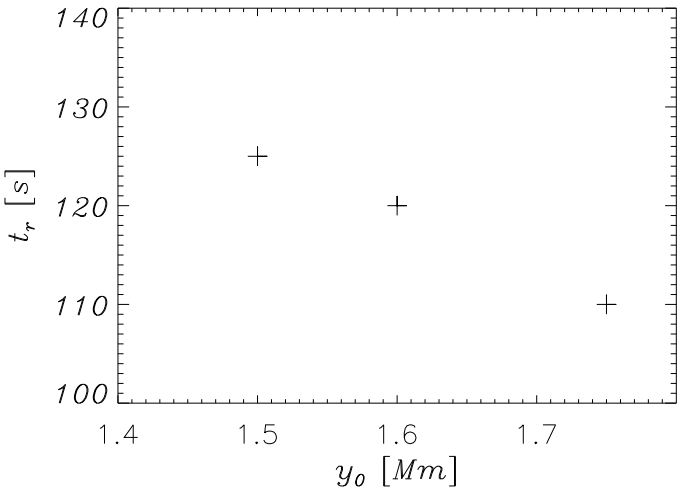

Fig. 11. Rise time of spicule t_r vs. vertical position of the initial pulse y_0 for $A_V = 40$ km s^{-1} and in the case of adiabatic MHD equations.

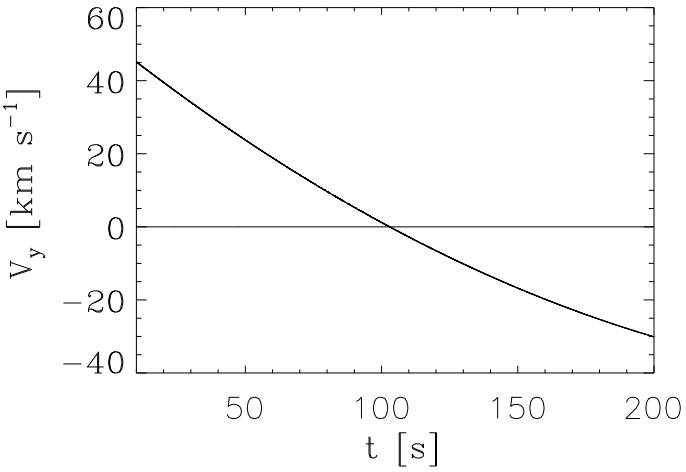

Fig. 12. Spicule velocity V_y vs. time for $y_0 = 1.75$ Mm, $A_V = 40$ km s^{-1} and adiabatic MHD equations.

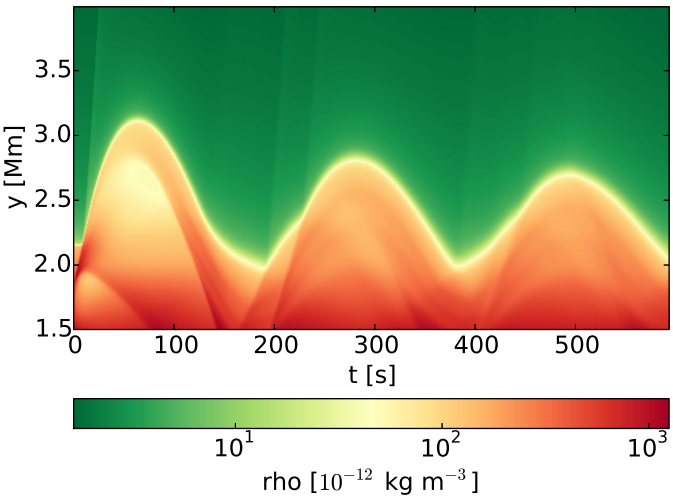

Fig. 13. Time-distance plot of $\varrho(r = 0, y, t)$ vs. time for $y_0 = 1.75$ Mm, $A_V = 30$ km s^{-1} and adiabatic MHD equations.

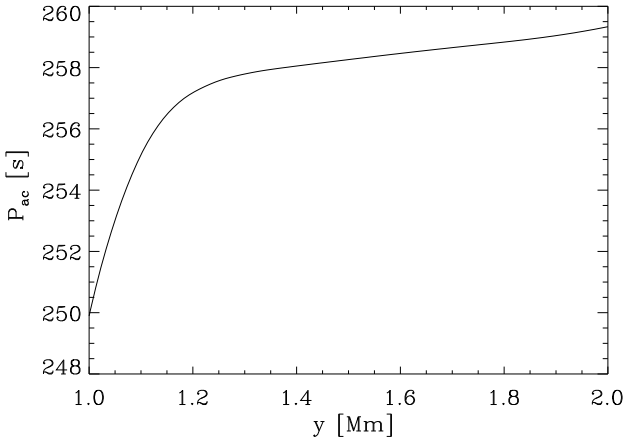

Fig. 14. Acoustic cut-off wave period P_{ac} vs. altitude y.

speed attains zero, which occurs at the highest location of the spicule. At the lowest location of the spicule, which is reached at $t = 200$ s, the vertical velocity of the decreasing plasma is about 30 km s^{-1}. After the first rise and fall, the transition region subsequently experiences oscillations.

The transition region exhibits oscillations that are due to the rebound shocks (Hollweg 1982). It is interesting that these oscillations occur with a wave period of about 250 s (Fig. 13). This wave period is close to the acoustic cut-off period,

$$P_{ac}(y) = \frac{4\pi c_s(y)}{\gamma g}, \quad (15)$$

which for $y = y_0 = 1.75$ Mm attains a value of about 259 s (Fig. 14).

4. Summary and conclusions

We performed numerical simulations of a spicule by launching initially (at $t = 0$ s) a localized pulse in the y-component of a plasma velocity in the upper chromosphere. The initial magnetic field configuration was force-free and the initial stratification remained in static equilibrium. We simulated both ideal and non-ideal MHD equations to reveal non-adiabatic effects such as thermal conduction and radiation. Numerical simulations showed that an upward-propagating signal quickly steepened into a shock that propagated into the corona along the magnetic field lines. This shock was followed by the cold and dense chromospheric plasma jet, which exhibited properties of a contact wave and reached a certain height (typically 4–5 Mm) and then returned to the chromosphere. The mean up-flow speed was 20–25 km s^{-1}. The obtained values match those given for the spicules observed by Beckers (1968, 1972). However, subsequent shocks come from the chromosphere with a periodicity of almost the chromospheric acoustic cut-off period, which is the result of the nonlinear wake behind the pulse that propagates in the stratified atmosphere (Kuridze et al. 2009). These shocks again lift up the chromospheric plasma into the corona and cause the quasi-periodic appearance of plasma jets. This is consistent with the rebound shock model suggested by Hollweg (1982). Numerical solutions show that the rarefaction wave that follows the shock-wave results in a reduction of the mass density inside the structure. Both ideal and non-ideal simulations give similar results for the maximum height, upward speed, rise time, and periodicity. Therefore, non-adiabatic effects do not significantly affect the dynamics of jets, but slightly increase the maximum heights and rise time.

In conclusion, our numerical simulations of the solar spicules approximately mimicked the observed properties of the spicules. Since we did not attempt to synthesize observables, an exact comparison with observations cannot be achieved here.

Acknowledgements. This work (B.K. and K.M.) was financially supported by the project from the Polish National Foundation (NCN) Grant No. 2014/15/B/ST9/00106. The work of T.V.Z. was supported by the Austrian "Fonds zur Förderung der Wissenschaftlichen Forschung" (FWF) under projects P26181-N27 and P25640-N27, by Austrian Scientific-Technology Collaboration (WTZ) Grant PL15/2013 and by FP7-PEOPLE-2010-IRSES-269299 project-SOLSPANET. The PLUTO code used in this work was developed by Andrea Mignone. Numerical simulations were performed on the Lunar/Solaris cluster at Institute of Mathematics of M. Curie-Skłodowska University. The visualizations of the simulation variables have been carried out using the IDL (Interactive Data Language) and VisIt software packages.

References

Avrett, E. H., & Loeser, R. 2008, ApJS, 175, 228
Beckers, J. M. 1968, Sol. Phys., 3, 367
Beckers, J. M. 1972, ARA&A, 10, 73
Dara, H. C., Koutchmy, S., & Sueamatsu, Y. 1998, in Solar Jets and Coronal Plumes, ESA SP, 421, 255
De Pontieu, B., McIntosh, S. W., & Hansteen, V. H., et al. 2007, PASJ, 59, 655
De Pontieu, B., McIntosh, S. W., Hansteen, V. H., & Schrijver, C. J. 2009, ApJ, 701, L1
Guerreiro, N., Carlsson, M., & Hansteen, V. 2013, APJ, 766, 128
Hansteen, V. H., De Pontieu, B., Rouppe van der Voort, L. H. M., van Noort, M., & Carlsson, M. 2006, ApJ, 647, L73
Heggland, L., De Pontieu, B., & Hansteen, V. H. 2007, ApJ, 666, 1267
Hollweg, J. V. 1982, ApJ, 257, 345
Kuridze, D., Zaqarashvili, T. V., Shergelashvili, B. M., & Poedts, S. 2009, A&A, 505, 763
Kuridze, D., Henriques, V., Mathioudakis, M., et al. 2015, ApJ, 802, 26
Martinez-Sykora, J., Hansteen, V., De Pontieu, B., & Carlsson, M. 2009, ApJ, 701, 1569
Mignone, A., Bodo, G., Massaglia, S., et al. 2007, ApJS, 170, 228
Mignone, A., Zanni, C., Tzeferacos, P., et al. 2012, ApJS, 198, 7
Miyoshi, T., & Kusano, K. 2005, JCP, 208, 315
Murawski, K., & Zaqarashvili, T. V. 2010, A&A, 519, A8
Nóbrega-Siverio, D., Moreno-Insertis, F., & Martínez-Sykora, J. 2016, ApJ, 822, 18
Pasachoff, J. M., Jacobson, W. A., & Sterling, A. C. 2009, Sol. Phys., 260, 59
Rouppe van der Voort, L. H. M., Leenaarts, J., De Pontieu, B., Carlsson, M., & Vissers, G. 2009, ApJ, 705, 272
Shibata, K. 1982, Sol. Phys., 81, 9
Sterling, A. C. 2000, Sol. Phys., 196, 79
Sterling, A. C., Shibata, K., & Mariska, J. T. 1993, ApJ, 407, 778
Suematsu, Y. 1998, in Solar Jets and Coronal Plumes, ESA SP, 421, 19
Suematsu, Y., Shibata, K., Neshikawa, T., & Kitai, R. 1982, Sol. Phys., 75, 99
Suematsu, Y., Ichimoto, K., Katsukawa, Y., et al. 2008, ASP Conf. Ser., 397, 27
Tanaka, K. 1974, in Chromospheric Fine Structure, ed. G. Athay, IAU Symp., 56, 239
Tsiropoula, G., Alissandrakis, C. E., & Schmieder, B. 1994, A&A, 290, 294
Tziotziou, K., Tsiropoula, G., & Mein, P. 2003, A&A, 402, 361
Tziotziou, K., Tsiropoula, G., & Mein, P. 2004, A&A, 423, 1133
Zaqarashvili, T. V., & Erdélyi, R. 2009, Space Sci. Rev., 149, 355

The Astrophysical Journal, 849:78 (9pp), 2017 November 10 https://doi.org/10.3847/1538-4357/aa8ea1

Two-fluid Numerical Simulations of Solar Spicules

Błażej Kuźma[1], Kris Murawski[1], Pradeep Kayshap[1], Darek Wójcik[1], Abhishek Kumar Srivastava[2], and Bhola N. Dwivedi[2]
[1] Group of Astrophysics, University of Maria Curie-Skłodowska, ul. Radziszewskiego 10, 20-031 Lublin, Poland; blazejkuzma1@gmail.com
[2] Department of Physics, Indian Institute of Technology (BHU), Varanasi-221005, India
Received 2017 May 15; revised 2017 September 18; accepted 2017 September 19; published 2017 November 3

Abstract

We aim to study the formation and evolution of solar spicules by means of numerical simulations of the solar atmosphere. With the use of newly developed JOANNA code, we numerically solve two-fluid (for ions + electrons and neutrals) equations in 2D Cartesian geometry. We follow the evolution of a spicule triggered by the time-dependent signal in ion and neutral components of gas pressure launched in the upper chromosphere. We use the potential magnetic field, which evolves self-consistently, but mainly plays a passive role in the dynamics. Our numerical results reveal that the signal is steepened into a shock that propagates upward into the corona. The chromospheric cold and dense plasma lags behind this shock and rises into the corona with a mean speed of 20–25 km s^{-1}. The formed spicule exhibits the upflow/downfall of plasma during its total lifetime of around 3–4 minutes, and it follows the typical characteristics of a classical spicule, which is modeled by magnetohydrodynamics. The simulated spicule consists of a dense and cold core that is dominated by neutrals. The general dynamics of ion and neutral spicules are very similar to each other. Minor differences in those dynamics result in different widths of both spicules with increasing rarefaction of the ion spicule in time.

Key words: magnetohydrodynamics (MHD) – methods: numerical – Sun: activity – Sun: corona – Sun: transition region

1. Introduction

Spicules are thin jet-like structures, which dominate in the lower layers of the solar corona. They are best seen at the solar limb in strong chromospheric and transition-region (TR) spectral lines such as Hα, Ca II H & K, Mg II H & K, C II, and Si IV lines (e.g., Roberts 1945; Matsuno & Hirayama 1988; Nishikawa 1988; Suematsu et al. 1995; De Pontieu et al. 2007b; Suematsu et al. 2008; Sterling et al. 2010; Madjarska et al. 2011; Pereira et al. 2012, 2014, 2016; Tsiropoula et al. 2012; Skogsrud et al. 2014, 2015; Rouppe van der Voort et al. 2015; Beck et al. 2016). Spicule observations have been carried out for about 130 years since they were first reported in 1877 (Secchi 1887). Therefore, a huge amount of observational literature about spicules is available, which is dedicated to understanding their basic properties (mass density, temperature, velocity, and magnetic field), initiation mechanisms, waves, and oscillations. These crucial aspects are very well documented in various review papers, i.e., basic properties by Beckers (1968, 1972) and Suematsu (1998), initiation mechanisms by Sterling (2000), and oscillations and waves by Zaqarashvili & Erdélyi (2009).

High-resolution observational data leads to continuous improvement of our knowledge about the spicules. Based on their properties, De Pontieu et al. (2007b) classified the spicules into two different categories (i.e., Types I and II). Type I spicules exhibit a slower velocity (15–40 km s^{-1}) and longer lifetime (3–10 minutes) compared to the velocity (30–110 km s^{-1}) and lifetime (50–150 s) of Type II spicules. Type I spicules reveal the rise and fall of plasma during its total life, while type II spicules fade from the view and the downfall of plasma is not visible (e.g., De Pontieu et al. 2007b; Pereira et al. 2012). Sterling & Hollweg (1984) have proposed that the heating rate is sufficient to heat the spicules to temperatures at which the hydrogen is fully ionized. Therefore, H-α spicules (cool temperature) may evolve into EUV spicules (hot temperature). Later, this thermal evolution (i.e., fading of the spicules from cool filters and appears in the hot filters) of the spicules was investigated in various other works as well (e.g., De Pontieu et al. 2009; McIntosh & De Pontieu 2009; McIntosh et al. 2010; Tian et al. 2011). Recently, Pereira et al. (2014) have reported the traces of spicules in the hot temperature filter after fading from the cool temperature filter.

The origin and excitation mechanisms of spicules are one of the most crucial issues of solar physics, which has been continuously investigated using observations as well as numerical simulations. Pulses in velocity or gas pressure, Alfvén waves, and p-modes are the three broad categories of drivers that may be responsible for the formation of spicules. Main physical process within the velocity/gas pressure pulse model is the formation of a shock front, which results in a generation of the spicule in the lower corona. Such a rebound shock model was developed by Hollweg (1982) who used a gas pressure pulse in one-dimensional (1D) MHD equations for the formation of a spicule. In another approach, Suematsu et al. (1982) performed a numerical experiment using a velocity pulse instead of a gas pressure pulse. Later, this rebound shock model was improved by including radiation and heat conduction in the model (e.g., Sterling & Mariska 1990; Cheng 1992; Sterling et al. 1993; Heggland et al. 2007; Kuźma et al. 2017). Recently, Sterling & Moore (2016) have reported that the microfilament-eruptions can be a potential candidate for the generation of spicules. Murawski & Zaqarashvili (2010) performed 2D numerical simulations with a velocity pulse to produce the spicule. Multistructural, bidirectional flows and 3–5 minute periodicity in the occurrence of spicules were successfully reproduced in that numerical experiment. This model was extended into its 2D counterpart with the inclusion of the nonadiabatic effects (Kuźma et al. 2017). A general conclusion drawn from the performed simulations was that the shocks play an important role in the dynamics and thermodynamics of impulsively generated spicules and the other

nonadiabatic terms (i.e., thermal conduction and radiative cooling terms) produce minor effects on the dynamics/thermodynamics of the spicule.

In the second category, it was proposed that the nonlinear coupling between Alfvén waves and slow magnetoacoustic shocks can lift up the TR, which produces the spicule (Hollweg et al. 1982). This idea for the generation of spicules was further investigated by Cranmer & Woolsey (2015, 2016). They have found that the magnetohydrodynamic turbulence is a potential driver for spicules. It was also reported that the random nonlinear Alfvén pulses may reproduce the spicules (Kudoh & Shibata 1999). More interestingly, the damping of Alfvén waves due to ion-neutral collisions can be an efficient mechanism for the formation of spicules in the solar atmosphere (Haerendel 1992; James et al. 2003).

In the third category, De Pontieu et al. (2004) showed that p-modes are the potential candidates for triggering spicules in the solar atmosphere, which was further investigated in various other works (e.g., Hansteen et al. 2006; De Pontieu et al. 2007a).

The above mentioned main three categories (i.e., gas pressure or velocity pulse, Alfvén waves and p-modes) are not the only mechanisms for the formation of spicules. Indeed, there are various other numerous proposed physical processes responsible for the formation of spicules. Among others, the compression of the plasma sheet by the magnetic field (Hollweg 1972), Joule heating in the current sheet (Hirayama 1992), thermal conduction from the corona (Kopp & Kuperus 1968; Moore & Fung 1972), and buffeting of anchored magnetic flux by granulation can lead to spicules (Roberts 1979). These and various other mechanisms are discussed by Sterling (2000).

Although spicules were discovered a long time ago (Secchi 1887), they are still not fully understood. Therefore, they remain the subject of further investigation. Advanced numerical simulations are an important means to reveal the nature of spicules. However, it is always difficult to implement the real solar conditions in the numerical experiment. Because low layers of the solar atmosphere contain large fraction of neutrals (e.g., Zaqarashvili et al. 2011), two-fluid plasma (i.e., ionized and neutral fluids) approach in the numerical experiment is more suitable than magnetohydrodynamics (MHD) to study the evolution of spicules in the solar atmosphere. This approach is used for the first time in the present numerical simulations of solar spicules. Specifically, we perform 2D numerical simulations of two-fluid equations to produce the spicule using pulses launched initially in vertical components of ion and neutral velocities. The adopted potential magnetic field configuration plays essentially a passive role in the present simulations. The paper is organized as follows. In Section 2, we describe the physical model of the solar atmosphere. Numerical simulations are presented in Section 3. Summary and conclusions are outlined in the last section.

2. Physical Model of the Solar Atmosphere

2.1. Two-fluid Equations

We consider a gravitationally stratified and magnetically confined plasma that consists of two components: ionized fluid (ions + electrons) and neutral fluid (neutrals). This model is governed by the following set of equations (Smith & Sakai 2008):

$$\frac{\partial \varrho_i}{\partial t} + \nabla \cdot (\varrho_i \boldsymbol{V}_i) = -\varrho_i(\alpha_r \varrho_i - \alpha_i \varrho_n), \tag{1}$$

$$\frac{\partial \varrho_n}{\partial t} + \nabla \cdot (\varrho_n \boldsymbol{V}_n) = \varrho_i(\alpha_r \varrho_i - \alpha_i \varrho_n), \tag{2}$$

$$\begin{aligned}\varrho_i\left(\frac{\partial \boldsymbol{V}_i}{\partial t} + (\boldsymbol{V}_i \cdot \nabla)\boldsymbol{V}_i\right) = &-\nabla p_i + \frac{1}{\mu}(\nabla \times \boldsymbol{B}) \times \boldsymbol{B} + \varrho_i \boldsymbol{g} \\ &- \alpha_c \varrho_i \varrho_n (\boldsymbol{V}_i - \boldsymbol{V}_n) \\ &- \varrho_i(\alpha_r \varrho_i \boldsymbol{V}_i - \alpha_i \varrho_n \boldsymbol{V}_n),\end{aligned} \tag{3}$$

$$\begin{aligned}\varrho_n\left(\frac{\partial \boldsymbol{V}_n}{\partial t} + (\boldsymbol{V}_n \cdot \nabla)\boldsymbol{V}_i\right) = &-\nabla p_n + \varrho_n \boldsymbol{g} \\ &+ \alpha_c \varrho_i \varrho_n (\boldsymbol{V}_i - \boldsymbol{V}_n) \\ &+ \varrho_i(\alpha_r \varrho_i \boldsymbol{V}_i - \alpha_i \varrho_n \boldsymbol{V}_n),\end{aligned} \tag{4}$$

$$\begin{aligned}&\frac{\partial p_i}{\partial t} + \boldsymbol{V}_i \cdot \nabla p_i + \gamma p_i \nabla \cdot \boldsymbol{V}_i \\ &\quad = (\gamma - 1)\alpha_c \varrho_i \varrho_n (\boldsymbol{V}_i - \boldsymbol{V}_n) \cdot \boldsymbol{V}_i,\end{aligned} \tag{5}$$

$$\begin{aligned}&\frac{\partial p_n}{\partial t} + \boldsymbol{V}_n \cdot \nabla p_n + \gamma p_n \nabla \cdot \boldsymbol{V}_n \\ &\quad = (\gamma - 1)\alpha_c \varrho_i \varrho_n (\boldsymbol{V}_i - \boldsymbol{V}_n) \cdot \boldsymbol{V}_n,\end{aligned} \tag{6}$$

$$\frac{\partial \boldsymbol{B}}{\partial t} = \nabla \times (\boldsymbol{V} \times \boldsymbol{B}), \nabla \cdot \boldsymbol{B} = 0, \tag{7}$$

where $\varrho_{i,n}$ is the mass density, $p_{i,n}$ the gas pressure, $\boldsymbol{V}_{i,n}$ represents the plasma velocity, $\boldsymbol{B}$ is the magnetic field, α_i is a coefficient of ionization, α_r coefficient of recombination, and α_c coefficient of collisions between particles, subscripts i and n correspond, respectively, to ions and neutrals, $\gamma = 5/3$ is the adiabatic index, and $\boldsymbol{g} = (0, -g, 0)$ is the gravitational acceleration. The value of g is equal to 274 m s^{-2}. For the sake of simplicity, all electron-components are neglected due to the small mass of electrons in relation to ions and neutrals.

2.2. Equilibrium Solar Atmosphere

In a static solar atmosphere, all plasma quantities are time-invariant, which means that $\partial f/\partial t = 0$, where f denotes an equilibrium plasma quantity. Then, from Equations (1)–(7), it follows that for still ions ($\boldsymbol{V}_i = 0$) and neutrals ($\boldsymbol{V}_n = 0$) the Lorentz force (if appropriate) must be balanced by the gravity force and the gas pressure gradient,

$$\frac{1}{\mu}(\nabla \times \boldsymbol{B}) \times \boldsymbol{B} - \nabla p_{i,n} + \varrho_{i,n} \boldsymbol{g} = 0. \tag{8}$$

2.2.1. Current-Free Magnetic Field and the Hydrostatic Atmosphere

A hydrostatic atmosphere for ions corresponds to the force-free ($(\nabla \times \boldsymbol{B}) \times \boldsymbol{B} = 0$) magnetic field with the solenoidal condition ($\nabla \cdot \boldsymbol{B} = 0$) being satisfied. We additionally assume a current-free ($\nabla \times \boldsymbol{B} = 0$) magnetic field whose horizontal B_x, vertical B_y, and transversal B_z components are given as

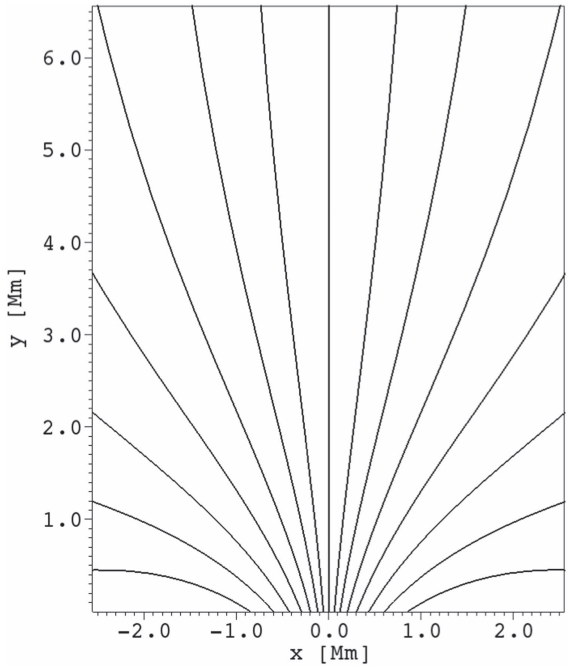

Figure 1. Magnetic field lines at the plasma equilibrium.

(Konkol et al. 2012)

$$B_x(x, y) = \frac{-2Sx(y-a)}{(x^2+(y-a)^2)^2},$$
$$B_y(x, y) = \frac{S(x^2-(y-a)^2)}{(x^2+(y-a)^2)^2} + B_v, \quad B_z(x, y) = 0, \qquad (9)$$

where B_v is a straight vertical magnetic field component, a and S are free parameters corresponding to the vertical location of the singularity in the magnetic field and the magnetic field strength, respectively. We set $B_v = 6$ Gs, $a = -1.5$ Mm and S in such a way that at the reference point ($x_r = 0$, $y_r = 10$) Mm the magnitude of magnetic field $B = 8$ Gs. The corresponding magnetic field lines are displayed in Figure 1. We note that the magnetic field lines become less divergent with height.

For a force-free magnetic field it follows from Equation (8) that at the equilibrium the gas pressure gradients have to be balanced by the gravity force,

$$\nabla p_{i,n} = \varrho_{i,n}\boldsymbol{g}. \qquad (10)$$

With the use of the ideal gas law and the vertical, y-component of Equation (10), we express the hydrostatic gas pressures and mass densities of ions and neutrals as

$$p_{i,n}(y) = p_{0\,i,n}\exp\left(-\int_{y_r}^{y}\frac{dy'}{\Lambda_{i,n}(y')}\right),$$
$$\varrho_{i,n}(y) = \frac{p_{i,n}(y)}{g\Lambda_{i,n}(y)}, \qquad (11)$$

where

$$\Lambda_{i,n}(y) = \frac{k_B T_{i,n}(y)}{mg} \qquad (12)$$

are the pressure scale heights of ions (Λ_i) and neutrals (Λ_n), and $p_{0\,i,n}$ denotes the gas pressure of ions and neutrals at the reference level, $y = y_r = 10$ Mm. In Equation (12), $T_i(y)$ and $T_n(y)$ stand for temperatures of ions and neutrals, respectively. These temperatures are taken from the model of Avrett & Loeser (2008; see Figure 2). Note that for $y > 0.2$ Mm the temperature of ions is higher than the temperature of the neutrals. In the photosphere, which is localized at $0 \leqslant y \leqslant 0.5$ Mm, $T_i(y)$ increases with y until close to the bottom of the chromosphere, specifically for $y \approx 0.7$ Mm, $T_i(y)$ reaches its local maximum of about $1.5 \cdot 10^5$ K. Higher up $T_i(y)$ decreases with height until at the TR it rises abruptly to the coronal value of about 1 MK. The neutral temperature attains its value of about 5 kK within the region of $0 \leqslant y \leqslant 1.75$ Mm. It decreases suddenly right below the TR attaining its minimum of about 150 K and higher up it increases with y reaching its coronal magnitude of about 0.8 MK at $y = 10$ Mm.

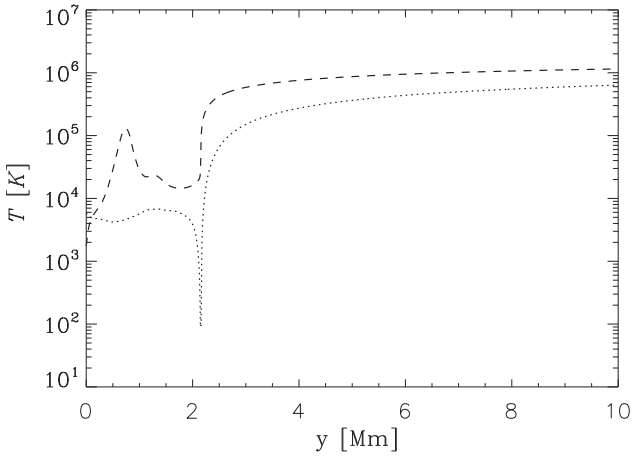

Figure 2. Vertical profiles of hydrostatic temperature of ions (dashed line) and neutrals (dotted line) vs. height y.

As a result of the adopted temperature profiles, the mass densities of ions and neutrals decline with height. The left panel of Figure 3 shows the ratio of the mass density of ions to the mass density of neutrals, $\varrho_i(x, y)/\varrho_n(x, y)$, which result from Equation (11). Note that below the level of $y = 2.1$ Mm the plasma is dominated by neutrals with a minimum of $\varrho_i/\varrho_n \approx 10^{-4}$, while the corona consists of essentially fully ionized plasma; we added a small amount of neutrals in the solar corona due to numerical reasons. We specify the plasma β as the ratio of ion plus neutral gas pressures to magnetic pressure,

$$\beta(y) = \frac{p_i(y) + p_n(y)}{B^2(y)/2\mu}. \qquad (13)$$

The spatial profile of plasma β is illustrated in the right panel of Figure 3. Note that within the displayed region for the coronal plasma, for $y > 2.1$ Mm, and along the entire $x = 0$ line β is smaller than 1.

2.2.2. Perturbations

Initially, at $t = 0$ s, we perturb the model equilibrium by launching, at the bottom boundary, simultaneously time-dependent signals in the ion and neutral gas pressures, which

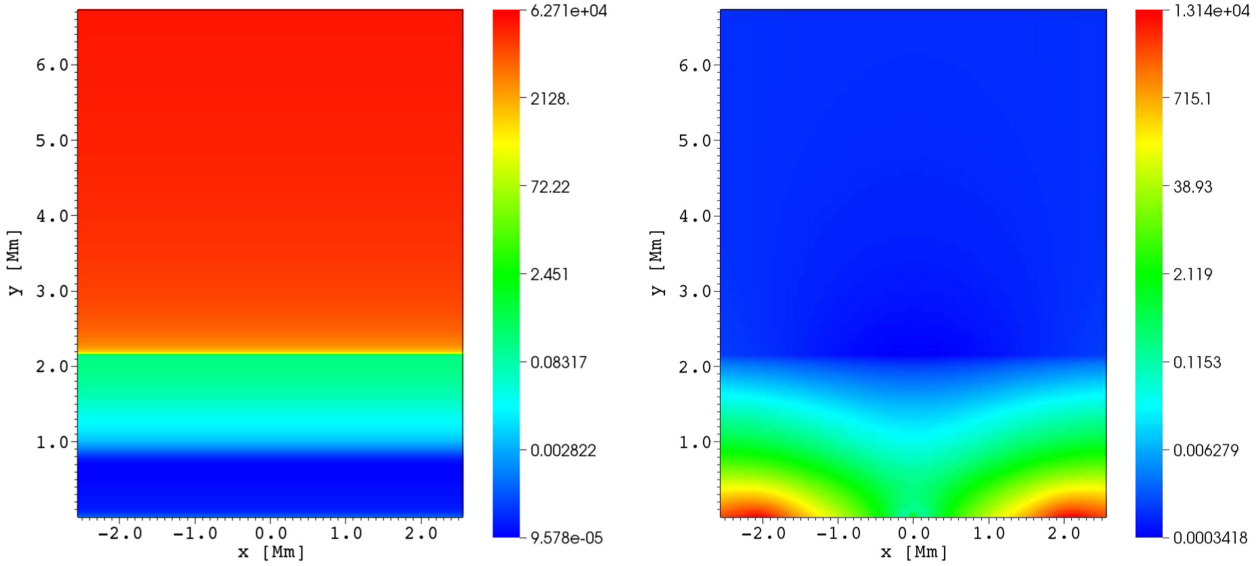

Figure 3. Ratio of the mass density of ions to the mass density of neutrals (left) and plasma beta (right) at the plasma equilibrium.

are expressed as follows:

$$p_{[i,n]}(x, y, t = 0) = p_0\left(1 + A_{p\,[i,n]} \exp\left(-\frac{x^2 + (y - y_0)^2}{w^2}\right) f(t)\right),$$
$$f(t) = \begin{cases} 1 - \exp(-t/\tau), & t \leqslant \tau_{\max} \\ \exp(-(t - \tau_{\max})/\tau), & t > \tau_{\max} \end{cases}. \quad (14)$$

Here y_0 is the vertical position of the signals, w is their width and $A_{p\,i}$, $A_{p\,n}$ their amplitudes. Function $f(t)$ denotes the temporal profile of the gas pressure signal, with τ being its characteristic growth/decay time and $\tau_{\max}$ time at which $f(t)$ reaches its maximum. We set and hold fixed $w = 0.1$ Mm, $\tau = 50$ s, and $\tau_{\max} = 30$ s, while allowing other parameters to vary. For our studies, the signal position, y_0, varies between 1.65 and 1.85 Mm and the amplitude A_p between 6 and 10. This signal position corresponds to a region of $\beta < 1$ (Figure 3, right). As a result of that, slow and fast magnetoacoustic waves are weakly coupled there and the initial pulse triggers slow waves, which propagate essentially along magnetic field lines (e.g., Nakariakov & Verwichte 2005). Unless otherwise stated, the further analysis focuses on the case for $A_p = 8$ and $y_0 = 1.75$ Mm, which corresponds to plasma heated to maximum temperature of 60 kK 1.75 Mm above the photosphere. We have verified that only such strong pulses launched at the top of the chromosphere result in spicules. Lower amplitude pulses excite smaller jets and pulses launched from the lower chromospheric layers lead to horizontally spread jets. The time-dependent signal launched at $y_0 = 1.75$ Mm may mimic a post-reconnection event.

3. Numerical Simulations of Two-fluid Equations

To solve two-fluid equations numerically, we use the JOANNA code (D. Wójcik et al. 2017, in preparation). In our problem, we set the Courant–Friedrichs–Lewy number (Courant et al. 1928) equal to 0.3 and specify the simulation box in (x, y) as $(-1.28, 1.28)$ Mm $\times$ $(1.75, 50.0)$ Mm, where $y = 0$ denotes the bottom of the photosphere. In the numerical simulations we adopt the uniform grid within the region $(-1.28 \leqslant x \leqslant 1.28)$ Mm $\times$ $(1.75 \leqslant y \leqslant 6.87)$ Mm, which is covered by 256×512 grid points. This grid leads to a resolution of 10 km in the main region of the simulation box that is below $y = 6.12$ Mm. Above this region, namely within the rectangle $(-1.28 \leqslant x \leqslant 1.28)$ Mm $\times$ $(6.87 \leqslant y \leqslant 50.0)$ Mm, we implement a stretched grid along the y-direction; this box is divided into 128 cells whose size grows with y. Such a stretched grid plays the role of a sponge as it absorbs incoming signal and minimizes reflections from the top boundary. We impose open boundary conditions for outflowing signal at the side boundaries, while at the top and bottom we fixed all plasma quantities to their equilibrium values.

We launch the gas pressure signals in the chromosphere varying their initial position, y_0, and amplitudes, $A_{p\,i}$ and $A_{p\,n}$, as described in Section 2.2.2. The basic mechanism behind the simulations is that the signals, while launched from the region of $\beta < 1$, essentially split into two, counter-propagating along the equilibrium magnetic field lines' slow magnetoacoustic (slow henceforth) waves; downwardly propagating slow waves decay in time (not shown in the framework of these simulations), while upwardly moving slow waves grow in their amplitudes. The latter convert into a slow shock at higher altitudes due to the decrease of mass density with height. The chromospheric plasma lags behind the shock front to form a contact wave consisting of a spicule. The simple waves structure associated with this phenomenon is described by Kuźma et al. (2017). Note that the signal in $A_{p\,i}$ excites fast magnetoacoustic waves too but they are of low amplitudes as they spread quasi-isotropically in space. The pulse in $A_{p\,n}$ generates neutral acoustic waves (Zaqarashvili et al. 2011).

The top row of Figure 4 shows the spatial profiles of log $(\varrho_i(x, y))$ at three instants of time, which are $t = 70$ s (top left), $t = 210$ s (top middle), and $t = 320$ s (top-right). The gas pressure drivers of Equation (14) operate at the point of $(x = 0, y = y_0 = 1.75)$ Mm, which is located in the chromosphere around 0.35 Mm below the TR, and they reach their maximum at $t = 30$ s. At $t = 70$ s, it is found that the ion shock front is followed by hot plasma, which results from the drivers,

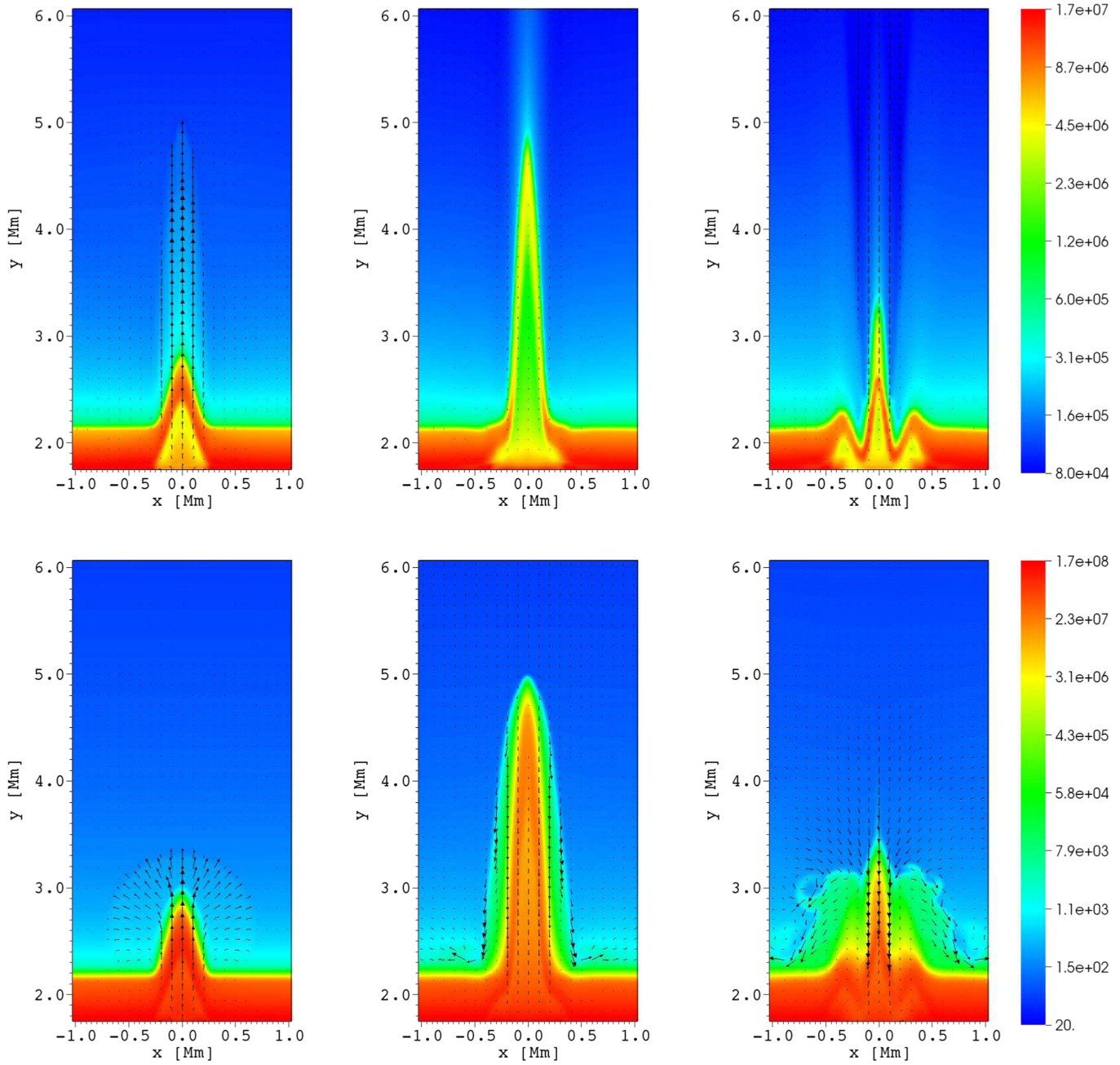

Figure 4. Temporal evolution of $\log(\varrho_i(x, y))$ at $t = 70$ s, $t = 210$ s, and $t = 320$ s (from top left to top right), and $\log(\varrho_n(x, y))$ (from bottom left to bottom right). Arrows represent ion and neutral velocity vectors in the $x-y$ plane. Hot coronal plasma is blue, cold chromospheric plasma is orange-red, and intermediate transition region plasma/interface between them is green on the colormap.

and it reaches a level of $y \approx 5.0$ Mm. It is followed by a second, stronger shock, which results at maximum of $f(t)$. However, the chromospheric (cold) ion plasma is located at $y \approx 2.8$ Mm at this time (see Figure 4, the top-left panel). The shock fronts move continuously upward, which attain the level of more than $y = 25$ Mm (not drawn here) and the chromospheric plasma reaches its maximum height of $y \approx 4.9$ Mm at $t = 210$ s (Figure 4, the top-middle panel). The head of the spicule remains denser (yellow color on the colormap), while its interior rarefies in time (green color on the colormap) due to rarefaction wave propagating upwards. Above the apex of the ion spicule, we can see a constant stream of ions injected into higher layers of the solar corona. In addition, the down-falling of the ion spicule plasma also starts as the time progresses. The reverse velocity arrows in the central region and sides of the ion spicule justifies downfall of the cold chromospheric plasma. This downfall is stronger during the decay phase (see reverse velocity arrows in the top-middle and top-right panels), which creates the V-shaped structure as the down-falling velocity is nonuniform along the horizontal direction (see the top-right panel).

We have implemented the two-fluid approach in our numerical experiment to understand the behavior of ions and neutrals in the spicule dynamics. It may be possible that the ions and neutrals may exhibit the different dynamics. Therefore, we show the corresponding profiles of $\log(\varrho_n(x, y))$ in the bottom panels of Figure 4. The overall dynamics of the neutrals

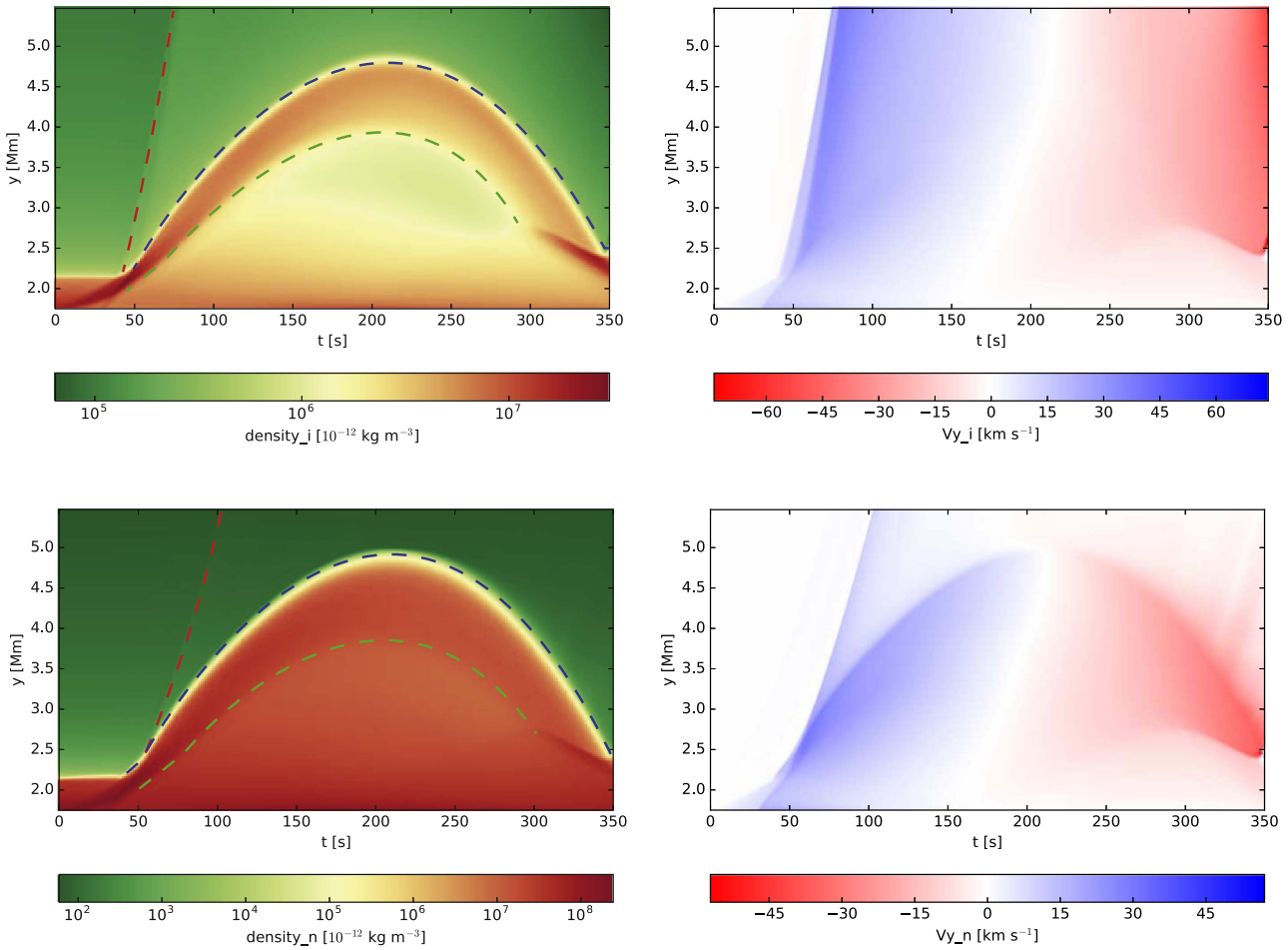

Figure 5. Temporal evolution of $\log(\varrho_{i,n}(x = 0, y))$ (left) and $V_{i,n\,y}(x = 0, y)$ (right) for the ions (top) and neutrals (bottom). The red, blue, and green dashed lines indicate slow shock, contact wave, and rarefaction wave, respectively. Transition from the red to the green area shows the contact waves.

(i.e., formation of a shock front and lagging off chromospheric plasma) are qualitatively similar to the dynamics of ions in this numerical experiment. However, the slow neutral shock does not propagate along magnetic field lines, forming a circle-like front (the bottom-left panel). There is also no upward stream consisting of neutrals above the apex of the ion spicule (the bottom-middle panel). The spicule is surrounded by the neutral cloud in which we can spot vortices of Rayleigh–Taylor instabilities during the decay phase. The down-falling of neutral gas is very weak during the maximum phase (the middle-right panel), which is mostly dominated toward the edges of the neutral spicule. However, the strong downflow of neutral gas occurs during the decay phase. The neutral spicule resembles a V-shaped structure in the decay phase (the bottom-right panel) but not as prominent as it occurs in the ion spicule. Because neutrals are not guided by the magnetic field, the neutral gas experiences more horizontal spread compared to the ions. So, the neutral spicule does not exhibit a very sharp V-shaped structure due to the dominance of the horizontal spreading of neutrals.

In addition, the top of the ion (neutral) spicule is suppressed until the height of $y = 3.4$ Mm ($y = 3.5$ Mm) due to the dominance of down-falling in the decay phase. This down-falling is strongest on sides of the ion/neutral spicule and decrease outward, which creates the V-shape structure at the bottom of ion/neutral spicules. Most of the chromospheric plasma, which was injected into the corona falls toward the chromosphere/TR.

We estimate now the width of the spicule in neutrals and ions at $y = 3.0$ Mm during the maximum phase of the spicule. By looking at horizontal mass density profiles and assuming that the mass density above (below) 1.2 times of the background mass density (i.e., mass density in the absence of any spicule; at $x = -1.0$ Mm) are considered as the starting (end) points of the spicules. We find that the neutral spicule is wider ($\sim$600 km) than the ion spicule than the spicule consisting of ions ($\sim$400 km).

We discuss now temporal evolution of mass densities and vertical velocities of ions and neutrals. Figure 5 displays time signatures of $\varrho_{i,n}(x = 0, y, t)$ (the left panels) and $V_{i,n\,y}(x = 0, y, t)$ (the right panels) for ions (the top panels) and neutrals (the bottom panels). The rise time of the chromospheric ions to their maximum height is about 210 s (see Figure 5, top-left). In the temporal evolution profile of the ions, we spot three major waves above the TR (the top-left panel): the leading wave is a slow shock wave (red line) that is followed by the contact wave (blue line) and the rarefaction wave (green line). The contact wave does not appear in the top-right panel since there is no jump in velocity of ions across a contact surface with normal almost perpendicular to $\boldsymbol{B}$. See also Kuźma et al. (2017) for a similar discussion in the MHD case. The light-green area between slow shock and contact

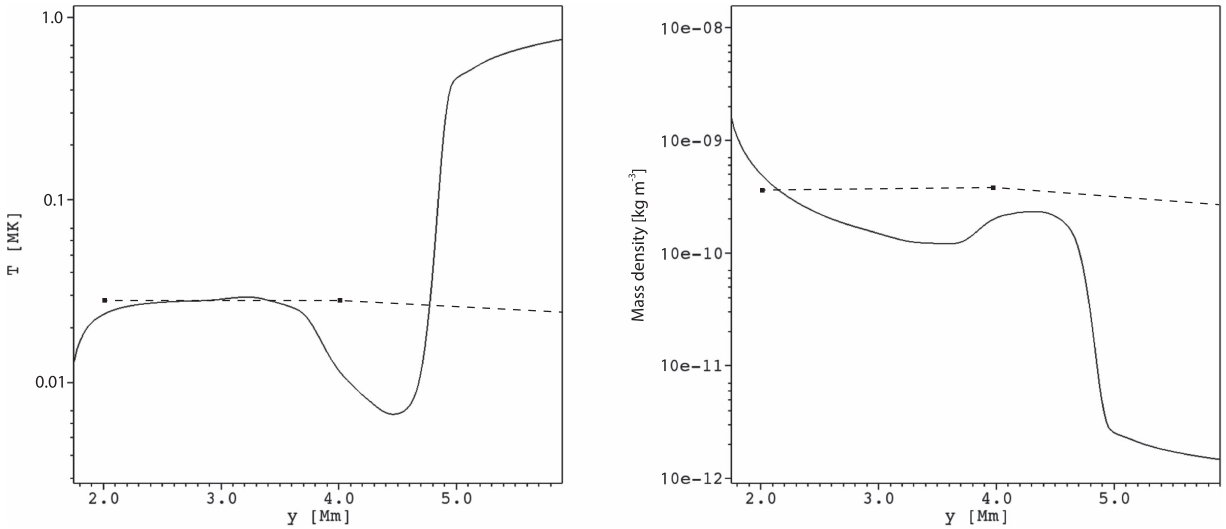

Figure 6. Vertical profiles of average temperature (the left panel) and mass density (the right panel) of the spicule in the simulation evaluated along $x = 0$ Mm, at $t = 210$ s (the solid lines) and observational data of Beckers (1968; the dashed lines).

wave reveals that a significant amount of ions are constantly injected above the spicule apex during its lifetime. This phenomenon is absent in the case of neutrals (the bottom-left panel). The ion slow shock travels with higher speed ($\sim$150 km s^{-1}) than neutral slow shock ($\sim$90 km s^{-1}; see the right panels). Both ions and neutrals injected into the corona above the spicule apex accelerate with height. The light-green area below the apex of the ion spicule reveals that the rarefaction wave exerts a greater impact on the already rarefied ion spicule. The boundary between chromospheric and coronal neutrals is also sharper than between chromospheric and coronal ions. This is a result of merging between the top of the ion spicule and highly ionized corona. From the temporal evolution profile of the neutrals, we infer that both shock and rarefaction waves are of low amplitudes, to the point, when the rarefaction wave is almost unnoticeable (green line, the bottom-left panel). At a later time, the chromospheric plasma, which was earlier injected into the corona, begins to fall toward the TR.

The spicule consists mostly of dense and cold neutrals. The ionization level at all stages of the spicule evolution remains at about 10%. Figure 6 (left) shows the vertical profile of the average temperature of the simulated spicule (solid line) along with the widely used observed values (dashed line; Beckers 1968). The average temperature of the spicule (solid line) is 100 times lower than the coronal plasma, which shows a constant value of temperature up to a height of $\sim$2.8 Mm. The spicule plasma exhibits its lowest temperature of 9000 K in the upper part of the spicule, $\sim$4500 km above the TR. Higher up, the temperature experiences an abrupt jump at the contact wave, reaching temperatures of up to 800,000 K and matching the local coronal temperature. Figure 6 (left) shows the vertical profile of mass density of the spicule (solid line). The cold head of the spicule is about twice denser than its core, which is resembled by the weak bump around $y = 4.2$ Mm. Above the apex of the spicule, mass density decreases to its coronal values. The temperature as well as mass density of the simulated spicule are compared with the classical results of the spicule (dashed line in both-panels of Figure 6; Beckers 1968). Observationally, it is reported that mass density and temperature are almost constant over the whole length of the spicule, which vary by about 10 % over the whole length of the spicule (Beckers 1968). However, the simulated spicule exhibits significant variations in the temperature and mass density along its length. It should be noted that the temperature of the spicule matches the observed values over a height range of 2.0 Mm $< y <$ 3.7 Mm.

We now discuss gradients of gas pressures of neutrals and ions. The corresponding vertical profiles are displayed in Figure 7. The dotted line shows the gas pressure gradient of neutrals, while the solid line illustrates the gas pressure gradient of ions along the y-direction.

The left (right) panel illustrates the vertical distribution of the gas pressure gradient at $t = 60$ s ($t = 70$ s). It is clear that the neutral gas pressure gradient (the dotted line) is very high in comparison to the ion gas pressure gradient (the solid line) at these instants of time. The difference between neutrals and ions pressure gradients is higher at about $y = 1.75$ Mm at which the driver in gas pressures operates. The gradients approach each other far away from the driver. The significant gas pressure gradient difference between the ions and neutrals is an important result, which clearly leads to a different dynamics of ions and neutrals.

4. Discussions and Conclusions

We have performed numerical simulations of a spicule by setting in the upper chromosphere localized time-dependent signals in ion and neutral gas pressures. The initial magnetic field configuration was current-free, and the atmosphere was stratified hydrostatically. The whole physical system was described by a set of two-fluid equations. Our numerical findings revealed that, as a result of the rapid decrease of the mass density with height, an upwardly propagating signal quickly steepens into a shock. This shock propagates along the magnetic field lines, reaching the low solar corona, and is followed by the chromospheric plasma, which consists of the cold and dense jet (spicule). This jet exhibits properties of a contact wave (Kuźma et al. 2017) and reaches upto a certain height (typically 4–6 Mm) and then returns to the chromosphere. The mean upflow speed was 20–25 km s^{-1}. The comparison between the numerical and observational data

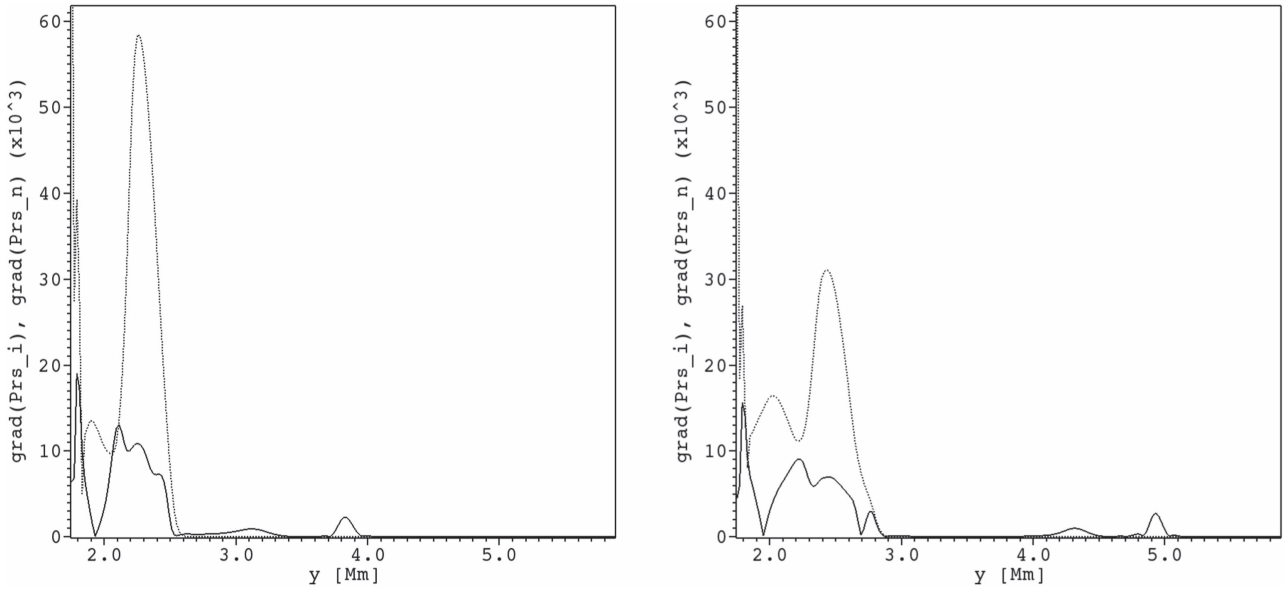

Figure 7. Vertical profiles of the gas pressure gradient of neutrals (the dotted line) and ions (the solid line) evaluated along $x = 0$ Mm, at $t = 60$ s (the left panel) and $t = 70$ s (the right panel).

always enlightens the path to go further. Therefore, we tried to compare the observed properties of the simulated spicule with the various spicule observations. Beckers (1968, 1972) reported that the average height of spicules can vary from 6500 km to 9500 km. Similarly, Lippincott (1957) reported the spicule height range from 7000 to 13,000 km and Pasachoff et al. (2009) inferred these numbers from 4200 to 12,200 km. Observed upward velocity of spicules exhibits variations within the range of 20.0–150.0 km s^{-1} (De Pontieu et al. 2007b) and 3.0–75.0 km s^{-1} (Pasachoff et al. 2009). The numerically obtained value of spicule height (∼4.9 Mm) and upward velocity (∼20–25 km s^{-1}) of the simulated spicule lies in the observed range of height and velocity (Beckers 1968, 1972; De Pontieu et al. 2007b; Pasachoff et al. 2009). It should also be noted that the numerical values of the spicule match those obtained for MHD (Kuźma et al. 2017).

Novelty of our numerical simulations lies in the usage of the two-fluid model, which was not investigated so far. The two-fluid simulations invoke real physical conditions of the lower solar atmosphere and plasma processes within various localized jets. It is noteworthy that a significant role of neutrals associated with confined pseudo-shocks in carrying substantial energy and mass into the overlying solar atmosphere was discovered by Srivastava et al. (2017). The key findings of our simulations can be summarized as follows. (a) The spicule dynamics is slightly different in ions and neutrals; (b) the core of the spicule is dominated by cold neutrals; (c) the neutral spicule is wider compared to the ion spicule; (d) the ionization remains essentially still with height and horizontal distance within the spicule, only the top of the spicule is significantly ionized; and (e) in later moments of time of the spicule evolution higher amplitude of the slow rarefaction wave for the ion spicule results in a different structure than for the neutral spicule. The general scenario of the rise and the downfall of the spicule is the same for ions and neutrals and it is close to that for MHD (Kuźma et al. 2017). The dispatches in gas pressure gradients between ions and neutrals is a key factor to understand the minor differences in the dynamics of ions and neutral spicules. Obviously, the magnetic field does not have any direct influence on the dynamics of neutrals, while the motion of ions is affected by the magnetic field directly. The direct influence of the magnetic field on the ions controls the width of the ion spicule. Therefore, the ion spicule is a very well collimated column of ions with its small width. In the absence of the influence of magnetic field, the neutrals get extra freedom to propagate in the horizontal direction; a constraint on them results from ion-neutral collisions. As a result, the neutral spicule is wider compared to the ion spicule. The V-shaped structure near the base of the ion/neutral spicule is an interesting phenomenon of these simulations, which results from down-falling gas. As ions are affected by magnetic field, the well collimated down-falling ion gas results in, which exerts the gas pressure force producing in the decay phase the sharp V-shaped structure near the base of the ion spicule.

Most of observations reveal that temperature and mass density of a spicule remain essentially constant along its height (Beckers 1968, 1972; see also review article by Sterling 2000). However, our simulated spicule shows a significant variations in its temperature as well as mass density. The temperature of the spicule is constant upto the height of $y = 3.5$ Mm, while higher up the temperature falls off abruptly. The constant phase of temperature matches the obervational findings. However, there is a sharp increase in the temperature above $y = 4.5$ Mm, which may suggest that the thermal evolution of the cold chromospheric plasma can be important as proposed by Pereira et al. (2014). Overall, the mass density of the spicule is decreasing with height, which is qualitatively consistent with the observed mass densities (Beckers 1968). However, the top of the spicule shows slightly higher densities. The high temperature near the top-part of the spicule significantly ionizes the neutrals, which were taken into account in the present scenario. Recently, Pereira et al. (2014) reported that spicules undergo thermal evolution using high-resolution observations. Spicules produce more emission near their bases compared to their apexes at chromospheric temperature (i.e., Ca II H & K and Mg II h & k lines). However, bases of spicules become dark and the top parts of spicules lead to more emissions at the TR temperature (i.e., Si IV; $T = 80$ kK). This

observational finding predicts that ionization grows with height within the spicule, which is successfully reproduced by our two-fluid numerical simulations of spicules.

In conclusion, our numerical simulations of the spicule performed within the framework of the two-fluid approach successfully mimics the averaged properties of classical spicules. Ion and neutral spicules follow the similar dynamics in terms of rise time and peak altitude. The core of the spicule exhibits an abundance of neutrals, with growing in time rarefaction of ions.

The authors express their thanks to the referee for comments on the earlier version of the draft. This work was financially supported by the project from the National Science Centre, Poland, (NCN) Grant No. 2014/15/B/ST9/00106. The JOANNA code used in this work was developed by Mr. Darek Wójcik. These numerical simulations were performed on the LUNAR cluster at Institute of Mathematics of University of M. Curie-Skłodowska. Visualization of the simulations data was done with the use of IDL (Interactive Data Language) and VisIt software packages.

References

Avrett, E. H., & Loeser, R. 2008, ApJS, 175, 228
Beck, C., Rezaei, R., Puschmann, K. G., & Fabbian, D. 2016, SoPh, 291, 2281
Beckers, J. M. 1968, SoPh, 3, 367
Beckers, J. M. 1972, ARA&A, 10, 73
Cheng, Q.-Q. 1992, A&A, 266, 537
Courant, R., Friedrichs, K., & Lewy, H. 1928, MatAn, 100, 32
Cranmer, S. R., & Woolsey, L. N. 2015, ApJ, 812, 71
Cranmer, S. R., & Woolsey, L. N. 2016, ApJ, 822, 119
De Pontieu, B., Erdélyi, R., & James, S. P. 2004, Natur, 430, 536
De Pontieu, B., Hansteen, V. H., Rouppe van der Voort, L., van Noort, M., & Carlsson, M. 2007a, ApJ, arXiv:astro-ph/0701786
De Pontieu, B., McIntosh, S., Hansteen, V. H., et al. 2007b, PASJ, 59, S655
De Pontieu, B., McIntosh, S. W., Hansteen, V. H., & Schrijver, C. J. 2009, ApJL, 701, L1
Haerendel, G. 1992, Natur, 360, 241
Hansteen, V. H., De Pontieu, B., Rouppe van der Voort, L., van Noort, M., & Carlsson, M. 2006, ApJL, 647, L73
Heggland, L., De Pontieu, B., & Hansteen, V. H. 2007, ApJ, 666, 1277
Hirayama, T. 1992, SoPh, 137, 33
Hollweg, J. V. 1972, CosEl, 2, 423
Hollweg, J. V. 1982, ApJ, 257, 345
Hollweg, J. V., Jackson, S., & Galloway, D. 1982, SoPh, 75, 35
James, S. P., Erdélyi, R., & De Pontieu, B. 2003, A&A, 406, 715
Konkol, P., Murawski, K., & Zaqarashvili, T. V. 2012, A&A, 537, A96
Kopp, R. A., & Kuperus, M. 1968, SoPh, 4, 212
Kudoh, T., & Shibata, K. 1999, ApJ, 514, 493
Kuźma, B., Murawski, K., Zaqarashvili, T. V., Konkol, P., & Mignone, A. 2017, A&A, 597, 133
Lippincott, S. L. 1957, SCoA, 2, 15
Madjarska, M. S., Vanninathan, K., & Doyle, J. G. 2011, A&A, 532, L1
Matsuno, K., & Hirayama, T. 1988, SoPh, 117, 21
McIntosh, S. W., & De Pontieu, B. 2009, ApJ, 707, 524
McIntosh, S. W., Innes, D. E., De Pontieu, B., & Leamon, R. J. 2010, A&A, 510, L2
Moore, R. L., & Fung, P. C. W. 1972, SoPh, 23, 78
Murawski, K., & Zaqarashvili, T. V. 2010, A&A, 519, A8
Nakariakov, V. M., & Verwichte, E. 2005, LRSP, 2, 3
Nishikawa, T. 1988, PASJ, 40, 613
Pasachoff, J. M., Jacobson, W. A., & Sterling, A. C. 2009, SoPh, 260, 59
Pereira, T. M. D., De Pontieu, B., & Carlsson, M. 2012, ApJ, 759, 18
Pereira, T. M. D., De Pontieu, B., Carlsson, M., et al. 2014, ApJL, 792, L15
Pereira, T. M. D., Rouppe van der Voort, L., & Carlsson, M. 2016, ApJ, 824, 65
Roberts, B. 1979, SoPh, 61, 23
Roberts, W. O. 1945, ApJ, 101, 136
Rouppe van der Voort, L., De Pontieu, B., Pereira, T. M. D., Carlsson, M., & Hansteen, V. 2015, ApJL, 799, L3
Secchi, P. A. 1887, Le Soleil, Vol. 2 (Paris: Gauthier-Villars)
Skogsrud, H., Rouppe van der Voort, L., & De Pontieu, B. 2014, ApJL, 795, L23
Skogsrud, H., Rouppe van der Voort, L., De Pontieu, B., & Pereira, T. M. D. 2015, ApJ, 806, 170
Smith, P. D., & Sakai, J. I. 2008, A&A, 486, 569
Srivastava, A. K., Murawski, K., Kuźma, B., et al. 2017, NatAs, in press
Sterling, A. C. 2000, SoPh, 196, 79
Sterling, A. C., & Hollweg, J. V. 1984, ApJ, 285, 843
Sterling, A. C., & Mariska, J. T. 1990, ApJ, 349, 647
Sterling, A. C., & Moore, R. L. 2016, ApJL, 828, L9
Sterling, A. C., Moore, R. L., & DeForest, C. E. 2010, ApJL, 714, L1
Sterling, A. C., Shibata, K., & Mariska, J. T. 1993, ApJ, 407, 778
Suematsu, Y. 1998, in ESA Special Publication 421, Solar Jets and Coronal Plumes, ed. T.-D. Guyenne (Paris: ESA), 19
Suematsu, Y., Ichimoto, K., Katsukawa, Y., et al. 2008, in ASP Conf. Ser. 397, First Results From Hinode, ed. S. A. Matthews, J. M. Davis, & L. K. Harra (San Francisco, CA: ASP), 27
Suematsu, Y., Shibata, K., Neshikawa, T., & Kitai, R. 1982, SoPh, 75, 99
Suematsu, Y., Wang, H., & Zirin, H. 1995, ApJ, 450, 411
Tian, H., McIntosh, S. W., Habbal, S. R., & He, J. 2011, ApJ, 736, 130
Tsiropoula, G., Tziotziou, K., Kontogiannis, I., et al. 2012, SSRv, 169, 181
Zaqarashvili, T. V., & Erdélyi, R. 2009, SSRv, 149, 355
Zaqarashvili, T. V., Khodachenko, M. L., & Rucker, H. O. 2011, A&A, 529, A82

nature astronomy

LETTERS

https://doi.org/10.1038/s41550-018-0590-1

Confined pseudo-shocks as an energy source for the active solar corona

Abhishek Kumar Srivastava[1]*, Krzysztof Murawski[2], Blażej Kuźma[2], Dariusz Patryk Wójcik[2], Teimuraz V. Zaqarashvili[3,4], Marco Stangalini[5], Zdzislaw E. Musielak[6,7], John Gerard Doyle[8], Pradeep Kayshap[2,9] and Bhola N. Dwivedi[1]

The Sun's active corona requires an energy flux of ~10^3 W m^{-2} to compensate for radiative losses and to maintain its high temperature[1]. Plasma moves in the corona through magnetic loops[2,3], which may be connected with the flows in and around sunspots[4–6]. Global energizing processes (for example, reconnection) play an important part in heating the corona[7–9]; however, energy and mass transport may also occur via shocks, waves or flows[5,10,11]. A full picture and the influence of such localized events, which significantly couple with various layers of the solar upper atmosphere, is still not clear. Using the Interface Region Imaging Spectrograph temporal image data of C II 1,330 Å, we observed the presence of pseudo-shocks around a sunspot. Unlike shocks[12], pseudo-shocks exhibit discontinuities only in the mass density. A two-fluid numerical simulation reproduces such confined pseudo-shocks with rarefied plasma regions lagging behind them. We find that these pseudo-shocks carry an energy of ~10^3 W m^{-2}, which is enough to locally power the inner corona and also generate bulk flows (~10^{-5} kg m^{-2} s^{-1}), contributing to the localized mass transport. If they are ubiquitous, such energized and bulky pseudo-shocks above active regions could provide an important contribution to the heating and mass transport in the overlying solar corona.

Pseudo-shocks were first noticed in supersonic duct flows decelerated to subsonic velocities, and were ascribed to a possible adjustment of the velocity distribution itself[13]. On the Sun, they can be observed in difference maps obtained from high-resolution observations. Here, we analyse the Interface Region Imaging Spectrograph (IRIS) difference maps taken in the line of C II at 1330Å around a sunspot on 8 October 2014 with a spatial resolution of 0.4″ per pixel (where 1″ = 725 km), equivalent to 290 km on the Sun[14]. We obtained a time sequence of running-difference maps at a cadence of 19 s for various observed pseudo-shock sources, covering a period of 2 h (see Figs. 1a,b and 2, and Supplementary Table 1). The running difference maps have been made by taking each particular image and subtracting its previous image in the time sequence. This sunspot is anchored by the diffused loop magnetoplasma threads that extend to the overlying active corona (Fig. 1a). Since these pseudo-shocks are formed locally on the top of the ejected plasma, they are termed confined pseudo-shocks. We detect a number of pseudo-shocks in the present observational baseline (see Supplementary Table 1 and Supplementary Videos 1–8). The pseudo-shocks are visible in the C II 1330Å line but not in the cooler Mg II 2796Å line maps, indicating that they are formed in the transition region/inner corona after the evolution of plasma perturbations somewhere at the top of the chromosphere. The representative context event (tadpole-shaped plasma ejecta) presents the evolution of a pseudo-shock source (Figs. 1b,c and 2), which elongates up to a height of ~5 Mm (Figs. 1c and 2). This bulky and localized feature is evolved at 14:22:08 UT (see top left panel of Fig. 2). The mass within it sweeps towards the head during its evolution to create its bulky head and rarefied tail (Figs. 1c and 2 and Supplementary Video 9).

The velocity of this pseudo-shock in the plane of sky is estimated as ~30 km s^{-1}. This is a lower bound projected value, which may be slightly higher than the sound speed estimated at the C II formation temperature (log[T] = 4.5)[15]. The characteristic reference sound speed at the C II formation temperature is estimated as 26 km s^{-1}. Since the pseudo-shock speed is marginally higher than the characteristic sound speed, this may indicate evolution of a weak shock system. As the pixel size of the IRIS slit-jaw images is 290 km and the cadence of the images is 19 s, the intrinsic motion of the feature in consecutive images is about 2 pixels. This is confirmed in the first two running-difference maps (Fig. 2). The sweeping of mass is evident along the confined magneto-plasma system, which constitutes the pseudo-shock (Figs. 1c and 2). Thereafter, the impulsively evolved pseudo-shock, along with its rarefied tail, further propels upwards before fading in the later part of its total lifetime of ~150 s (Fig. 2). In the present observational baseline, we observe only the evolution of one pseudo-shock. A weak, slow shock with a Mach number (M) slightly greater than one may also be present in the system. However, such weak and faint slow shock may not be evident against the bright and dynamical chromosphere.

We developed a physical model of such localized pseudo-shocks for a weakly diverging, current-free equilibrium magnetic field embedded in a hydrostatic two-fluid atmosphere with an appropriate temperature profile[16–18]. We used a two-fluid (ions: protons and electrons; and neutrals: hydrogen atoms) code, known as the joint analytical and numerical approach (JOANNA), developed by D. Wójcik[16,19] (Fig. 3; see the Methods for details; http://kft.umcs.lublin.pl/dwojcik/) to simulate

[1]Department of Physics, Indian Institute of Technology (BHU), Varanasi, India. [2]Group of Astrophysics, Institute of Physics, UMCS, Lublin, Poland. [3]Space Research Institute, Austrian Academy of Sciences, Graz, Austria. [4]Abastumani Astrophysical Observatory at Ilia State University, Tbilisi, Georgia. [5]INAF-OAR National Institute for Astrophysics, Rome, Italy. [6]Department of Physics, University of Texas at Arlington, Arlington, TX, USA. [7]Kiepenheuer-Institut für Sonnenphysik, Freiburg, Germany. [8]Armagh Observatory and Planetarium, Armagh, UK. [9]Institute of Physics and Biophysics, Faculty of Science, University of South Bohemia, Ceské Budejovice, Czech Republic. *e-mail: asrivastava.app@iitbhu.ac.in

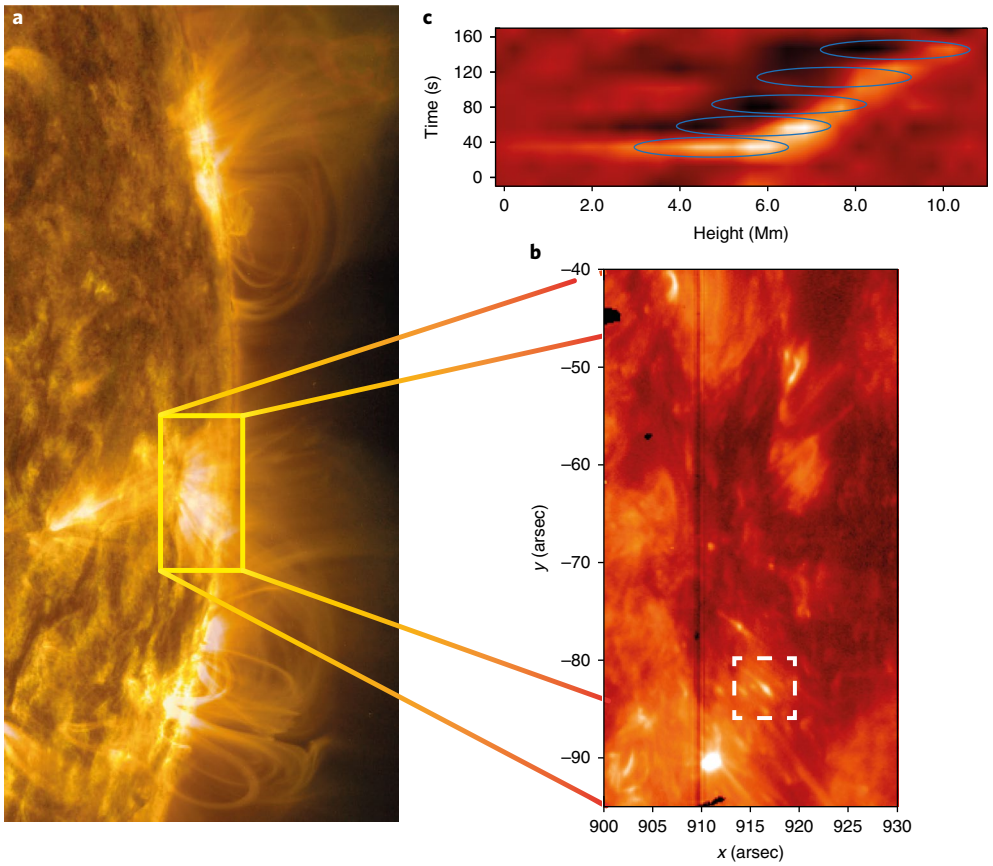

Fig. 1 | Direct imaging of the confined pseudo-shocks around a sunspot. a, Composite image of 171, 304 and 1600Å emissions taken by the Solar Dynamics Observatory/Atmospheric Imaging Assembly, showing diffused loop threads anchored into the sunspot, enabling propulsion of mass and energy to the overlying magnetic domain of the corona through pseudo-shocks that are injected from the lower solar atmosphere at their footpoints. Such pseudo-shock sources are abundant in and around the observed sunspot. **b**, The evolution of a representative pseudo-shock is shown in C II 1,330 Å emission using IRIS slit-jaw imaging on 8 October 2014 at 14:22 UT (Supplementary Table 1 and Supplementary Video 11). **c**, A time–distance map along the representative pseudo-shock (a tadpole-shaped jet) indicated by a white dashed box in **b** exhibits the evolution of its bulky, bright head and rarefied tail as shown within blue ovals.

the observed pseudo-shocks. The hydrostatic plasma equilibrium is perturbed by localized drivers in ion and neutral gas pressure as:

$$[p_i, p_n](x,y,t) = [p_{i0}, p_{n0}]\left(1 + A_{p[i,n]}\ \exp\left(-\frac{(x-x_0)^2}{w^2} - \frac{(y-y_0)^2}{w^2}\right) f(t)\right) \quad (1)$$

$$f(t) = \begin{cases} 1-\exp(-t/\tau), & t \le \tau_{max} \\ \exp(-(t-\tau_{max})/\tau), & t > \tau_{max} \end{cases}$$

Here, x_0 and y_0 are, respectively, the horizontal and vertical position of the drivers, w is their widths, and $A_{p,i}$ and $A_{p,n}$ are their relative amplitudes. The time-dependence of the driver is described by τ (growth/decay time) and τ_{max}, the time at which $f(t)$ reaches a maximum value. We set $w = 0.05$ Mm, $x_0 = 0.7$ Mm, $y_0 = 1.75$ Mm, $A_{p,i} = A_{p,n} = 6$, $\tau = 50$ s and $\tau_{max} = 30$ s. The analytical form of the drivers used here mimics the response of impulsive heating in the localized lower solar atmosphere, which perturbs the gas pressure and generates pseudo-shocks. The perturbations rise with a certain growth rate, while they decay at later times, making their nature episodic and impulsive.

The position of the drivers corresponds to a plasma region of $\beta < 1$, where plasma β is the ratio of gas pressure to the magnetic pressure. The drivers are set at the top of the chromosphere, where the plasma is partially ionized and dominated by a magnetic field over the neutral gas pressure. Therefore, the slow and fast magnetoacoustic waves are weakly coupled there. The drivers essentially excite slow magnetoacoustic waves, which propagate along the magnetic field lines. The waves evolve into a faint and weak slow shock when they cross the solar transition region at $y = 2.1$ Mm, the where density falls rapidly. The plasma behind the shock is swept ahead to create a rarefied tail and a bright and dense pseudo-shock (Fig. 3, middle panel, and Supplementary Video 10) resembling the observations (Figs. 1 and 2, and Supplementary Table 1). The faint, slow shock leaves the domain as a detached leading front ahead of the pseudo-shock. The ongoing magnetic reconnection between penumbral filaments and pre-existing ambient open field lines at the outer periphery of the sunspot may result in such localized perturbations, which move in the overlying stratified atmosphere and create moving shocks/pseudo-shocks (Fig. 1b)[6,20].

The spatiotemporal evolution of the faint slow shock and pseudo-shock (Fig. 4a,c) indicate that the faint slow shock leaves the magnetoplasma domain in the early phase of its evolution, while the pseudo-shock remains associated with it during its total lifespan of ~150 s. Therefore, the energy and mass transport are basically governed by the pseudo-shock source. The energy flux associated

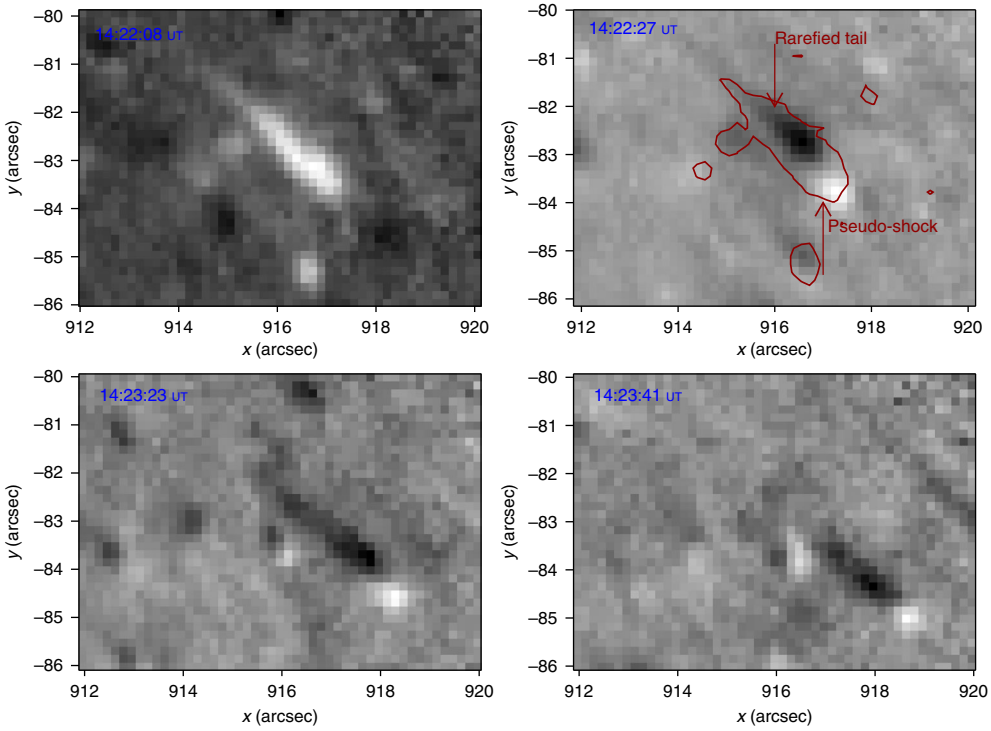

Fig. 2 | Evolution of a pseudo-shock. A running-difference image sequence shows that the plasma is swept along the magnetic field lines, resulting in the formation of a confined pseudo-shock on 8 October 2014 at 14:22 UT. It is elongated up to a height of ~5 Mm and propagates through the solar atmosphere with continuous evolution of rarefied plasma lagging behind. This bright magnetoplasma structure originates impulsively, and an associated pseudo-shock evolves for a finite time. The red contour in the top right image represents the intensity feature of the pseudo-shock when it appeared.

with the pseudo-shock (dashed blue line in Fig. 4a) is greater than the faint, slow shock (dashed red line in Fig. 4a). The pseudo-shock consists of one order of magnitude higher energy (~8×10^3 W m^{-2}) in the upper chromosphere and transition region compared with the slow shock. Therefore, the energy flux of the pseudo-shock is sufficient to energize the lower solar atmosphere locally. Comparison of energy fluxes carried by the pseudo-shock (blue squares in Fig. 4b) and slow shock (red diamonds) exhibits the significance of the pseudo-shock in the inner corona as it carries a substantial amount of energy (~10^3 W m^{-2}) that may be sufficient to compensate for its radiative losses if they dissipate there[1]. Also, the mass flux carried by the pseudo-shock (blue squares in Fig. 4d) is larger than the slow shock front (red diamonds). The value of the mass transport (~10^{-5} kg m^{-2} s^{-1}) due to the pseudo-shocks as computed by the model indicates that the pseudo-shocks may contribute to feeding the plasma into the inner corona above active regions.

Most of the mass and energy fluxes are transported to the transition region and inner corona by neutral particles, while only a fraction of it is due to ions (see Supplementary Text). The transported neutrals impulsively expand in the inner corona and frictional heating may be produced across the pseudo-shock due to strong ion-neutral collisions, which thermalize its kinetic energy to heat the plasma locally[21]. Thus, the pseudo-shock sources may fade gradually after reaching the inner corona, where its energy is dissipated. The study of dissipation of these new energy sources is beyond the scope of this Letter, and will be considered in future study.

This work demonstrates the role of pseudo-shocks in carrying sufficient amounts of energy that may balance the localized coronal losses above solar active regions. These pseudo-shocks are recurrent on the Sun, and present an abundant measure in and around the sunspot (see Supplementary Video 11). Therefore, they may play a crucial role in locally compensating the radiative losses in the overlying corona. We also show that these pseudo-shocks can transport substantial amounts of mass above an active region. However, further studies are required to determine whether they are directly linked to the formation of the slow solar wind[22]. The quiet-Sun heating mechanism has been explored in the form of a variety of competing plasma processes; for example, magnetohydrodynamic waves[23–25] and braiding of magnetic field lines[26], while heating of active regions has typically been associated with nanoflares and reconnection[7]. Pseudo-shocks can potentially provide the required energy and mass transport above solar active regions to balance the coronal losses.

Pseudo-shocks may also be associated with penumbral jets[6], light bridge peacock jets[27] and penumbral dots[28,29], which occur in abundant measures in and around sunspots. These sunspot jets sometimes show the evolution of bright, bulky heads and comparatively rarefied tails, which may suggest the presence of pseudo-shocks within them. If pseudo-shocks evolve in these active-region plasma jets, they may contribute significantly to their energetics and formation. Future observations by the next generation of ultra-high-resolution telescopes (for example, the Daniel K. Inouye Solar Telescope, European Solar Telescope, National Large Solar Telescope, and so on), as well as future theoretical investigations, such as dissipation of these high-energy pseudo-shocks, will be able to constrain the global role of pseudo-shocks in the solar energy budget.

Methods

In this section, we describe the two-fluid equations, initial set-up of the numerical simulation, and solar model atmosphere with realistic temperature and magnetic fields. We have used this two-fluid model and described basic set-up (initial and boundary conditions) to simulate the evolution of pseudo-shocks mimicking the physical properties of the observed pseudo-shocks in the solar chromosphere.

Two-fluid equations. To model the evolution of pseudo-shocks, we consider a gravitationally stratified and magnetically confined plasma made up of two species (that is, ionized (ions + electrons) and neutral fluids). This plasma is governed by a

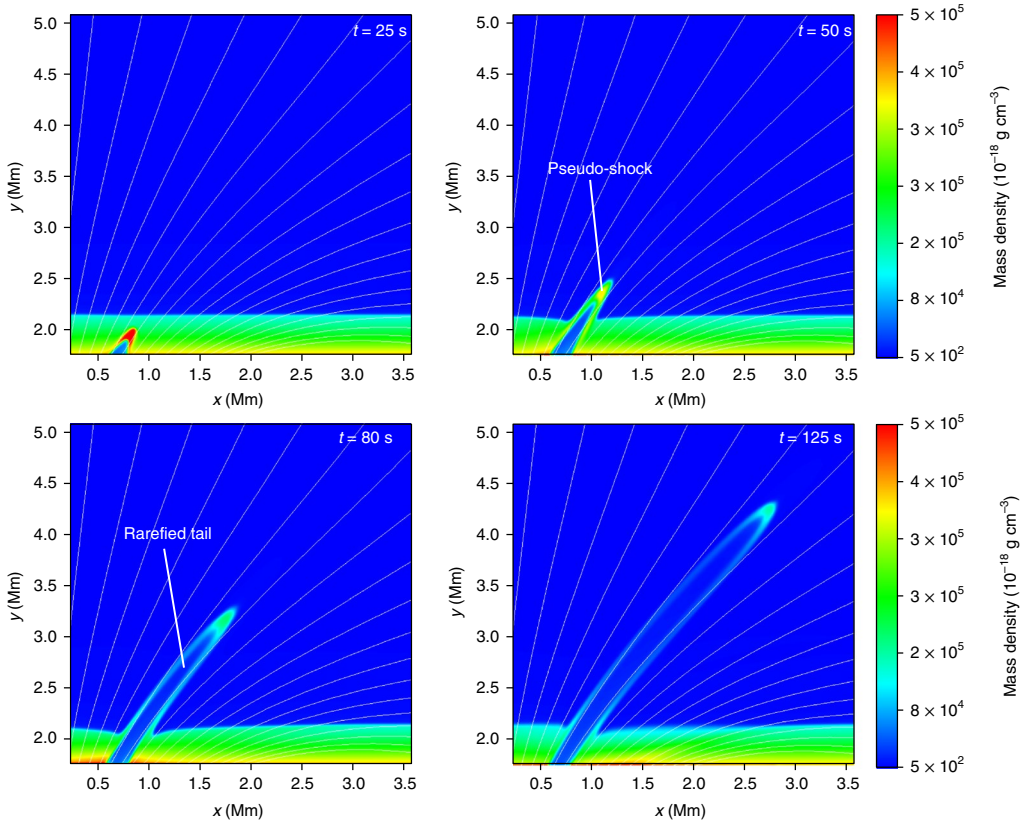

Fig. 3 | Two-fluid simulations of a pseudo-shock using newly developed JOANNA code[15]. The pseudo-shock evolves in the gravitationally stratified and magnetized solar atmosphere. The leading slow shock (weak and invisible), pronounced pseudo-shock (or entropy mode) in the form of a dense and bright contact surface and rarefied tail evolve in the solar atmosphere. Thereafter, they fade and subside gradually. *x* and *y* are the horizontal and vertical spatial extent of the localized model solar atmosphere, respectively.

set of two-fluid equations[19,20]. The resulting equations describing neutral fluids are written as follows:

$$\frac{\partial \varrho_n}{\partial t} + \nabla \cdot (\varrho_n \mathbf{V}_n) = 0 \tag{2}$$

$$\frac{\partial \varrho_n \mathbf{V}_n}{\partial t} + \nabla \cdot (\varrho_n \mathbf{V}_n \mathbf{V}_n + p_n \mathbf{I}) = \alpha_c (\mathbf{V}_i - \mathbf{V}_n) + \varrho_n \mathbf{g} \tag{3}$$

$$\frac{\partial E_n}{\partial t} + \nabla \cdot [(E_n + p_n)\mathbf{V}_n] = \alpha_c \left[\frac{1}{2} |\mathbf{V}_i - \mathbf{V}_n|^2 + \frac{3}{2} \frac{k_B}{m_H} \left(\frac{T_n}{\mu_n} - \frac{T_i}{\mu_i} \right) \right] + \varrho_n \mathbf{g} \cdot \mathbf{V}_n \tag{4}$$

$$E_n = \frac{p_n}{\gamma - 1} + \frac{\varrho_n |\mathbf{V}_n|^2}{2} \tag{5}$$

while ions + electrons are described by:

$$\frac{\partial \varrho_i}{\partial t} + \nabla \cdot (\varrho_i \mathbf{V}_i) = 0 \tag{6}$$

$$\frac{\partial \varrho_i \mathbf{V}_i}{\partial t} + \nabla \cdot (\varrho_i \mathbf{V}_i \mathbf{V}_i + p_i \mathbf{I}) + \mathbf{J} \times \mathbf{B} = -\alpha_c (\mathbf{V}_i - \mathbf{V}_n) + \varrho_i \mathbf{g} \tag{7}$$

$$\frac{\partial \mathbf{B}}{\partial t} - \nabla \times (\mathbf{V}_i \times \mathbf{B}) = 0 \tag{8}$$

$$\nabla \cdot \mathbf{B} = 0 \tag{9}$$

$$\frac{\partial E_i}{\partial t} + \nabla \cdot [(E_i + p_i)\mathbf{V}_i - \mathbf{B}(\mathbf{V} \cdot \mathbf{B})] = \alpha_c \left[\frac{1}{2} |\mathbf{V}_i - \mathbf{V}_n|^2 + \frac{3}{2} \frac{k_B}{m_H} \left(\frac{T_i}{\mu_i} - \frac{T_n}{\mu_n} \right) \right] + \varrho_i \mathbf{g} \cdot \mathbf{V}_i \tag{10}$$

$$E_i = \frac{p_i}{\gamma - 1} + \frac{\varrho_i |\mathbf{V}_i|^2}{2} + \frac{\mathbf{B}^2}{2\mu_0} \tag{11}$$

where $\varrho_{i,n}$, $p_{i,n}$, $\mathbf{V}_{i,n}$, T, $\mathbf{B}$ and α_c are, respectively, the mass density, gas pressure, plasma velocity, plasma temperature, magnetic field and coefficient of collisions between particles. Subscripts *i* and *n* correspond respectively to ions and neutrals, $\mathbf{J} = \nabla \times \mathbf{B}/\mu_0$ is the current density, m_H is the hydrogen mass, k_B is Boltzmann's constant, $\gamma = 5/3$ is an adiabatic index and $\mathbf{g} = (0, -g, 0)$ is the gravitational acceleration. The value of the gravitational acceleration (g) is taken as 274 m s^{-2}. For the sake of simplicity, we limit ourselves to the two-dimensional case with the system being invariant along the *z* direction, and neglect the effect of ionization and recombination (due to the small mass of electrons compared with the ions and neutrals), as well as all electron components.

Numerical simulations using two-fluid equations. To solve the two-fluid equations numerically in the presented simulations, we use JOANNA code[16,19]. We set the Courant–Friedrichs–Lewy (CFL) number equal to 0.3 and specify the simulation box in (x, y) as $(-2.56, 2.56) \times (1.75, 15.0)$ Mm^2, where $y = 0$ denotes the bottom of the photosphere. In the numerical simulations, we adopt the uniform grid within the region $(-2.56 \le x \le 2.56) \times (1.75 \le y \le 6.87)$ Mm^2, which is covered by $1{,}024 \times 1{,}024$ grid points, leading to a resolution of 5 km there. Above this region, we implement a stretched grid of 64 cells along the *y* direction whose size grows with *y*. Such a stretched grid plays the role of a sponge to absorb the incoming signals and it minimizes reflections from the top boundary of the simulation box. We impose open boundary conditions for the outflowing signal at the side boundaries. At the top and bottom of the numerical simulation box, we fix all plasma quantities to their initial equilibrium values, and solve two-fluid equations with the use of a mixed HLLC/HLLD Riemann solver.

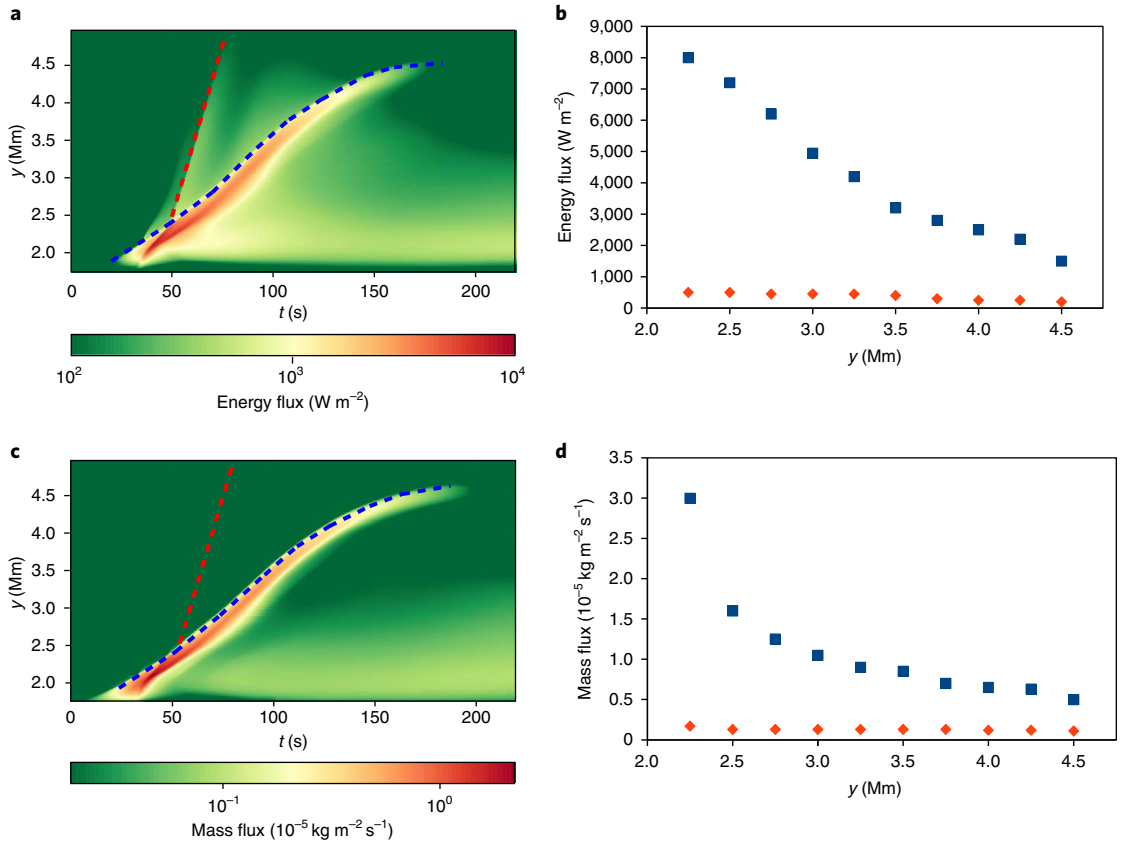

Fig. 4 | Total energy and mass fluxes (for protons + electrons and hydrogen atoms) in a pseudo-shock. a,**c**, Spatiotemporal maps of energy (**a**) and mass fluxes (**c**) are displayed along the moving magnetoplasma system consisting of a faint, slow shock and bright pseudo-shock (Fig. 2). Dashed red and blue curves display the evolution of the slow and pseudo-shock, respectively. **b**,**d**, Comparison of the energy (**b**) and mass fluxes (**d**) carried by the pseudo-shock (blue rectangles) and slow shock (red diamonds) exhibits the significance of the pseudo-shock as it carries high energy (~10^3 W m^{-2}) and mass fluxes (~10^{-5} kg m^{-2} s^{-1}), which may be sufficient to compensate for some part of the radiative (~10^3 W m^{-2}) and mass losses (~10^{-10} kg m^{-2} s^{-1}) in the inner solar corona up to 5.0 Mm height above an active region.

Force-free magnetic field and realistic temperature conditions. The hydrostatic atmosphere for the ions corresponds to a force-free ($\mathbf{J}\times\mathbf{B}=0$) magnetic field with the solenoidal condition ($\nabla\times\mathbf{B}=0$), which is being satisfied. We also assume a current-free ($\mathbf{J}=0$) magnetic field whose horizontal B_x, vertical B_y and transversal B_z components are given as[19]:

$$\begin{aligned} B_x(x,y) &= \frac{-2Sx(y-a)}{(x^2+(y-a)^2)^2} \\ B_y(x,y) &= \frac{S(x^2-(y-a)^2)}{(x^2+(y-a)^2)^2} + B_v \\ B_z(x,y) &= 0 \end{aligned} \tag{12}$$

where B_v is a straight vertical magnetic field component, and a and S are free parameters corresponding to the vertical location of the singularity in the magnetic field and its strength, respectively. We set $B_v=8$ G, $a=-7.5$ Mm and S in such a manner that at the reference point ($x_r=0$, $y_r=6$) Mm, the magnitude of the magnetic field is $B=4$ G. We have examined that the energetics, mass flux and evolution of the pseudo-shocks are almost the same for 1–2 kG magnetic field strength. Therefore, we have taken a 1 kG average magnetic field at the photosphere to prepare our numerical simulations as we notice that these pseudo-shocks are prevalent in the outer part of the sunspot penumbra, as well as nearby regions. The magnetic field lines are displayed in Supplementary Fig. 3.

The realistic temperature profile for ion and neutrals in the solar atmosphere, along with the height, is shown in Supplementary Fig. 4. This temperature is taken from the model[18]. In the photosphere, which is localized at $0\le y\le 0.5$ Mm, $T(y)$ decreases with y until close to the bottom of the chromosphere. Specifically for $y\sim 0.5$ Mm, $T(y)$ reaches a local minimum of about 4.5×10^3 K. Higher up in the atmosphere, $T(y)$ grows with height until the transition region is reached. Thereafter, it rises abruptly to the coronal heights about the values of 1 MK.

Perturbations at the upper chromosphere and generation of pseudo-shocks. We perturb the equilibrium model of the structured solar atmosphere by implementing simultaneously the drivers in ion and neutral gas pressures. These drivers are expressed by equation (1). These drivers are operated at the top of the chromosphere, and as a result slow and fast magnetoacoustic ion waves are weakly coupled there. Therefore, these drivers execute slow magnetoacoustic ion waves, which propagate essentially along the magnetic field lines. As neutrals do not directly feel magnetic field, the drivers generate ion-neutral entropy mode (pseudo-shock) and neutral acoustic waves that propagate quasi-isotropically in the medium. Neutrals are affected there by ion-neutral collisions, which are significant in the low atmospheric region of the Sun. The modelled pseudo-shock resembles the cases observed by IRIS on 8 October 2014, and demonstrates their physical significance.

Data availability

The data that support the plots within this paper and other findings of this study are available from the corresponding author upon reasonable request.

Received: 3 August 2017; Accepted: 5 September 2018;
Published online: 08 October 2018

References

1. Withbroe, G. L. & Noyes, R. W. Mass and energy flow in the solar chromosphere and corona. *Annu. Rev. Astron. Astrophys.* **15**, 363–387 (1977).
2. Feldman, U., Landi, E. & Schwadron, N. A. On the sources of fast and slow solar wind. *J. Geophys. Res.* **110**, A07109 (2005).
3. Harra, L. K. et al. Outflows at the edges of active regions: contribution to solar wind formation? *Astrophys. J.* **676**, L147–L150 (2008).
4. Katsukawa, Y. et al. Small-scale jetlike features in penumbral chromospheres. *Science* **318**, 1594–1597 (2007).

5. Vissers, G. J. M., Rouppe van der Voort, L. H. M. & Carlsson, M. Evidence for a transition region response to penumbral microjets in sunspots. *Astrophys. J.* **811**, 33–38 (2015).
6. Tiwari, S. K., Moore, R. L., Winebarger, A. R. & Alpert, S. E. Transition-region/coronal signatures and magnetic setting of sunspot penumbral jets: Hinode (SOT/FG), Hi-C, and SDO/AIA observations. *Astrophys. J.* **816**, 92 (2016).
7. Cargill, P. J. & Klimchuk, J. A. Nanoflare heating of the corona revisited. *Astrophys. J.* **605**, 911–920 (2004).
8. Aschwanden, M. J., Winebarger, A., Tsiklauri, D. & Peter, H. The coronal heating paradox. *Astrophys. J.* **659**, 1673–1681 (2007).
9. Klimchuk, J. A. Key aspects of coronal heating. *Phil. Trans. R. Soc. A* **373**, 20140256 (2015).
10. Ryutova, M., Berger, T., Frank, Z. & Title, A. On the penumbral jetlike features and chromospheric bow shocks. *Astrophys. J.* **686**, 1404–1419 (2008).
11. Bharti, L., Solanki, S. K. & Hirzberger, J. Lambda-shaped jets from a penumbral intrusion into a sunspot umbra: a possibility for magnetic reconnection. *Astron. Astrophys.* **597**, A127 (2017).
12. Priest, E. R. *Magnetohydrodynamics of the Sun* (Cambridge Univ. Press, Cambridge, 2014).
13. Crocco, L. in *High Speed Aerodynamics and Jet Propulsion: Fundamentals of Gas Dynamics* Vol III (ed. Emmons, H. W.) 110–130 (Princeton Univ. Press, Princeton, 1958).
14. De Pontieu, B. et al. The interface region imaging spectrograph (IRIS). *Sol. Phys.* **289**, 2733–2779 (2014).
15. De Pontieu, B. et al. On the prevalence of small-scale twist in the solar chromosphere and transition region. *Science* **346**, 1255732 (2014).
16. Wójcik, D. P. *Numerical Model of Magnetohydrodynamic Waves in the Solar Atmosphere.* MSc thesis, Maria Curie-Skłodowska Univ. (2016).
17. Konkol, P., Murawski, K. & Zaqarashvili, T. V. Numerical simulations of magnetoacoustic oscillations in a gravitationally stratified solar corona. *Astron. Astrophys.* **537**, A96 (2012).
18. Avrett, E. H. & Loeser, R. Models of the solar chromosphere and transition region from SUMER and HRTS observations: formation of the extreme-ultraviolet spectrum of hydrogen, carbon, and oxygen. *Astrophys. J. Suppl.* **175**, 229–276 (2008).
19. Kuźma, B. et al. 2-fluid numerical simulations of solar spicules. *Astrophys. J.* **849**, 78 (2017).
20. Oliver, R., Soler, R., Terradas, J. & Zaqarashvili, T. V. Dynamics of coronal rain and descending plasma blobs in solar prominences. II. Partially ionized case. *Astrophys. J.* **818**, 128 (2016).
21. Khomenko, E. On the effects of ion-neutral interactions in solar plasmas. *Plasma Phys. Contr. Fusion* **59**, 014038 (2017).
22. Edwards, S. J., Parnell, C. E., Harra, L. K., Culhane, J. L. & Brooks, D. H. A comparison of global magnetic field skeletons and active-region upflows. *Sol. Phys.* **291**, 117–142 (2016).
23. Jess, D. et al. Alfvén waves in the lower solar atmosphere. *Science* **323**, 1582–1585 (2009).
24. McIntosh, S. et al. Alfvénic waves with sufficient energy to power the quiet solar corona and fast solar wind. *Nature* **475**, 477–480 (2011).
25. Srivastava, A. K. et al. High-frequency torsional Alfvén waves as an energy source for coronal heating. *Sci. Rep.* **7**, 43147 (2017).
26. Cirtain, J. W. et al. Energy release in the solar corona from spatially resolved magnetic braids. *Nature* **493**, 501–503 (2013).
27. Yang, S., Zhang, J., Jiang, F. & Xiang, Y. Oscillating light wall above a sunspot light bridge. *Astrophys. J.* **804**, L27 (2015).
28. Tian, H. et al. Observations of subarcsecond bright dots in the transition region above sunspots with the interface region imaging spectrograph. *Astrophys. J.* **790**, L29 (2014).
29. Alpert, S. E., Tiwari, S. K., Moore, R. L., Winebarger, A. R. & Savage, S. L. Hi-C observations of sunspot penumbral bright dots. *Astrophys. J.* **822**, 35 (2016).

Acknowledgements

A.K.S. and B.N.D. acknowledge the RESPOND-ISRO (DOS/PAOGIA205-16/130/602) project. A.K.S. acknowledges the SERB-DST project (YSS/2015/000621) grant, and the Advanced Solar Computational and Analyses Laboratory (ASCAL). Armagh Observatory and Planetarium is grant-aided by the Northern Ireland Department for Communities. J.G.D. acknowledges the DJEI/DES/SFI/HEA Irish Centre for High-End Computing for provision of computing facilities and support. J.G.D. also thanks the STFC for PATT travel and subsistence and the SOLARNET project, which is supported by the European Commission's FP7 Capacities Programme under grant agreement number 312495, for travel and subsistence. M.S. acknowledges support from 'Progetti di ricerca INAF di Rilevante Interesse Nazionale' (PRIN-INAF 2014) and project 2012P2HRCR 'Il sole attivo ed i suoi effetti sul clima dello spazio e della terra' (PRIN MIUR 2012) grants, funded by the Italian National Institute for Astrophysics (INAF) and Ministry of Education, Universities and Research (MIUR), respectively. Work by K.M., B.K. and D.P.W. was supported financially by projects at the National Science Centre, Poland (grant numbers 2014/15/B/ST9/00106 and 2017/25/B/ST9/00506). T.V.Z. was supported by the Austrian Science Fund 'FWF' project P30695-N27 and Georgian Shota Rustaveli National Science Foundation project DI-2016-17. Z.E.M. acknowledges support from the Alexander von Humboldt Foundation. The authors express thanks to A. Kaczmarczyk for assistance with creating the Adobe illustrations. They also acknowledge the use of IRIS and Solar Dynamics Observatory/Atmospheric Imaging Assembly observations in this work.

Author contributions

A.K.S. led the project by defining the novel science case, analysing and making the IRIS observations, and writing the paper. K.M., B.K. and D.P.W. constructed the numerical model based on the two-fluid JOANNA code, which was developed by D.P.W. All co-authors (A.K.S., K.M., B.N.D., J.G.D., T.V.Z., M.S., Z.E.M., B.K., D.P.W. and P.K.) participated in studying the science and editing the draft.

Competing interests

The authors declare no competing interests.

Additional information

Supplementary information is available for this paper at https://doi.org/10.1038/s41550-018-0590-1.

Reprints and permissions information is available at www.nature.com/reprints.

Correspondence and requests for materials should be addressed to A.K.S.

Publisher's note: Springer Nature remains neutral with regard to jurisdictional claims in published maps and institutional affiliations.

A&A 577, A138 (2015)
DOI: 10.1051/0004-6361/201424601

Astronomy & Astrophysics

Numerical simulations of sheared magnetic lines at the solar null line⋆

B. Kuźma[1], K. Murawski[1], and A. Solov'ev[2]

[1] Group of Astrophysics, University of Maria Curie-Skłodowska, ul. Radziszewskiego 10, 20-031 Lublin, Poland
e-mail: blazejkuzma1@o2.pl
[2] Central (Pulkovo) Astronomical Observatory, Russian Academy of Sciences, 196140 St. Petersburg, Russia

Received 14 July 2014 / Accepted 26 February 2015

ABSTRACT

Aims. We perform numerical simulations of sheared magnetic lines at the magnetic null line configuration of two magnetic arcades that are settled in a gravitationally stratified and magnetically confined solar corona.
Methods. We developed a general analytical model of a 2.5D solar atmospheric structure. As a particular application of this model, we adopted it for the curved magnetic field lines with an inverted Y shape that compose the null line above two magnetic arcades, which are embedded in the solar atmosphere that is specified by the realistic temperature distribution. The physical system is described by 2.5D magnetohydrodynamic equations that are numerically solved by the FLASH code.
Results. The magnetic field line shearing, implemented about 200 km below the transition region, results in Alfvén and magnetoacoustic waves that are able to penetrate solar coronal regions above the magnetic null line. As a result of the coupling of these waves, partial reflection from the transition region and scattering from inhomogeneous regions the Alfvén waves experience fast attenuation on time scales comparable to their wave periods, and the physical system relaxes in time. The attenuation time grows with the large amplitude and characteristic growing time of the shearing.
Conclusions. By having chosen a different magnetic flux function, the analytical model we devised can be adopted to derive equilibrium conditions for a diversity of 2.5D magnetic structures in the solar atmosphere.

Key words. magnetohydrodynamics (MHD) – waves – Sun: corona – Sun: magnetic fields

1. Introduction

It is commonly accepted that the magnetic field plays a vital role in the development of solar activity. Extrapolation of the magnetic field from the photospheric level reveals the presence of ubiquitous magnetic null points in which the field vanishes (e.g., Brown & Priest 2001). The generation and propagation of magnetohydrodynamic (MHD) waves, which are omnipresent throughout the solar atmosphere, is one of the basic phenomena of the solar activity. Among them, Alfvén waves are of particular interest (e.g., Van Doorsselaere et al. 2008; Fujimura & Tsuneta 2009; Jess et al. 2009). A natural property of these waves is to propagate along the magnetic field lines without introducing (in the limit of small-amplitude waves) any mass density perturbations (e.g., Nakariakov & Verwichte 2005; Vasheghani Farahani et al. 2012). As Alfvén waves approach the null point, they spread out as a result of the diverging magnetic lines (Bulanov & Syrovatskii 1980; McLaughlin & Hood 2004). The authors found that as the waves approach the separatrix (which separate the magnetic field into two distinct regions), they deposit energy, leading to a potential heating region there.

Extensive studies of Alfvén waves in the solar atmosphere have been performed so far. For instance, the nonlinear wave equations were derived for magnetoacoustic waves driven by Alfvén waves (Murawski 1992; Nakariakov et al. 1997, 1998). Alfvén waves were found to be attenuated by energy leakage into the ambient plasma (Gruszecki et al. 2007). Torsional Alfvén waves were analytically and numerically explored by Zaqarashvili & Murawski (2007) in a coronal loop that was inhomogeneous along the longitudinal direction. That the propagation of torsional Alfvén waves along isothermal and thin magnetic flux tubes is cutoff-free has recently been demonstrated by Musielak et al. (2007). Murawski & Musielak (2010) extended the previous studies of Alfvén waves by refining both analytical and numerical methods, including a temperature distribution typical of the solar chromosphere, transition region, and corona, and considering the impulsively generated waves. Chmielewski et al. (2013) studied the impulsively generated nonlinear Alfvén waves in the solar atmosphere and describe their most likely role in the observed nonthermal broadening of some spectral lines in solar coronal holes. Chmielewski et al. (2014) performed numerical simulations of Alfvén waves in asymmetric coronal arcade and find that the asymmetry plays an important role in Alfvén waves propagation, leading to such phenomena as phase mixing and wave attenuation.

The goal of this paper is to develop analytical and numerical models of magnetic field line shearing, which excite Alfvén and magnetoacoustic waves and lead to a relaxation of the system that consists of the magnetic null line above two magnetic arcades that are embedded in a gravitationally stratified solar atmosphere. We limit ourself to the 2.5 dimensional (2.5D) case. In the magnetic-free case, this atmosphere would be determined by the hydrostatic condition with the realistic temperature profile. In such an atmosphere, we determine a nonpotential magnetic field, which corresponds to the magnetic structure, and the corresponding equilibrium mass density and gas pressure that vary both along horizontal and vertical directions, but are invariant along the arcades' axis.

⋆ Movie associated to Fig. 5 is available in electronic form at http://www.aanda.org

This paper is organized as follows. Our model of the magnetic structure and the description of the numerical simulations are introduced in Sects. 2 and 3, respectively. Results of our numerical simulations of wave propagation at the magnetic null line are presented and discussed in Sect. 4. Conclusions are given in Sect. 5.

2. Physical model of two magnetic arcades with a null line above

2.1. MHD equations

We consider a solar plasma that is described by the following set of ideal MHD equations:

$$\frac{\partial \varrho}{\partial t} + \nabla \cdot (\varrho \boldsymbol{V}) = 0, \tag{1}$$

$$\varrho \frac{\partial \boldsymbol{V}}{\partial t} + \varrho\,(\boldsymbol{V} \cdot \nabla)\,\boldsymbol{V} = -\nabla p + \frac{1}{\mu}(\nabla \times \boldsymbol{B}) \times \boldsymbol{B} + \varrho \boldsymbol{g}, \tag{2}$$

$$\frac{\partial p}{\partial t} + \boldsymbol{V} \cdot \nabla p = -\gamma p \nabla \cdot \boldsymbol{V}, p = \frac{k_{\rm B}}{m}\varrho T, \tag{3}$$

$$\frac{\partial \boldsymbol{B}}{\partial t} = \nabla \times (\boldsymbol{V} \times \boldsymbol{B}), \nabla \cdot \boldsymbol{B} = 0, \tag{4}$$

where ϱ is mass density, p gas pressure, $\boldsymbol{V}$ represents the plasma velocity, $\boldsymbol{B}$ is the magnetic field, T a temperature, $k_{\rm B}$ the Boltzmann's constant, $\gamma = 5/3$ is the adiabatic index, m a particle mass that is specified by a mean molecular weight of 0.6, and $\boldsymbol{g} = (0, -g, 0)$ is the gravitational acceleration. The value of g is equal to 274 m s^{-2}.

In Eqs. (1)–(4), we neglected both the nonideal and nonadiabatic terms that usually lead to attenuation of wave amplitudes. Their presence in the physical system is not expected to significantly modify the general behavior of waves. However, we aim to study them in the near future.

2.2. The equilibrium solar atmosphere

We consider a model of the equilibrium ($\partial/\partial t = 0$) solar atmosphere with an invariant horizontal coordinate z ($\partial/\partial z = 0$), but allow the z-components of velocity (V_z) and magnetic field (B_z) to vary with x and y. In this 2.5D model, the solar atmosphere is in static equilibrium ($\boldsymbol{V} = \boldsymbol{0}$) with the Lorentz force balanced by the pressure gradient and gravity, and the divergence-free magnetic field,

$$\frac{1}{\mu}(\nabla \times \boldsymbol{B}) \times \boldsymbol{B} - \nabla p + \varrho \boldsymbol{g} = \boldsymbol{0}, \tag{5}$$

$$\nabla \cdot \boldsymbol{B} = 0. \tag{6}$$

2.2.1. Hydrostatic atmosphere

A hydrostatic atmosphere corresponds to the magnetic-free ($\boldsymbol{B} = \boldsymbol{0}$) case in which the gas pressure gradient is balanced by the gravity force,

$$\nabla p_{\rm h} = \varrho_{\rm h} \boldsymbol{g}. \tag{7}$$

With the use of the ideal gas law given by Eq. (3) and the vertical y-component of Eq. (7), we express the hydrostatic gas pressure and mass density as

$$p_{\rm h}(y) = p_{\rm ref} \exp\left(-\int_{y_{\rm r}}^{y} \frac{{\rm d}y'}{\Lambda(y')}\right), \quad \varrho_{\rm h}(y) = \frac{p_{\rm h}(y)}{g\Lambda(y)}, \tag{8}$$

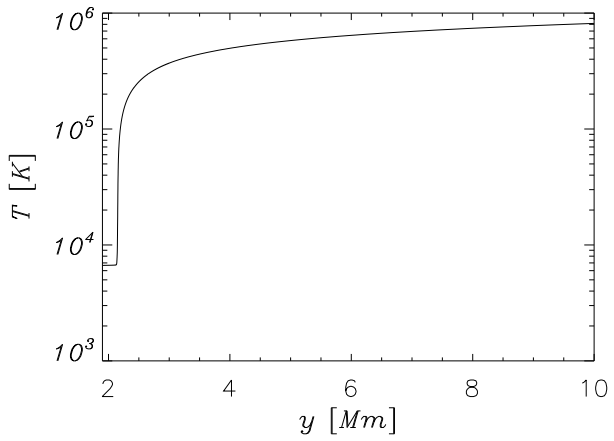

Fig. 1. Hydrostatic solar atmospheric temperature vs. height y.

where

$$\Lambda(y) = \frac{k_{\rm B} T(y)}{mg} \tag{9}$$

is the pressure scale height, and $p_{\rm ref}$ denotes the gas pressure at the reference level $y_{\rm r}$, which we set and hold fixed at $y_{\rm r} = 10$ Mm.

We adopt a realistic plasma temperature profile given by the semi-empirical model of Avrett & Loeser (2008) that is extrapolated into the solar corona (Fig. 1). In this model, the temperature attains a value of about 7×10^3 K at the top of the chromosphere, $y \approx 2.0$ Mm. At the transition region, which is located at $y \simeq 2.1$ Mm, T exhibits an abrupt jump (Fig. 1), and it grows to about 0.8×10^6 K in the solar corona at $y = 10$ Mm. Higher up in the solar corona, the temperature increases very slowly, tending to its asymptotical value of about 1.6 MK. The temperature profile uniquely determines the equilibrium mass density and gas pressure profiles, which fall off with height (not shown).

2.2.2. Magnetohydrostatic equilibrium

Multiplying Eq. (5) by $\boldsymbol{B}$, we obtain

$$\boldsymbol{B} \cdot (-\nabla p + \varrho \boldsymbol{g}) = 0. \tag{10}$$

The solenoidal condition of Eq. (6) is automatically satisfied if we express the equilibrium magnetic field with the use of magnetic flux function $A(x, y)$ as

$$\boldsymbol{B} = \nabla \times (A \boldsymbol{e}_z) + B_z \boldsymbol{e}_z, \tag{11}$$

where $\boldsymbol{e}_z$ is a unit vector along z-direction, and B_z is the z-component of the magnetic field. We therefore have

$$B_x = -\frac{\partial A}{\partial y}, \quad B_y = \frac{\partial A}{\partial x}, \quad B_z = B_z(x, y). \tag{12}$$

We set

$$p = p(x, y) = p(y, A). \tag{13}$$

Then from Eq. (10) we get

$$-B_x \frac{\partial p}{\partial A}\frac{\partial A}{\partial x} + B_y\left(-\frac{\partial p}{\partial y} - \frac{\partial p}{\partial A}\frac{\partial A}{\partial y} - \varrho g(y)\right) = 0. \tag{14}$$

With the use of Eq. (12), we simplify this equation to the hydrostatic condition along the magnetic field line, which is specified by the equation $A = \text{const}$.

$$\varrho(y,A)g = -\frac{\partial p(y,A)}{\partial y}. \tag{15}$$

We can express the x-, y-, and z-components of Eq. (5) as

$$\frac{1}{\mu}\left[B_y\left(\frac{\partial B_x}{\partial y} - \frac{\partial B_y}{\partial x}\right) - B_z\frac{\partial B_z}{\partial x}\right] = B_y\frac{\partial p}{\partial A}, \tag{16}$$

$$\frac{1}{\mu}\left[-B_z\frac{\partial B_z}{\partial y} - B_x\left(\frac{\partial B_x}{\partial y} - \frac{\partial B_y}{\partial x}\right)\right] = \frac{\partial p}{\partial y} + \frac{\partial p}{\partial A}\cdot\frac{\partial A}{\partial y} + \varrho(y)g = -B_x\frac{\partial p}{\partial A}, \tag{17}$$

$$B_y\frac{\partial B_z}{\partial y} + B_x\frac{\partial B_z}{\partial x} = J\left(\frac{A, B_z}{x, y}\right) = 0, \tag{18}$$

where J() is the Jacobian. From the last equation it follows that

$$B_z = B_z(A). \tag{19}$$

Multiplying Eq. (16) by B_x and Eq. (17) by B_y and taking their sum, we obtain the equilibrium equation for a system with translational symmetry (Low 1975; Priest 1982):

$$\Delta A = -\frac{1}{2}\frac{\mathrm{d}B_z^2}{\mathrm{d}A} - \mu\frac{\partial p(y,A)}{\partial A}, \tag{20}$$

where $\Delta = \left(\frac{\partial^2}{\partial x^2} + \frac{\partial^2}{\partial y^2}\right)$ is the Laplacian. This equation, Eqs. (14), (15), and the equation of ideal gas comprise the system of equations of magnetohydrostatics.

We consider the inverse problem of magnetohydrostatics (Low 1980, 1982; Solov'ev 2010; Shapovalov & Shapovalova 2003), assuming that the flux function $A(x, y)$ is known, and find the corresponding expressions for ϱ and p. Guided by this, we integrate Eq. (20) over A from infinity, where $A = 0$, $p = p_\mathrm{h}(y)$ and the external field $B_z(0) = B_{z,\mathrm{ex}} = \text{const.}$, to some point of the configuration, and keep the coordinate y as a fixed parameter. As a result we get (see also Solov'ev 2010)

$$p(y,x) = p_\mathrm{h}(y) + \frac{B_{z,\mathrm{ex}}^2}{2\mu} - \frac{B_z^2(A)}{2\mu} - \frac{1}{2\mu}\left(\frac{\partial A}{\partial x}\right)^2 + \frac{1}{\mu}\int_x^\infty \frac{\partial^2 A}{\partial y^2}\frac{\partial A}{\partial x}\mathrm{d}x. \tag{21}$$

When the external field $B_{z,\mathrm{ex}}$ is large enough, which may be the case for an active region, we can maintain a strong magnetic field in equilibrium thanks to the second positive term on the righthand side of Eq. (21).

To calculate the equilibrium mass density, we have to find $\partial p(y,A)/\partial y$. For any differentiable function $S(x, y)$, we satisfy the following relations:

$$\frac{\partial S(x,y)}{\partial x} = \frac{\partial S(y,A)}{\partial A}\frac{\partial A}{\partial x}, \tag{22}$$

$$\frac{\partial S(x,y)}{\partial y} = \frac{\partial S(y,A)}{\partial y} + \frac{\partial S(y,A)}{\partial A}\frac{\partial A}{\partial y}. \tag{23}$$

We calculate the derivative $\partial S(y,A)/\partial A$ taking into account that in our case $S(x, y) = p(x, y)$. We rewrite Eq. (20) as

$$B_z\frac{\partial B_z}{\partial A} + \frac{\partial^2 A}{\partial x^2} + \frac{\partial^2 A}{\partial y^2} = -\mu\frac{\partial p(y,A)}{\partial A}. \tag{24}$$

From Eq. (23) we find

$$\frac{\partial p(y,A)}{\partial y} = \frac{\partial p(x,y)}{\partial y} - \frac{\partial p(y,A)}{\partial A}\frac{\partial A}{\partial y}. \tag{25}$$

Using this expression in Eq. (24), we get

$$\frac{\partial p(y,A)}{\partial y} = \frac{\partial p_\mathrm{h}(y)}{\partial y} - \frac{1}{\mu}B_z\frac{\partial B_z}{\partial A}\frac{\partial A}{\partial y} - \frac{\partial}{\partial y}\left[\frac{1}{2\mu}\left(\frac{\partial A}{\partial x}\right)^2 - \frac{1}{\mu}\int_x^\infty \frac{\partial^2 A}{\partial y^2}\frac{\partial A}{\partial x}\mathrm{d}x\right] + \frac{1}{\mu}B_z\frac{\partial B_z}{\partial A}\frac{\partial A}{\partial y} + \frac{1}{\mu}\Delta A\frac{\partial A}{\partial y}. \tag{26}$$

With the use of Eqs. (15) and (26), we obtain

$$\varrho(x,y) = \varrho_\mathrm{h}(y) + \frac{1}{2\mu g}\frac{\partial}{\partial y}\left[\left(\frac{\partial A}{\partial x}\right)^2 - 2\int_x^\infty \frac{\partial^2 A}{\partial y^2}\frac{\partial A}{\partial x}\mathrm{d}x\right] - \frac{1}{\mu}\frac{\partial A}{\partial y}\Delta A. \tag{27}$$

Equations (21) and (27) comprise the solution to the problem. They are valid for any choice of magnetic field that is determined by the magnetic flux function $A(x, y)$ and transversal component $B_z(A)$. The only condition is that the equilibrium gas pressure and mass density, given respectively by Eqs. (21) and (27), must be positive.

2.2.3. The magnetic null line

Consider now the transversal magnetic-free case, $B_z(A) = 0$. From Eqs. (21) and (27), it follows that the equilibrium mass density, ϱ, and a gas pressure, p, simplify to the following expressions (see also Solov'ev 2010; Kraśkiewicz et al. 2015):

$$\varrho(x,y) = \varrho_\mathrm{h}(y) + \frac{1}{\mu g}\left[\frac{\partial}{\partial y}\left(\int_\infty^x \frac{\partial^2 A}{\partial y^2}\frac{\partial A}{\partial x}\mathrm{d}x + \frac{1}{2}\left(\frac{\partial A}{\partial x}\right)^2\right) - \frac{\partial A}{\partial y}\nabla^2 A\right], \tag{28}$$

$$\mu p(x,y) = \mu p_\mathrm{h}(y) - \frac{1}{2}\left(\frac{\partial A}{\partial x}\right)^2 - \int_\infty^x \frac{\partial^2 A}{\partial y^2}\frac{\partial A}{\partial x}\mathrm{d}x. \tag{29}$$

For the solar magnetic null line, we choose the magnetic flux function as

$$A(x,y) = \frac{B_0}{k}\left[kx\,\mathrm{e}^{-k^2x^2}\mathrm{e}^{-k(y-y_\mathrm{r})} + akx\right], \tag{30}$$

where k is the inverse scale length, y_r the vertical coordinate of the null line, and $a = \text{const.}$ is a dimensionless parameter that is associated with the external magnetic field along the y-direction, which is specified as

$$B_y\boldsymbol{e}_y = -B_0 a\boldsymbol{e}_y. \tag{31}$$

Here $\boldsymbol{e}_y$ is a unit vector along the y-direction. We set $k = 1/3$, $a = -0.75$, and hold them fixed. Since a magnetic flux function, $A(x, y)$, can be chosen arbitrarily, we set it in the form of Eqs. (30), (31). As for $a < 0$, it corresponds to two arcades that emerged from lower atmospheric layers into an originally vertical magnetic field, creating the null line above these arcades. It is noteworthy that any choice of $A(x, y)$ corresponds to an equilibrium.

Magnetic field lines resulting from Eq. (30) are illustrated in Fig. 2. We note the presence of the null line located at ($x = 0$, $y \cong 4.2$) Mm, where the magnetic field is zero. Below this point, close to the line $x = 0$ Mm, the magnetic field is essentially vertical, and it points downward. However, farther out from the line $x = 0$, the magnetic field lines reveal their curved nature. Above the null line, magnetic field lines are directed upward,

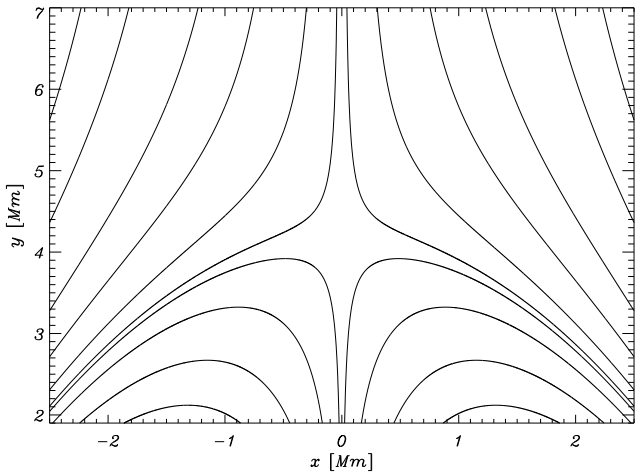

Fig. 2. Equilibrium magnetic field lines. The magnetic null line is located at ($x = 0$, $y \cong 4.2$) Mm.

and they are less curved than below the null line, which have the inverted Y-shape.

In this system the Alfvén speed, $c_{\rm A}$, varies along both the x- and y-directions, and it is expressed as

$$c_{\rm A}(x,y) = \sqrt{\frac{B^2(x,y)}{\mu\varrho_{\rm e}(x,y)}}, \tag{32}$$

where $\boldsymbol{B}$ is evaluated from Eq. (11) with $B_z = 0$ and the use of Eq. (30). The profile of $\log c_{\rm A}$ is displayed in Fig. 3 (top). The Alfvén speed is non-isotropic; highest values of $c_{\rm A}$ are located at the places where the plasma is hottest (not shown), which is at the points ($x = \pm 2, y = 3$) Mm. We specify the plasma β as the ratio of gas-to-magnetic pressures,

$$\beta(x,y) = \frac{p_e(x,y)}{B^2(x,y)/2\mu}. \tag{33}$$

The spatial profiles of $\log\beta$ are illustrated in Fig. 3 (bottom). As $\boldsymbol{B} = \boldsymbol{0}$ at the null line, β is infinitely large there. But it falls off with distance away from the null line.

3. Numerical simulations of MHD equations

To solve Eqs. (1)–(3) numerically, we use the FLASH code (Fryxell et al. 2000; Lee & Deane 2009; Lee 2013), in which a third-order unsplit Godunov-type solver with various slope limiters and Riemann solvers, as well as adaptive mesh refinement (AMR; MacNeice et al. 1999), are implemented. The minmod slope limiter and the Roe Riemann solver (e.g., Tóth 2000) are used. We set the simulation box as $(-3\,\mathrm{Mm}, 3\,\mathrm{Mm}) \times (1.9\,\mathrm{Mm}, 7.9\,\mathrm{Mm})$, while all plasma quantities remain invariant along the z-direction; however, both V_z and B_z generally differ from zero.

In our present work, we use an AMR grid with a minimum (maximum) level of refinement set to 3 (6). We performed the grid convergence studies by refining the grid by a factor of two. Because the numerical results remained essentially same for the grid of maximum block levels 6 and 7, we adopted the former to get the results presented in this paper. Small-size blocks of the numerical grid occupy the altitude of up to $y \approx 5.1$ Mm, which is about 3 Mm above the solar transition region (Fig. 4), and every numerical block consists of 8×8 identical numerical cells. This results in an excellent resolution of steep spatial profiles and greatly reduces the numerical diffusion in these regions.

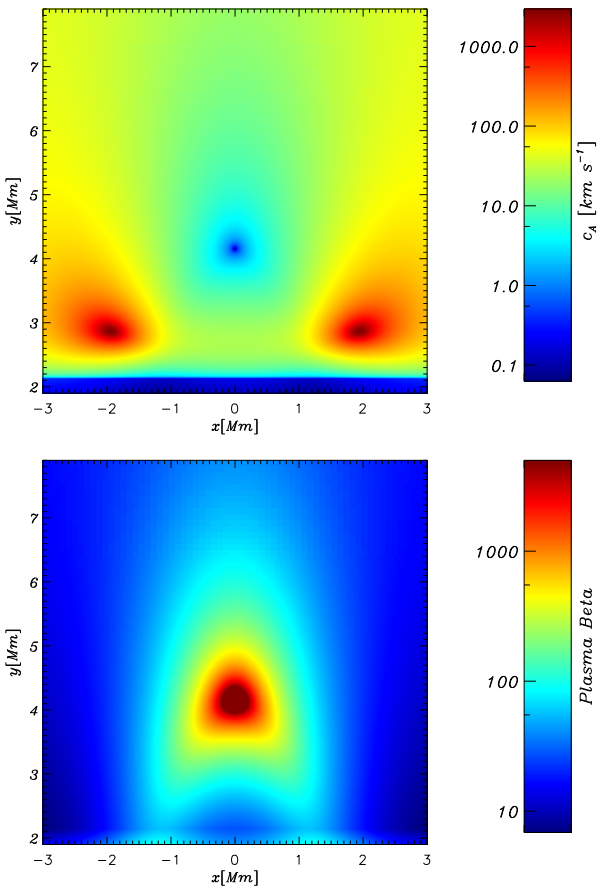

Fig. 3. Spatial profiles of $c_{\rm A}(x,y)$ (*top*) and $\beta(x,y)$ (*bottom*).

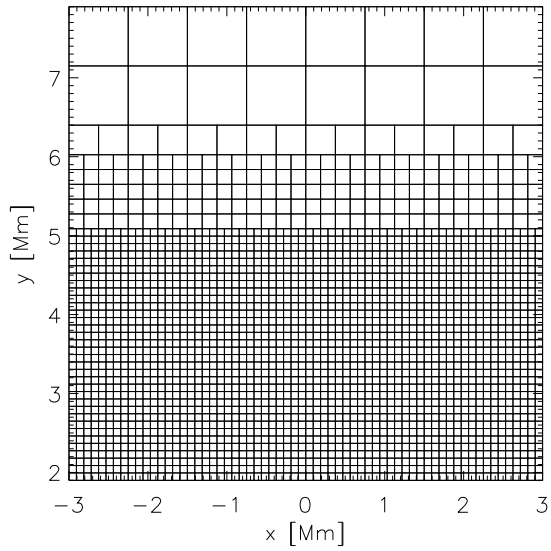

Fig. 4. Numerical blocks used in the numerical simulations.

3.1. Shearing of magnetic field lines

At all four boundaries, we set all plasma quantities to their equilibrium values. The only exception is the bottom boundary, where we additionally place the shearing of magnetic field, described by

$$B_z(x,y,t) = A_{\rm d}\,\frac{x}{w}\,\exp\left(-\frac{x^2+(y-y_0)^2}{w^2}\right)\left(1-\exp\left(-\frac{t}{\tau_{\rm B}}\right)\right). \tag{34}$$

Here A_d is the amplitude of the shearing, $(0, y_0)$ is its position, w denotes its width, and τ_B is the growth time of the shearing. We set and hold $y_0 = 1.9$ Mm, $w = 100$ km, and $\tau_B = 100$ s fixed, allowing A_d to vary. The value of y_0 corresponds to the magnetic shearing working about 200 km below the transition region. The width $w = 100$ km mimics a localized source of the shearing. The implemented value of the growth time models a fast shearing, while long-lasting (over hours) shearings would be more realistic. However, such shearings would be expensive for numerical modelling, and therefore they are devoted for potential future studies.

4. Results of numerical simulations

Without shearing ($A_d = 0$) in our 2.5D model with the transverse magnetic-free case, $B_z(A) = 0$, the Alfvén waves would decouple from magnetoacoustic waves, and the Alfvén waves would be described solely by $V_z(x, y, t)$ and $B_z(x, y, t)$. As a result, Alfvén waves in the linear, one-dimensional limit would be approximately governed by the following wave equation:

$$\frac{\partial^2 V_z}{\partial t^2} = c_A^2(l)\frac{\partial^2 V_z}{\partial l^2}, \tag{35}$$

where l is the coordinate along a magnetic field line.

Figure 5 shows the spatial profiles of $V_z(x, y)$ at three instants of time. A part of the simulation region is only displayed. Since the Alfvén speed is zero at the magnetic null line, the Alfvén waves are not able to reach this point. At $t = 200$ s, Alfvén waves propagate upward, approaching the null line (the top panel). As the magnetic field lines diverge with height, Alfvén waves follow them by turning in the left and right directions in the left ($x < 0$ Mm) and right ($x > 0$ Mm) half planes, respectively. This is seen at later moments of time (the middle and bottom panels). However, the Alfvén speed is highly inhomogeneous along magnetic field lines (Fig. 3). As a result of this inhomogeneity, the Alfvén waves experience scattering. However, the shearing of magnetic lines results in linear coupling between Alfvén and magnetoacoustic waves (e.g., Wołoszkiewicz et al. 2014), and although V_z corresponds essentially to Alfvén waves, it is also associated with fast magnetoacoustic waves. The latter are able to propagate across the null line, where as a result of disappearing magnetic field, they temporarily become acoustic waves. They enter the coronal region above the magnetic null line, which is clearly seen at $t = 2 \times 10^3$ s (bottom).

Figure 5 illustrates the velocity vectors $[V_x, V_y]$ that at the initial stage of the system's evolution, correspond to magnetoacoustic waves. At $t = 200$ s, two eddies appear at ($x \cong \pm 0.5$, $y \cong 3.2$) Mm. At a later time, the flow in the $x - y$ plane is more complex, but since it follows magnetic field lines, it is essentially associated with slow magnetoacoustic waves.

Figure 6 shows the evolution in time of $V_z(x = 0.05$ Mm, $y)$ above the null line. The maximum of the absolute value of $V_z(x = 0.05$ Mm, $y)$ increases in time, which proves that the wave signal indeed penetrates the coronal region above the null line.

As different parts of Alfvén waves move along magnetic field lines of different lengths, along which Alfvén speed varies differently, Alfvén waves experience phase-mixing (Fig. 5 middle and bottom) which is further illustrated in Fig. 7, which illustrates vertical profiles of $V_z(x = 0.5$ Mm, $y)$ at $t = 500$ s, $t = 600$ s, and $t = 10^3$ s. At $t = 500$ s, the oscillations at $y \approx 3.3$ Mm are approximately in anti-phase to the oscillations at the later moments of time, which reveal a high level of complexity, resulting from phase mixing and wave scattering.

Figure 8 clearly shows that the oscillations are present in the time signature of V_z collected at the point ($x = 0.5$, $y = 3.5$) Mm. The Fourier waveperiod of these oscillations, P, is about 333 s, which is close to the waveperiod of 5-min oscillations. However, P depends on a number of plasma quantities, such as a length of magnetic line and a profile of Alfvén speed along this line. These oscillations result essentially from partial reflection of Alfvén waves from the inhomogeneous region of high Alfvén speed located at ($x = 1.9$, $y = 2.9$) Mm (Fig. 3, bottom), and they decay in time as $\exp(-t/\tau)$ (Fig. 8), where τ is a decaying time. The envelopes fit to the time signature (Fig. 8) show that for $A_d = 2.28$ Gauss, τ is approximately 362 s, which is only about 30 s longer than the waveperiod. As a result we infer that Alfvén waves are attenuated on time scales that are comparable to their waveperiod.

The transmission coefficient of the Alfvén waves signal through the transition region can be evaluated as

$$C_t = \frac{A_t}{A_i}, \tag{36}$$

where $A_i = 2.2$ km s^{-1} and $A_t = 0.7$ km s^{-1} are amplitudes of respectively incident (Fig. 9) and transmitted Alfvén waves (Fig. 9). As a result we get $C_t \approx 0.3$. Because the reflection coefficient is $C_r = 1 - C_t$, we find that $C_r \approx 0.7$, which means that about 70% of the waves amplitude became reflected from the transition region, and about 30% was transmitted into lower atmospheric layers. This rather high value of C_t means that Alfvén waves are strongly attenuated by a significant amount of Alfvén waves energy that is transmitted through the transition region into lower regions of the solar atmosphere.

Figure 10 shows a dependence of τ/P on A_d. A lower value of τ/P corresponds to stronger attenuation and τ/P attains a value of about 1.95 for $A_d = 1.1$ Gauss. For a bit higher values of A_d, τ/P falls off with A_d, attaining its minimum of about 1.05 at $A_d = 2.2$ Gauss. This behavior fulfils our expectations; for a higher value of A_d, we would expect that more magnetoacoustic waves are present in the system because Alfvén waves are strongly coupled to these waves owing to the presence of the sheared magnetic field. Indeed, Fig. 11 illustrates the ratio of kinetic energies of magnetoacoustic and Alfvén waves Ekm/EkA vs. A_d. The kinetic energy of magnetoacoustic waves increases with A_d. Figure 12 shows the evolution of the ratio of the total kinetic energy to the total magnetic energy in time. This ratio grows in time reaching its maximum of about 8.5×10^{-3} at $t \approx 1400$ s and then, as the fast magnetoacoustic waves leave the simulation region, it subsides in time.

From Fig. 10 we infer that for $A_d > 2$ Gauss τ/P grows with A_d. While P decreases slightly with A_d (not shown), a larger amplitude of the shearing results in less attenuation, which results from a prevalence of relaxation process over wave propagation, for which τ is larger. As a result, τ/P grows with A_d for $A_d > 2.2$ Gauss (Fig. 10).

The attenuation time also varies with a characteristic growing time of the shearing, τ_B (see Eq. (34)). For a higher value of τ_B, thereare supposed to be fewer oscillations, because the system essentially relaxes to a new quasi-equilibrium. That results in a higher value of τ. This effect is presented in Fig. 13. For $\tau_B = 200$ s, we get $\tau \simeq 5.5 \times 10^3$ s, while $\tau_B = 400$ s corresponds to $\tau \simeq 12 \times 10^3$ s.

It is noteworthy that in many cases when shearing perturbations are applied in the vicinity of nulls, significant dissipation and perhaps reconnection occurs around the null/separatrices

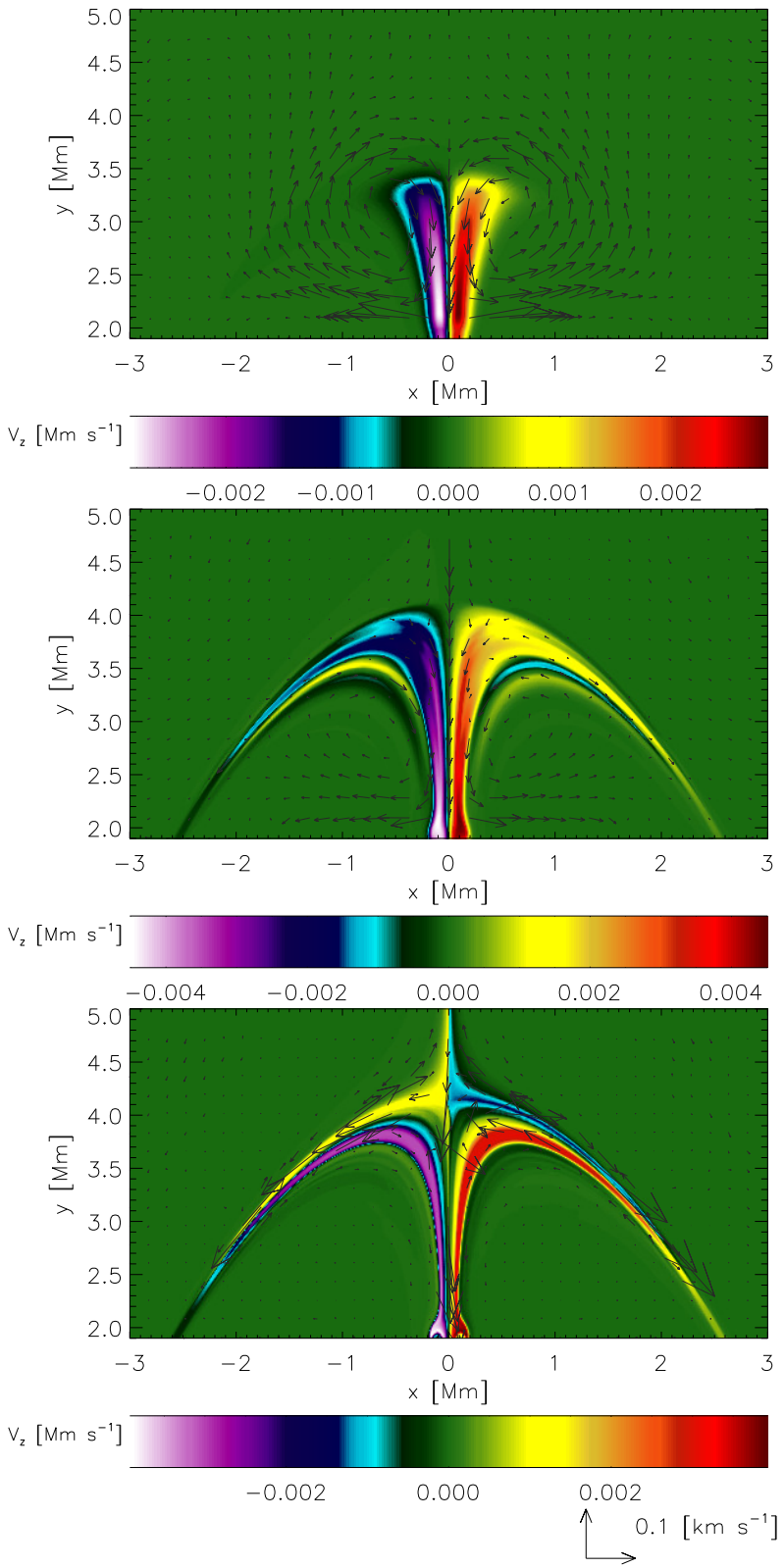

Fig. 5. Temporal evolution of $V_z(x, y)$ for $A_d = 2.28$ Gauss at $t = 200$ s, $t = 600$ s, and $t = 2 \times 10^3$ s (*from top to bottom*). Arrows represent velocity vectors in the x-y plane, $[V_x, V_y]$, expressed in the units of 0.1 km s^{-1}. (Movie available online.)

(e.g., Hassam & Lambert 1996; Craig & McClymont 1997; Antiochos & Linton 2002; Galsgaard et al. 2003; Craig & Litvinenko 2005; Pontin & Galsgaard 2007). However, the grid refinement studies that we performed showed that such phenomena are absent around the null line in our system.

5. Summary and conclusions

It is important to investigate the role of Alfvén waves on some solar phenomena, particularly when they are associated with the coronal heating and solar wind acceleration that remain

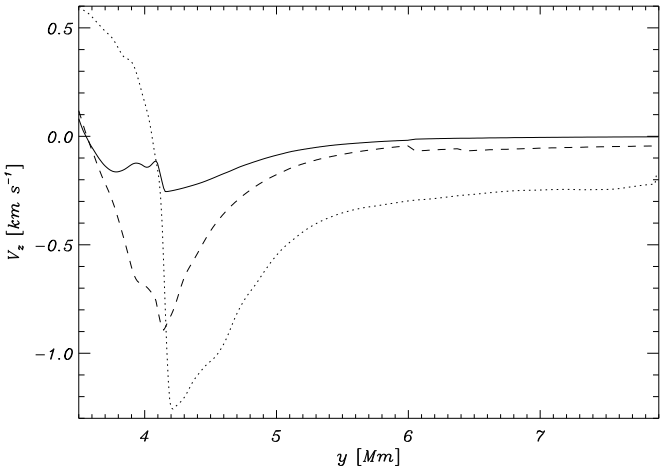

Fig. 6. Evolution of $V_z(x = 0.05$ Mm, $y)$ above the null line at $t = 10^3$ s (solid line), $t = 1.6 \times 10^3$ s (dashed line), and $t = 5 \times 10^3$ s (dotted line) for $A_d = 2.28$ Gauss.

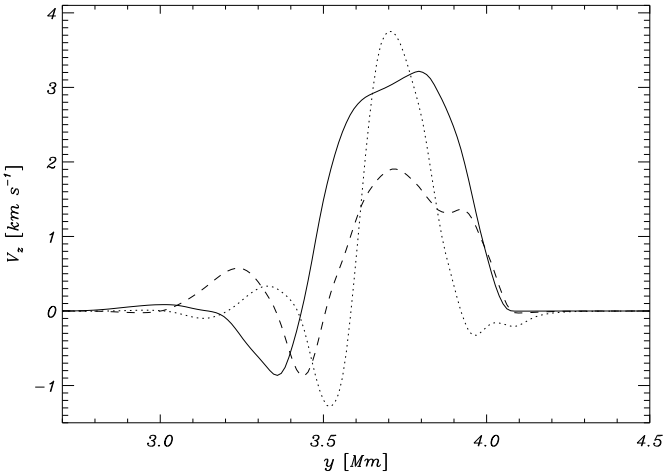

Fig. 7. Evolution of $V_z(x = 0.5$ Mm, $y)$ at $t = 500$ s (solid line), $t = 600$ s (dashed line), and $t = 10^3$ s (dotted line) for $A_d = 2.28$ Gauss.

long-standing problems of heliophysics. Leading into this framework, we generalized the analytical model of Kraśkiewicz et al. (2015) by implementing a magnetic field component along the invariant direction B_z. The model we devised can be adopted to derive equilibrium conditions for any 2.5D magnetic structure in the solar atmosphere. A magnetic field is specified by an arbitrary choice of a magnetic flux function $A(x, y)$ and $B_z(A)$. Having specified $A(x, y)$, the equilibrium mass density and a gass pressure are expressed by Eqs. (21) and (27).

Using the devised analytical model of the magnetic null line, we performed the 2.5D numerical simulations of the shearing magnetic field lines, implemented about 200 km below the transition region. These simulations adapt the realistic model of the hydrostatic solar atmosphere in the FLASH code. Our model exhibits the formation of the Alfvén waves at the initial phase of temporal evolution, linear coupling between Alfvén and magnetoacoustic waves at a later time, and relaxation of the system in the final phase. Our results reveal the complex picture of interaction between Alfvén waves and magnetic null lines. We found that as a result of highly inhomogeneous Alfvén speed and different lengths of magnetic field lines, Alfvén waves experience phase mixing, scattering from inhomogeneous regions of Alfvén speed, and partial reflection from the transition region and other

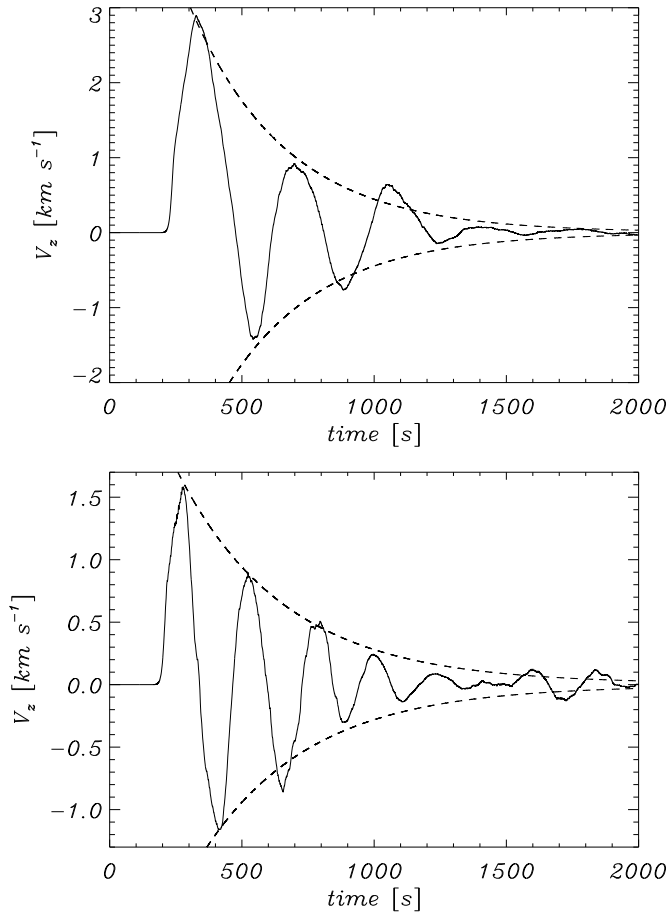

Fig. 8. Time history of $V_z(x = 0.5$ Mm, $y = 3.5$ Mm) (solid line) and its envelope (dashed lines) for $A_d = 2.28$ Gauss (*top*) and of $V_z(x = 0.6$ Mm, $y = 3.3$ Mm) and its envelope for $A_d = 5.7$ Gauss (*bottom*).

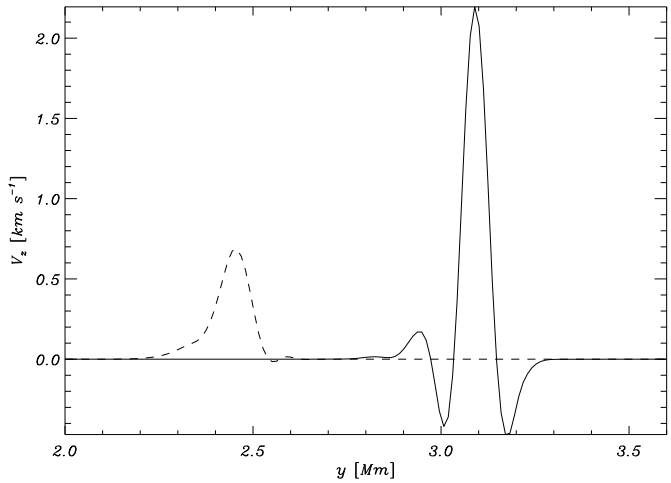

Fig. 9. Vertical profiles of $V_z(x = 1.7$ Mm, $y)$ (solid line) and $V_z(x = 2.2$ Mm, $y)$ (dashed line) at $t = 10^3$ s for $A_d = 2.28$ Gauss.

areas of highly varying Alfvén speed. As a consequence, Alfvén waves become attenuated with the attenuation time varying with the amplitude and characteristic time of the shearing. A larger shearing of magnetic field lines results in stronger linear coupling between Alfvén and magnetoacoustic waves. The kinetic energy of the latter waves increases with the amplitude of the shearing, but it remains lower than the kinetic energy of Alfvén waves (Fig. 11).

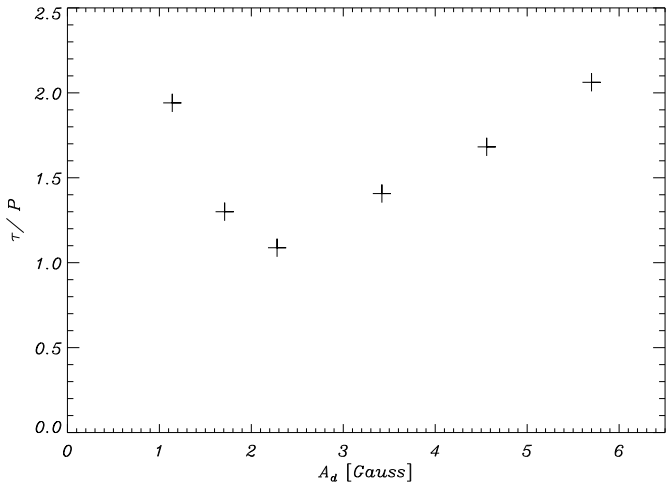

Fig. 10. Ratio of the attenuation time over wave period, τ/P, vs. the amplitude of the shearing, A_d.

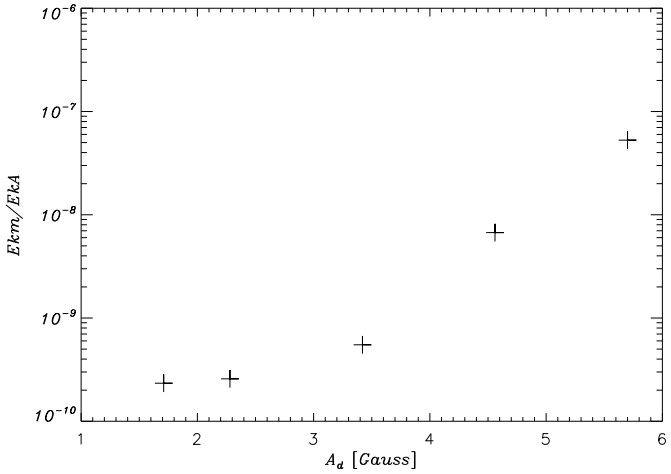

Fig. 11. Ratio of the kinetic energy of magnetoacoustic waves, *Ekm*, to the kinetic energy of Alfvén waves, *EkA*, within the simulation region at $t = 10^3$ s vs. the amplitude of the shearing, A_d.

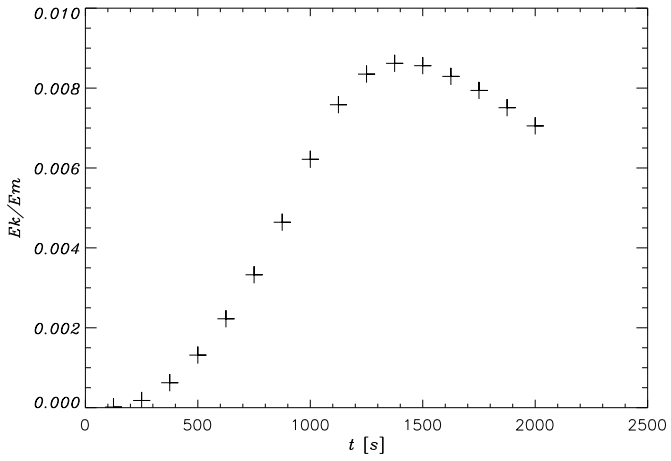

Fig. 12. Ratio of the total kinetic energy, *Ek*, to the the total magnetic energy, *Em*, within the simulation region vs. time t for $A_\mathrm{d} = 2.28$ Gauss.

Acknowledgements. The work was supported by a Marie Curie International Research Staff Exchange Scheme Fellowship within the 7th European Community Framework Program. A.S. thanks the Presidium of Russian Academy of Sciences for support in the frame of Program 9 and the Russian Foundation of Fundamental Research under the grant. The software used in this work was developed in part by the DOE-supported ASCI/Alliance Center for Astrophysical Thermonuclear Flashes at the University of Chicago. The visualizations of the simulation variables were carried out using the Interactive Data Language (IDL) software package.

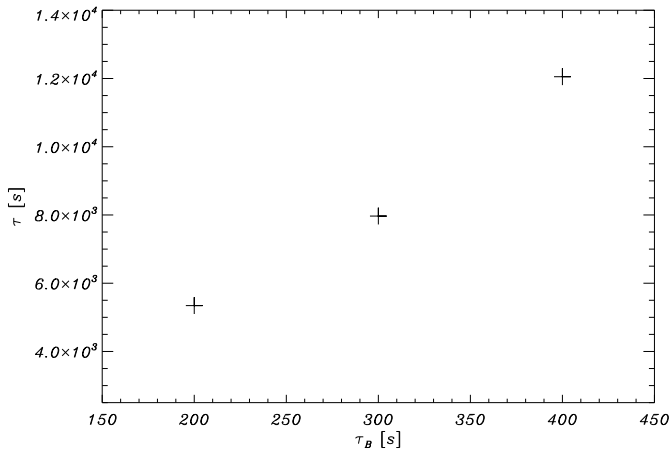

Fig. 13. Attenuation time, τ, vs. time of shearing τ_B.

References

Antiochos, S. K., & Linton, M. G. 2002, ApJ, 581, 703
Avrett, E. H., & Loeser, R. 2008, ApJS, 175, 228
Brown, D. S., & Priest, E. R. 2001, A&A, 367, 339
Bulanov, S. V., & Syrovatskii, S. I. 1980, Fiz. Plazmy., 6, 1205
Chmielewski, P., , & Murawski, K. 2014, ApJ, submitted
Chmielewski, P., Srivastava, A. K., Murawski, K., & Musielak, Z. E. 2013, MNRAS, 428, 40
Craig, I. J. D., & Litvinenko, Y. E. 2005, Phys. Plasmas, 12, 032301
Craig, I. J. D., & McClymont, A. N. 1997, ApJ, 481, 996
Fryxell, B., Olson, K., & Ricker, P. 2000, ApJS, 131, 273
Fujimura, D., & Tsuneta, S. 2009, ApJ, 702, 1443
Galsgaard, K., Priest, E. R., & Titov, V. S. 2003, J. Geophys. Res., 108, 1042
Gruszecki, M., Murawski, K., Solanki, S., & Ofman, L. 2007, A&A, 469, 1117
Hassam, A. B., & Lambert, R. P. 1996, ApJ, 472, 832
Jess, D. B., Mathioudakis, M., Erdélyi, R., et al. 2009, Science, 323, 1582
Kraśkiewicz, J., Murawski, K., Solov'ev, A., & Srivastava, A. K. 2015, Sol. Phys., submitted
Lee, D. 2013, J. Comput. Phys., 243, 269
Lee, D., & Deane, A. E. 2009, J. Comput. Phys., 228, 952
Low, B. C. 1975, ApJ, 197, 251
Low, B. C. 1980, Sol. Phys., 65, 147
Low, B. C. 1982, Sol. Phys., 75, 119
MacNeice, P., Spicer, D. S., & Antiochos, S. 1999, 8th SOHO Workshop: Plasma Dynamics and Diagnostics in the Solar Transition Region and Corona, ESA SP, 446, 457
McLaughlin, J. A., & Hood, A. W. 2004, A&A, 420, 1129
Murawski, K. 1992, Sol. Phys., 139, 279
Murawski, K., & Musielak, Z. E. 2010, A&A, 518, A37
Musielak, Z. E., Routh, S., & Hammer, R. 2007, ApJ, 659, 650
Nakariakov, V. M., & Verwichte, E. 2005, Liv. Rev. Sol. Phys., 2, 3
Nakariakov, V. M., Roberts, B., & Murawski, K. 1997, Sol. Phys., 175, 93
Nakariakov, V. M., Roberts, B., & Murawski, K. 1998, A&A, 332, 795
Pontin, D. I., & Galsgaard, K. 2007, J. Geophys. Res., 112, 3103
Priest, E. R. 1982, Solar magnetohydrodynamics (London: D. Reidel Publ. Comp.)
Shapovalov, V. N., & Shapovalova, O. V. 2003, Izvestia Vuzov. Fisika., 46, 74
Solov'ev, A. 2010, Astron. Rep., 54, 85
Tóth, G. 2000, J. Comput. Phys., 161, 605
Van Doorsselaere, T., Nakariakov, V. M., & Verwichte, E. 2008, ApJ, 676, L73
Vasheghani Farahani, S., Nakariakov, V. M., & Verwichte, E. 2012, A&A, 544, A127
Wołoszkiewicz, P., Murawski, K., Musielak, Z. E., & Mignone, A. 2014, Contr. Cyber., 43, 321
Zaqarashvili, T. V., & Murawski, K. 2007, A&A, 470, 353

The Astrophysical Journal, 866:50 (8pp), 2018 October 10 https://doi.org/10.3847/1538-4357/aadd00

Numerical Simulations of Transverse Oscillations of a Finely Structured Solar Flux Tube

Błażej Kuźma and Kris Murawski
Group of Astrophysics, University of Maria Curie-Skłodowska, ul. Radziszewskiego 10, 20-031 Lublin, Poland; blazejkuzma1@gmail.com
Received 2017 May 22; revised 2018 August 16; accepted 2018 August 24; published 2018 October 10

Abstract

In the light of recent CRISP/SST observations we aim to study transverse oscillations of a finely structured flux tube. With the use of PLUTO code, we numerically solve ideal magnetohydrodynamic equations in three-dimensional Cartesian geometry. With a pressure signal we generate a finely structured magnetic flux tube that consists of a central strand and four off-central strands. This flux tube is perturbed by a periodic driver in the azimuthal component of velocity. This driver results in transverse oscillations that propagate upward along these strands. The central strand experiences torsional Alfvén waves, while the off-central strands exhibit fast magnetoacoustic kink oscillations. The latter are guided by the off-central strands, which are regions of depression in Alfvén speed.

Key words: magnetohydrodynamics (MHD) – methods: numerical – Sun: activity – Sun: corona – Sun: transition region

1. Introduction

Much of the dynamics of the solar plasma is determined by the magnetic field, which is the key to understanding many physical processes on the Sun. The magnetic field is distributed all over the Sun in the form of very complex configurations (i.e., active regions) and simple ones (i.e., quiet Sun, coronal holes). Magnetic flux tubes with a concentrated magnetic field of about 10^3 G reside in internetwork regions. These flux tubes are the basic building blocks of the magnetic field, and are mainly present in the quiet Sun. In this era of high-resolution observations, flux tubes seem to be omnipresent in the solar chromosphere (e.g., Hansteen et al. 2006; De Pontieu et al. 2007; Rouppe van der Voort et al. 2009; Kuridze et al. 2015; Srivastava et al. 2017). The combined dynamics of the flux tubes and the solar plasma leads to the diversity of structures in the chromosphere (e.g., spicules, fibrils, mottles, jets). MHD waves are an integral part of these magnetic structures and can be studied with the help of high-resolution observations and advanced numerical simulations (e.g., De Pontieu et al. 2007; Zaqarashvili & Erdélyi 2009; Okamoto & De Pontieu 2011; Tavabi et al. 2015; Wójcik et al. 2017).

Recent observations with high spatial resolution using CRISP/SST (CRisp Imaging SpectroPolarimeter/Swedish 1 m Solar Telescope) have revealed that flux tubes are not monolithic entities in the solar atmosphere, but instead are further fragmented into very fine magnetic strands. Srivastava et al. (2017) reported for the first time that such flux tubes experience transverse oscillations with a short period (∼50 s). The authors devised a monolithic model of a flux tube to perform 3D numerical simulations of these oscillations and showed that they exhibit the potential to heat the solar corona.

The main goal of our paper is to contribute to the above studies by performing numerical simulations of a finely structured magnetic flux tube that is generated by a signal in the gas pressure and determining whether a high-frequency driver is able to induce the observed oscillations of this flux tube.

This paper is organized as follows. In Section 2, we describe the physical model of the solar atmosphere. Numerical simulations of MHD equations are presented in Section 3. A summary and conclusions of the present work are outlined in the last section.

2. Physical Model of the Solar Atmosphere

We describe the solar atmospheric plasma by the ideal, 3D MHD equations with all plasma quantities having the standard notation, the adiabatic index $\gamma = 5/3$, the mean molecular weight is 0.6, and the gravitational acceleration $\boldsymbol{g} = (0, -g, 0)$ with $g = 274\,\mathrm{m\,s^{-2}}$.

For a still atmosphere (with velocity $\boldsymbol{V} = 0$) we assume that the equilibrium magnetic field $\boldsymbol{B}$ is current-free ($\nabla \times \boldsymbol{B} = 0$) with its horizontal ($B_x$), vertical ($B_y$), and transverse ($B_z$) components given as (Low 1985; Konkol et al. 2012)

$$[B_x, B_y, B_z] = \frac{S[-3x(y-b), x^2 - 2(y-b)^2 + z^2, -3(y-b)z]}{(x^2 + (y-b)^2 + z^2)^{5/2}} + [0, B_v, 0], \quad (1)$$

where B_v denotes the magnitude of a uniform vertical magnetic field, and b and S are free parameters corresponding to the vertical location of the singularity and the magnetic field strength, respectively. We set $b = -0.2$ Mm, $B_v = 10$ G, and S in such a way that at the reference point ($x = 0$, $y = 10$, $z = 0$) Mm the magnitude of magnetic field is $B = 12.56$ G. The corresponding magnetic field lines diverge with height (Figure 1, left). Note that $B \approx 50$ G at $y \approx 2$ Mm and it declines with height until $B \approx 11$ G at $y \approx 20$ Mm (not shown).

For a current-free magnetic field, such as given by Equation (1), the equilibrium gas pressure $p_0(y)$ and mass density $\varrho_0(y)$ are hydrostatic and they are determined by the semi-empirical temperature $T(y)$ model of Avrett & Loeser (2008), which is smoothly extrapolated into the corona. In this model, the transition region is located at $y \approx 2.1$ Mm, and it separates the low-lying chromosphere from the settled corona above it. For more details see Murawski et al. (2015b).

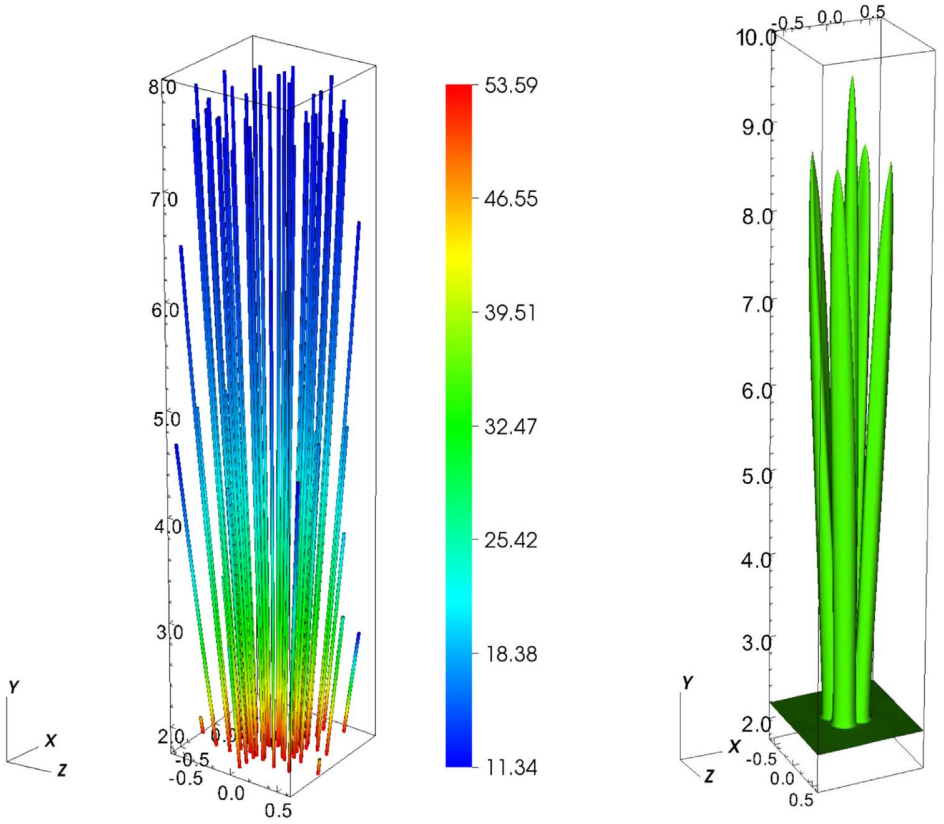

Figure 1. The equilibrium magnetic field lines (left) and isosurface of mass density $\varrho(x, y, z) = 10\,\bar{\varrho}_0$ at $t = 100$ s with $\bar{\varrho}_0 = 10^{-12}$ kg m^{-3} (right). The color map corresponds to the magnitude of the magnetic field $\boldsymbol{B}$, which is expressed in G. Only part of the simulation region is displayed.

We perturb the above-described hydrostatic equilibrium by a signal in the gas pressure,

$$p(x, y, z, t) = p_0(y) \times\left(1 + A_{\rm p}\sum_{i=1}^{5}\exp\left(-\frac{(x - x_{0_i})^2 + (y - y_0)^2 + (z - z_{0_i})^2}{w^2}\right)f(t)\right),$$
$$f(t) = \begin{cases} t/\tau, & t \leqslant \tau \\ 1, & t > \tau \end{cases}, \tag{2}$$

where (x_{0_i}, y_0, z_{0_i}), $i = 1, \ldots, 5$, are coordinates of the signal, w is its width, $A_{\rm p}$ its amplitude, and τ its growth time. In order to obtain a finely structured flux tube that would mimic the observational data of Srivastava et al. (2017), we set $x_{0_1} = 0$, $x_{0_{2,\ldots,5}} = \pm 0.1$ Mm, $y_0 = 1.75$ Mm, $z_{0_1} = 0$, $z_{0_{2,\ldots,5}} = \pm 0.1$ Mm, $w = 40$ km, and hold them fixed. To reduce the formation of transient phenomena, the pressure signal is ramped in time with the use of a temporal function $f(t)$ by setting it to grow linearly in time from 0 to 1 at $t = \tau = 5$ s and then the signal is kept constant in time.

Additionally, we set the periodic driver in the azimuthal component of velocity, written in Cartesian coordinates as

$$[V_x, V_y, V_z] = A_V\left[-\frac{z}{r}, 0, \frac{x}{r}\right] \times \exp\left(-\frac{r^2 + (y - y_0)^2}{w_d^2}\right)\sin\left(\frac{2\pi}{P_{\rm d}}t\right),$$
$$r^2 = x^2 + y^2, \tag{3}$$

where $y_0 = 1.75$ Mm is the vertical position of the driver, $A_V = 5$ km s^{-1} is the relative amplitude of the driver, and the width of the driver, $w_d = 0.5$ Mm, allows us to perturb the whole system of five strands that constitute a finely structured magnetic flux tube. The period of the driver is set as $P_{\rm d} = 50$ s, unless stated otherwise, which lies within the range of short-period oscillations detected by Srivastava et al. (2017). The drivers specified by Equations (2) and (3) may result from enhanced vorticity (i.e., swirls) associated with shear in the downdrafts at convection cell boundaries (Kitiashvili et al. 2011, 2012; Kosovichev et al. 2012); the pressure signal mimics thermal energy release while the velocity driver models a plasma twist, which may potentially originate at the reconnection site.

3. Numerical Simulations of MHD Equations

To solve MHD equations numerically, we use the PLUTO code (Mignone et al. 2007, 2012). In our problem, we set the Courant–Friedrichs–Lewy number equal to 0.3 and choose piecewise TVD WENO3 interpolation with the third-order Runge–Kutta method, which leads to third-order accuracy in space and time. Additionally, we adopt the Harten–Lax–van Leer Discontinuities (HLLD) approximate Riemann solver of Miyoshi & Kusano (2005).

We set the simulation box in (x, y, z) as $(-0.64, 0.64)$ Mm $\times$ $(1.75, 20.0)$ Mm $\times$ $(-0.64, 0.64)$ Mm, where $y = 0$ Mm denotes the bottom of the photosphere. In the numerical simulations we use a uniform grid within the region

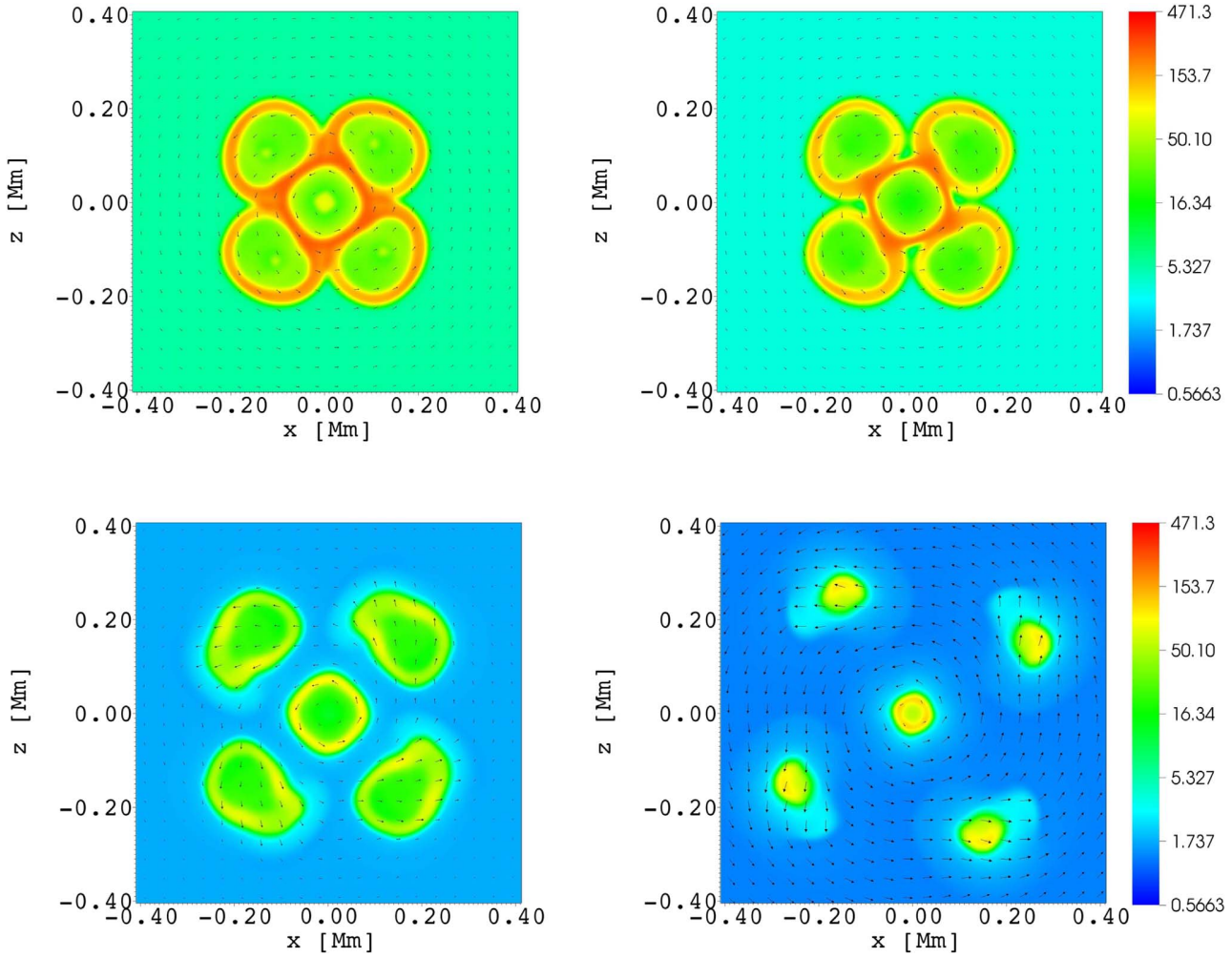

Figure 2. Horizontal profiles of $\varrho(x, y, z, t = 70\ \mathrm{s})$ drawn for $y = 2.3$ Mm, $y = 2.5$ Mm, $y = 4$ Mm, and $y = 5.5$ Mm (from top left to bottom right). Mass density is expressed in units of the coronal mass density, $\bar{\varrho}_0 = 10^{-12}\ \mathrm{kg\ m^{-3}}$. Arrows represent velocity vectors in the x–z plane, expressed in arbitrary units.

$(-0.64 \leqslant x \leqslant 0.64)$ Mm $\times$ $(1.75 \leqslant y \leqslant 4.31)$ Mm $\times$ $(-0.64 \leqslant z \leqslant 0.64)$ Mm. This region is covered by $256 \times 512 \times 256$ grid points, which lead to a resolution of 5 km there. Above this region, namely within the box $(-0.64 \leqslant x \leqslant 0.64)$ Mm $\times$ $(4.31 \leqslant y \leqslant 20.0)$ Mm $\times$ $(-0.64 \leqslant z \leqslant 0.64)$ Mm, we implemented a stretched grid along the y-direction, which is divided into 128 cells whose size grows with y.

Figure 1 (right) shows an isosurface of mass density $\varrho(x, y, z) = 10\ \bar{\varrho}_0$ at $t = 100$ s, where $\bar{\varrho}_0 = 10^{-12}\ \mathrm{kg\ m^{-3}}$ is the hydrostatic mass density at the reference point. The driver in the gas pressure, given by Equation (2), ejects cold chromospheric plasma into the low corona, above the transition region, and it generates jets in the form of five strands. As a result of the short magnetic field lines along which the signals propagate and the larger tube speed $c_\mathrm{T}(x = 0, y, z = 0)$ (not shown), with which a signal in ϱ driven by the driver of Equation (2) evolves, the central strand reaches a higher altitude than the off-central strands. Here the tube speed is $c_\mathrm{T} = c_\mathrm{S} c_\mathrm{A} / \sqrt{c_\mathrm{S}^2 + c_\mathrm{A}^2}$, where the sound speed is $c_\mathrm{S} = \sqrt{\gamma p_0 / \varrho_0}$ and the Alfvén speed is $c_\mathrm{A} = B/\sqrt{\mu \varrho_0}$.

Figure 2 illustrates the spatial distribution of $\varrho(x, y, z, t = 70\ \mathrm{s})$ at four different altitudes. At the bottom of the magnetic flux tube the strands are close to each other, creating essentially a monolithic structure. However, these strands can be distinguished because of dense shells located at their outskirts. Higher up, at $y > 2.5$ Mm, the strands begin to split. As the plasma $\beta = 2\ \mu p/B^2$ is lower than 1 (Figure 3, left) the outer strands follow the magnetic field lines that diverge with height (Figure 1, left), and the diameter of the strands varies between 100 and 250 km. These values lie within the range of the recent observational data of Srivastava et al. (2017). The central strand oscillates in the form of torsional Alfvén waves with a velocity amplitude of about $5\ \mathrm{km\ s^{-1}}$ (Figure 2). The off-central strands experience fast magnetoacoustic kink (kink, henceforth) oscillations and their amplitude grows with height. As the Alfvén speed c_A attains its local minima in the strands (Figure 3, right), the excited kink waves are trapped therein.

The regions of low Alfvén speed inside the strands can trap fast magnetoacoustic waves. Figure 3 shows the spatial profiles (in the vertical s–y plane) of β (left panel) and c_A (right panel), where s is the horizontal diagonal of the simulation box, $x = z$. As the upper sections of the strands carry rarefied plasma, $c_\mathrm{A}(s, y = \text{fixed})$ exhibits its minimum within these strands, which guide fast magnetoacoustic waves. Thus, the presence of torsional motions at the bottom of the system of strands results in transverse motions of separated off-central strands that grow with height. The small-scale vortex results from kink waves

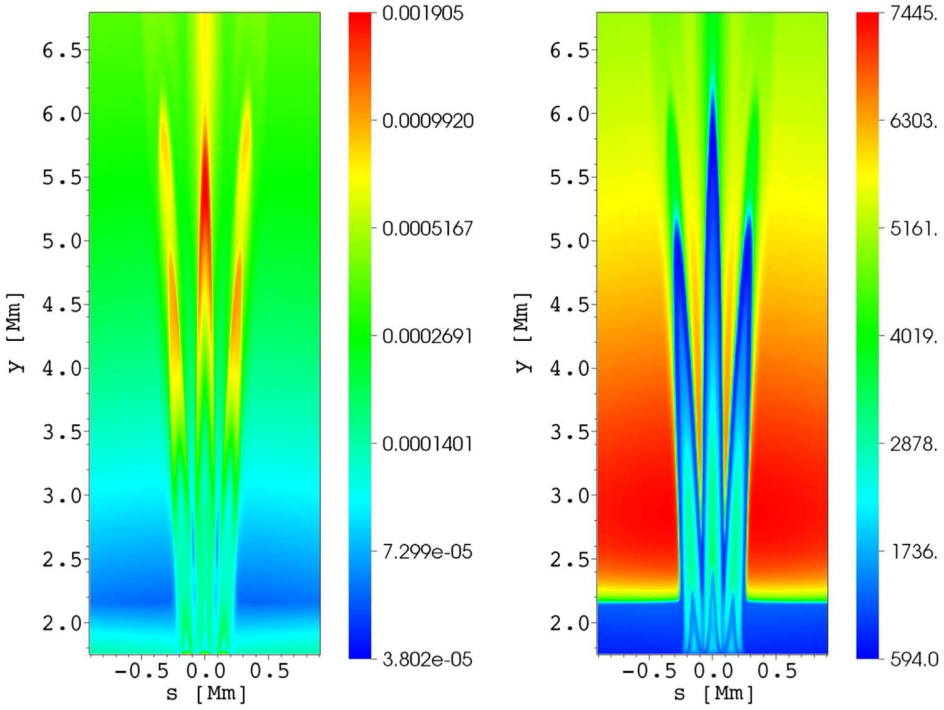

Figure 3. Spatial profile of the plasma β (left) and the Alfvén speed, $c_A(s, y)$, expressed in units of km s^{-1} (right) at $t = 70$ s.

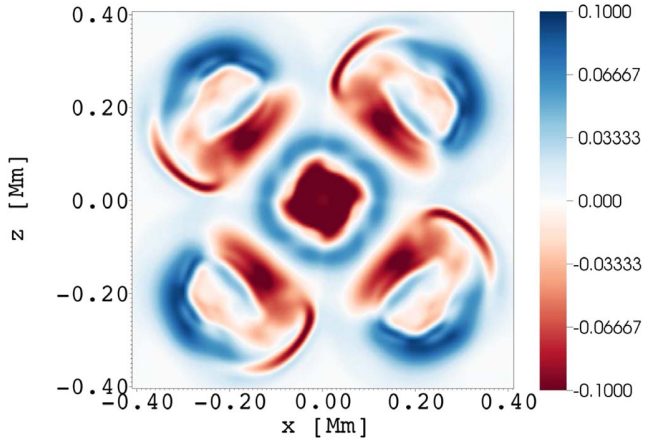

Figure 4. Vertical component of $\nabla \times \boldsymbol{V}_h(x, y = 4$ Mm, $z, t = 80$ s), where $\boldsymbol{V}_h$ is the horizontal component of $\boldsymbol{V}$.

propagating along the strands, which are clearly visible on the plot of $\nabla \times \boldsymbol{V}_h$ (Figure 4), where $\boldsymbol{V}_h$ is the horizontal velocity component.

We investigate the temporal evolution of mass density and vertical velocity. Figure 5 shows six snapshots of $\varrho(x, y = 4$ Mm, $z)$ drawn at $t = 50$ s, $t = 55$ s, $t = 60$ s, $t = 65$ s, $t = 70$ s, $t = 75$ s. Arrows represent horizontal components of velocity vectors $[V_x, V_z]$. In all strands we can see shells reported previously by Murawski et al. (2015b), which may also constitute evidence of resonant absorption as discussed by Goossens et al. (2013). A shell structure may also result from varying temperature across structures, influencing sound speed and wave propagation.

Figure 6 (top panels) illustrates the temporal evolution of the azimuthal velocity component, V_θ, in the finely structured flux tube. The left panel corresponds to transverse MHD waves in the central strand, $s = 0.02$ Mm (thus for Alfvén waves); the right panel is associated with transverse MHD waves in the off-central strand, $s = 0.25$ Mm (for kink waves). From these time–distance plots we estimate characteristic speeds of upwardly propagating waves. We find that the characteristic speed of Alfvén waves in the central strand lies in the range 420–510 km s^{-1}. The physical properties of the off-central strands change drastically in time compared to those of the central strand (see Figure 5) and result in a wide range of variations in the speed of kink waves, which extends from 10^2 to 10^3 km s^{-1}. Figure 6 (bottom panels) shows the corresponding periods of propagating Alfvén (left) and kink (right) waves. We infer that the periods of the waves excited in the upper chromosphere do not change significantly with height. As a result of the inhomogeneity of the plasma along the y-direction, few periods shorter or longer than the dominant period, $P = 50$ s, are generated in the system. For $P = 50$ s, we evaluate the wavelength, λ, of Alfvén waves to be within the range 20–25 Mm, while the wavelength of kink waves varies between 5 and 50 Mm.

The transverse MHD waves (i.e., Alfvén and kink waves) carry the energy into the upper solar atmospheric layers, which can play a significant role in the heating of the corona (e.g., Sakurai et al. 1995; Kudoh & Shibata 1999; De Pontieu et al. 2007; Dwivedi & Srivastava 2010; Sokolov et al. 2013; Murawski et al. 2015a; Murawski & Musielak 2016; Srivastava et al. 2017). Figure 7 shows spatial profiles of energy flux, $F \approx 0.5\, \varrho_0\, c_A\, V_\theta^2$, where V_θ is the velocity along the azimuthal direction, at $t = 92$ s (left) and $t = 100$ s (right). As can be seen, the strands carry an energy flux of about 10^3 W m^{-2}. At the bottom of the finely structured flux tube this flux is dominant in the central strand (left). This changes, as the energy flux in the central strand decreases significantly with height, while we do not observe such a process in the off-

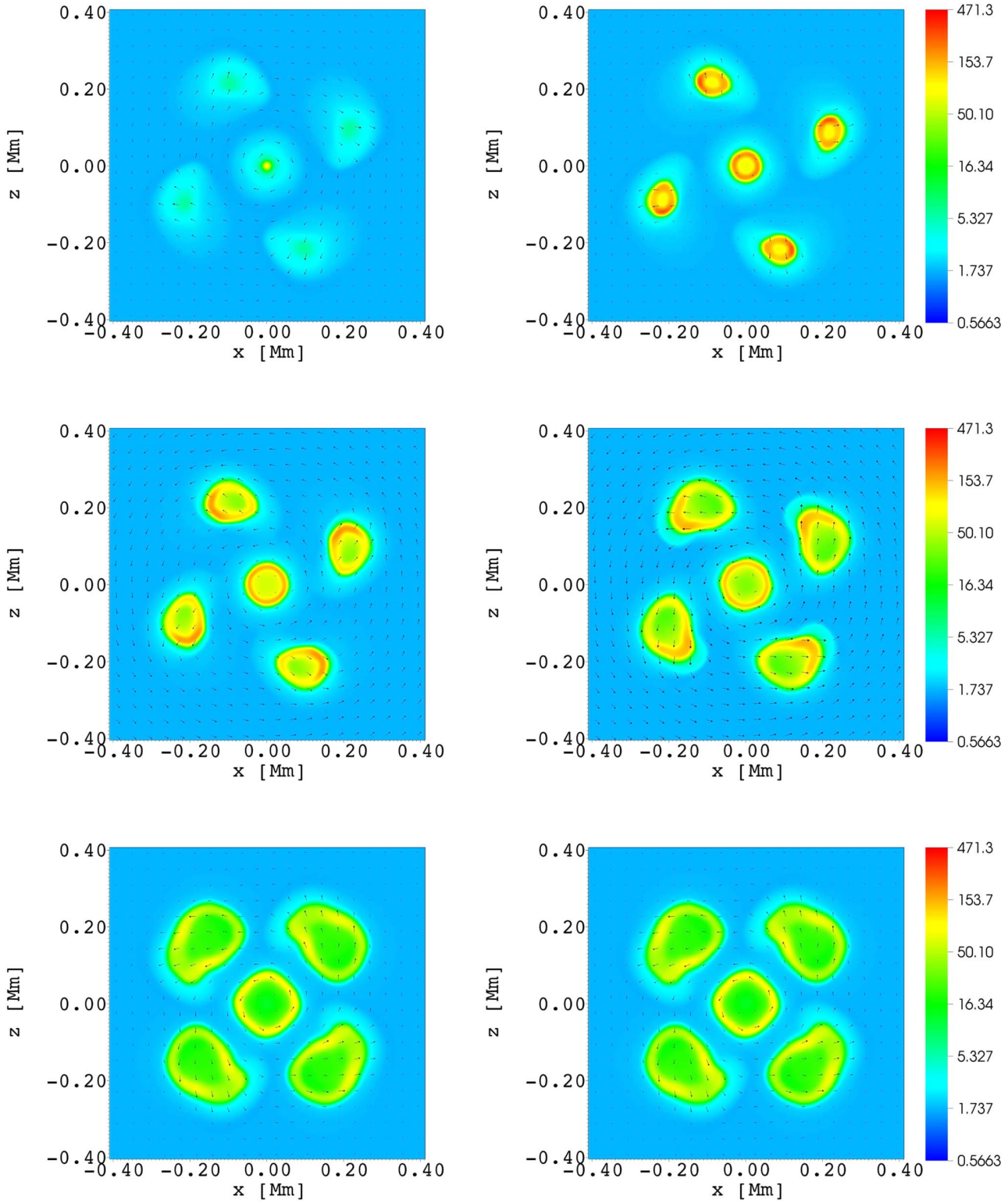

Figure 5. Spatial profiles of $\varrho(x, y = 4\,\mathrm{Mm}, z)$, expressed in units of $\bar{\varrho}_0 = 10^{-12}\,\mathrm{kg\,m^{-3}}$, and velocity vectors in the x–z plane at $t = 50$ s, $t = 55$ s, $t = 60$ s, $t = 65$ s, $t = 70$ s, $t = 75$ s (from top left to bottom right).

central strands (right). Ultimately, we conclude that in a finely structured flux tube the off-central strands, and thus kink waves, carry more energy to higher layers of the solar corona than torsional Alfvén waves. With proper dissipation mechanisms, which are absent from our model, this amount of energy can be sufficient to heat the solar corona (Withbroe & Noyes 1977).

Figure 8 illustrates the temporal evolution of energy flux along the finely structured flux tube for drivers with four different periods. In addition to newly found short-period

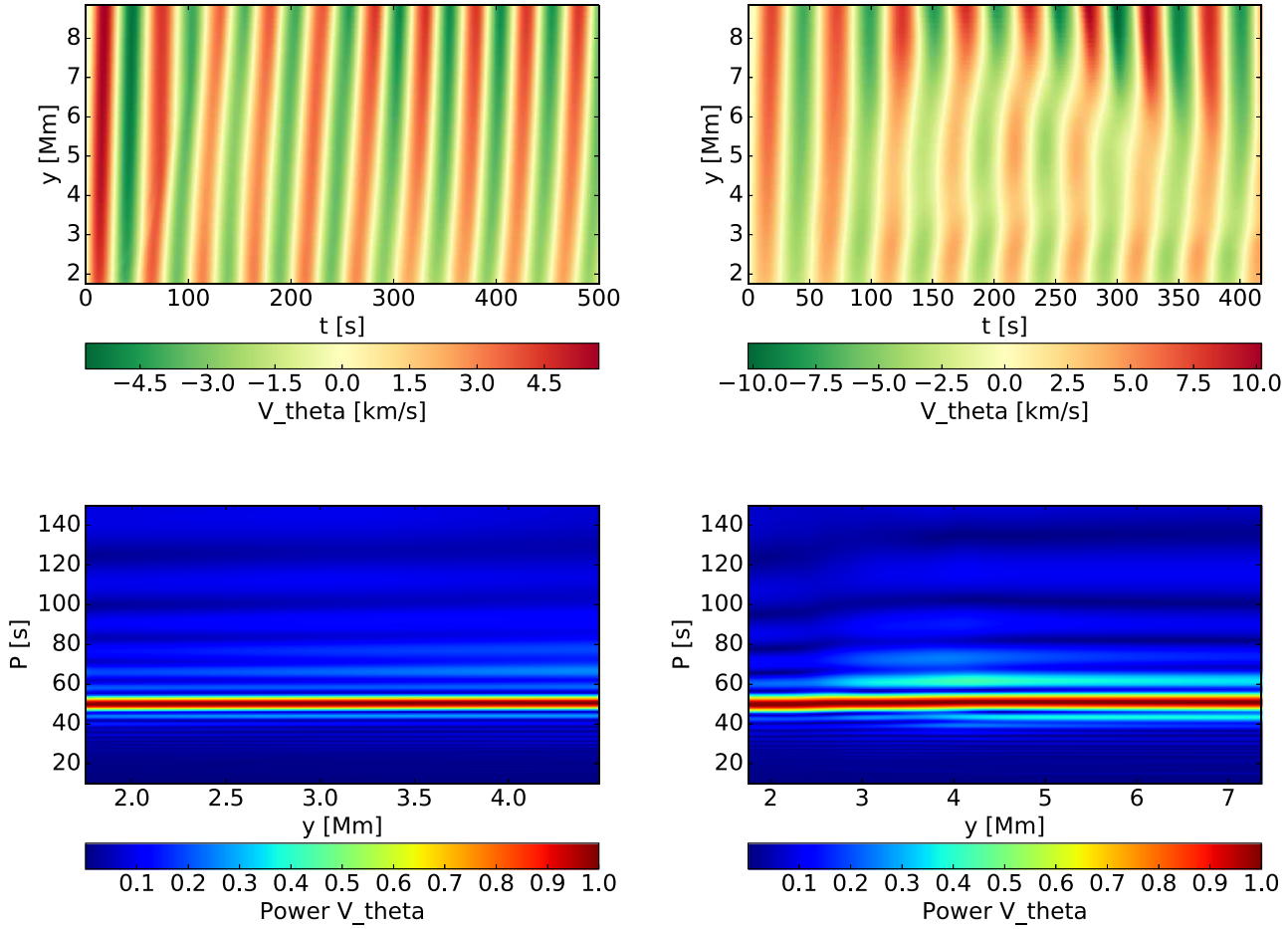

Figure 6. Time signatures of the transverse component of velocity, $V_\theta(s, y, t)$ (top), and the corresponding Fourier periodograms (bottom), in the case of the central strand, $s = 0.02$ Mm (left), and the off-central strand, $s = 0.25$ Mm (right).

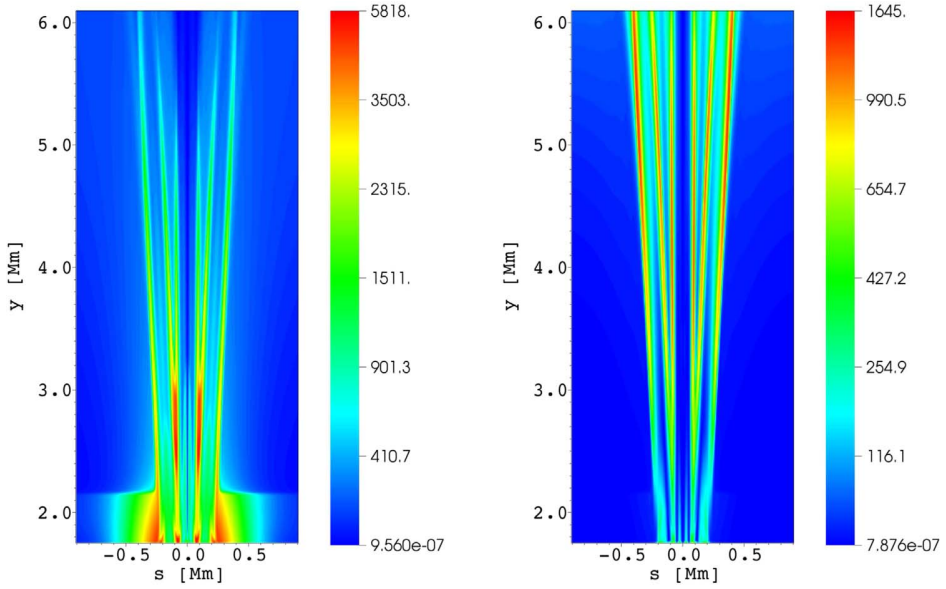

Figure 7. Spatial profiles of the energy flux, $F \approx 0.5\, \varrho_0\, c_A\, V_\theta^2$, expressed in units of W m^{-2}, at $t = 92$ s (left) and $t = 100$ s (right).

transverse oscillations ($P_d = 50$ s), we investigate Alfvén oscillations with $P_d = 126$ s (Jess et al. 2009), as well as oscillations of 3 and 5 minutes ($P_d = 180$ s and 300 s). The short-period transverse oscillations carry an energy flux of about 2.5×10^3 W m^{-2} at its maximum at the bottom of a finely structured flux tube (top left, solid line). This value

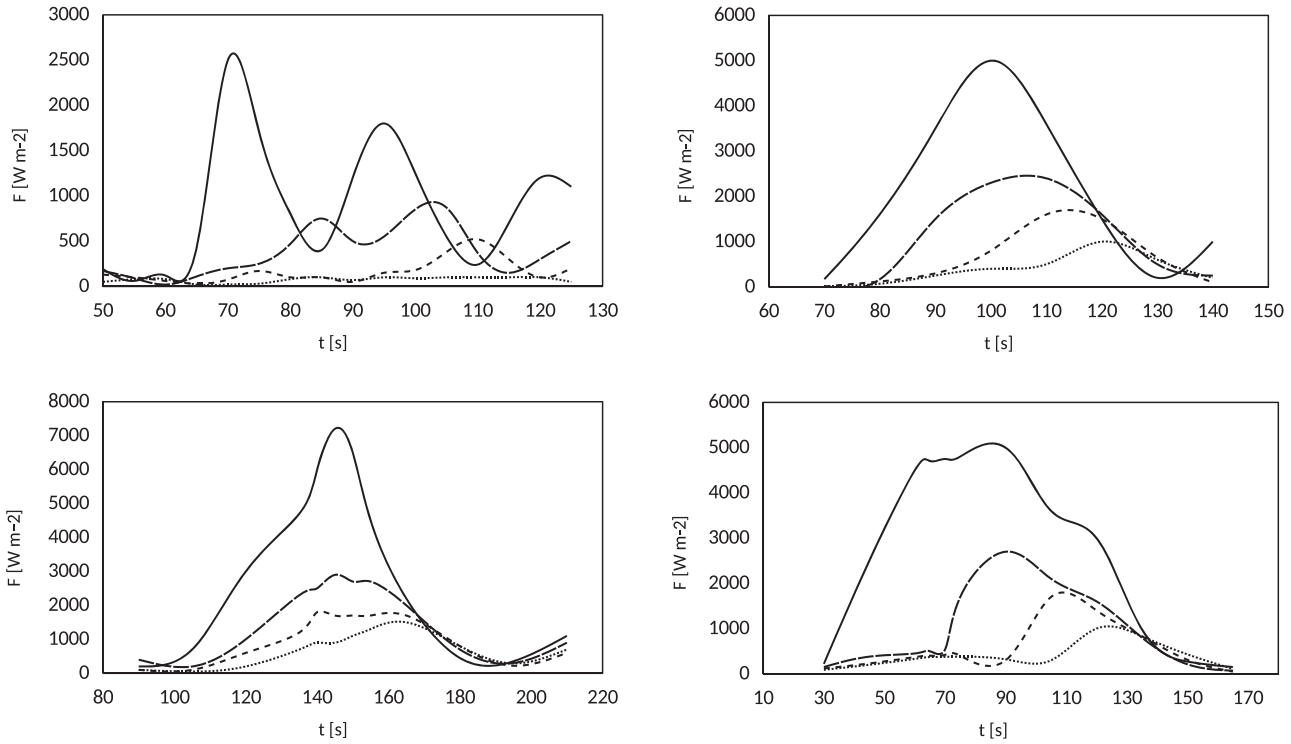

Figure 8. Temporal evolution of the energy flux, $F \approx 0.5\ \varrho_0\ c_A\ V_\theta^2$, expressed in units of W m^{-2}, at $y = 3$ Mm (solid line), $y = 5$ Mm (long-dashed line), $y = 7$ Mm (short-dashed line), and $y = 9$ Mm (dotted line), in the case of $P_d = 50$ s, $P_d = 126$ s, $P_d = 180$ s, and $P_d = 300$ s (from top left to bottom right).

decreases in subsequent periods due to expansion and ongoing rarefaction of strands in time. It also falls off significantly with height (top left, long-dashed and short-dashed lines). At a height of $y = 9$ Mm it attains a negligibly small value below 10^2 W m^{-2} (top left, dotted line). Longer-period waves carry energy more efficiently to the higher layers of the solar corona (top right and bottom). It is noteworthy that minimum energy losses correspond to oscillations of 3 minutes. The obtained results reveal that the short-period transverse oscillations decay quickly with height, while longer-period oscillations effectively propagate above the altitude of $y = 9$ Mm.

In conclusion, we infer that the finely structured flux tubes can effectively guide both kink and Alfvén waves, and a substantial part of their energy flux is carried to upper layers of the solar corona.

4. Summary

It was recently discovered that magnetic flux tubes in the quiet Sun consist of fine strands along with the presence of transverse waves (Srivastava et al. 2017). To understand the wave dynamics of a finely structured magnetic flux tube a monolithic flux tube was used in the numerical simulations of Srivastava et al. (2017). In the present simulations, we have produced a finely structured flux tube, which consists of five strands—one central and four off-central—to mimic the observed flux tube of Srivastava et al. (2017), and we have investigated its associated wave dynamics.

A flux tube of moderate strength, which mimics a typical quiet-Sun flux tube, has been used to produce the fine strands. These strands form when the denser chromospheric plasma fills in the magnetic fine structures. We have launched pulses in gas pressure at five different spatial positions to reproduce five strands (one central and four off-centrally located) of the flux tube. We have performed numerical simulations of transverse waves in this finely structured flux tube. Various kinds of dynamics are present near the flux tubes in the solar photosphere (convective flows, horizontal flows, granular buffeting), which may participate in the generation of various MHD waves in these flux tubes (e.g., Murawski et al. 2015a; 2015b). The amplitude of the physical driver (i.e., rotation in the azimuthal component of velocity) is large close to the center of the flux tube; it decreases toward the outward directions. Therefore, the central strand experiences more rotation in the form of torsional Alfvén waves, while the four off-centrally located strands, being regions of depression in the Alfvén speed, guide fast magnetoacoustic kink oscillations. Both the Alfvén and fast magnetoacoustic kink oscillations are driven by a periodic driver in the azimuthal component of velocity, which operates about 350 km below the transition region. These kink oscillations carry energy into the solar corona; the major contribution results from Alfvén waves.

Finally, we conclude that our numerical model successfully reproduces the fine strands within a flux tube along with associated wave dynamics. MHD waves in a finely structured magnetic flux tube depend completely on the nature of their physical drivers (i.e., vortex motion, granular buffeting, horizontal flow, etc.).

The authors express their thanks to the referee for stimulating comments, to Dr. Pradeep Kayshap for a few discussions, and to Dr. Piotr Konkol for his assistance in setting the PLUTO code for this project. This work was done in the framework of the project from the National Science Centre, Poland (NCN), Grant No. 2014/15/B/ST9/00106. Numerical simulations were performed on the LUNAR/SOLARIS cluster at Institute of Mathematics of University of M. Curie-Skłodowska, Lublin, Poland.

ORCID iDs

Kris Murawski https://orcid.org/0000-0002-0184-2117

References

Avrett, E. H., & Loeser, R. 2008, ApJS, 175, 228
De Pontieu, B., McIntosh, S. W., Hansteen, V. H., et al. 2007, PASJ, 59, S655
Dwivedi, B. N., & Srivastava, A. K. 2010, CSci, 98, 295
Goossens, M., Van Doorsselaere, T., Soler, R., et al. 2013, ApJ, 768, 191
Hansteen, V. H., De Pontieu, B., Rouppe van der Voort, L., van Noort, M., & Carlsson, M. 2006, ApJL, 647, L73
Jess, D. B., Mathioudakis, M., Erdélyi, R., et al. 2009, Sci, 323, 1582
Kitiashvili, I. N., Kosovichev, A. G., Mansour, N. N., & Wray, A. A. 2011, ApJ, 727, 50
Kitiashvili, I. N., Kosovichev, A. G., Lele, S. K., Mansour, N. N., & Wray, A. A. 2012, in SDO-4: Dynamics and Energetics of the Coupled Solar Atmosphere. The Synergy Between State-of-the-art Observations and Numerical Simulations, 96
Konkol, P., Murawski, K., & Zaqarashvili, T. V. 2012, A&A, 537, A96
Kosovichev, A., Kitiashvili, I. N., Mitra-Kraev, U., & Sekii, T. 2012, in SDO-4: Dynamics and Energetics of the Coupled Solar Atmosphere. The Synergy Between State-of-the-art Observations and Numerical Simulations, 97
Kudoh, T., & Shibata, K. 1999, ApJ, 514, 493
Kuridze, D., Henriques, V., Mathioudakis, M., et al. 2015, ApJ, 802, 26
Low, B. C. 1985, ApJ, 293, 31
Mignone, A., Bodo, G., Massaglia, S., et al. 2007, ApJS, 170, 228
Mignone, A., Zanni, C., Tzeferacos, P., et al. 2012, ApJS, 198, 7
Miyoshi, T., & Kusano, K. 2005, JCP, 208, 315
Murawski, K., & Musielak, Z. E. 2016, MNRAS, 463, 4433
Murawski, K., Solovev, A., & Kraśkiewicz, J. 2015a, SoPh, 290, 1909
Murawski, K., Solovev, A., Musielak, Z. E., Srivastava, A. K., & Kraśkiewicz, J. 2015b, A&A, 577, A126
Okamoto, T. J., & De Pontieu, B. 2011, ApJL, 736, L24
Rouppe van der Voort, L. H. M., Leenaarts, J., De Pontieu, B., Carlsson, M., & Vissers, G. 2009, ApJ, 705, 272
Sakurai, T., Kitayama, O., & Ma, J. 1995, GApFD, 79, 277
Sokolov, I. V., van der Holst, B., Oran, R., et al. 2013, ApJ, 764, 23
Srivastava, A. K., Shetye, J., Murawski, K., et al. 2017, NatSR, 7, 43147
Tavabi, E., Ajabshirizadeh, A., Ahangarzadeh Maralani, A. R., & Zeighami, S. 2015, JApA, 36, 307
Withbroe, G. L., & Noyes, R. W. 1977, ARA&A, 15, 363
Wójcik, D., Murawski, K., Musielak, Z. E., Konkol, P., & Mignone, A. 2017, SoPh, 292, 31
Zaqarashvili, T. V., & Erdélyi, R. 2009, SSRv, 149, 355

The Astrophysical Journal, 878:81 (6pp), 2019 June 20 https://doi.org/10.3847/1538-4357/ab1b4a

Heating of a Quiet Region of the Solar Chromosphere by Ion and Neutral Acoustic Waves

B. Kuźma, D. Wójcik, and K. Murawski
Group of Astrophysics, Institute of Physics, University of M. Curie-Skłodowska, ul. Radziszewskiego 10, 20-031 Lublin, Poland
Received 2019 January 30; revised 2019 April 3; accepted 2019 April 20; published 2019 June 17

Abstract

Using high-resolution numerical simulations we investigate the plasma heating driven by periodic two-fluid acoustic waves that originate at the bottom of the photosphere and propagate into the gravitationally stratified and partially ionized solar atmosphere. We consider ions+electrons and neutrals as separate fluids that interact between themselves via collision forces. The latter play an important role in the chromosphere, leading to significant damping of short-period waves. Long-period waves do not essentially alter the photospheric temperatures, but they exhibit the capability of depositing a part of their energy in the chromosphere. This results in up about a five times increase of ion temperature that takes place there on a timescale of a few minutes. The most effective heating corresponds to waveperiods within the range of about 30–200 s with a peak value located at 80 s. However, we conclude that for the amplitude of the driver chosen to be equal to 0.1 km s^{-1}, this heating is too low to balance the radiative losses in the chromosphere.

Key words: methods: numerical – Sun: activity – Sun: chromosphere – Sun: transition region

1. Introduction

One of the main open questions of solar physics is energy transport from the photosphere to the chromosphere and further up to the corona. It is well known that chromospheric plasma radiates more than that of the corona, thus an additional source of chromospheric heating is required (e.g., Narain & Ulmschneider 1996). The photosphere is fulfilled by a wide range of oscillations and is considered a main source of waves in the solar atmosphere. Among others, the excited acoustic waves propagate into upper, quiet, and essentially magnetic-free atmospheric regions (e.g., Nakariakov & Verwichte 2005). So far, wave processes have been investigated mainly within the framework of magnetohydrodynamics, which is a good model for a fully ionized plasma. However, the photospheric and chromospheric plasma are only partially ionized and neutrals play an important role in their dynamics (e.g., Zaqarashvili et al. 2011). The ion–neutral collisions can lead to a range of phenomena, such as, for instance, wave damping (e.g., Piddington 1956; Watanabe 1961; Kulsrud & Pearce 1969; Haerendel 1992; De Pontieu & Haerendel 1998; James & Erdélyi 2002; Erdélyi & James 2004; Khodachenko et al. 2004; Forteza et al. 2007).

The idea that acoustic waves can heat the solar atmosphere was developed by Bierman (1946) and Schwarzschild (1948), who originally proposed that acoustic waves can be the main heating agents of the chromosphere, with wavefront steepening with height and dissipation in shocks in the chromosphere being considered the main mechanisms behind plasma heating. Later on, the problem of chromospheric heating by acoustic waves was investigated widely. For instance, Carlsson & Stein (1995) questioned the average plasma temperature growth in the acoustically heated chromosphere. Fossum & Carlsson (2005, 2006) performed numerical simulations of high-frequency acoustic waves and concluded that they are not sufficient to heat the chromosphere. On the other hand, Ulmschneider & Musielak (2003) stated that acoustic waves are the main source of heating in non-magnetic regions of the chromosphere and Cuntz et al. (2007) provided significant evidence that this heating can be locally dominant. Using two-fluid numerical simulations, Maneva et al. (2017) showed that magnetoacoustic waves, while propagating through the gravitationally stratified medium of the chromosphere, lead to alterations in plasma temperature.

We aim to contribute to the investigations mentioned above by performing novel and high-resolution two-fluid simulations of acoustic waves propagating in the solar atmosphere and to quantify the amount of heating occurring in the chromosphere. This paper is organized as follows. In Section 2, we describe the physical model of the solar atmosphere. Numerical simulations are presented in Section 3. A summary and conclusions are presented in the last section.

2. Physical Model

Here we describe the physical model of the solar atmosphere we employed. In particular, we consider a gravitationally stratified and partially ionized solar atmosphere. With the use of a realistic height-dependent temperature profile of the semi-empirical model of Avrett & Loeser (2008), we determine uniquely the equilibrium mass density and gas pressure profiles that fall off with height. To describe chromospheric plasma we adopt the set of equations for two fluids, mainly for ions +electrons and neutrals, with the contribution of both species depending on local ionization level. These two-fluid equations were derived by a number of authors (e.g., Smith & Sakai 2008; Zaqarashvili et al. 2011; Meier & Shumlak 2012; Soler et al. 2013; Ballester et al. 2018, and references therein). They were implemented into the JOANNA code (Wójcik 2017), which was recently used by Kuźma et al. (2017) and Srivastava et al. (2018) to simulate two-fluid jets and by Wójcik et al. (2018) to study two-fluid acoustic cutoff periods. In our model we assume initial thermal balance between ion and neutral components of plasma, $T_{\rm i} = T_{\rm n} = T_0$ (Oliver et al. 2016), and neglect all electron components due to the small mass of electrons in relation to ions and neutrals. Note that the subscripts $_{\rm i}$ and $_{\rm n}$ correspond to ions (protons) and neutrals (hydrogen atoms), respectively. See also Section 3 of Wójcik

et al. (2018) for an extended discussion on two-fluid hydrostatic equilibrium.

The two-fluid equations are taken from Zaqarashvili et al. (2011), with the exception for the heat production terms in the total energy equations that result from ion–neutral collisions. These terms are written here in similar (but generalized here for the solar mean atomic masses) form as in Oliver et al. (2016). See also Wójcik et al. (2018). Thus, ion and neutral components of plasma are governed by the following set of equations:

$$\frac{\partial \varrho_{\rm i}}{\partial t} + \nabla \cdot (\varrho_{\rm i} \boldsymbol{V}_{\rm i}) = 0, \tag{1}$$

$$\frac{\partial \varrho_{\rm n}}{\partial t} + \nabla \cdot (\varrho_{\rm n} \boldsymbol{V}_{\rm n}) = 0, \tag{2}$$

$$\varrho_{\rm i}\left[\frac{\partial \boldsymbol{V}_{\rm i}}{\partial t} + (\boldsymbol{V}_{\rm i} \cdot \nabla)\boldsymbol{V}_{\rm i}\right] = -\nabla p_{\rm ie} + \varrho_{\rm i}\boldsymbol{g} - \alpha_{\rm in}(\boldsymbol{V}_{\rm i} - \boldsymbol{V}_{\rm n}), \tag{3}$$

$$\varrho_{\rm n}\left[\frac{\partial \boldsymbol{V}_{\rm n}}{\partial t} + (\boldsymbol{V}_{\rm n} \cdot \nabla)\boldsymbol{V}_{\rm n}\right] = -\nabla p_{\rm n} + \varrho_{\rm n}\boldsymbol{g} + \alpha_{\rm in}(\boldsymbol{V}_{\rm i} - \boldsymbol{V}_{\rm n}), \tag{4}$$

$$\frac{\partial E_{\rm i}}{\partial t} + \nabla \cdot ((E_{\rm i} + p_{\rm ie})\boldsymbol{V}_{\rm i}) = -\alpha_{\rm in}\boldsymbol{V}_{\rm i}(\boldsymbol{V}_{\rm i} - \boldsymbol{V}_{\rm n}) + Q_{\rm i}^{\rm in} + \varrho_{\rm i}\boldsymbol{g} \cdot \boldsymbol{V}_{\rm i}, \tag{5}$$

$$\frac{\partial E_{\rm n}}{\partial t} + \nabla \cdot ((E_{\rm n} + p_{\rm n})\boldsymbol{V}_{\rm n}) = \alpha_{\rm in}\boldsymbol{V}_{\rm n}(\boldsymbol{V}_{\rm i} - \boldsymbol{V}_{\rm n}) + Q_{\rm n}^{\rm in} + \varrho_{\rm n}\boldsymbol{g} \cdot \boldsymbol{V}_{\rm n}, \tag{6}$$

$$Q_{\rm i}^{\rm in} = \alpha_c\left[\frac{1}{2}|\boldsymbol{V}_{\rm i} - \boldsymbol{V}_{\rm n}|^2 + \frac{3k_{\rm B}}{m_{\rm H}(\mu_{\rm i} + \mu_{\rm n})}(T_{\rm n} - T_{\rm i})\right], \tag{7}$$

$$Q_{\rm n}^{\rm in} = \alpha_c\left[\frac{1}{2}|\boldsymbol{V}_{\rm i} - \boldsymbol{V}_{\rm n}|^2 + \frac{3k_{\rm B}}{m_{\rm H}(\mu_{\rm i} + \mu_{\rm n})}(T_{\rm i} - T_{\rm n})\right]. \tag{8}$$

These equations are supplemented by the ideal gas laws as

$$p_{\rm n} = \frac{k_{\rm B}}{m_{\rm H}\,\mu_{\rm n}}\varrho_{\rm n}T_{\rm n}, \quad p_{\rm i} = \frac{2k_{\rm B}}{m_{\rm H}\,\mu_{\rm i}}\varrho_{\rm i}T_{\rm i}. \tag{9}$$

Here $E_{\rm i}$ and $E_{\rm n}$ are, respectively, ion and neutral energy densities:

$$E_{\rm i} = \frac{p_{\rm ie}}{\gamma - 1} + \frac{1}{2}\varrho_{\rm i}\boldsymbol{V}_{\rm i}^2, \quad E_{\rm n} = \frac{p_{\rm n}}{\gamma - 1} + \frac{1}{2}\varrho_n\boldsymbol{V}_{\rm n}^2, \tag{10}$$

where $\gamma = 5/3$ is the ratio of specific heats, $\alpha_{\rm in}$ and $\alpha_{\rm ni}$ are friction coefficients between ions and neutrals, $\mu_{\rm i}$ and $\mu_{\rm n}$ are mean atomic masses of, respectively, ions and neutrals, which are taken from the solar abundance model (e.g., Vögler et al. 2005), t is time, $k_{\rm B}$ is the Boltzmann constant, $m_{\rm H}$ is hydrogen mass, and $T_{\rm i}$ and $T_{\rm n}$ are temperatures of, respectively, ions and neutrals, $\boldsymbol{V}_{\rm i}$ and $\boldsymbol{V}_{\rm n}$ are their corresponding velocities, and $_{\rm pi}$ and $p_{\rm n}$ are gas pressures. A constant solar gravity of magnitude $g = 274.78\ {\rm m\ s^{-1}}$ points in the negative y-direction. To estimate $\alpha_{\rm in}$, we use the formula provided by Braginskii (1965), with the collisional cross section taken as the quantum-mechanical from Vranjes & Krstic (2013), who showed that the classical hard-sphere model may lead to underestimation of the cross-section values; they also derived from the quantum-mechanical model the integral cross section $\sigma_{\rm in}$ for ions (protons) collisions with neutrals (neutral hydrogen atoms). For typical chromospheric plasma temperature in the range of (6–10) $\times$ 10^3 K this cross section is equal to 1.89 $\times$ 10^{-18} m^2, that is, about three orders of magnitude larger than that in the hard-sphere model. Following Zaqarashvili et al. (2011), we assumed $\alpha_{\rm in} = \alpha_{\rm ni}$. However, the ion–neutral collision frequency differs from the neutral–ion collision frequency (Ballester et al. 2018).

At the bottom of the photosphere, given by $y = 0$, we set the periodic driver in the vertical component of ion and neutral velocities, i.e.,

$$V_{{\rm i},ny}(y, t) = V_0 \sin\left(\frac{2\pi t}{P_{\rm d}}\right), \tag{11}$$

where V_0 is the amplitude of the driver and $P_{\rm d}$ its period. This driver excites upwardly propagating ion and neutral acoustic waves (e.g., Zaqarashvili et al. 2011). We set $V_0 = 0.1\ {\rm km\ s^{-1}}$, but allow $P_{\rm d}$ to vary within the range of $5\ {\rm s} \leqslant P_{\rm d} \leqslant 300\ {\rm s}$. These values fit to the typical characteristics of flow associated with the solar granulation (e.g., Musielak et al. 1994; Hirzberger 2003). Among others, Tu & Song (2013) and Arber et al. (2016) determined the amplitude of Alfvén waves with the use of a piecewise power law. Thus, more realistic ways of implementing the amplitude V_0 are possible.

3. Numerical Results

We solve the two-fluid system of equations numerically using the JOANNA code (Wójcik 2017). In our problem, we set the Courant–Friedrichs–Lewy number (Courant et al. 1928) equal to 0.8 and adopt WENO3 with HLLD Riemann solver (Miyoshi et al. 2010). Typically, our one-dimensional numerical box covers the region between the bottom of the photosphere ($y = 0$ Mm) and the low corona ($y = 2.5$ Mm), and by default it is represented by 25 $\times$ 10^3 identical numerical cells. This results in the uniform spatial grid of size $\Delta y = 100$ m. Above this region, namely for 2.5 Mm $< y <$ 30 Mm, we stretch the grid, dividing it into 128 cells who size increase with height. As short-waveperiod waves require very a fine spatial resolution, we refine our spatial grid for shorter $P_{\rm d}$.

We investigate the impact of acoustic waves propagating through the photosphere and chromosphere on plasma heating. Figure 1 shows the vertical profile of $V_{\rm iy}$ (solid line) and $V_{\rm ny}$ (dashed line) drawn at $t = 10^4$ s for $P_{\rm d} = 5$ s (top) and the zoomed in regions in the photosphere (panel (a)) and upper chromosphere (panel (b)). In the photosphere, where ions and neutrals are strongly coupled, both $V_{\rm iy}$ and $V_{\rm ny}$ essentially overlap each other (panel (a)). Higher up, in the chromosphere and upper chromosphere, where ions and neutrals start to decouple, the difference between ion and neutral wavefront positions is clearly seen. We infer that the amplitudes of the excited ion and neutral acoustic waves are essentially not affected by ion–neutral collisions in the photosphere. However, higher up, the amplitude grows e-times with the pressure-scale height, while waves steepen into shocks.

From Equations (7) and (8) we infer that the velocity difference between ions and neutrals, $\delta V_y = V_{\rm iy} - V_{\rm ny}$, plays a role in plasma heating associated with propagating acoustic waves. Figure 2 illustrates $\delta V_y(y)$ for the driving period $P_{\rm d} = 5$ s at $t = 10^4$ s. At the bottom of the photosphere both

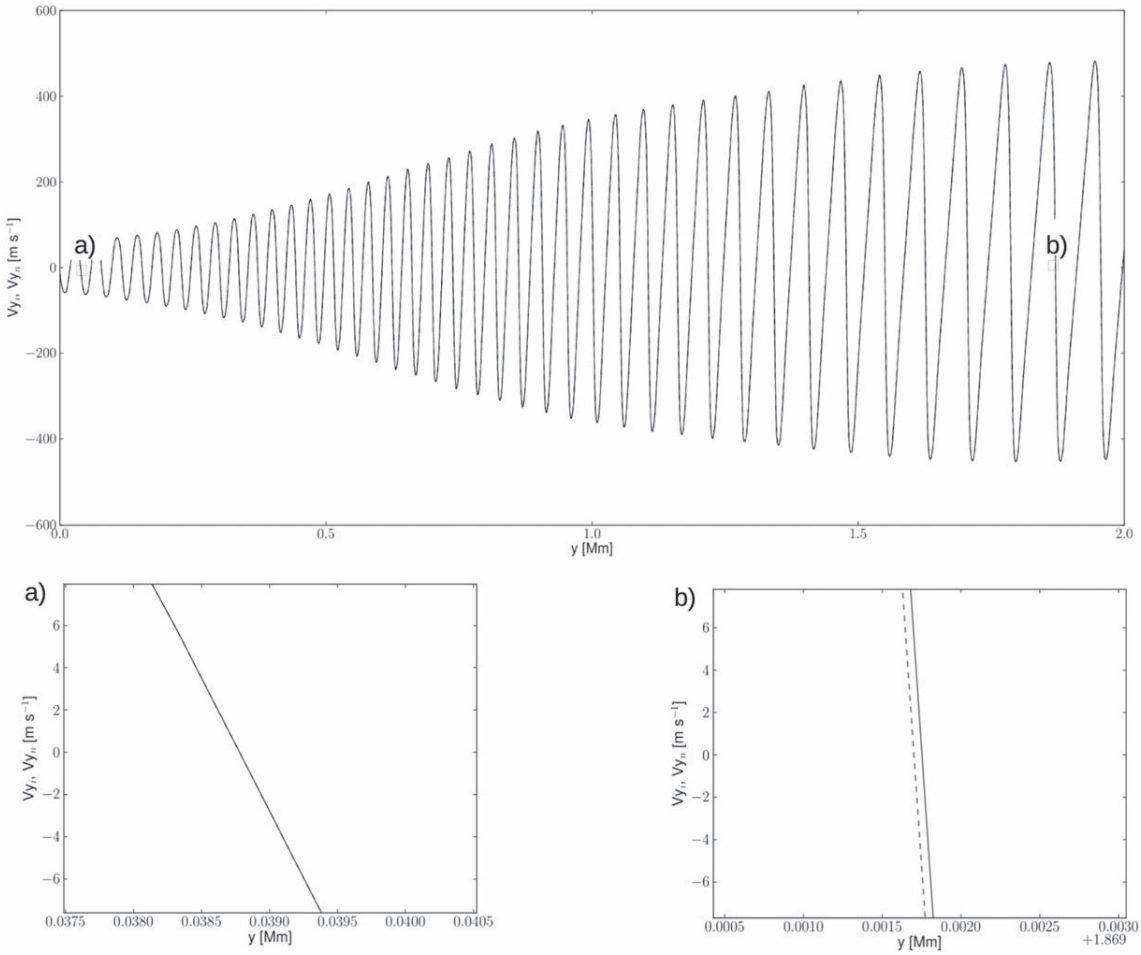

Figure 1. Vertical components of ion, V_{iy}, (solid) and neutral, V_{ny}, (dashed) velocities vs. height, y, drawn at time $t = 10^4$ s for $P_d = 5$ s. The bottom panels show zoomed in regions (a) and (b).

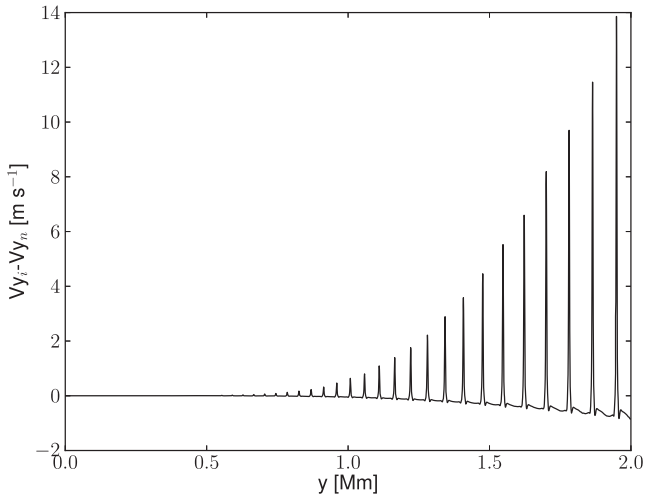

Figure 2. Difference between vertical components of ion (V_{iy}) and neutral (V_{ny}) velocities vs. height, y, at $t = 10^4$ s for $P_d = 5$ s.

ions and neutrals remain strongly coupled, therefore they propagate with essentially the same velocity. The difference between ion and neutral velocities grows with height, reaching a magnitude of about 14 m s^{-1} at the transition region, which is located at $y \approx 2.1$ Mm. Because at higher altitudes, the acoustic wave profiles steepen into shocks, these differences are present at these shocks and they result from the structured nature of shocks in a two-fluid regime (Hillier et al. 2016), which is clearly seen in Figure 1 (top and panel (b)).

Figure 3 shows the temporal and spatial evolution of relatively perturbed temperatures of ions, $\delta T_i/T_i = (T_i - T_0)/T_0$, where $T_0(y)$ is the hydrostatic temperature (Avrett & Loeser 2008). The low-period waves, mainly of $P_d = 5$ s, are significantly damped with height (top left), and this damping results from ion–neutral collisions. It is expected, as oscillation periods are larger than ion–neutral collision times, that the damping efficiency will decrease and e-times growth of the wave amplitude with a pressure-scale height takes a leading role. During the damping process the energy carried by shocking acoustic waves is dissipated in the upper photosphere and lower chromosphere. For $P_d = 5$ s, the increase of the initial temperature is up to 16% on a timescale of 10^3 s, and the heating occurs mainly from the level $y = 0.6$ Mm up to $y = 0.8$ Mm and from $y = 1.1$ Mm up to $y = 1.4$ Mm.

According to linear theory (e.g., Zaqarashvili et al. 2011), acoustic waves with longer periods, which thus have oscillation frequencies that are much lower than ion–neutral collision frequencies, are weakly damped and they possess the capability to propagate upward, reaching upper atmospheric regions if their periods are lower than cutoff periods (Wójcik et al. 2018).

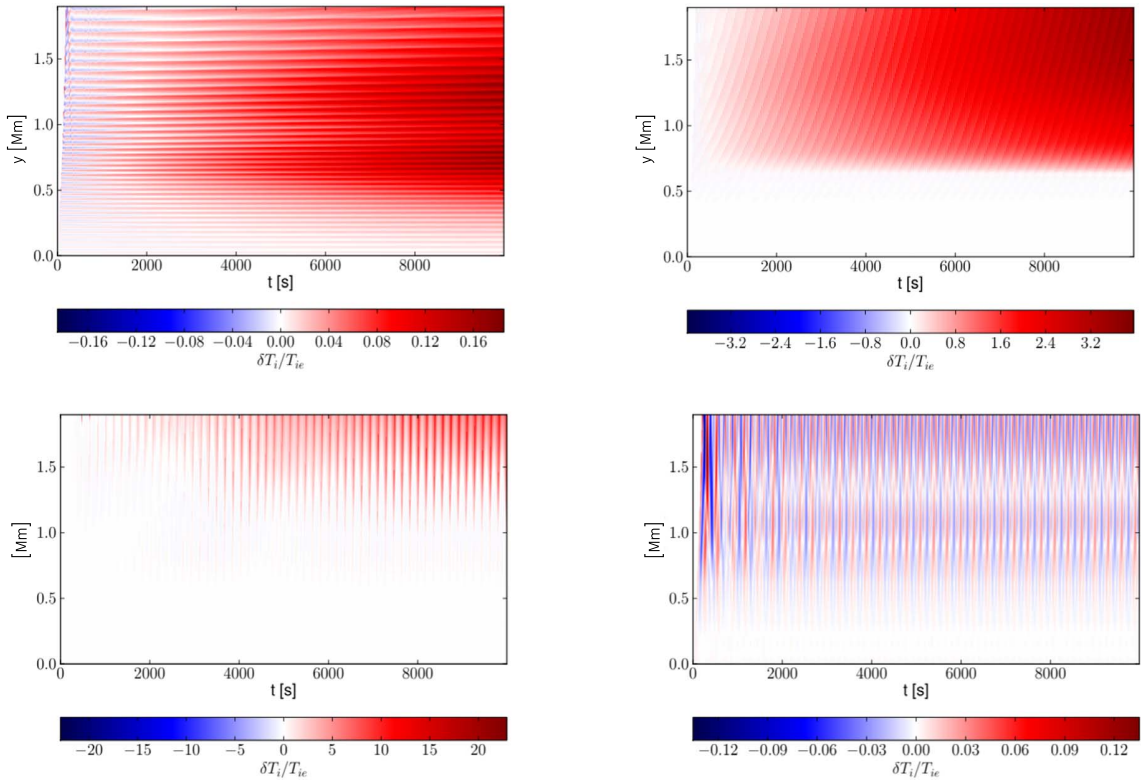

Figure 3. Time–distance plots of relative perturbed temperature of ions, $\delta T_i/T_i$, in the case of the driving period $P_d = 5$ s, $P_d = 30$ s, $P_d = 180$ s, and $P_d = 300$ s (from top left to bottom right).

Wave amplitude growth with height is a dominant factor over the wave amplitude damping resulting from ion–neutral collisions. As a result, the wave amplitude experiences a net growth with height and linear theory is too approximate.

The top right panel of Figure 3 corresponds to $P_d = 30$ s. Acoustic waves deposit their energy mainly in the chromosphere, at the height of $y > 0.5$ Mm. The waves propagate higher up. However, as the damping depends on the ion–neutral collision coefficient (Equations (1)–(2)), and thus effectively on the mass density and temperature, higher up, the amplitude of disturbance is not sufficient to heat the chromosphere significantly. As $P_d = 180$ s is lower than the acoustic cutoff period (Wójcik et al. 2018), according to the theory originally developed by Lamb (1909) the excited acoustic waves propagate freely across the chromosphere up to the transition region (bottom left panel). See Wójcik et al. (2018) for the corresponding numerical simulations. For $P_d = 300$ s cooling events discernible in Figure 4 are related to the fluctuations of perturbed ion temperature associated with acoustic waves; rarefactions that follow shock-fronts lead to pressure decrease (e.g., Kuźma et al. 2017) and consequently act contrary to plasma heating. Energy dissipated by these waves in the chromosphere is sufficient to heat up the plasma up to 10^4 K on a timescale of 10^3 s. We conclude here that shorter-waveperiod waves heat more lower atmospheric heights than higher-waveperiod waves. In all cases, plasma heating grows with height, up to $y = 1.5$–1.8 Mm. Higher up, $\delta T_i/T_i$ falls off with height.

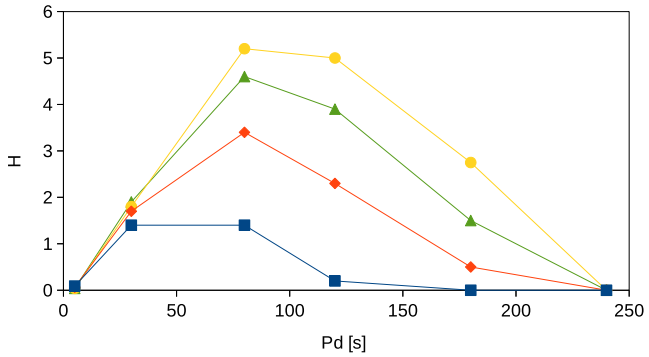

Figure 4. Averaged over time relative perturbed temperature of ions, H, vs. driving period P_d, at $y = 1.0$ Mm (squares), $y = 1.25$ Mm (diamonds), $y = 1.5$ Mm (triangles), and $y = 1.75$ Mm (circles).

Figure 4 illustrates the averaged over time relative perturbed temperature, H, given as

$$H(y) = \frac{1}{t_a}\int_0^{t_a} \frac{T_i(y,t) - T_0(y)}{T_0(y)}\, dt, \qquad (12)$$

versus P_d. Here $t_a = 5 \times 10^3$ s is the averaging time. The upper photosphere, at $y = 0.5$ Mm, is a bit heated solely by short-period waves (not shown), while the chromospheric plasma is effectively heated by waves with periods higher than 30 s and shorter than 120 s (diamonds), with a maximum close to $P_d = 80$ s. Note that the upper chromosphere is heated by a wider range of waves and more thermal energy is dissipated there (triangles and circles).

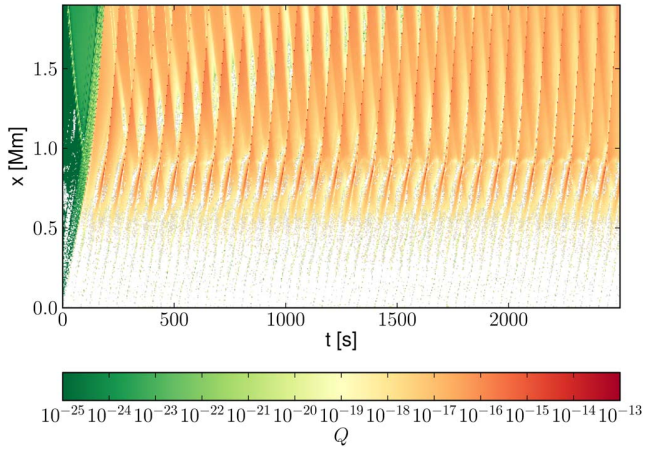

Figure 5. Time–distance plot of the thermal energy heating rate due to ion–neutral collisions, taken from Q_i^{in} term, for $P_d = 80$ s, in units of W m^{-3}.

The total vertical energy flux transported through the medium can be estimated as

$$F(y, t) \approx \varrho_i(y) c_s(y) V_{iy}^2(y, t) + \varrho_n(y) c_s(y) V_{ny}^2(y, t), \quad (13)$$

where $c_s(y)$ is the sound speed at the equilibrium, given by

$$c_s(y) = \sqrt{\frac{\gamma(p_i(y) + p_n(y))}{\varrho_i(y) + \varrho_n(y)}}. \quad (14)$$

Wave energy is deposited in the form of thermal energy to overlying plasma by ion–neutral collisions. Figure 5 illustrates the collisional heating (first) part of the Q_i^{in} term (see Equations (7)–(8)) in the case of a driving period $P_d = 80$ s. In Table 1 we compare $F(y, t = 2.5 \times 10^3$ s), evaluated at $y = 0.5$ Mm, $y = 1.0$ Mm and $y = 1.75$ Mm (from Figure 3), that correspond to the lower, middle, and upper chromosphere, with the corresponding radiative energy losses as estimated by Withbroe & Noyes (1977). Note that the numerically obtained values are lower than the predictions. Thus, we conclude that acoustic waves with realistic amplitudes in the chromosphere do not carry a sufficient amount of energy to compensate radiative losses.

We have verified by inspection that for waveperiods $P_d = 180$ s and $P_d = 300$ s consecutive heating shock-fronts are separated in space along the y-direction. The localized plasma pressure increase is compensated by rarefactions that follow the leading shock-front, before the consecutive shock-front arrives at the same region, increasing the plasma temperature even more. Due to rarefactions, plasma temperature attains its quasi-stationary value. As a result, the temporally averaged relative perturbed temperature, H, tends to be constant (0 in the case of $P_d = 300$ s) (see the bottom right panel of Figure 3 and the bottom panel of Figure 4). Thus, we infer that for very high period waves, plasma heating does not accumulate in the chromosphere, and the oscillations with these characteristic periods cannot effectively heat the plasma.

4. Summary and Conclusions

We performed numerical simulations of two-fluid acoustic waves propagating in the gravitationally stratified and partially ionized solar photosphere and chromosphere. We perturbed the initial hydrostatic equilibrium with the periodic driver in vertical components of both ion and neutral velocities, which operates at the bottom of the photosphere. We found that waveperiods between about 30 and 200 s lead to significant heating of the chromosphere, while the upper photosphere remain hardly affected. The wave amplitude grows with height due to mass density falloff (e.g., Murawski et al. 2018), thus the amplitude growth can dominate over ion–neutral collisions damping. Such waves possess the capability to penetrate the upper layers of the solar atmosphere and dissipate their energy in the chromosphere. However, for low-amplitude waves, the deposited energy remains low and plasma heating is insignificant there.

Table 1
Radiative Energy Losses and Averaged Energy Flux of Acoustic Waves in the Solar Chromosphere, $F(y, t = 2.5 \times 10^3$ s), in the Case of the Driving Period $P_d = 80$ s

	Radiative Losses (erg cm^{-2} s^{-1})	F (erg cm^{-2} s^{-1})
Low chromosphere	2×10^6	2×10^3
Middle chromosphere	2×10^6	2×10^3
Upper chromosphere	3×10^5	5×10^2

By performing our two-fluid simulations, we contributed to ongoing discussions of plasma heating by means of acoustic waves. Previous works such as Carlsson et al. (2007), Andic et al. (2008), and Sobotka et al. (2014) were based on observational estimations and single-fluid equations, and they reached the conclusion that energy carried by acoustic waves may compensate a substantial fraction of the radiative losses. Our results reveal that by implementing ion–neutral collisions, the plasma heating, which corresponds to the amplitude of the driver equal to 0.1 km s^{-1}, is not sufficient to compensate the radiative losses.

The authors thank the referee for the stimulating comments, Dr. Nikola Vinas for discussions on solar abundance, and Dr. Istvan Ballai for stimulating discussions. This work was done in the framework of the projects from the Polish Science Center (NCN) grants No. 2014/15/B/ST9/00106, 2017/25/B/ST9/0050, and 2017/27/N/ST9/01798. The JOANNA code was developed by Darek Wójcik at UMCS, Lublin, Poland.

References

Andic, A., Mathioudakis, M., Keenan, F. P., Jess, D. B., & Bloomfield, D. S. 2008, IAU Symp. 247, Waves & Oscillations in the Solar Atmosphere: Heating and Magneto-Seismology (Cambridge: Cambridge Univ. Press), 312
Arber, T. D., Brady, C. S., & Shelyag, S. 2016, ApJ, 817, 94
Avrett, E., & Loeser, R. 2008, ApJS, 175, 229
Ballester, J. L., Alexeev, I., Collados, M., et al. 2018, SSRv, 214, 58
Bierman, L. 1946, NW, 33, 118
Braginskii, S. 1965, RvPP, 1, 205
Carlsson, M., Hansteen, V. H., de Pontieu, B., et al. 2007, PASJ, 59, S663
Carlsson, M., & Stein, R. F. 1995, ApJL, 440, L29
Courant, R., Friedrichs, K., & Lewy, H. 1928, MatAn, 100, 32
Cuntz, M., Rammacher, W., & Musielak, Z. E. 2007, ApJL, 657, L57
De Pontieu, B., & Haerendel, G. 1998, A&A, 338, 729
Erdélyi, R., & James, S. P. 2004, A&A, 427, 1055
Forteza, P., Oliver, R., Ballester, J. L., & Khodachenko, M. L. 2007, A&A, 461, 731
Fossum, A., & Carlsson, M. 2005, in ESA SP-600, The Dynamic Sun: Challenges for Theory and Observations, ed. D. Danesy et al. (Noordwijk: ESA), 17.1
Fossum, A., & Carlsson, M. 2006, ApJ, 646, 579

Haerendel, G. 1992, Natur, 360, 241
Hillier, A., Takasao, S., & Nakamura, N. 2016, A&A, 591, A112
Hirzberger, J. 2003, AN, 324, 344
James, S. P., & Erdélyi, R. 2002, in ESA SP-506, Solar Variability: From Core to Outer Frontiers, ed. A. Wilson (Noordwijk: ESA), 649
Khodachenko, M. L., Arber, T. D., Rucker, H. O., & Hanslmeier, A. 2004, A&A, 422, 1073
Kulsrud, R., & Pearce, W. P. 1969, ApJ, 156, 445
Kuźma, B., Murawski, K., Kayshap, P., et al. 2017, ApJ, 849, 78
Lamb, H. 1909, Proc. London Math. Soc., s2-7, 122
Maneva, Y. G., Laguna, A. A., Lani, A., & Poedts, S. 2017, ApJ, 836, 197
Meier, E. T., & Shumlak, U. 2012, PhPl, 19, 072508
Miyoshi, T., Terada, N., Matsumoto, Y., et al. 2010, ITPS, 38, 9
Murawski, K., Kayshap, P., Srivastava, A. K., et al. 2018, MNRAS, 474, 77
Musielak, Z. E., Rosner, R., Stein, R. F., & Ulmschneider, P. 1994, ApJ, 423, 474
Nakariakov, V. M., & Verwichte, E. 2005, LRSP, 2, 3
Narain, U., & Ulmschneider, P. 1996, SSRv, 75, 453
Oliver, R., Soler, R., Terradas, J., & Zaqarashvili, T. V. 2016, ApJ, 818, 128
Piddington, J. H. 1956, MNRAS, 116, 314
Schwarzschild, M. 1948, ApJ, 107, 1
Smith, P. D., & Sakai, J. I. 2008, A&A, 486, 569
Sobotka, M., Švanda, M., Jurčak, J., et al. 2014, Central Eur. Astrophys. Bull., 38, 53, https://hrcak.srce.hr/143591
Soler, R., Carbonell, M., & Ballester, J. L. 2013, ApJS, 209, 16
Srivastava, A. K., Murawski, K., Kuźma, B., et al. 2018, NatAs, 2, 951
Tu, J., & Song, P. 2013, ApJ, 777, 53
Ulmschneider, P., & Musielak, Z. 2003, in ASP Conf. Ser. 286, Current Theoretical Models and Future High Resolution Solar Observations: Preparing for ATST, ed. A. Pevtsov & H. Uitenbroek (San Francisco, CA: ASP), 363
Vögler, A., Shelyag, S., Schüssler, M., et al. 2005, A&A, 429, 335
Vranjes, J., & Krstic, P. S. 2013, A&A, 554, A22
Watanabe, T. 1961, CaJPh, 39, 1197
Withbroe, G. L., & Noyes, R. W. 1977, ARA&A, 15, 363
Wójcik, D. 2017, MSc thesis, UMCS, Lublin
Wójcik, D., Murawski, K., & Musielak, Z. E. 2018, MNRAS, 481, 262
Zaqarashvili, T. V., Khodachenko, M. L., & Rucker, H. O. 2011, A&A, 529, A82

The Astrophysical Journal, 884:127 (5pp), 2019 October 20 https://doi.org/10.3847/1538-4357/ab26b1

Two-fluid Numerical Simulations of the Origin of the Fast Solar Wind

D. Wójcik[1], B. Kuźma[1], K. Murawski[1], and A. K. Srivastava[2]
[1] Group of Astrophysics, Institute of Physics, University of M. Curie-Skłodowska, ul. Radziszewskiego 10, 20-031 Lublin, Poland; dwojcik@kft.umcs.lublin.pl
[2] Department of Physics, Indian Institute of Technology (Banaras Hindu University), Varanasi-221005, India
Received 2019 February 26; revised 2019 May 29; accepted 2019 June 2; published 2019 October 17

Abstract

With the use of our JOANNA code, which solves radiative equations for ion + electron and neutral fluids, we perform realistic 2.5D numerical simulations of plasma outflows associated with the solar granulation. These outflows exhibit physical quantities that are consistent, to the order of magnitude, with the observational findings for mass and energy losses in the upper chromosphere, transition region, and inner corona, and they may originate the fast solar wind.

Key words: magnetohydrodynamics (MHD) – methods: numerical – solar wind – Sun: activity – Sun: corona

1. Introduction

The solar wind is a stream of energized, charged particles (primarily electrons and protons from hydrogen, along with atomic nuclei like helium, alpha particles) flowing outward from the Sun (Bierman 1951; Parker 1965). There is a fast, widely uniform wind, emanating from polar coronal holes and at a distance of 1 au from the Sun traveling at about 750 km s^{-1}, and a slow, sporadic one, pouring from active equatorial regions and moving at about half that speed. The magnetic field lines stretch out radially in coronal holes, and do not loop directly back to the Sun, providing an open path for the fast plasma to escape the grasp of gravity. As the corona expands, these winds must be replaced by plasma moving up from below to feed them.

In the modern era of high-resolution spaceborne and ground-based observations, special attention has been paid to studying the origin of plasma outflows that form the solar wind. Early models of the wind assumed the inner corona to be its origin (e.g., Tu 1987). Recently, Tu (2005) detected such outflows in coronal funnels at altitudes between 5 and 20 Mm above the photosphere, and found that they reach a speed of up to 10 km s^{-1} at the height of 20 Mm. Emphasis was also placed on searching for the outflows in the chromosphere/transition region (e.g., Marsch et al. 2008; Tian et al. 2009; 2010; McIntosh et al. 2011; McIntosh 2012; Yang et al. 2013; Kayshap et al. 2015). It was found that these outflows can be generated by a variety of jets (De Pontieu et al. 2007; Wedemeyer-Böhm et al. 2012; Kayshap et al. 2013; Tian et al. 2014; Martínez-Sykora et al. 2017), and the injection of an often twisted magnetic field and its subsequent reconnection may also contribute to the bulk plasma outflows in coronal holes (e.g., Krieger et al. 1973; Zirker 1977; Kayshap et al. 2013; Yang et al. 2013).

It was showed theoretically that magnetohydrodynamic waves may be responsible for providing momentum to the upwardly moving plasma (e.g., Ofman 2005; Suzuki & Inutsuka 2005; Marsch 2006; Srivastava & Dwivedi 2006; De Pontieu et al. 2007; Arber et al. 2016). Among others, Hollweg (1978; 1981; 1986; Hollweg et al. 1982), Kudoh & Shibata (1999), and Matsumoto & Suzuki (2012) concluded that Alfvén waves possess a potential to drive plasma outflows. He et al. (2008) developed a model of plasma outflows in the coronal funnels, which includes Alfvén waves (Ofman et al. 1995). Along this line of investigation, Yang et al. (2016) found that Alfvén waves are able to form fast plasma outflows. See also Ofman et al. (1995) and Shestov et al. (2017) for a similar analysis. However, Alfvén waves are difficult for detection, particularly when high-frequency waves are concerned (Srivastava et al. 2017); in an inhomogeneous and structured medium, these waves can experience reflection, mode coupling, phase-mixing, and resonant absorption (Ofman et al. 1995; Nakariakov et al. 1997; Zaqarashvili & Roberts 2006; Goossens et al. 2012; Chmielewski et al. 2014; Shestov et al. 2017).

Despite the abovementioned achievements, the origin of the solar wind still remains one of the central issues of heliophysics. We investigate here the role of granulation in generation of chromospheric ejecta and associated plasma outflows in coronal holes. We are motivated by the fact that a base of the corona is filled with dynamic jets, propelled from below the transition region upwards at speeds of about 25 km s^{-1} into higher layers, that carry a significant amount of momentum (e.g., Sterling 2000; Zaqarashvili & Erdélyi 2009).

This paper is organized as follows. A physical model is presented in Section 2 and the corresponding numerical results are shown in Section 3. Our paper is concluded by discussion and summary of the numerical results in Section 4.

2. Two-fluid Model of a Partially Ionized Coronal Hole

We consider a solar coronal hole that is magnetically structured and gravitationally stratified, and its dynamics is described by two-fluid equations for ions + electrons treated as one fluid and neutrals regarded as second fluid. These equations can be written as follows:

$$\frac{\partial \varrho_{\rm n}}{\partial t} + \nabla \cdot (\varrho_{\rm n} \boldsymbol{V}_{\rm n}) = 0, \tag{1}$$

$$\frac{\partial \varrho_{\rm i}}{\partial t} + \nabla \cdot (\varrho_{\rm i} \boldsymbol{V}_{\rm i}) = 0, \tag{2}$$

$$\frac{\partial (\varrho_{\rm n} \boldsymbol{V}_{\rm n})}{\partial t} + \nabla \cdot (\varrho_{\rm n} \boldsymbol{V}_{\rm n} \boldsymbol{V}_{\rm n} + p_{\rm n} \boldsymbol{I}) = \alpha_c (\boldsymbol{V}_{\rm i} - \boldsymbol{V}_{\rm n}) + \varrho_{\rm n} \boldsymbol{g}, \tag{3}$$

$$\frac{\partial(\varrho_{\rm i}\boldsymbol{V}_{\rm i})}{\partial t} + \nabla\cdot(\varrho_{\rm i}\boldsymbol{V}_{\rm i}\boldsymbol{V}_{\rm i} + p_{\rm ie}\boldsymbol{I}) = \frac{1}{\mu}(\nabla\times\boldsymbol{B})\times\boldsymbol{B} + \alpha_c(\boldsymbol{V}_{\rm n}-\boldsymbol{V}_{\rm i}) + \varrho_{\rm i}\boldsymbol{g}, \quad (4)$$

$$\frac{\partial\boldsymbol{B}}{\partial t} = \nabla\times(\boldsymbol{V}_{\rm i}\times\boldsymbol{B}),\ \nabla\cdot\boldsymbol{B} = 0, \quad (5)$$

$$\frac{\partial E_{\rm n}}{\partial t} + \nabla\cdot[(E_{\rm n}+p_{\rm n})\boldsymbol{V}_{\rm n}] = \alpha_c\boldsymbol{V}_{\rm n}\cdot(\boldsymbol{V}_{\rm i}-\boldsymbol{V}_{\rm n}) + Q_{\rm n}^{\rm in} + q_{\rm n} + \varrho_{\rm n}\boldsymbol{g}\cdot\boldsymbol{V}_{\rm n}, \quad (6)$$

$$\frac{\partial E_{\rm i}}{\partial t} + \nabla\cdot\left[\left(E_{\rm i}+p_{\rm ie}+\frac{\boldsymbol{B}^2}{2\mu}\right)\boldsymbol{V}_{\rm i} - \frac{\boldsymbol{B}}{\mu}(\boldsymbol{V}\cdot\boldsymbol{B})\right] = \alpha_c\boldsymbol{V}_{\rm i}\cdot(\boldsymbol{V}_{\rm n}-\boldsymbol{V}_{\rm i}) + Q_{\rm i}^{\rm in} + Q_R^i + q_{\rm i} + \varrho_{\rm i}\boldsymbol{g}\cdot\boldsymbol{V}_{\rm i}, \quad (7)$$

where the heat production terms are

$$Q_{\rm n}^{\rm in} = \alpha_c(\Delta\tilde{V} + \Delta\tilde{T}), \quad (8)$$

$$Q_{\rm i}^{\rm in} = \alpha_c(\Delta\tilde{V} - \Delta\tilde{T}) \quad (9)$$

with

$$\Delta\tilde{V} = \frac{1}{2}|\boldsymbol{V}_{\rm i}-\boldsymbol{V}_{\rm n}|^2, \quad (10)$$

$$\Delta\tilde{T} = \frac{3k_{\rm B}}{m_{\rm H}(\mu_{\rm i}+\mu_{\rm n})}(T_{\rm i}-T_{\rm n}), \quad (11)$$

and the energy densities are given by

$$E_{\rm n} = \frac{p_{\rm n}}{\gamma-1} + \frac{\varrho_{\rm n}\boldsymbol{V}_{\rm n}^2}{2}, \quad (12)$$

$$E_{\rm i} = \frac{p_{\rm ie}}{\gamma-1} + \frac{\varrho_{\rm i}\boldsymbol{V}_{\rm i}^2}{2} + \frac{\boldsymbol{B}^2}{2\mu}. \quad (13)$$

Here subscripts $_{\rm i}$, $_{\rm n}$, and $_{\rm e}$ correspond to ions, neutrals, and electrons, respectively. The symbols $\varrho_{\rm i,n}$ denote mass densities, $\boldsymbol{V}_{\rm i,n}$ velocities, $p_{\rm ie,n}$ ion+electron and neutral gas pressures, $\boldsymbol{B}$ magnetic field, and $T_{\rm i,n}$ temperatures specified by ideal gas laws,

$$p_{\rm n} = \frac{k_{\rm B}}{m_{\rm H}\mu_{\rm n}}\varrho_{\rm n}T_{\rm n},\ p_{\rm ie} = \frac{k_{\rm B}}{m_{\rm H}\mu_{\rm i}}\varrho_{\rm i}T_{\rm i}. \quad (14)$$

A gravity vector is $\boldsymbol{g} = [0, -g, 0]$ with its magnitude $g = 274.78\ {\rm m\ s^{-2}}$, $\alpha_{\rm c}$ is the coefficient of collisions between ion and neutral particles (e.g., Oliver et al. 2016; Ballester et al. 2018, and references cited therein). $Q_R^{\rm i}$ is a radiative loss term that is implemented here in the framework of Abbett & Fisher (2012) in the low atmospheric regions and of thin radiation (Moore & Fung 1972) in the top atmospheric layers, $q_{\rm i,n}$ are thermal conduction terms (Spitzer 1962), $\mu_{\rm i} = 0.58$ and $\mu_{\rm n} = 1.21$ are the mean masses of respectively ions and neutrals, which are taken from the OPAL solar abundance model (e.g., Vögler et al. 2004), $m_{\rm H}$ is the hydrogen mass, $k_{\rm B}$ is the Boltzmann constant, $\gamma = 1.4$ is the specific heat ratio, and μ is magnetic permeability of the medium. The other symbols have their standard meanings.

We consider the case of the z-invariant system and start our simulations at $t = 0$ s with the hydrostatic equilibrium being supplemented by transversal and vertical magnetic fields, given as $\boldsymbol{B} = [B_x, B_y, B_z] = [0, B_0, B_0]$, where $B_0 = 5/\sqrt{2}$ Gs. The transversal component, B_z, results in Alfvén waves being linearly coupled to magnetoacoustic waves. The presence of Alfvén waves is essential in the model, because in the nonlinear regime they are capable of driving vertical flow (e.g., Hollweg 1986; Murawski 1992; Shestov et al. 2017).

In the framework of the implemented magnetic field model we set at $t = 0$ s identical hydrostatic temperature for ions and neutrals, $T_{\rm i}(y) = T_{\rm n}(y) = T(y)$ (Martínez-Gómez et al. 2016, 2017; Oliver et al. 2016; Soler et al. 2017; Srivastava et al. 2018). This temperature is determined by the semiempirical model of Avrett & Loeser (2008) that is extrapolated into the corona.

The hydrostatic equilibrium is restructured in time by the solar granulation. This granulation appears naturally in the convection zone, which is convectively unstable. First signs of granulation are seen already after about 5 minutes from the start of the simulations with a fully developed state occurring after about 3000 s of the solar time.

3. Numerical Simulations of Two-fluid Plasma Outflows

To solve two-fluid equations numerically, we use the JOANNA code (Wójcik et al. 2018). We set in our numerical experiments the Courant–Friedrichs–Lewy number equal to 0.9 and choose a second-order accuracy in space and a four stage, third-order strong stability preserving the Runge–Kutta method (Durran 2010) for integration in time, supplemented by adopting the Harten–Lax–van Leer Discontinuities approximate Riemann solver (Miyoshi & Kusano 2005) and the Global Lagrange Multiplier method of Dedner et al. (2002). The simulation box extends from the convection zone (2.56 Mm below the bottom of the photosphere) to the corona (up to 30 Mm above the photosphere) in the y-direction and horizontally from $x = -2.56$ Mm to $x = 2.56$ Mm. This box is divided into several patches. The bottom region, specified by $-2.56\ {\rm Mm} \leqslant y \leqslant 7.68$ Mm, is covered by the 1024×1024 identical cells, leading to the spatial resolution of 10 km. Within the layer of $7.68\ {\rm Mm} \leqslant y \leqslant 30$ Mm, we implement several patches of progressively larger cells along the y-direction. On the left and right sides of the simulation box we set periodic boundary conditions, while the top and bottom ghost cells are filled by plasma quantities equal to their equilibrium values. The layer for the optical depth greater than 10 is additionally heated by implementing an extra source term in the energy equation of ions that balances the energy losses there.

Figure 1 (colormap) shows typical spatial profiles of $\log\varrho_{\rm i}$ (top) and the vertical component of ion velocity (bottom). The granulation excites a wide range of waves deep in the photosphere. Some of these waves steepen into shocks while propagating upwards. This steepening results from wave amplitude growth with height, and chromospheric jets are excited (top). The plasma above the apices of these jets moves upwards reaching its maximum speed of around 100 km s^{-1} (bottom). The outflowing plasma essentially follows open magnetic field lines (black lines) of magnetic funnels that are formed by the granulation. The footpoints of these funnels are rooted deep in the photosphere between granules, while higher up, above the transition region, the magnetic field lines remain essentially vertical. The plasma outflows form strand-like structures along magnetic field lines in the corona, with subsiding plasma taking place at lower altitudes.

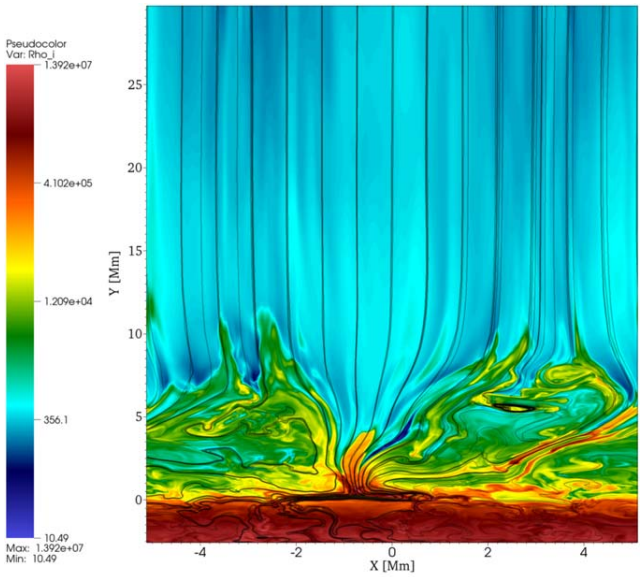

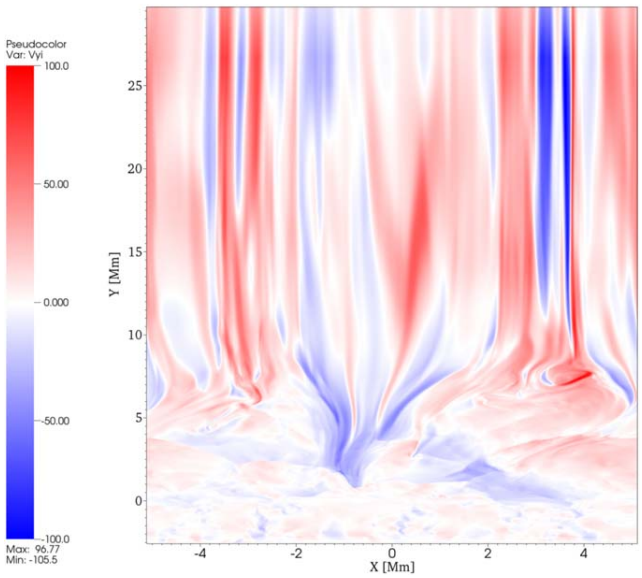

Figure 1. Typical spatial profiles of $\log \varrho_{\rm i}$ overlayed by magnetic field (solid lines; top) and vertical component of velocity $V_{{\rm i}\,y}(x, y)$ (bottom). Ion mass density is given in units of 10^{-18} g cm^{-3} and $V_{{\rm i}\,y}$ is expressed in units of 1 km s^{-1}.

We have run the code with extra nonadiabatic terms such as thermal conduction and magnetic diffusion included along with radiation. However, due to the computational effort we have not yet obtained satisfactory results. We have also run the code with the spatial resolution of 20 km × 20 km and the results are shown in Figure 2. The results are close to those shown in Figure 1 (bottom), which confirms that the chosen spatial resolution of 10 km × 10 km is sufficient to resolve plasma outflows.

Figure 3 displays a time–distance plot of the vertical component of ion velocity that is averaged over the whole horizontal distance, $\langle V_{{\rm i}\,y}\rangle$. The plasma jets emerge from the chromospheric background and move into the corona. Some of the injected plasma subsides rapidly after reaching its maximum phase (e.g., Kuźma et al. 2017; Srivastava et al. 2018). This

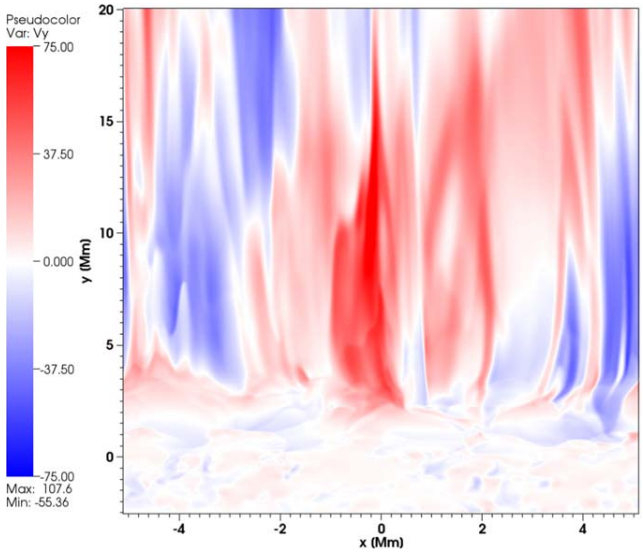

Figure 2. Spatial profile of the vertical component $V_{{\rm i}\,y}(x, y)$, expressed in units of 1 km s^{-1} for the spatial resolution of 20 km × 20 km.

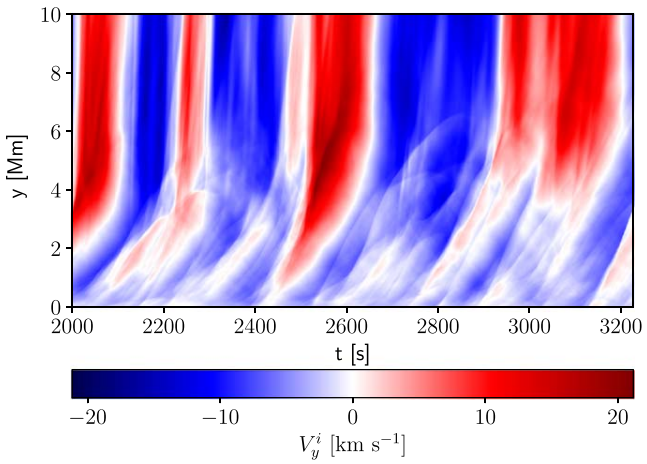

Figure 3. Time–distance plot of horizontally averaged vertical component of ion velocity, $\langle V_{{\rm i}\,y}(y, t)\rangle$.

entire process is driven by ongoing granulation in the photosphere. Analyzing $\langle V_{{\rm i}\,y}(y, t)\rangle$ we find that the solar corona experiences about 1−3 minute period oscillations and $\langle V_{{\rm i}\,y}\rangle$ reaches a magnitude of 10−20 km s^{-1} at $y = 8$ Mm and it grows with height. The physical properties of these outflows are akin to the flow characteristics reported by Tu (2005).

Figure 4 (top) illustrates the time–distance plot of the horizontally averaged total vertical ion mass flux, $F_m(y, t) = \langle \varrho_{\rm i} V_{{\rm i}\,y}\rangle$, which attains its maximum in the photosphere and lower chromosphere and falls off with height due to rapidly decreasing ion mass density. However, even above the transition region the estimated magnitude of this mass flux lays within the range of 10^{-6} and 10^{-5} g cm^{-2} s^{-1} and it matches the prediction for solar mass losses in the low corona (Withbroe & Noyes 1977).

Vertical component of ion energy flux transported through the medium can be calculated as $F_{\rm E}(x, y, t) = \varrho_{\rm i} V_{\rm i}^2 V_{\rm iy}/2$. The time–distance plot of horizontally averaged vertical energy flux, $\langle F_{\rm E}(y, t)\rangle$, is shown in Figure 4 (bottom). We see that plasma escaping into the corona above the transition region

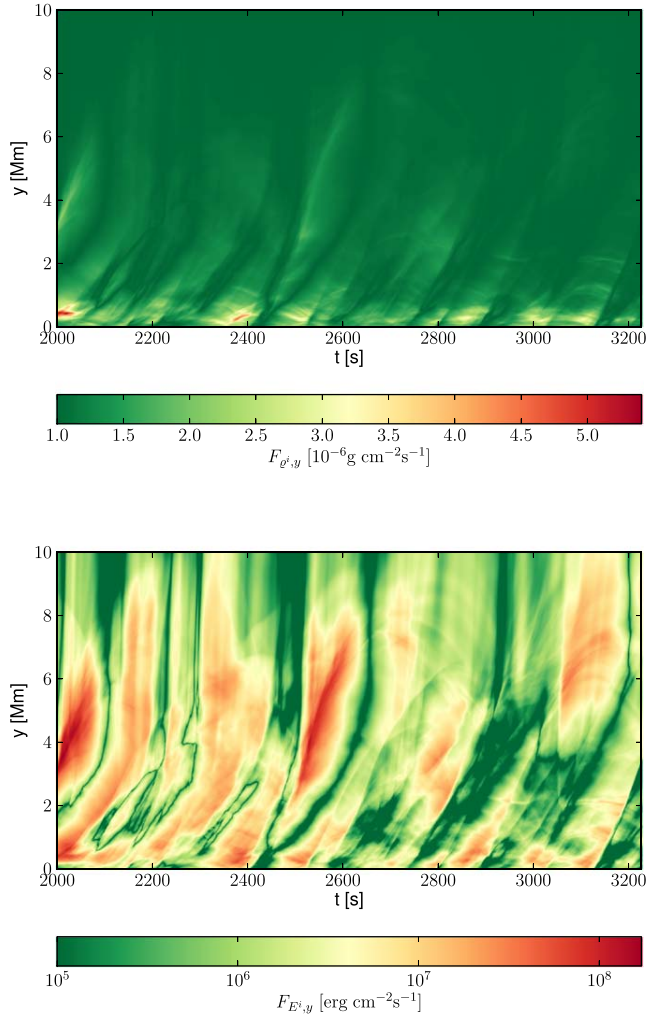

Figure 4. Time–distance plots of the horizontally averaged total vertical mass, $\langle F_m(y, t)\rangle$, (top) and energy, $\langle F_E(y, t)\rangle$, (bottom) fluxes.

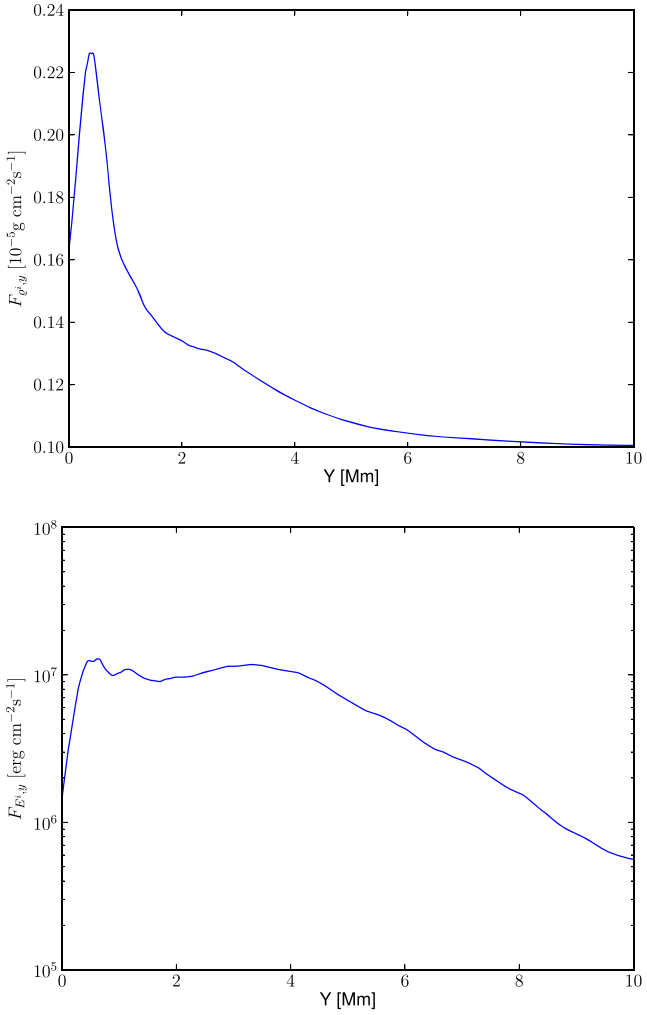

Figure 5. Vertical variation of the temporarily and horizontally averaged mass, $\langle F_m(y)\rangle$ (top), and energy, $\langle F_E(y)\rangle$ (bottom), fluxes.

carries a significant amount of energy (orange and yellow patches). By comparison with time–distance plots of $\langle V_{\mathrm{i}\,y}\rangle$ (Figure 3) we infer that the energy flux associated with the upflowing plasma is higher than for the descending plasma. Note that the obtained values lay within the range of theoretical findings for energy losses in the upper chromosphere, transition region, and low corona (Withbroe & Noyes 1977).

Figure 5 shows vertical variation of the temporarily and horizontally averaged mass, $\langle F_{\mathrm{m}}\rangle$ (top), and energy, $\langle F_{\mathrm{E}}(y)\rangle$ (bottom), fluxes. Note that $\langle F_{\mathrm{E}}(y)\rangle$ grows abruptly within the region of $0 < y < 0.5$ Mm, where the dense photospheric plasma experiences a push from the below operating granulation. Higher up, that is, for $y > 0.5$ Mm, $\langle F_{\mathrm{m}}(y)\rangle$ declines with height attaining a value of 10^{-6} g cm^{-2} s^{-1} at $y = 10$ Mm. On the other hand, $\langle F_{\mathrm{E}}(y)\rangle$ remains close to 10^7 erg cm^{-2} s^{-1} in the entire chromosphere and transition region, attaining its local maxima at $y = 0.25$ Mm and $y = 3.5$ Mm. Higher up, it slowly falls off with height, reaching its value of $5 \cdot 10^5$ erg cm^{-2} s^{-1} at $y = 10$ Mm.

4. Discussion and Summary

Within the framework of two-fluid equations for ion-neutral plasma, we performed numerical simulations of the origin of the solar wind that results from plasma outflows. These outflows are associated with jets excited by the solar granulation, which develops in the medium with a initially straight magnetic field overlaying a hydrostatic equilibrium. This configuration well mimics the expanding open magnetic field region in a polar coronal hole. Our simulations show that this configuration is restructured later on by granulation, which operates in the photosphere. The whole scenario is associated with the energy and mass leakage into higher atmospheric layers in the form of plasma outflows. Our results successfully match the expected values of mass and energy losses in the upper chromosphere, transition region, and low corona (Withbroe & Noyes 1977).

It is noteworthy here that Tu (2005) obtained a correlation of the Doppler-velocity and radiance maps of spectral lines emitted by various ions (Ne VIII, C IV, and Si II) with the force-free magnetic field that was extrapolated from the photospheric magnetogram (*SOHO*/MDI) in a polar coronal hole. Tu found that Ne VIII ions mostly radiate around the height of 20 Mm above the photosphere, where they reveal the outflow speed of about 10 km s^{-1}, while C IV ions with no average flow speed form essentially around the altitude of 5 Mm. Hence, Tu inferred that the plasma outflows start in the coronal funnels at altitudes in between 5 and 20 Mm. Yang et al. (2013) proposed

that magnetic reconnection, which took place in the open and closed magnetic field region, triggers the plasma outflows observed by Tu (2005). The results of our simulations performed with a novel two-fluid model of a partially ionized solar atmospheric plasma confirm these observational findings.

Ten years before the plasma outflows were announced by Tu (2005), there was essentially no report on finely structured jets. The exceptions were spicules/macrospicules diversely filling the chromosphere and contributing to the mass cycle of the corona (e.g., Wedemeyer-Böhm et al. 2012; Tian et al. 2014). In the limit of current observational resolution, it is established that the overlaying plasma outflows in the corona must have originated due to the contribution from various plasma ejecta. Therefore, without emphasizing a particular type of a jet, we simulated the solar granulation that resulted in jets and studied their contribution to formation of the solar wind.

In summary, we investigated formation of plasma outflows between 5 and 10 Mm above the photosphere in the open magnetic field region in a coronal hole as observed by Tu (2005). The outflows in such regions consist of continuous streaming of plasma particles from the lower solar atmosphere outward. We point out its linkage to the granulation and associated with them the ubiquitous chromospheric jets that lead to mass and energy leakage into the inner corona. Our model is based on gravitationally stratified and partially ionized bottom layers of the solar atmosphere with adequate temperature and magnetic field conditions to mimic the ion-neutral plasma outflows. Our studies determine that multiple jets excited by operating in the photosphere granulation are able to stimulate continuous plasma outflows in the solar atmosphere, which may result in the fast solar wind at higher altitudes in the solar corona.

The authors express their thanks to Drs. Ramon Oliver, Roberto Soler, and David Martinéz-Gómez for their comments on the hydrostatic model of the solar atmosphere. We would like to thank the reviewer for their time and valuable remarks. The JOANNA code has been developed by Darek Wójcik. This work was done within the framework of the projects from the Polish National Foundation (NCN) grant Nos. 2017/25/B/ST9/00506 and 2017/27/N/ST9/01798. Numerical simulations were performed on the LUNAR cluster at Institute of Mathematics of University of M. Curie-Skłodowska, Lublin, Poland.

ORCID iDs

D. Wójcik https://orcid.org/0000-0002-4200-3432

References

Abbett, W. P., & Fisher, G. H. 2012, SoPh, 277, 3
Arber, T. D., Brady, C. S., & Shelyag, S. 2016, ApJ, 817, 94
Avrett, E., & Loeser, R. 2008, ApJS, 175, 229
Ballester, J. L., Alexeev, I., Collados, M., et al. 2018, SSRv, 214, 58
Bierman, L. 1951, ZA, 29, 274
Chmielewski, P., Murawski, K., Musielak, Z. E., & Srivastava, A. K. 2014, ApJ, 793, 43
De Pontieu, B., McIntosh, S. W., Carlsson, M., et al. 2007, Sci, 318, 1574
Dedner, A., Kemm, F., Kröner, D., et al. 2002, JCoPh, 175, 645
Durran, D. R. 2010, Numerical Methods for Fluid Dynamics (Berlin: Springer)
Goossens, M., Andries, J., Soler, R., et al. 2012, ApJ, 753, 111
He, J.-S., Tu, C.-Y., & Marsch, E. 2008, SoPh, 250, 147
Hollweg, J. V. 1978, SoPh, 56, 305
Hollweg, J. V. 1981, SoPh, 70, 25
Hollweg, J. V. 1986, ApJ, 306, 730
Hollweg, J. V., Jackson, S., & Galloway, D. 1982, SoPh, 75, 35
Kayshap, P., Banerjee, D., & Srivastava, A. K. 2015, SoPh, 290, 2889
Kayshap, P., Srivastava, A. K., Murawski, K., & Tripathi, D. 2013, ApJL, 770, L3
Krieger, A. S., Timothy, A. F., & Roelof, E. C. 1973, SoPh, 29, 505
Kudoh, T., & Shibata, K. 1999, ApJ, 514, 493
Kuźma, B., Murawski, K., Kayshap, P., et al. 2017, ApJ, 849, 78
Marsch, E. 2006, LRSP, 3, 1
Marsch, E., Tian, H., Sun, J., Curdt, W., & Wiegelmann, T. 2008, ApJ, 685, 1262
Martínez-Gómez, D., Soler, R., & Terradas, J. 2016, ApJ, 832, 101
Martínez-Gómez, D., Soler, R., & Terradas, J. 2017, ApJ, 837, 80
Martínez-Sykora, J., Pontieu, B. D., Hansteen, V. H., et al. 2017, Sci, 356, 1269
Matsumoto, T., & Suzuki, T. K. 2012, ApJ, 749, 8
McIntosh, S. W. 2012, SSRv, 172, 69
McIntosh, S. W., De Pontieu, B., & Mats, C. 2011, Natur, 475, 477
Miyoshi, T., & Kusano, K. 2005, JCoPh, 208, 315
Moore, R. L., & Fung, P. C. W. 1972, SoPh, 23, 78
Murawski, K. 1992, SoPh, 139, 279
Nakariakov, V. M., Roberts, B., & Murawski, K. 1997, SoPh, 175, 93
Ofman, L. 2005, SSRv, 120, 67
Ofman, L., Davila, J. M., & Steinolfson, R. S. 1995, ApJ, 444, 471
Oliver, R., Soler, R., Terradas, J., & Zaqarashvili, T. V. 2016, ApJ, 818, 128
Parker, E. N. 1965, SSRv, 4, 666
Shestov, S. V., Nakariakov, V. M., Ulyanov, A. S., Reva, A. A., & Kuzin, S. V. 2017, ApJ, 840, 64
Soler, R., Terradas, J., Oliver, R., & Ballester, J. L. 2017, ApJ, 840, 20
Spitzer, L. 1962, Physics of Fully Ionized Gases (New York: Interscience)
Srivastava, A. K., & Dwivedi, B. N. 2006, JApA, 27, 353
Srivastava, A. K., Murawski, K., Kuźma, B., et al. 2018, NatAs, 2, 951
Srivastava, A. K., Shetye, J., & Murawski, K. 2017, NatSR, 7, 43147
Sterling, A. C. 2000, SoPh, 196, 79
Suzuki, T. K., & Inutsuka, S. 2005, ApJL, 632, L49
Tian, H., Li, G., Reeves, K. K., et al. 2014, ApJL, 797, L14
Tian, H., Marsch, E., Curdt, W., & He, J. 2009, ApJ, 704, 883
Tian, H., Tu, C., Marsch, E., He, J., & Kamio, S. 2010, ApJL, 709, L88
Tu, C.-Y. 1987, SoPh, 109, 149
Tu, C.-Y. 2005, Sci, 308, 519
Vögler, A., Shelyag, S., Schüssler, M., et al. 2004, A&A, 429, 335
Wedemeyer-Böhm, S., Scullion, E., Steiner, O., et al. 2012, Natur, 486, 505
Withbroe, G. L., & Noyes, R. W. 1977, ARA&A, 15, 363
Wójcik, D., Murawski, K., & Musielak, Z. E. 2018, MNRAS, 481, 262
Yang, L., He, J., Peter, H., et al. 2013, ApJ, 777, 16
Yang, L., Lee, L. C., Chao, J. K., et al. 2016, ApJ, 817, 178
Zaqarashvili, T. V., & Erdélyi, R. 2009, SSRv, 149, 355
Zaqarashvili, T. V., & Roberts, B. 2006, A&A, 452, 1053
Zirker, J. B. 1977, RvGeo, 15, 257

Astronomy & Astrophysics manuscript no. AA_wkmm_R2b
February 20, 2020

Wave heating of the solar atmosphere without shocks

D. Wójcik[1], B. Kuźma[1], K. Murawski[1], and Z.E Musielak[2,3]

[1] Group of Astrophysics, University of Maria Curie-Skłodowska, ul. Radziszewskiego 10, 20-031 Lublin, Poland

[2] Department of Physics, University of Texas at Arlington, Arlington, TX 76019, USA

[3] Leibniz-Institut für Sonnenphysik (KIS),Schöneckstr. 6, 79104 Freiburg, Germany

Received; accepted

Abstract

Context. We investigate the wave heating problem of a solar quiet region and present its plausible solution without involving shock formation.

Aims. By performing numerical simulations, we aim to study wave propagation and dissipation in the partially-ionized solar atmosphere, whose model includes both neutrals and ions.

Methods. With use of a 2.5D two-fluid model of the solar atmosphere, we study the wave generation and propagation. The source of these waves is the solar convection located beneath the photosphere.

Results. The energy carried by the waves is dissipated through ion-neutral collisions, which replace shocks used in some previous studies as the main source of local heating in quiet regions.

Conclusions. It is demonstrated that the resulting wave dissipation is sufficient to balance radiative and thermal energy losses, and to sustain a quasi-stationary atmosphere whose averaged temperature profile well-agrees with the observationally based semi-empirical model of Avrett & Loeser (2008).

Key words. Sun: atmomosphere - magnetohydrodynamics (MHD) - methods: numerical

1. Introduction

The heating problem of the solar atmosphere is very challenging as it requires to explain the counter-intuitive atmospheric temperature raise from about 5600 K at the solar surface by about 200-500 times over the height of about two thousand km. Two main families of heating mechanisms have been proposed: one uses microflaring, while the other is based on energy carried by various waves present in the solar atmosphere. There is observational evidence for the existence of both microflares and waves in the solar atmosphere, with the former likely contributing to the heating at higher altitudes, whereas the latter is expected to

Send offprint requests to: D. Wójcik

be responsible for the heating of lower atmospheric layers. The main unsolved heating problem is how the wave energy is generated and dissipated. A solution of this longstanding solar physics problem is proposed in this paper.

The most efficient source of waves is the convection zone. Laying below the photosphere, this zone is populated by highly turbulent motions that generate magnetohydrodynamic-gravity waves (e.g., Musielak & Ulmschneider 2001). Recent observations reveal a diversity of waves in the solar atmosphere and they also demonstrate that some of these waves carry enough energy to heat this atmosphere (e.g., Jess et al. 2009, Srivastava et al. 2018). Propagation of these waves in the atmosphere is affected by cutoff frequencies. Waves with frequencies higher than their cutoffs are propagating, however, waves with lower frequencies are evanescent and their amplitudes decay with height.

The concept of cutoff was originally introduced by Lamb (1909) and later modified to be applicable to the solar atmosphere by others (e.g., Roberts 2004, Musielak et al. 2006). A strong observational evidence for the existence of cutoffs in the atmosphere and their variations with the atmospheric height was presented by Wiśniewska et al. (2016) and Kayshap et al. (2018). Several theoretical attempts were undertaken in the past to fit the observational data (e.g., Murawski et al. 2016, Wójcik et al. 2018) but without achieving a satisfactory agreement with the available data. However, in the most recent work by Wójcik et al. (2019a), a good agreement between the numerical simulations and observations was finally achieved, and the authors pointed out the importance of partially ionized effects that were accounted for by their numerical code. Similar code is used in this paper but with the exception that all non-ideal and non-adiabatic terms are switched on. However, the main goal of this paper is different than that of Wójcik et al., as here we concentrate on the wave generation and dissipation, and the solar atmosphere wave heating problem.

Waves in the solar atmosphere may form shocks that heat the plasma locally (e.g., Ulmschneider et al. 1978, Carlsson & Stein 1995). Fawzy et al. (2002) constructed theoretical models of the chromosphere that are based on the waves generated in the convection zone and using the dissipation of wave energy by shock formation (Hillier et al. 2016). The constructed models were purely theoretical, one-dimensional (1D) and they included both non-magnetic and magnetic regions as well as full treatment of non-LTE ionization and radiation. The only free parameter in these models was a filling factor, which was used to explain different levels of activity observed in solar-like stars. The models were used to compute profiles of Ca II and Mg II lines, which were compared to observational data. The comparison shows a good agreement between the theoretically predicted line profiles and observations, and also demonstrated that the theoretically predicted temperature variations in the solar atmosphere were in an agreement with the

semi-empirical VAL model (Vernazza et al. 1982). The main difference between their approach, which was based on fully ionized plasma, and the one presented in this paper is that our numerical model is 2D and it properly accounts for partially ionized plasma in the solar atmosphere.

In the chromosphere models described above as well as in the most previous theoretical work, the effects of partially ionized plasma in the gravitationally-stratified solar atmosphere were often neglected or considered under some assumptions. For instance, Wójcik et al. (2018) and Kuźma et al. (2019a) devised 1D models of dynamics of ions and neutrals and then the models were extended to 2D geometry (e.g., Srivastava et al. 2018, Wójcik et al. 2019a,b). Moreover, Maneva et al. (2017) developed a 2D model of non-adiabatic and non-ideal atmosphere to show that ion magnetoacoustic-gravity and neutral acoustic-gravity waves (e.g., Vigeesh et al. 2017) lead to local heating of a magnetic flux-tube. In addition, Martínez-Sykora et al. (2017) and Khomenko et al. (2018) included neutrals into their respectively 2D and 3D models of self-generated solar granulation. The contribution of neutrals was taken into account by amending few extra terms in the induction equation. These models were recently generalized onto dynamic ions and neutrals in the chromosphere by Popescu Braileanu et al. (2019) who reported on a development of a new two-fluid code and its numerical verification. We present here an approach in which ions and neutrals are included self-consistently in our numerical model, and their dynamical effects on the wave propagation and dissipation are fully accounted for. Our approach gives a new insight into the wave heating problem.

Our paper is organized as follows: our two-fluid (ions + electrons and neutrals) model is described in Sect. 2; wave heating resulting from our numerical simulations is presented and discussed in Sect. 3; our conclusions are given in Sect. 4.

2. Two-fluid model of a partially ionized solar atmosphere

We consider a gravitationally-stratified and partially ionized solar atmosphere, whose evolution is described by the set of two-fluid equations (e.g., Zaqarashvili et al. 2011, Leake et al. 2012, Martínez-Gomez et al. 2018, Soler et al. 2013, Oliver et al. 2016, Ballester et al. 2018 and references cited therein). We take into account hydrogen as a main dynamic plasma ingredient; the influence of heavier plasma species is considered with use of the OPAL solar abundance model (e.g. Vögler et al. 2005). Additionally, for simplicity reasons we assume that ions and electrons consist a single ion-electron fluid, while neutrals are described by a second fluid. Interaction between both fluids occurs through the ion-neutral collisions. In this model we neglect effects of recombination, ionization and charge exchange, as well as effects of electrons exerted on ions, mimicked by extra terms in the generalized Ohm's law (e.g. Khomenko et al. 2017). As

a result of complexity of the present model, these effects are left for future studies.

2.1. Two-fluid equations for ions and neutrals

We write the equations that describe dynamics of neutral and ion+electron fluids as

$$\frac{\partial \varrho_{\rm n}}{\partial t} + \nabla \cdot (\varrho_{\rm n} \mathbf{V}_{\rm n}) = 0\,, \tag{1}$$

$$\frac{\partial \varrho_{\rm i}}{\partial t} + \nabla \cdot (\varrho_{\rm i} \mathbf{V}_{\rm i}) = 0\,, \tag{2}$$

$$\frac{\partial (\varrho_{\rm n} \mathbf{V}_{\rm n})}{\partial t} + \nabla \cdot (\varrho_{\rm n} \mathbf{V}_{\rm n} \mathbf{V}_{\rm n} + p_{\rm n} \mathbf{I}) = \alpha_c (\mathbf{V}_{\rm i} - \mathbf{V}_{\rm n}) + \varrho_{\rm n} \mathbf{g}\,, \tag{3}$$

$$\frac{\partial (\varrho_{\rm i} \mathbf{V}_{\rm i})}{\partial t} + \nabla \cdot (\varrho_{\rm i} \mathbf{V}_{\rm i} \mathbf{V}_{\rm i} + p_{\rm ie} \mathbf{I}) = \frac{1}{\mu} (\nabla \times \mathbf{B}) \times \mathbf{B} + \alpha_c (\mathbf{V}_{\rm n} - \mathbf{V}_{\rm i}) + \varrho_{\rm i} \mathbf{g}\,, \tag{4}$$

$$\frac{\partial \mathbf{B}}{\partial t} = \nabla \times (\mathbf{V}_{\rm i} \times \mathbf{B})\,, \quad \nabla \cdot \mathbf{B} = 0\,, \tag{5}$$

$$\frac{\partial E_{\rm n}}{\partial t} + \nabla \cdot [(E_{\rm n} + p_{\rm n}) \mathbf{V}_{\rm n}] = \alpha_c \mathbf{V}_{\rm n} \cdot (\mathbf{V}_{\rm i} - \mathbf{V}_{\rm n}) + Q_{\rm n}^{\rm in} + q_{\rm n} + \varrho_{\rm n} \mathbf{g} \cdot \mathbf{V}_{\rm n}\,, \tag{6}$$

$$\frac{\partial E_{\rm i}}{\partial t} + \nabla \cdot \left[\left(E_{\rm i} + p_{\rm ie} + \frac{\mathbf{B}^2}{2\mu} \right) \mathbf{V}_{\rm i} - \frac{\mathbf{B}}{\mu} (\mathbf{V} \cdot \mathbf{B}) \right] = \alpha_c \mathbf{V}_{\rm i} \cdot (\mathbf{V}_{\rm n} - \mathbf{V}_{\rm i}) + Q_{\rm i}^{\rm in} + Q_R^i + q_{\rm i} + \varrho_{\rm i} \mathbf{g} \cdot \mathbf{V}_{\rm i}\,, \tag{7}$$

where the heat production terms are

$$Q_{\rm n}^{\rm in} = \alpha_c \left(\frac{1}{2} |\Delta \mathbf{V}|^2 + a \Delta T \right)\,, \tag{8}$$

$$Q_{\rm i}^{\rm in} = \alpha_c \left(\frac{1}{2} |\Delta \mathbf{V}|^2 - a \Delta T \right)\,, \tag{9}$$

with $\Delta \mathbf{V} = \mathbf{V}_{\rm i} - \mathbf{V}_{\rm n}$, $\Delta T = T_{\rm i} - T_{\rm n}$, and $a = 3 k_{\rm B} / (m_{\rm H} (\mu_{\rm i} + \mu_{\rm n}))$. Here $\mathbf{I}$ is the identity matrix, and subscripts $_{\rm i}$, $_{\rm n}$ and $_{\rm e}$ correspond respectively to ions, neutrals and electrons. The symbols $\varrho_{\rm i,n}$ denote mass densities, $\mathbf{V}_{\rm i,n}$ velocities, $p_{\rm ie,n}$ ion+electron and neutral gas pressures, $\mathbf{B}$ is magnetic field, $\mathbf{\Pi}_{\rm i,n}$ are viscous stress tensors (Hollweg 1986), η is magnetic diffusivity coefficient and $T_{\rm i,n}$ are temperatures specified by ideal gas laws,

$$p_{\rm n} = \frac{k_{\rm B}}{m_{\rm H} \mu_{\rm n}} \varrho_{\rm n} T_{\rm n}\,, \qquad p_{\rm ie} = \frac{k_{\rm B}}{m_{\rm H} \mu_{\rm i}} \varrho_{\rm i} T_{\rm i}\,, \tag{10}$$

where gravity vector is $\mathbf{g} = [0, -g, 0]$ with its magnitude $g = 274.78$ m s^{-2}, $\alpha_{\rm c}$ is the coefficient of collisions between ion and neutral particles, $q_{\rm i,n}$ describe thermal conduction (Spitzer 1962), $Q_R^{\rm i}$ represents radiative losses, $\mu_{\rm ie} = 0.58$ and $\mu_{\rm n} = 1.21$ are the mean masses of electrons + ionized plasma species and neutrals, respectively, and they are taken from the OPAL solar abundance model (e.g., Vögler et al. 2004), $m_{\rm H}$ is the hydrogen mass, $k_{\rm B}$ is the Boltzmann constant, $\gamma = 1.4$ is the specific heats ratio, and μ is magnetic permeability of the medium. All other symbols have their standard meaning.

The radiative losses term, $Q_R^{\rm i}$, consists of two separate parts: thick cooling which operates in the low atmospheric layers and thin cooling, which works in the upper atmospheric regions. In every time-step we calculate the optical depth, starting from infinity and ending at the bottom boundary. For optical depths higher than 0.1 we use thick cooling approximation of Abbett and Fisher (2012). For optical depths lower than 0.1 we use thin cooling curve (Cox & Tucker 1969), which is interpolated by 10th order polynomial. In order to mimic energy transport into the simulation box from lower lying convective regions, we supplemented the radiative term by the heating term which balances cooling at optical depths $\tau > 10$.

Following Zaqarashvili et al. (2011), we assume coefficient of collisions between ions and neutrals $\alpha_{\rm in} = \alpha_{\rm ni} = \alpha_{\rm c}$, and to estimate its value we use the following formula provided by Braginskii (1965):

$$\alpha_{\rm c} = \frac{4}{3}\sigma_{\rm in}\frac{\varrho_{\rm i}\varrho_{\rm n}}{m_{\rm H}\mu_{\rm i} + m_{\rm H}\mu_{\rm n}}\sqrt{\frac{8k_{\rm B}}{\pi m_{\rm H}}\left(\frac{T_{\rm i}}{\mu_{\rm i}} + \frac{T_{\rm n}}{\mu_{\rm n}}\right)}. \tag{11}$$

Here the collisional cross-section $\sigma_{\rm in}$ is taken from quantum-mechanical model of Vranjes & Krstic (2013) who showed that the classical hard-sphere model may lead to underestimation of the cross-section values. For typical chromospheric plasma temperature in the range of $6 \cdot 10^3 - 10^4$ K this cross-section is equal to $1.89 \cdot 10^{-18}$ m^2, that is about three orders of magnitude larger than in the hard-sphere model. We experienced for acoustic waves that the released heating due to ion-neutral collisions is higher for the classical cross-section than for its quantum analog (Kuźma et al. 2019a). Note, that the ion-neutral collision frequency differs from the neutral-ion collision frequency (Ballester et al. 2018), and they are given as $\nu_{\rm in} = \alpha_{\rm c}/\varrho_{\rm i}$ and $\nu_{\rm ni} = \alpha_{\rm c}/\varrho_{\rm n}$.

2.2. Initial hydrostatic equilibrium of the solar atmosphere

In this part of the paper we consider the initial conditions of the solar atmosphere. We assume that the atmosphere is initially in a hydrostatic ($\mathbf{V}_{\rm i,n} = \mathbf{0}$) equilibrium. The equilibrium mass density profiles of ions and neutrals (Fig. 1) are specified uniquely by the temperature profile, taken to be the same for ions and neutrals (e.g. Oliver et al. 2016) from the quiet solar atmosphere model of Avrett & Loeser (2008). Note that the ion mass density is much lower than the neutral mass density in the photosphere and the low chromosphere. They become comparable about 900 km below the transition region which is located at $y \approx 2.1$ Mm. Higher up the neutrals are less abundant than ions; in the corona the mass density of neutrals experiences a sudden fall-off with height. As a result of ions and neutral distributions, the ionization degree depends on height in the solar atmosphere; in the photosphere, where the temperature is only about 5800 K, the plasma is very weakly ionized with only one ion per about 10^3 neutrals, while in the one million hot solar corona the plasma there is essentially fully ionized.

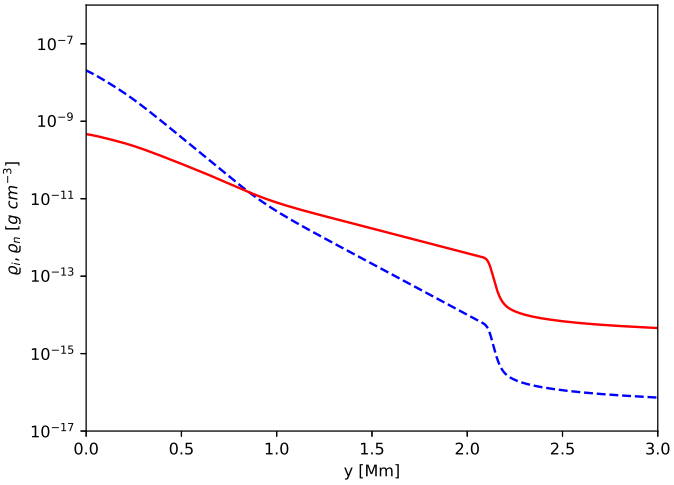

Figure 1: Initial vertical profiles of ion, $\varrho_{\rm i}$, (solid line) and neutral, $\varrho_{\rm n}$, (dashed line) mass densities.

Interaction between ion+electron and neutral fluids occurs through the ion-neutral collisions that are determined by the ion-neutral friction coeffi-

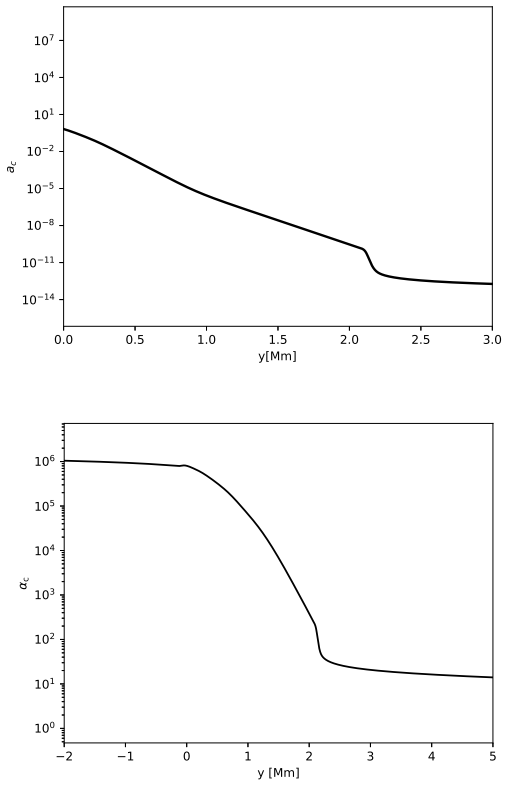

Figure 2: Vertical profiles of ion-neutral friction coefficient, α_c, (left panel) and sound speed, c_s, (right panel).

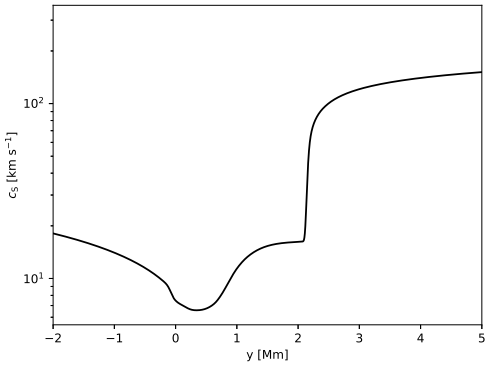

Figure 3: Profile of the initial Alfvén speed, c_A, versus height y.

cient (Eq. 11). Vertical profile of α_c is illustrated on Fig. 2 (left). Below the photosphere α_c retains its high value, therefore both fluids are strongly coupled there, as a result acting as a single fluid. At the bottom of the photosphere, that is at $y = 0$ the value of α_c begins to decrease with altitude. Higher up both fluids decouple, enabling ion-neutral drift, $\Delta\mathbf{V} = \mathbf{V}_i - \mathbf{V}_n$, to take place in the chromospheric and transition region layers. This drift is essential for collisional heating (Eqs. 8 - 9). The sound speed c_s can be given as

$$c_s(y) = \sqrt{\frac{\gamma(p_{\mathrm{h\,ie}}(y) + p_{\mathrm{h\,n}}(y))}{\varrho_{\mathrm{h\,i}}(y) + \varrho_{\mathrm{h\,n}}(y)}}\,. \qquad (12)$$

In the photosphere c_s is close to 6 km s^{-1} (Fig. 2, right). Right below the transition region, $c_s(y = 2$ Mm$) \approx 11$ km s^{-1}. Higher up c_s grows, following the trend of $\sqrt{T(y)}$; right above the transition region this growth is abrupt, and at larger altitudes c_s rises slowly to a value of about 150 km s^{-1} at $y \approx 30$ Mm (not shown).

We adopt here the uniform magnetic field with its vertical and transverse components given as $\mathbf{B} = [0, B_0, B_0]$ with $B_0 = 15/\sqrt{2}$ Gs. A non-zero transversal magnetic field permits transversal Alfvén waves to be present in the system. These waves are linearly coupled to magnetoacoustic waves and are essential in the model, as in the nonlinear regime they are capable of driving vertical flow (e.g. Hollweg 1986; Murawski 1992; Shestov et al. 2017). The mode conversion between slow-acoustic and Alfvén modes in regions of $\beta \approx 1$ can take place in this system. A nonlinear coupling between slow and Alfvén waves near these re-

gions has been studied by Zaqarashvili and Roberts (2006). The detailed discussion on 2-fluid Alfvén waves can be found in Kuźma et al. (2019b). The vertical profile of the corresponding Alfvén speed, $c_{\rm A}(x,y) = B/\sqrt{\mu(\varrho_{\rm i}+\varrho_{\rm n})}$, is illustrated on Fig. 3. In the upper photosphere and lower chromosphere $c_{\rm A}$ attains values lower than 10 km s^{-1} up to $y \approx 1$ Mm. Higher-up, as a result of low ion mass density $\varrho_{\rm i}$, $c_{\rm A}$ rises until the transition region, where it experiences a sudden growth to values close to 800 km s^{-1}.

3. Numerical simulations of two-fluid wave heating

To solve the 2-fluid equations numerically, we use JOANNA code (Wójcik et al. 2018). We set in our numerical experiments the Courant-Friedrichs-Lewy (Courant et al. 1928) number equal to 0.3 and choose a second-order accuracy in space and a second-order accurate Runge-Kutta method (Durran et al. 2010) for integration in time, supplemented by adopting the Harten-Lax-van Leer Discontinuities (HLLD) approximate Riemann solver (Miyoshi & Kusano 2010) and divergence of magnetic field cleaning method of Dedner et al. (2002).

The simulation box is specified along horizontal (x-) and vertical (y-) directions as $(-5.12 < x < 5.12)$ Mm $\times$ $(-5.12 < y < 30)$ Mm. This allows us to simulate convectively unstable region just below the photosphere which occupies the layer $0 \le y \le 0.5$ Mm. Below the height $y = 5.12$ Mm, we set a uniform grid with cell size 20 km $\times$ 20 km, while higher up, at the base of the corona, which is located at $y = 2.1$ Mm, we stretch the grid along $y-$direction dividing it into cells whose size grows with height. Two different types of boundary conditions are implemented at four edges of the simulation box. All plasma quantities at the top and bottom boundaries are set to their hydrostatic values. At the right and left boundary we use periodic boundary conditions. With the use of the stretched grid above $y = 5.12$ Mm we damp any incoming signal in layers close to the upper boundary. We have found that such stretched grid, supplemented by fixing all plasma quantities to their hydrostatic conditions at the top boundary significantly reduced spurious reflections of the incoming signal. Additionally, we implemented a plasma inflow at the bottom boundary with its vertical velocity equal to 0.3 km s^{-1}. This allows us to compensate the outflowing plasma mass losses. The value of inflow velocity is calculated by assuming that the incoming flux supposed to compensate the radiative losses (Chatterjee 2018). The convection zone is heated by overwhelming the radiative rate by 10%.

In our numerical simulations we consider plasma that is initially (at t = 0 s) set to its hydrostatic state with the vertical and transverse components of magnetic field. Later on, horizontal motions of plasma due to spontaneously generated granulation reshuffles magnetic field lines in the photosphere in the form of small flux-tubes (Fig. 4,

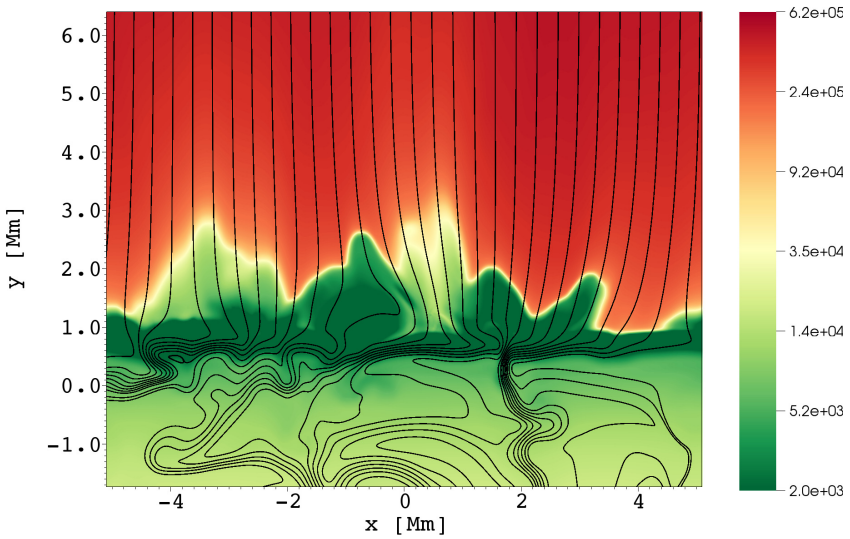

Figure 4: Spatial profile of logarithm of ion temperature, $T_{\rm i}$, expressed in unit of Kelvins (colormap) overlayed by magnetic field lines at $t = 5000$ s.

solid lines). These horizontal plasma motions reveal mean velocity close to 2.5 km s^{-1} at the $y = 0$ Mm (not shown) with maximum value up to 5 km s^{-1}, and thus they remain sub-sonic. This figure also shows above the photosphere the presence of well-defined cool and dynamic chromosphere. This layer is filled with both hot and cold jets visible at $x \approx 2.5$ Mm.

Hot plasma associated with granulation (Fig. 4, colormap) drifts towards the chromosphere and forms plasma upflows (Fig. 5, top). At the bottom of the chromosphere this plasma radiates its energy and gets cooled. Between sibling granules the downdrafts with cold plasma flowing down settle in the convection zone (Fig. 5, top). Both these upflows and downdrafts are accompanied by two-fluid waves (Fig. 5, bottom), which in our model atmosphere are neutral acoustic-gravity, ion magnetoacoustic-gravity (Vigeesh et al. 2017) and Alfvén waves.

The periods of the excited waves, obtained from the Fourier spectra for ion vertical velocity, are plotted in Fig. 5 (bottom). Note that at the height within the range of 0 Mm $< y <$ 0.5 Mm, the dominant wave-period P is about 340 s. However, higher up, for $y > 0.5$ Mm, the signal associated with large values of P decays fast with y, and the main wave-period is associated with $P \approx 180$ s. It was demonstrated that acoustic waves of $P \approx 300$ s are evanescent in the photosphere (e.g., Wójcik et al. 2018) but they are filtered out in higher layers, thus the package of waves consists of the main wave-period of about 180 s (Fig. 5, bottom). The described filtering process dominates in the chromosphere and it lowers periods and allows the waves to reach the transition region located at $y = 2.1$ Mm, where the waves become partially reflected back to the chromosphere. As a result of ion-neutral collisions, energy of these excited waves is dissipated. This dissipation is most effective for largest dispatches

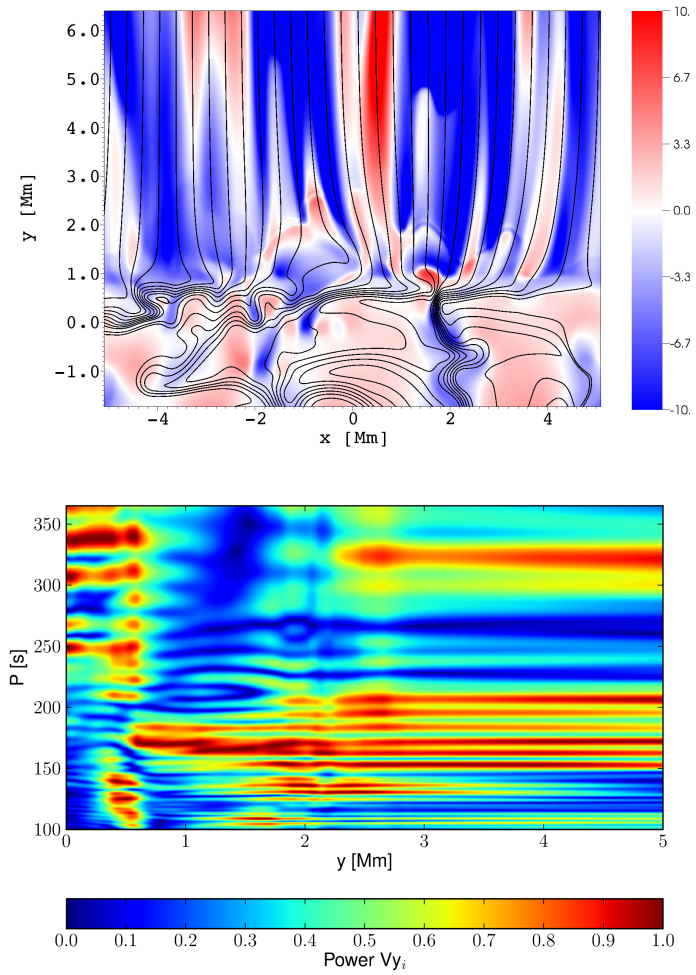

Figure 5: Spatial profile of vertical component of ion velocity, $V_{\rm i}$, expressed in units of 1 km s^{-1} (top) and its spatially averaged Fourier power periods vs height (bottom) at $t = 5000$ s.

between ion and neutral velocities, and these waves may convert their energy into heat mostly in the chromosphere (Fig. 6), compensating radiative and thermal losses.

A strong damping of low frequency (with period $>$ 80 s) Alfvén waves does not follow the conclusions drawn from the analytical studies of Zaqarashvili et al. (2013) who showed that short wave-period waves are rapidly damped due to ion-neutral collisions. However, our two-fluid model describes highly dynamic (yet remaining in quasi-equilibrium) solar atmosphere and differs significantly from those developed so far. A signal present in $V_{\rm iy}$ is partially converted through ion-neutral collisions into a signal in $V_{\rm ny}$. It follows from the dispersion relation that $V_{\rm ny}$ is associated with a purely imaginary frequency which corresponds to a strongly damped wave (Zaqarashvili et al. 2013). As a result of this damping and the energy transfer from $V_{\rm iy}$ into $V_{\rm ny}$ Alfvén waves, which correspond to $V_{\rm iy}$, are strongly damped. We found that longer waveperiods are not the main agent behind heating

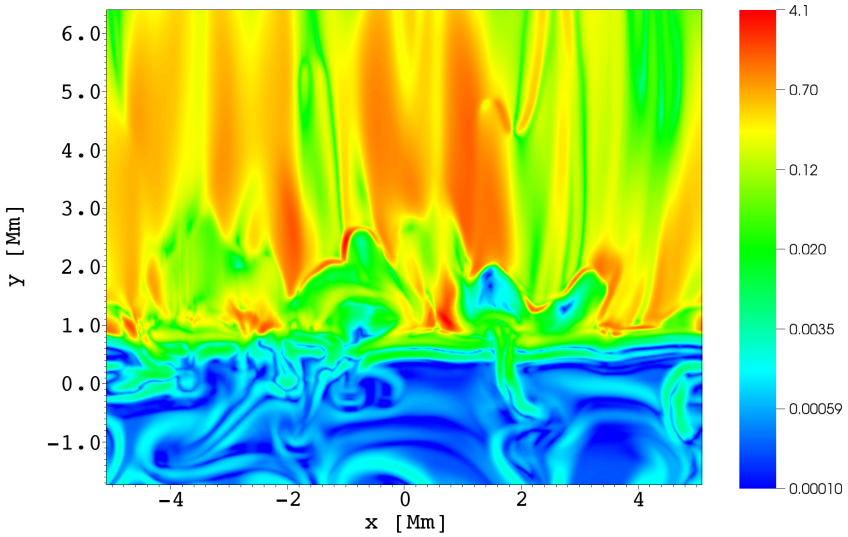

Figure 6: Spatial profile of the absolute difference between ion and neutral velocities ($|V_\mathrm{i} - V_\mathrm{n}|$) expressed in units of 1 km s^{-1} at $t = 5000$ s.

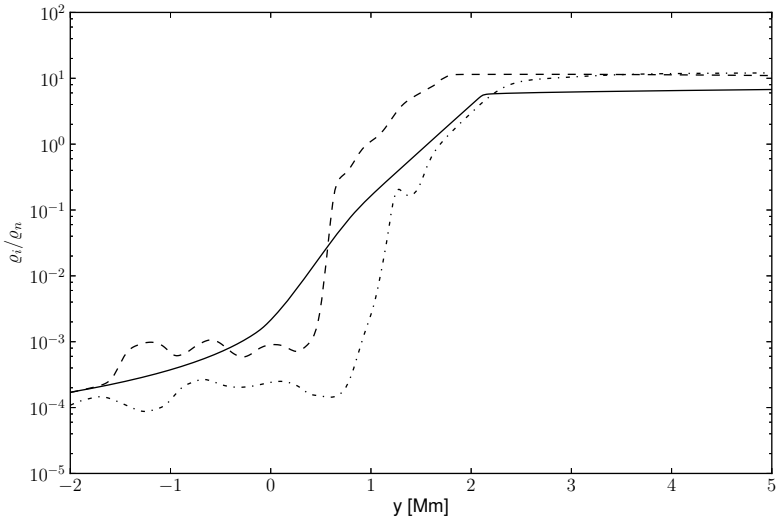

Figure 7: Horizontally averaged vertical profile of ionization, $\varrho_\mathrm{i}/\varrho_\mathrm{n}$, at $t = 0$ s (solid line), $t = 2000$ s (dashed line) and $t = 4000$ s (dash-dotted line).

of the solar atmosphere which agree with the numerical results of Kuźma et al. (2019) who found that for acoustic waves of their waveperiods longer than 80 s the plasma heating decreases.

Figure 7 illustrates vertical profile of horizontally averaged ionization, $\varrho_\mathrm{i}/\varrho_\mathrm{n}$, at three moments of time, namely at $t = 0$ s (solid line), that is initial ionization, at $t = 2000$ s (dashed line) and $t = 4000$ s (dotted line), that corresponds to fully developed and ongoing granulation. From this plot we can see, that $\varrho_\mathrm{i}/\varrho_\mathrm{n}$ drops about one order of magnitude in the upper chromosphere. The ionization level in

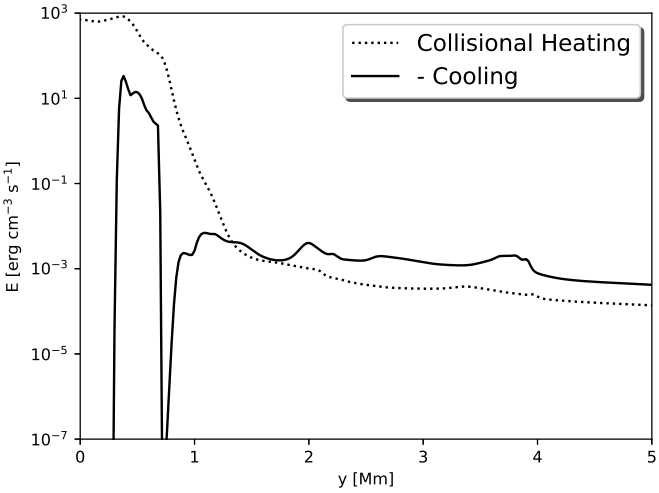

Figure 8: Horizontally averaged vertical profiles of collisional heating (dotted line) and minus cooling term (solid line) vs height y, drawn at $t = 5000$ s.

the photosphere, lower chromosphere and corona remains close to its initial value.

The numerically obtained quasi-stationary solar atmosphere is the result of subtle balance between radiative cooling, thermal conduction and energy dissipation mechanisms. This equilibrium is illustrated on Fig. 8 in the form of horizontally averaged collisional heating and minus cooling rates vs height. Note, that by definition heating rate attains positive, while cooling negative values. Deep below the photosphere heating from the deeper layers overcomes cooling, and leads to hot plasma upflows in the convectively unstable layer. At the photosphere, that is for $0 < y < 0.5$ Mm, the optical opacity abruptly falls off and hot plasma rapidly radiates its energy. Henceforth, the heating term overwhelms the cooling term in this layer. Higher up, i.e. in the chromosphere and low corona, these two terms reaches a similar value, with cooling term being slightly dominant in the corona. It is demonstrated that the wave energy dissipation, supplemented by viscous and ohmic heatings, is sufficient to balance radiative and thermal energy losses above the photosphere, and to sustain a quasi-stationary solar atmosphere.

Figure 9 shows temporal evolution of horizontally averaged $T_{\rm i}$. We see that, as a result of cooling-heating balance in the chromosphere, the system arrives to a quasi-equilibrium state of the solar atmosphere. The chromosphere in our simulations is a highly dynamic medium filled with jets and spicules that transport mass to balance losses due to plasma outflows (Wójcik et al. 2019b). The well-defined transition region oscillates close to its initial position at $y = 2.1$ Mm.

Figure 10 reveals that the radiative cooling and thermal energy losses are in a balance with collisional heating, sustaining a quasi-stationary atmo-

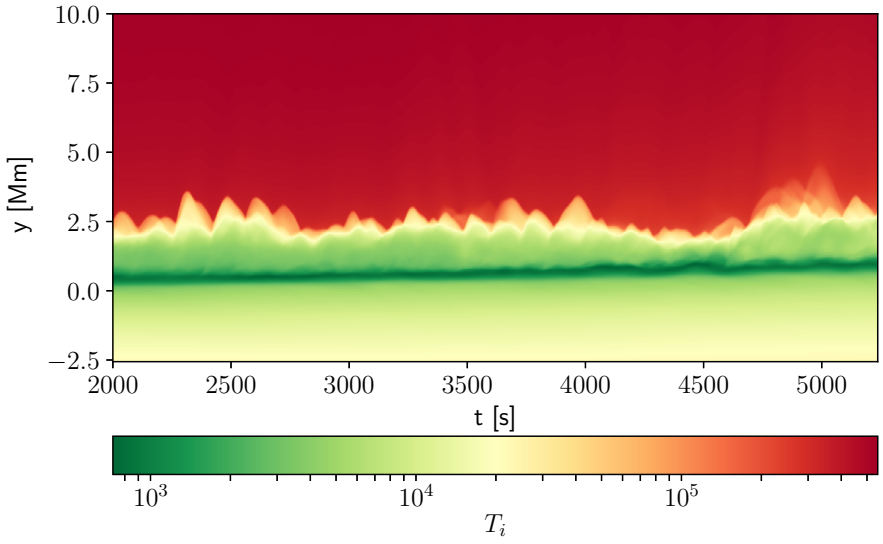

Figure 9: Time distance plot of the horizontally averaged T_i.

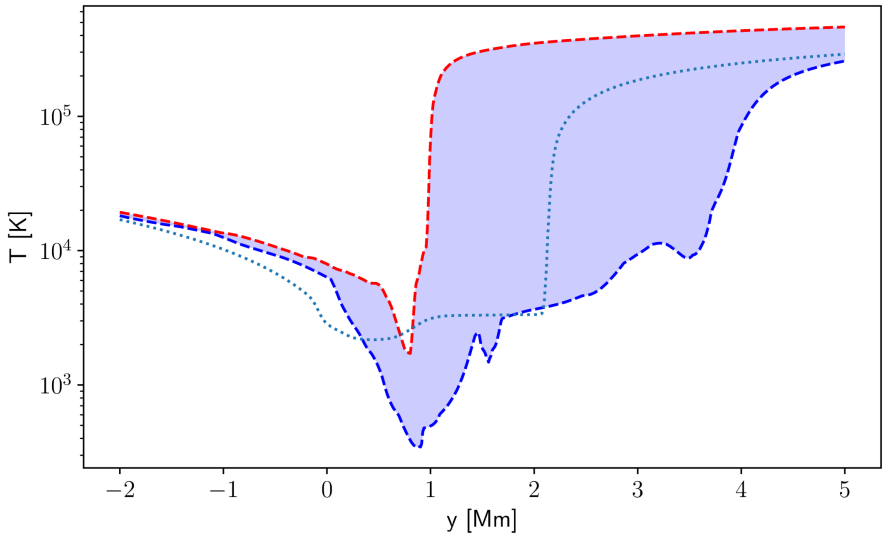

Figure 10: Numerically obtained minimum of $T_\mathrm{i}(y)$ (blue dashed line), maximum of $T_\mathrm{i}(y)$ (red dashed line) at $x = 0$, and semi-empirical data of Avrett & Loeser (2008) (dotted line) vs height.

sphere with the transition region located around $y = 2.1$ Mm. As a result of this balance, the numerically obtained vertical profile of ion temperature is close to the semi-empirical data of Avrett & Loeser (2008). A better fit would require tuning the inflow or the extra heating which we impose below the photosphere. However, such parametric studies are very costly as they require a number of jobs to be run. It must be pointed out that this agreement was obtained without invoking shocks that were previously considered as the main sources of local heating in the solar chromo-

sphere (e.g., Ulmschneider et al. 1978, Carlsson & Stein 1995, Fawzy et al. 2002). Such shocks are occasionally generated in the top chromosphere. Actually, our results show that the efficient wave heating by ion-neutral collisions and with some additions from viscous and ohmic heatings prevents shock formation in the lower and middle chromosphere. Thus, a new insight into the wave heating problem is our demonstration that the waves dissipate their energy without forming shocks; another important aspect of this result is that short period waves, which were the main sources of heating of the lower chromosphere in the previous work cited above, can now reach much higher layers of the chromosphere, including the transition region and corona. Our results allow us to obtain the averaged temperature distribution very similar to that in the semi-empirical model of Avrett & Loeser (2008), which is a good confirmation of validity of our approach and the code used to perform the simulations. Moreover, we also demonstrate how the ion temperature varies locally in the chromosphere, and the predicted range is consistent with the results of the numerical simulations reported by Carlsson & Stein (1995). The latter show that temperature variation grows with height, attaining largest values in the low corona. Figure 10 presents a similar trend, albeit the temperature variations are smaller than these of Carlsson & Stein (1995), which may result from the presence of ions and neutrals in the model we developed.

Recent observations of Grant et al. (2018) showed that Alfvén waves are steepening into shocks at lower heights of the solar atmosphere. With observed local temperature enhancements of 5% it is the first observational evidence of Alfvén waves heating chromospheric plasma in a sunspot umbra through the formation of shock fronts. In our simulations, thermal energy is released during collisions between ions and neutrals which may lead to ion-neutral velocity drift, and this is a pure two-fluid effect. In the case of a shock, kinetic energy at the front of this shock is converted to thermal energy as a result of the friction between ion+electron fluid and neutral species. This phenomenon takes place not only at a shock but also at all other waves in general. However, it is more efficient for steeper wave profiles and its impact on overlaying plasma temperature depends on ion-neutral drift. So, in conclusion it is largest in the case of shocks.

Finally, it must also be emphasized that similar code was used by Wójcik et al. (2019 a,b) to propose that the solar wind origin is associated with granulation and to predict theoretically the variations of acoustic cutoff frequency in the solar atmosphere and that these variations are in a good agreement with the observational results obtained by Wiśniewska et al. (2016) and Kayshap et al. (2018). This is another independent verification of the validity of our approach and the code, and it shows that the effects of partial ionization become very important in lower and middle chromospheric layers.

4. Conclusions

We performed numerical simulations of two-fluid waves in a partially ionized solar atmosphere with radiation and thermal conduction taken self-consistently into account. The considered neutral acoustic-gravity, Alfvén and ion magnetoacoustic-gravity waves were generated by spontaneously evolving and self-organizing convection with granulation cells. We found that the granulation excites a wide spectrum of wave-periods (Fig. 5, bottom) and that only sufficiently short period acoustic and long period gravity waves propagate through the atmosphere and reach the corona (Vigeesh et al. 2017).

A part of energy carried by these waves is dissipated in the photosphere and in the chromosphere due to ion-neutral collisions. As a result, these two-fluid waves generated by the granulation effectively heat the plasma, compensating radiative and thermal energy losses there. The atmosphere gets also extra heat from viscosity and magnetic diffusivity, which are most effective at the places of sheared flow and opposite orientated magnetic field lines. It takes place at the downdrafts below the photosphere, contributing to plasma temperatures there and leading to a quasi-stationary solar atmosphere with its temperature distribution being close to the semi-empirical model of Avrett & Loeser (2008).

This is the first time when the agreement with the observationally based semi-empirical model was obtained without involving heating by shocks, we conclude that our results unravel the main mechanism of the wave heating quiet regions of the chromosphere, and that the basic physical processes of this mechanism are collisions between neutrals and ions. Our conclusion has important implications on constructing theoretical solar atmospheric models in the near future as it shows that the effects of partially ionized plasma must be included in these models and that they may prevent the shock formation, which was a dominant physical process for waves in a fully ionized solar atmosphere.

Acknowledgements The JOANNA code was developed by Darek Wójcik. This work was done within the framework of the projects from the Polish Science Center (NCN) Grant Nos. 2017/25/B/ST9/00506 and 2017/27/N/ST9/01798.

References

Abbett, W. P., & Fisher, G. H. 2012, Sol. Phys., 277, 3

Avrett, E., & Loeser, R. 2008, ApJS, 175, 229

Ballester, J. L., Alexeev, I., Collados, M., et al. 2018, Space Science Reviews, 214, 58B

Braginskii, S. 1965, Reviews of Plasma Physics, 1, 205

Carlsson, M., & Stein, R. F. 1995, ApJ, 440, L29

Chatterjee, P. 2018, arXiv e-prints, arXiv:1806.08166

Courant, R., Friedrichs, K., & Lewy, H. 1928, Mathematische Annalen, 100, 32

Cox, D. P. & Tucker, W. H. 1969, ApJ, 157, 1157

Dedner, A., Kemm, F., Kröner, D., et al. 2002, Journal of Computational Physics, 175, 645

Durran, D. R. 2010, Numerical Methods for Fluid Dynamics by Dale R. Durran. New York: Springer

Fawzy, D., Stępień, K., Ulmschneider, P., et al. 2002, A&A, 386, 994

Grant, S. D. T., Jess, D. B., Zaqarashvili, T. V., et al. 2018, Nature Physics, 14, 480

Hillier, A., Takasao, S., & Nakamura, N. 2016, A&A, 591, A112

Hollweg, J. V. 1986, ApJ, 306, 730

Jess, D. B., Mathioudakis, M., Erdélyi, R., et al. 2009, Science, 323, 1582

Kayshap, P., Murawski, K., Srivastava, A. K., et al. 2018, MNRAS, 479, 5512

Khomenko, E. 2017, Plasma Physics and Controlled Fusion, 59

Khomenko, E., Vitas, N., Collados, M., et al. 2018, A&A, 618, A87

Kuźma, B., Wójcik, D., Murawski, K. 2019a, ApJ, 878, 81

Kuźma, B., Wójcik, D., Murawski, K., Poedts, S., Yuan, D., 2019b, in preparation

Lamb, H. 1909, Proc. R. Soc., s2-7, 122

Leake, J. E., Lukin, V. S., Linton, M. G., Meier, E. T. 2012, ApJ, 760, 109

Low, B. C. 1985, ApJ, 293, 31

Maneva, Y. G., Alvarez Laguna, A., Lani, A., et al. 2017, ApJ, 836, 197

Martínez-Sykora, J., Pontieu, B. D., Hansteen, V. H., et al. 2017, Science, 356, 1269

Martínez-Gómez, D., Soler, R., & Terradas, J. 2018, ApJ, 856, 16M

Matsumoto, T., & Kitai, R. 2010, ApJ, 716, L19

Miyoshi, T., & Kusano, K. 2005, JCP, 208, 315

Moore, R. L., & Fung, P. C. W. 1972, Sol. Phys., 23, 78

Murawski, K. 1992, Sol. Phys., 139, 279

Murawski, K., Musielak, Z. E., Konkol, P., et al. 2016, ApJ, 827, 37

Musielak, Z. E., Musielak, D. E., & Mobashi, H. 2006, Phys. Rev. E, 73, 036612-1

Musielak, Z. E., Rosner, R., Stein, R. F., et al. 1994, ApJ, 423, 474

Musielak, Z. E., & Ulmschneider, P. 2001, A&A, 370, 541

Oliver, R., Soler, R., Terradas, J., & Zaqarashvili, T. V. 2016, ApJ, 818, 128

Popescu Braileanu, B., Lukin, V. S., Khomenko, E., et al. 2019, A&A, 627, A25

Roberts, B. 2004, Proceedings of 'SOHO 13 Waves, Oscillations and Small-scale Transients Events in the Solar Atmosphere: Joint View from SOHO and TRACE', Compiled by: H. Lacoste, p. 1

Shestov, S. V., Nakariakov, V. M., Ulyanov, A. S., Reva, A. A., & Kuzin, S. V. 2017, ApJ, 840, 64

Soler, R., Carbonell, M., & Ballester, J. L. 2013, ApJS, 209, 16

Spitzer, L. 1962, Physics of Fully Ionized Gases, Dover, New York

Srivastava, A. K., Murawski, K., Kuźma, B., et al. 2018, Nature Astronomy, 2, 951

Ulmschneider, R., Schmitz, F., Kalkofen, W., et al. 1978, A&A, 70, 487

Vernazza, J. E., Avrett, E. H., & Loeser, R. 1981, ApJS, 45, 635

Vigeesh, G., Jackiewicz, J., & Steiner, O. 2017, ApJ, 835, 148

Vögler, A., Bruls J. H. M. J., & Schüssler, M. 2004, A&A, 421, 741

Vranjes, J. & Krstic, P. S. 2013, A&A, 554, A22

Wiśniewska, A., Musielak, Z. E., Staiger, J., et al. 2016, ApJ, 819, L23

Wójcik, D., Murawski, K., & Musielak, Z. E. 2018, MNRAS, 481, 262

Wójcik, D., Murawski, K., & Musielak, Z. E. 2019, ApJ, 882, 1

Wójcik, D., Kuźma, B., Murawski, K., & Srivastava, A. K. 2019, ApJ, 884,2

Zaqarashvili, T. V., & Roberts, B. 2006, A&A, 452, 1053

Zaqarashvili, T. V., Khodachenko, M. L., & Rucker, H. O. 2011, A&A, 534, A93

Zaqarashvili, T. V., Khodachenko, M. L., & Soler, R. 2013, A&A, 549, A113